



UNIVERSITY
OF TRENTO - Italy
DEPARTMENT OF INDUSTRIAL ENGINEERING

XXXI cycle

Doctoral School in Materials, Mechatronics
and Systems Engineering

XRF/XRD
COMBINED SPECTROSCOPY
for material characterization
in the fields of
Material science and Cultural heritage

Damiano Martorelli

XRF/XRD
COMBINED SPECTROSCOPY
for material characterization
in the fields of
Material science and Cultural heritage

DAMIANO MARTORELLI
MARTORELLI.DAMIANO@GMAIL.COM

APPROVED BY:

PROF. LUCA LUTTEROTTI, ADVISOR
DEPARTMENT OF INDUSTRIAL ENGINEERING
UNIVERSITY OF TRENTO, ITALY

DR. GIANCARLO PEPPONI, PhD, ADVISOR
FBK-CMM
FONDAZIONE BRUNO KESSLER, ITALY

PH.D. COMMISSION:

PROF. QUARANTA, ALBERTO,
DEPARTMENT OF IND. ENGINEERING
UNIVERSITY OF TRENTO, ITALY

PROF. DIPL. ING. STRELI, CHRISTINA,
ATOMINSTITUT
TU WIEN, AUSTRIA

SIANO, SALVATORE, PhD
ISTITUTO DI FISICA APPLICATA
“NELLO CARRARA”, ITALY

UNIVERSITY OF TRENTO
DEPARTMENT OF INDUSTRIAL ENGINEERING
[SEPTEMBER 2019]

University of Trento - Department of Industrial Engineering

Doctoral Thesis

Damiano Martorelli - 2019

Published in Trento (Italy) – by University of Trento

ISBN: - - - - -

To my parents

ABSTRACT

Every investigation technique has its specific advantages: this is the reason why, in modern research, it is common to combine many investigation techniques – especially the non-destructive ones - to achieve deeper structural information about a sample.

X-ray diffraction (XRD) and fluorescence (XRF) techniques are useful non-destructive analytical techniques, with application not only in industrial field and mining but also in environmental control and cultural heritage monitoring and conservation.

In the present research, the advantages of a combined approach with XRF and XRD techniques are considered, due to their complementarity, and a new method of combining data is presented, executing the simultaneous computation of the refinement both for XRF and XRD. In this case, instead of the common approach with an iterative refinement, passing from XRF to XRD and vice versa, both XRF and XRD data are processed simultaneously with a combined Rietveld refinement.

This innovative approach has been implemented in the program MAUD, combining original XRD algorithm with the XRF module implementation from the GimPy and JGIXA programs, creating comprehensive radiation–matter interaction model, which takes care of both elastic scattering and photoelectric absorption/fluorescence.

Moreover, through a plugin-based application container, Eagle-X, specifically developed for this research project, some easy external wizards have been developed using JAVA language for preliminary XRF analysis and model set-up, which will be in the next future integrated into the MAUD current interface.

This new approach has been applied to two case studies.

The first study was in the cultural heritage field with the analysis of ancient Venetian coins, called *sesimi*, which were never investigated before.

These coins were widely used in the Venetian Republic over a time span ranging from the second half of the 16th until the early years of the 17th century. The rationale of the study was to establish a multilayer model that once validated could be used for fully non-destructive characterization of similar items. The approach, applied to 20 samples from different time periods, has given interesting results. First, the actual composition of the copper-based alloy used for these specific types of Venetian coin has been measured for the first time, using a three-layer model, with also direct measurements on the coin cross-section for validating the data obtained. Second, the detailed characterization of the coins provided essential background knowledge for fully non-

destructive characterization of the same kind of coins. Third, the data obtained were very interesting from a historical point of view, because the silver depletion, which this research has investigated over the coin series, reflects a political and economic situation in strong evolution for the Venetian Republic in the second half of 16th century. Political and economic competitors and a continuous effort in military confrontations obliged Venice to revise its coin system and values not only for *sesini* but also for the other silver-based coins, with larger value, in a process called debasement.

The second application of the combined approach regarded an industrial application concerning a sintered titanium alloy, Ti6AlV4, that has the widest use (about 45% of the total production), because of good machinability and excellent mechanical properties. This is an alloy which contains the two allotropic forms of Ti, the Ti- α , which has compact hexagonal cell, stable at room temperature, and Ti- β phase, which has a body-centered cubic lattice, stable over 882°C. The presence of the two phases is related to the presence of atomic elements which are α - and β -stabilizers.

In this case study six samples, produced with Selective Laser Melting (SLM) technology, with different production parameters, has been considered, and a model based on a surface layer of compact oxide and a bulk with the alloy only has been adopted. The model has evidenced the presence of the TiO₂ oxide on the surface, as attended from existing literature, and confirmed the quality of the alloy because for all the samples, the investigated areas report Al e V content inside the ranges required by ASTM and ISO specifications.

The analysis has allowed also to investigate the presence of contaminants like copper due to the cutting process by Electrical Discharge Machining (EDM), and to find a correlation between the content of Ti- β phase inside the samples and the combined presence of iron and silicon, which increases as soon as increase also the two elements. Moreover, the increase of Ti- β phase is boosted by the contemporary increase in energy density during SLM production process. This is consistent with the fact that higher energy allows a higher localized temperature in SLM process and the equilibrium fraction of β phase rises at high temperatures. This then leads to a higher fraction of α + β phases at room temperature and, because the cooling rate was the same for all samples, this means a higher fraction of β phase at room temperature.

The application of the technique to the two case studies is very productive from the informational point of view, but a critical aspect for a successful application of the technique is the sample.

No preparation is virtually needed for analysis but, of course, this is immediately true for industrial components as soon as they are produced, but it is not so true for archaeological artefacts, where the condition of production, history and store conditions are unknown.

Corrosion patinas can alter the read of the data, and some care must be taken for analysis, not only because the patinas may not be homogenous, but also because the depth of penetration for XRF and XRD are not the same, respect to the same substrate.

The cleaning of the artefacts is not always possible or desired by the owners, so this can at first stage complicate the approach to combined analysis, regarding the model to be adopted in material simulation for data interpretation.

In any case, the combined analysis remains a valid approach provided that the user is conscious of the limits in terms of depth of analysis, linked to the analysis tool (X-ray beam, detector, etc...) and to the surface conditions of the sample.

TABLE OF CONTENTS

ABSTRACT	7
TABLE OF CONTENTS	11
1 INTRODUCTION	15
1.1 WORK PLAN	15
2 X-RAY FLUORESCENCE	17
2.1 THE BASICS FROM THEORY	17
2.1.1 <i>Energy dispersive XRF (ED-XRF)</i>	18
2.2 THE SHERMAN EQUATION	18
2.2.1 <i>Infinite thickness approximation</i>	22
2.2.2 <i>Thin layer approximation</i>	23
2.2.3 <i>Enhancement effect</i>	24
2.3 XRF DETECTION	24
2.3.1 <i>Silicon Drift Detectors</i>	25
2.3.2 <i>Detector efficiency</i>	28
2.3.3 <i>Detector resolution</i>	29
2.4 MINIMUM DETECTION LIMIT	31
3 X-RAY DIFFRACTION	33
3.1 POLYCRYSTALS X-RAY DIFFRACTION	34
3.2 STRUCTURE DETERMINATION AND QUANTITATIVE ANALYSIS	36
3.3 RIETVELD CLASSICAL METHOD	38
3.4 ANATOMY OF THE CALCULATED INTENSITY	39
3.4.1 <i>Scale factor</i>	40
3.4.2 <i>Lorentz-polarization factor</i>	40
3.4.3 <i>Structure factor</i>	40
3.4.4 <i>Temperature factor</i>	41
3.4.5 <i>Profile shape function</i>	42
3.4.6 <i>Absorption factor</i>	43
3.4.7 <i>Texture weight factor</i>	43
3.4.8 <i>Background contribution</i>	44
3.5 QUALITY OF REFINEMENT	45
4 COMBINED XRF & XRD	47
4.1 COMPLEMENTARITY	47
4.2 CURRENT APPROACH	48
4.3 AN INNOVATIVE APPROACH	49

4.4	MODEL BUILD-UP	50
4.4.1	<i>Phase definition</i>	50
4.4.2	<i>Substitutional element and impurities</i>	52
4.4.3	<i>Texture and strain</i>	53
4.4.4	<i>Problem analysis</i>	54
4.4.5	<i>Software for analysis</i>	55
4.4.6	<i>Elaboration tips</i>	57
5	SOFTWARE DEVELOPMENT	59
5.1	COMMON DEVELOPMENT LIBRARIES	60
5.2	SOFTWARE DEVELOPMENT TOOLS	61
5.3	THE FBK X-RAY JAVA LIBRARY	62
5.4	EAGLE-X	63
5.4.1	<i>Common aspects</i>	65
5.4.2	<i>Periodic table of elements</i>	67
5.4.3	<i>FBK SQLite Viewer</i>	68
5.5	ED-XRF SPECTRUM VIEWER	69
5.5.1	<i>Save Chart</i>	70
5.5.2	<i>Enable/disable mouse wheel and reset zoom</i>	70
5.5.3	<i>Chart parameters</i>	71
5.5.4	<i>Calibration of spectrum</i>	71
5.5.5	<i>Element picking</i>	77
5.6	MATERIAL LIST MANAGER	80
5.7	ED DETECTOR MANAGER	81
5.8	X-RAY BEAM MANAGER	82
5.9	LAYERED SAMPLE MANAGER	83
5.10	EXPERIMENTAL SET-UP MANAGER	84
5.11	LASAX SIMULATOR	85
6	CASE STUDY: VENETIAN <i>SESINI</i>	88
6.1	HISTORICAL CONTEXT	89
6.2	RESEARCH SAMPLES	90
6.2.1	<i>First inspection</i>	92
6.3	EXPERIMENTAL SETUP	95
6.4	FIRST EXPERIMENTAL RESULTS	96
6.4.1	<i>First contact with XRF and XRD</i>	97
6.5	MULTILAYER APPROACH	102
6.5.1	<i>Three-layer model</i>	102
6.5.2	<i>Software implementation</i>	103
6.5.3	<i>Layer model result</i>	104
6.5.4	<i>Qualitative SEM-EDXS surface scan</i>	108
6.6	CROSS TEST OF THE APPROACH	110

6.6.1	XRF-XRD <i>experimental results</i>	112
6.6.2	SEM-EDXS <i>surface analysis</i>	114
6.6.3	<i>Coin section analysis</i>	116
6.7	RESULT DISCUSSION	118
6.7.1	<i>Historical implications</i>	118
6.7.2	<i>Bulk model vs multilayer model</i>	120
7	CASE STUDY: SINTERED ALLOY	125
7.1	INTRODUCTION	125
7.2	TITANIUM	126
7.2.1	<i>Titanium alloys</i>	128
7.3	RESEARCH SAMPLES: TiAl6V4 ALLOY	131
7.3.1	<i>Selective Laser Melting</i>	132
7.4	EXPERIMENTAL SETUP	134
7.5	EXPERIMENTAL RESULTS	135
7.5.1	<i>Combined XRF-XRD analysis</i>	136
7.5.2	<i>SEM-EDXS</i>	139
7.6	RESULT DISCUSSION	140
8	CONCLUSION AND FUTURE PERSPECTIVES	144
A.	APPENDIX – SDD DETECTOR BY KETEK	146
A)	SDD BOX GEOMETRY	147
B)	SDD GEOMETRY	147
C)	OPERATION REQUIREMENTS	149
D)	AXAS-D DETECTOR BEHAVIOUR	150
B.	MACHINE CALIBRATION REFERENCES	152
	BCR 090 TITANIUM WITH ADDED IMPURITIES	152
	NIST 612 GLASS WITH TRACE ELEMENTS	152
	RAUP7 GOLD REFERENCE MATERIAL	153
	MIXTURE Al_2O_3 - TiO_2	153
	INDEXES AND BIBLIOGRAPHY	156
	INDEX OF FIGURES	157
	REFERENCES	162
	SCIENTIFIC PRODUCTION	172
	PARTICIPATION TO CONGRESSES, SCHOOLS AND WORKSHOPS	174
	ACKNOWLEDGEMENTS	178

1 INTRODUCTION

Every investigation technique has its specific advantages, but rarely can cover all the aspect needed for a comprehensive result about a specimen. Moreover, the information desired or needed can change according to the type of the sample.

This is the reason why, in modern research, it is common to proceed with many investigation techniques – especially the non-destructive ones - to achieve a deeper structural information about a generic sample.

X-ray diffraction (XRD) and fluorescence (XRF) techniques are useful non-destructive analytical techniques, with application not only in industrial field and mining [37,100,154], but also in environmental control and cultural heritage monitoring and conservation [42,107].

In the present research, the advantages of a combined approach with XRF and XRD techniques will be considered, due to their complementarity [16,100]: XRD allows structural and crystallographic characterization of polycrystalline mixture, including phase identification and quantification, microstructure and texture analysis; on the other side, XRF allows accurate quantitative chemical characterization of materials.

1.1 Work plan

Firstly, some aspects of X-ray fluorescence (Chapter 2) and X-ray diffraction (Chapter 3) will be shortly recalled.

Then, a new method of combining XRF and XRD data (Chapter 4), executing the simultaneous computation of the refinement both for XRF and XRD, will be presented. In this case, instead of the common approach with an iterative refinement, passing from XRF to XRD and vice versa, both XRF and XRD data are processed simultaneously with a combined Rietveld refinement.

This innovative approach has been implemented in the program MAUD, combining original XRD algorithm with the XRF module implementation from the GimPy and JGIXA programs, creating a comprehensive radiation–matter interaction model, which takes care of both elastic scattering and photoelectric absorption/fluorescence. Moreover, through a plugin-based application container, Eagle-X, specifically developed for this research project, some easy external wizards have been developed for preliminary XRF analysis and model set-up (Chapter 5), which will be in the next future integrated into the MAUD current interface.

After, the application of this new approach to two case studies will be presented: the first one regarding the cultural heritage field with the analysis of ancient Venetian coins (Chapter 6), the second one regarding an industrial application concerning a sintered titanium alloy with different production parameters (Chapter 7).

2 X-RAY FLUORESCENCE

X-ray fluorescence (in the following, XRF) analysis is a non-destructive multi-elemental analysis technique for the determination of almost all the elements present in a sample [80]. Abbott created the first commercial X-ray fluorescence spectrometer in 1948 [6].

After a short recall of the basics of XRF, in the remaining part of the present Chapter we will concentrate only on the energy dispersive technique, used in the case studies.

2.1 The basics from theory

XRF radiation occurs when photons of sufficiently high energy impinge on a sample [81,82]; these primary X-rays undergo different processes with the atoms of the sample material, as recalled in Figure 2.1 [35,89,118].

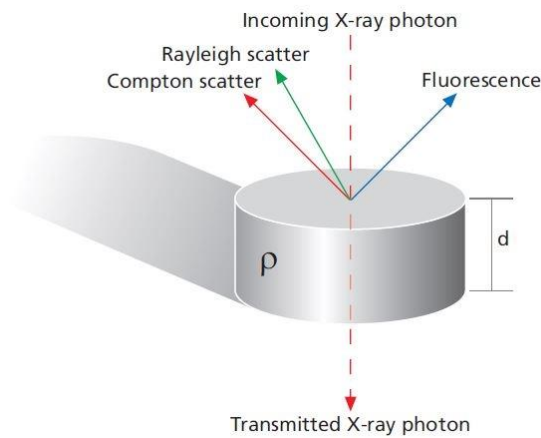


Figure 2.1 The three main interactions of X-rays with matter [18].

The principle of XRF analysis is the measurement of wavelength or energy and intensity of the characteristic photons emitted from the sample under analysis, taking care of the fact that the energy, E , of this radiation is uniquely dependent on the element, which emits the characteristic X-rays by Moseley's law Eq. 2.1:

$$\text{Eq. 2.1} \quad \nu = K \cdot (Z - \sigma)^2$$

This allows the identification of the atomic elements present in the sample and the determination of their concentration. XRF is in principle applicable to all elements except the first two of the periodic table, hydrogen, H, and helium, He, thus covering an energy region from about 50 eV to 100 keV [18,116]. However, many light elements are difficult to measure and require advanced instrumentation, which often limits practical lab work to elements with atomic numbers above 10, i.e. sodium, Na.

The data for the analysis are obtained from the measured spectrum, with all characteristic lines superimposed above a background, generated not only by the unavoidable electronic noise of the detector, but also mainly the elastic and inelastic scattering of the primary radiation on the sample [179,187].

Measurement of the emitted characteristic fluorescence radiation is performed using wavelength-dispersive (WD) and energy-dispersive (ED) spectrometers.

Neither the observed photon energies of fluorescent lines, nor their intensities are noticeably affected by the chemical state of the sample, so that no preparation or only a minimum preparation of the sample is generally required, as is usually the case in optical emission (and absorption) methods; moreover, the materials can be in liquid or solid form [18,149]. If required, possible sample preparation steps may include simple procedures (cutting, grinding, milling, and mixing, or a combination of them) in order to get a homogenous sample. An important issue is that the treatment must be practicable for both samples and standards.

Matrix effects are predictable and correctable through accurate calibration and computation [82,158]. Due to small penetration of the X-rays in the sample, typically from 1 to 1000 μm , the only issue is the homogeneity of the specimen over the depth contributing to the signal.

The technique can be applied successfully in various field, from mining to geology, from archaeology to environmental control, from waste analysis to industrial production quality control.

2.1.1 Energy dispersive XRF (ED-XRF)

In ED-XRF, the X-rays emitted by a sample are detected by a solid-state detector (SSD), which counts the photons reaching its active window, simultaneously sorting them according to energy and storing the result in a multi-channel memory (see Appendix A for an example of SSD detector, used in this research project). The result is recorded as an X-ray *energy* vs. *intensity* spectrum.

In air, the range of detectable elements ranges from sodium, Na ($Z = 11$) for the light elements and goes up to uranium, U ($Z = 92$) on the high atomic number Z side [158].

Nowadays, many ED-XRF spectrometers exist, with different degrees of sophistication, ranging from advanced laboratory instruments to small portable instruments for on-field observations (e.g. in mining or archaeological excavations). They can be designed for analysis of bulk material or for scanning of small areas.

2.2 The Sherman equation

The determination of the elemental concentration in the sample is possible because the detected intensity of fluorescence is proportional to the concentration of the respective element

In 1955, Sherman proposed a mathematical formula to calculate radiation intensity of analyte in a specimen of a known composition when this one is irradiated by a polychromatic X-ray beam.

Later, Shiraiwa and Fujino corrected the enhancement part of this formula by introducing a missing factor of 0.5 [145,158].

The incoming X-rays, to reach position at depth x of a sample, must pass the atoms above them, and the fluorescence must also pass the atoms above to exit and reach the detector (Figure 2.2).

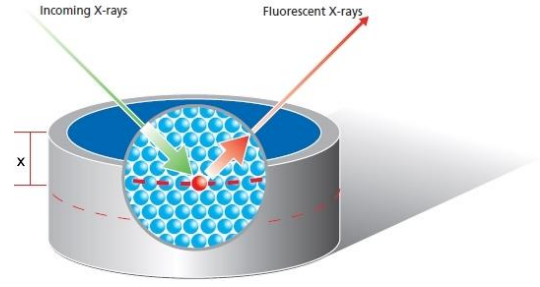


Figure 2.2 Matrix absorption effect [18]

This means that the layer of atoms over the considered one will absorb part of the impinging energy and part of the fluorescent radiation, and the absorption will be related to the atomic number of the elements involved. If for simplicity we assume a point x-ray source and detector, the number of x-ray photons per second emitted by the excitation source in the energy interval E_0 to E_0+dE_0 , within the differential solid angle $d\Omega_0$, are defined as $I_0(E_0)dE_0d\Omega_0$.

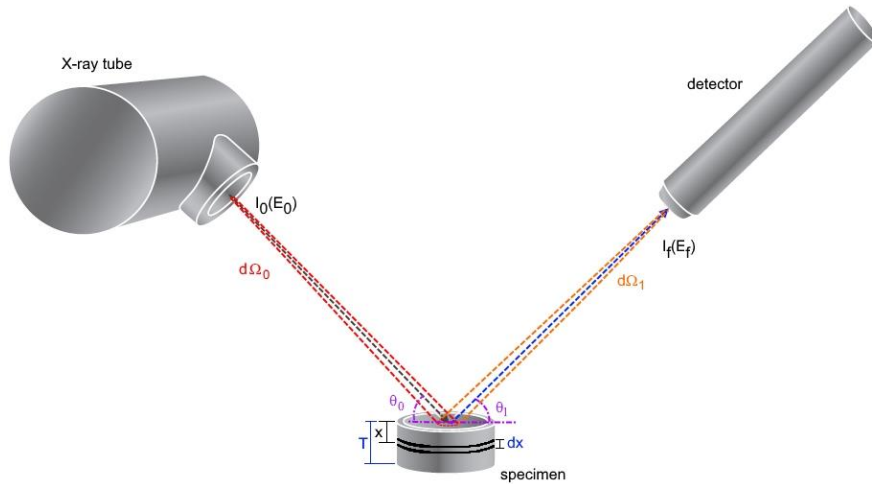


Figure 2.3 Calculation of the intensity characteristic radiation from a homogeneous sample.

These photons imping on the surface of an homogeneous specimen of thickness T at an incidence angle θ_0 , therefore before the radiation reach the atom at deepness x (see Figure 2.3), we have absorption according to the Beer-Lambert law:

$$\text{Eq. 2.2} \quad I_1 = I_0(E_0)dE_0d\Omega_0 e^{-\left(\frac{\mu}{\rho}\right)_s \rho_s \frac{x}{\sin \theta_0}}$$

where $(\mu/\rho)_s$ is the total mass absorption coefficient (in cm^2/g) of the specimen for energy E_0 [82,158]. If now we consider the differential element dx , the number of photoelectric interactions will be described by the following:

$$\text{Eq. 2.3} \quad I_2 = I_1 \left(1 - e^{-\left(\frac{\tau}{\rho}\right)_s \rho_s \frac{dx}{\sin \theta_0}} \right)$$

where $(\tau/\rho)_s$ is the photoelectric mass absorption coefficient (in cm^2/g) of the specimen for energy E_0 . Being dx infinitely small, we can write:

$$\text{Eq. 2.4} \quad I_2 = I_1 \left(\frac{\tau}{\rho} \right)_s \rho_s \frac{dx}{\sin \theta_0}$$

Because we are interested only in the excitation of the i^{th} element of interest, the number of photoelectric interactions to be considered is the following [82]:

$$\text{Eq. 2.5} \quad I_3 = I_2 \frac{w_i \left(\frac{\tau}{\rho} \right)_i}{\left(\frac{\tau}{\rho} \right)_s}$$

I_3 represents the number of ionisation processes occurring in all the shells of the atom of interest (K, L1, L2, L3, M1, etc.).

The processes occurring in one only shell can be evaluated considering the various components of the photoelectric coefficients. Therefore, if we define j as the index of the shell where the vacancy was produced by an excitation energy E_0 greater than the edge energy $E_{\text{edge}, i,j}$, we have the following:

$$\text{Eq. 2.6} \quad I_4 = I_3 \frac{\left(\frac{\tau}{\rho} \right)_{i,j}}{\left(\frac{\tau}{\rho} \right)_s}$$

Combining this equation with the *absorption jump ratio* J_K defined as [171]:

$$\text{Eq. 2.7} \quad J_K = (r_K - 1)/r_K$$

we obtain the following relation [182]:

$$\text{Eq. 2.8} \quad I_4 = I_3 \left(\frac{r_{i,j} - 1}{r_{i,j}} \right)$$

which defines the rate of ionization of the j -shell of the i^{th} element. A fraction of such processes, given by the fluorescent yield for the j -shell of element i , $\omega_{i,j}$, will result in the emission of a characteristic photon and the remaining part will generate Auger electrons.

Moreover, the vacancies in the j -shell can be filled by electrons from the upper levels with different probabilities $p_{i,j,k}$, where the index k is the upper level taking part in the transition. Therefore, the rate of emission of characteristic photons becomes:

$$\text{Eq. 2.9} \quad I_5 = I_4 \omega_{i,j} p_{i,j,k}$$

Because the emission of radiation is isotropic, distributed on the whole solid angle of 4π steradians, if the extension of detector covers a solid angle $d\Omega_i$, as shown in Figure 2.3, and the

emission has an angle of θ_1 , the radiation reaching the surface of the sample towards the detector will be the following [83,158]:

$$\text{Eq. 2.10} \quad I_6 = I_5 \frac{d\Omega_1}{4\pi} e^{-\left(\frac{\mu}{\rho}\right)_{s,E_{i,j,k}} \rho_s \frac{x}{\sin \theta_1}}$$

where $(\mu/\rho)_{s,E_{i,j,k}}$ is the specimen total mass attenuation coefficient for the energy $E_{i,j,k}$, which is the energy of the transition $k \rightarrow j$ for the i^{th} atomic element.

If we define with $\epsilon_{E_{i,j,k}}$ the detector efficiency for recording a photon of energy $E_{i,j,k}$, then the detected photon rate in the detector is the following:

$$\text{Eq. 2.11} \quad I_7 = I_6 \epsilon_{E_{i,j,k}}$$

If we now recombine all the equations derived until now, we obtain the following intensity:

$$\text{Eq. 2.12} \quad I(E_{i,j,k}) = \frac{d\Omega_0 d\Omega_1}{4\pi} \left[I_0(E_0) \cdot e^{-\left(\frac{\mu}{\rho}\right)_s \rho_s \frac{x}{\sin \theta_0}} \cdot W_i \frac{\left(\frac{\tau}{\rho}\right)_s \rho_s}{\sin \theta_0} \left(\frac{r_{ij}-1}{r_{ij}}\right) \cdot e^{-\left(\frac{\mu}{\rho}\right)_{s,E_{i,j,k}} \rho_s \frac{x}{\sin \theta_1}} \cdot \omega_{ij} p_{i,j,k} \epsilon_{E_{i,j,k}} \right] dx dE_0$$

In the derivation the possible attenuations of the x-rays in the path between the source (the X-ray tube) and the sample, and between the sample and the detector were ignored.

Now, Eq. 2.12 has to be integrated with respect to x variable between 0 and the thickness T of the sample in order to get the complete contribution from the specimen [82]. Moreover, if the X-ray source is not monochromatic, we also need an integration with respect to energy between the absorption edge of the shell j for i^{th} element and the maximum energy of the source.

$$\text{Eq. 2.13} \quad I(E_{i,j,k}) = \frac{d\Omega_0 d\Omega_1}{4\pi} \int_0^T \int_{E_{edge,i,j}}^{E_{max}} \left[I_0(E_0) \cdot e^{-\left(\frac{\mu}{\rho}\right)_s \rho_s \frac{x}{\sin \theta_0}} \cdot W_i \frac{\left(\frac{\tau}{\rho}\right)_s \rho_s}{\sin \theta_0} \left(\frac{r_{ij}-1}{r_{ij}}\right) \cdot e^{-\left(\frac{\mu}{\rho}\right)_{s,E_{i,j,k}} \rho_s \frac{x}{\sin \theta_1}} \cdot \omega_{ij} p_{i,j,k} \epsilon_{E_{i,j,k}} \right] dx dE_0$$

If we assume that the sample is homogeneous, we can perform the integration on the thickness for Eq. 2.13 and we obtain the following [118,182]:

$$\text{Eq. 2.14} \quad I(E_{i,j,k}) = \frac{d\Omega_0 d\Omega_1}{4\pi} \int_{E_{edge,i,j}}^{E_{max}} \left[I_0(E_0) \cdot \frac{1 - e^{\left(-\left(\frac{\mu}{\rho}\right)_s \rho_s \frac{T}{\sin \theta_0} - \left(\frac{\mu}{\rho}\right)_{s,E_{i,j,k}} \rho_s \frac{T}{\sin \theta_1} \right)}}{\left(\frac{\mu}{\rho}\right)_s \rho_s \frac{x}{\sin \theta_0} + \left(\frac{\mu}{\rho}\right)_{s,E_{i,j,k}} \rho_s \frac{x}{\sin \theta_1}} \cdot W_i \frac{\left(\frac{\tau}{\rho}\right)_s \rho_s}{\sin \theta_0} \left(\frac{r_{i,j}-1}{r_{i,j}} \right) \omega_{i,j} p_{i,j,k} \varepsilon_{E_{i,j,k}}} \right] dE_0$$

The Eq. 2.14 is valid for the differential solid angles $d\Omega_0$ and $d\Omega_1$, but often the solid angles cannot be considered really infinitesimal: in practical spectrometers, usually large solid angles Ω_0 and Ω_1 are used, and this means that we need to integrate over finite solid angles [82,171].

Furthermore, all the parameters present in Eq. 2.12 cannot often be considered constant over the whole solid angles. For example, the source of X-rays has a finite dimension, and this means that we need to integrate also over the source dimension, in order to be rigorous. The same arguments are valid for the detector size.

Important for the aims of this research work is that the intensity of the radiation is proportional to the concentration of the element in the sample, i.e. his concentration, expressed in the Eq. 2.14 by the weight fraction W_i .

As last remark we remember here that the intensity of the fluorescent radiation coming from a certain atomic element is also dependent on the concentration of the other elements through the total absorption coefficients [145].

This equation is of fundamental importance in XRF analysis for two main reasons: first, it enables to calculate what is measured and second, the Sherman equation can provide the theoretical base of all modern methods for the correction of matrix effects [82,115].

2.2.1 Infinite thickness approximation

In the previous paragraph, we have seen the complexity of the Eq. 2.13. If we suppose that $T \rightarrow \infty$, i.e. the sample has an *infinite thickness*, the Eq. 2.13 simplifies as in the following [171,182]:

$$\text{Eq. 2.15} \quad I(E_{i,j,k}) = \frac{d\Omega_0 d\Omega_1}{4\pi} \times \int_{E_{edge,i,j}}^{E_{max}} \left[\frac{I_0(E_0)}{\left(\frac{\mu}{\rho}\right)_s \rho_s \frac{x}{\sin \theta_0} + \left(\frac{\mu}{\rho}\right)_{s,E_{i,j,k}} \rho_s \frac{x}{\sin \theta_1}} \cdot W_i \frac{\left(\frac{\tau}{\rho}\right)_s \rho_s}{\sin \theta_0} \left(\frac{r_{i,j}-1}{r_{i,j}} \right) \omega_{i,j} p_{i,j,k} \varepsilon_{E_{i,j,k}}} \right] dE_0$$

To decide how thick a real specimen must be in order to allow this approximation, we can calculate the depth x at which the fluoresced intensity reduces to 1% of the intensity produced at the surface of the sample. This means that we must compute the following:

$$\text{Eq. 2.16} \quad 0.01 = e^{\left(-\left(\frac{\mu}{\rho}\right)_s \rho_s \frac{x}{\sin \theta_0} - \left(\frac{\mu}{\rho}\right)_{s,E_{i,j,k}} \rho_s \frac{x}{\sin \theta_1}\right)}$$

This give the desired thickness $T_{1\%}$ as the following:

$$\text{Eq. 2.17} \quad T_{1\%} = \frac{-\ln 0.01}{\rho_s \left(\left(\frac{\mu}{\rho}\right)_s \frac{1}{\sin \theta_0} + \left(\frac{\mu}{\rho}\right)_{s,E_{i,j,k}} \frac{1}{\sin \theta_1} \right)}$$

If the specimen thickness is greater than $T_{1\%}$, then the approximation is licit. In any case, the criterion is related to the X-ray line considered. If we have a sample with various atomic elements, the one with the higher atomic number must be considered as reference for evaluation, because its characteristic radiation is the least affected by the absorption.

2.2.2 Thin layer approximation

Another common approach is the so-called *thin layer approximation*: in this case, the absorption in the specimen is completely ignored, and this means that we take the limit of $T \rightarrow 0$ of Eq. 2.13. The new equation is, therefore:

$$\text{Eq. 2.18} \quad I(E_{i,j,k}) = \frac{d\Omega_0 d\Omega_1}{4\pi} \int_{E_{edge,i,j}}^{E_{max}} \left[I_0(E_0) W_i \frac{\left(\frac{\tau}{\rho}\right)_s \rho_s}{\sin \theta_0} \left(\frac{r_{i,j}-1}{r_{i,j}}\right) \omega_{i,j} p_{i,j,k} \varepsilon_{E_{i,j,k}} \right] T dE_0$$

To calculate the thickness of the sample to get at least 99% of radiation going through, we need to solve the following equation:

$$\text{Eq. 2.19} \quad 0.99 = e^{\left(-\left(\frac{\mu}{\rho}\right)_s \rho_s \frac{x}{\sin \theta_0} - \left(\frac{\mu}{\rho}\right)_{s,E_{i,j,k}} \rho_s \frac{x}{\sin \theta_1}\right)}$$

This give the desired thickness $T_{99\%}$ as reference, solving the following:

$$\text{Eq. 2.20} \quad T_{99\%} = \frac{-\ln 0.99}{\rho_s \left(\left(\frac{\mu}{\rho}\right)_s \frac{1}{\sin \theta_0} + \left(\frac{\mu}{\rho}\right)_{s,E_{i,j,k}} \frac{1}{\sin \theta_1} \right)}$$

As opposed to the infinite thickness approximation, in this approach we must consider the element of interest with the lower atomic number in the calculation, because its characteristic radiation will be the most strongly absorbed.

2.2.3 Enhancement effect

The enhancement effect is illustrated in Figure 2.4: in this case, the incoming radiation excites an atom, but the outgoing (primary) fluorescent radiation can exit from the sample or contribute

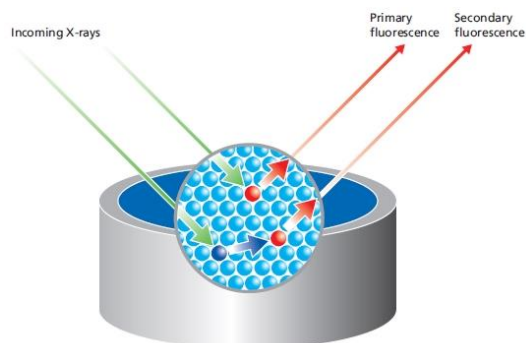


Figure 2.4 Matrix enhancements effect [18]

in activating the fluorescence, called *secondary fluorescence*, of other atomic elements, whose presence will be then enhanced on the spectrum and will appear in greater concentration than real [18,115].

Moreover, a second level of interaction can be observed, when secondary fluorescent photons excite again another atom, generating a *tertiary fluorescent photon*. Higher levels of interactions are

possible but have no practical importance.

In the range of transition atomic elements, secondary excitation is particularly evident for atomic elements with atomic number Z differing by 2. Stainless steel (Cr–Fe–Ni) is a good example for demonstrating the secondary effect ($\text{Fe} \rightarrow \text{Cr}$, $\text{Ni} \rightarrow \text{Cr}$, and $\text{Ni} \rightarrow \text{Fe}$) as well as tertiary excitation ($\text{Ni} \rightarrow \text{Fe} \rightarrow \text{Cr}$). The actual contributions sum up to 30% from secondary excitation and up to 2÷3% from tertiary excitation [82,171], so the last one is usually considered negligible.

Excitation effects in the range of light elements appear to be of considerable importance, when direct excitation is inefficient, but their mathematical treatment is complex. All excitation processes, which create fluorescence in addition to primary fluorescent photons, are also called *indirect excitation* [158].

2.3 XRF detection

X-ray detectors are devices used to measure the flux, spectrum, and/or other properties of X-rays. Detectors can be divided into two major categories:

- imaging detectors, e.g. photographic plates and X-ray photographic films now mostly replaced by various digitizing devices;
- single channel devices, e.g. Solid-State Detectors (SSD), ionization chambers, Geiger counters, and dosimeters, which are used to measure the local radiation exposure, dose, and/or dose rate, in order to verify, for example, radiation protection equipment.

For the scope of this work, we concentrate briefly on single channel. All of them use the interaction of X-ray with matter [82] and, in this context, we can distinguish two classes [32]:

- direct detectors, so-called because they directly convert X-ray photons to electrical charge and then in a digital image;
- indirect detectors, which have intervening steps, for example first converting X-Ray photons to visible light, and then an electronic signal.

In the first class we have semiconductor detectors, among which we cite here the following examples:

- Liquid-nitrogen-cooled Si(Li) detectors, one of the most old type yet used, having their best performance for X-rays in range $1\div 25$ keV;
- planar high-purity Ge detectors, preferable for analysis *K*-lines from heavier elements (30–100 keV);
- CdTe and CdZnTe detectors, used and under further development for some application (e.g. medical diagnostics);
- Silicon Drift Detectors (SDDs), where charges are collected with the sideward drift, based on the principle of sideward depletion introduced by Gatti and Rehak in 1984 [112].

In the second class we have:

- gas detectors, where the exchange of energy occurs between the incident photons and gas atoms or molecules. These are useful for ionisation chambers, proportional counters or Geiger-Mueller counters. These detectors have a low efficiency for high energy photons because of the low density of the gas and are used in the region $\lambda > 0.2$ nm.
- scintillation detectors, which exploit thallium-doped sodium iodide [NaI(Tl)]; the higher density make them efficient for high energy photons, in the region where $\lambda < 0.2$ nm.

In the next paragraphs, we will deepen a bit more the working principles of Solid-State Detectors, which were used in the case studies for XRF analysis, and then we will resume the concept of detector efficiency already encountered in Eq. 2.11.

2.3.1 Silicon Drift Detectors

Semiconductor detectors are well suited for detection and measurement of the energy of ionizing radiation caused by interaction with charged particles and (X-ray) photons. Precise position, time and energy measurement can easily be combined [112].

If we consider silicon, having a band gap of 1.12 eV, an average energy of 3.6 eV is needed for creation of a pair [113].

In the simplest detector, a reversely biased diode (see Figure 2.5), electrons and holes will be separated by the electric field within the space charge region and collected at the electrodes on opposite sides of the diode [112,113].

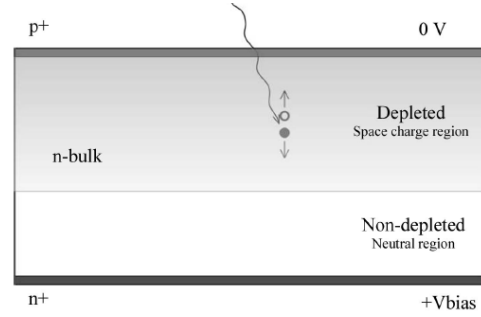


Figure 2.5 Schematic structure of a reversely biased semiconductor diode used as a photon detector [112]

The small band gap and the corresponding large signal charge generated in the photon absorption process give excellent properties to semiconductor radiation detectors, with very good spectroscopic resolution down to low energies. Moreover, we have short charge collection time due to high charge carrier mobility combined with small detector volume, and the mechanical rigidity allows operation in a vacuum. Consequently, we can have very thin entrance windows and high quantum efficiency down to low energies. The high quality reached in the technology of semiconductor doping allows construction of detectors with sophisticated electric field configurations and intrinsically new properties. This is accompanied by developments in electronics coupled to the detector.

In this context the innovative idea of Silicon Drift Detectors (SDDs) was conceived. This device, schematically presented in Figure 2.6, is built with a special way of collecting charges with the sideward drift, based on the principle of sideward depletion introduced by Gatti and Rehak in 1984 [26,112].

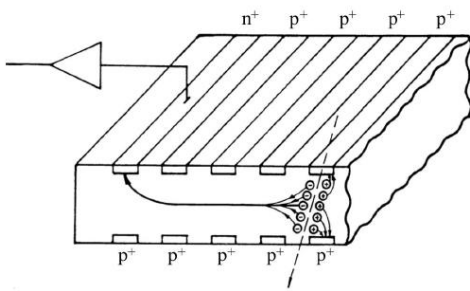


Figure 2.6 Semiconductor drift chamber structure using the sideward depletion method [112].

Fully depleting the device by applying a reverse bias voltage between p - and n -contacts generates an electron potential valley in the middle plane of the detector. Thus, electrons generated by an impinging photon will collect themselves in this area and subsequently move until they reach the n -doped anode.

In order to get a faster and controlled collection, a horizontal drift field is added which drives the generated electrons towards the n^+ anode, connected to detector electronics. This effect is obtained because the diodes are divided into strips and raising voltages are applied from strip to strip [93,112,113].

This device can measure position by calculating the time difference between particle interaction and arrival of the signal at the anode, as well as the energy of particle. In most applications the latter aspect is the most important one.

The early SDD used drift rings on both sides to produce the radial field, and a variety of SDD have been developed for specific applications.

In 1987, Kemmer introduced a new design using only a planar contact on one side with drift rings on the opposite side: in this way, only one structured surface provides the drift field in the valley which is now at an angle with respect to the wafer surface (see Figure 2.7).

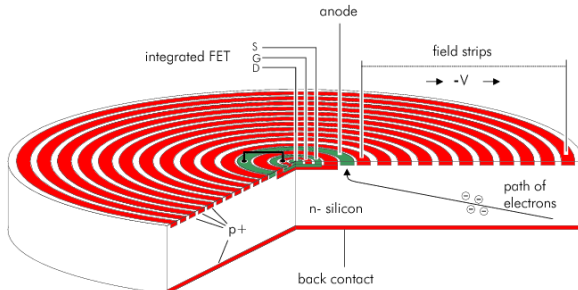


Figure 2.7 Cylindrical silicon drift chamber with an integrated amplifier for spectroscopic applications [112].

This new type of SDD is much easier to fabricate: having only one surface structured brings about the possibility of using the unstructured surface of the fully depleted device as radiation entrance window. Moreover, using a circular geometry with a very small charge-collecting anode in its centre reduces the capacitive load to the amplifier and therefore the noise in the signal [112,113]. The amount of noise depends on the detector parameters: to get better resolution, leakage current and output capacitance should be minimized [63]. The leakage current of a detector has three components:

- bulk generation current: this is caused by thermal generation;
- diffusion leakage current: this is caused by minority carrier's diffusion from undepleted areas to the depletion region;
- surface generation current caused by defects on the surface during processing.

Surface leakage current increases with detector area and can surpass the bulk leakage current by a factor of 3÷8.

In order to lower the surface leakage current contribution, fabrication process have been optimized: nowadays there are many commercially available SDD with and without integrated pre-amplifier, assembled also with a Peltier cooler in a gas-tight housing with thin radiation entrance window (see Figure 2.8), usually in beryllium which

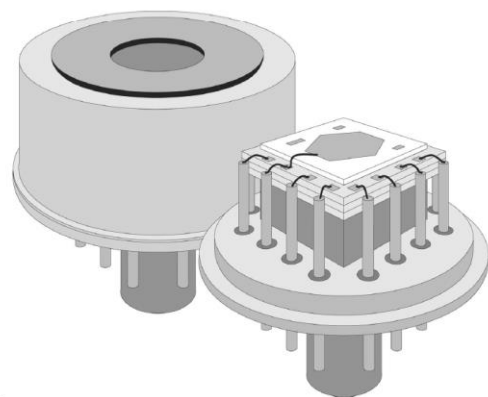


Figure 2.8 Single-sided structured SDD with integrated transistor, cooled by a Peltier element [112].

conjugates lowest atomic number and mechanical properties. Also, for the present research, a Peltier-cooled SDD, produced by Ketek, has been used for XRF detection, and its characteristics are summarized in Appendix A.

Different geometries have been developed in recent times for special application: for example, a ‘droplet’ geometry, where the collecting anode and transistor are outside the sensitive area, avoids the problem of the small centre region, where some electrons may reach the clear contact instead of the collecting anode [93].

The development of the McDrift (Multichannel Drift detector) gives response to the need of larger sensitive area using 5 mm² SDD [92,112]: it is a gapless arrangement of many SDDs with individual readout, but with common voltage supply, entrance window, and guard ring structure. It allows to fill any area without losing energy resolution and count rate capability. The 2D shape of these detectors can be adapted to the specific experiment.

2.3.2 Detector efficiency

A photon impinging on the detector must cross some barriers in order to reach the active part of the detector (see Figure 2.9): the vacuum window of the package (Beryllium, silicon nitride, graphite); a possible contact layer or optical barrier (gold, aluminium, nickel, ...), an inactive semiconductor region where the field is not yet strong enough to drive the charge in the wanted direction [151].

Moreover, a high energy photon may not be absorbed by the silicon crystal and leave it without being detected.

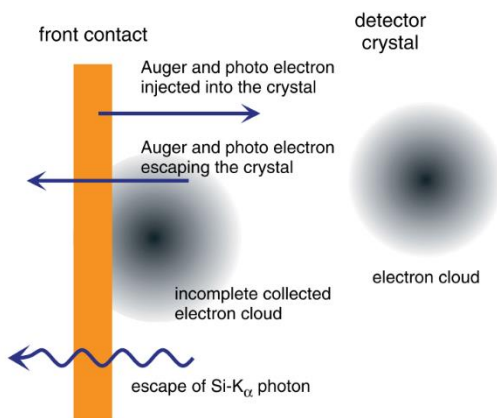


Figure 2.9 Physical processes in a semiconductor detector [151]

These are the main phenomena occurring in a detector and on this basis is possible to get a good approximation of the efficiency.

The *efficiency of a detector* ε can be defined as the ratio between the number of photons leading to a pulse and the number of photons reaching the crystal, as in the following:

$$\text{Eq. 2.21} \quad \varepsilon = \frac{\text{number of photons collected}}{\text{number of photons impinging}}$$

To have a measure of the photons absorbed in the interaction with the active volume of the detector, we can again use the Beer-Lambert law [94,150,172]:

$$\text{Eq. 2.22} \quad \varepsilon(E) = R e^{-\left(\frac{\mu}{\rho}\right)_{Wi} \rho_{Wi} T_{Wi}} \cdot e^{-\left(\frac{\mu}{\rho}\right)_{CL} \rho_{CL} T_{CL}} \cdot e^{-\left(\frac{\mu}{\rho}\right)_{DL} \rho_{DL} T_{DL}} \left[1 - e^{-\left(\frac{\mu}{\rho}\right)_{AL} \rho_{AL} T_{AL}} \right]$$

where Wi stands for “window”, CL stands for “contact layer”, DL stands for the “dead layer” of the detector, AL stands for ‘active layer’, the active part of the detector, T_x are the thicknesses of the layers (window, contact, dead layer and active layer) and R is the ratio of actually illuminated crystal surface and illuminated area in front of the detector: in fact, apertures in front of the detector and the window support grid of the detector lead to $R < 1$.

Because the mass absorption coefficient in the Eq. 2.22 are energy dependent, also the efficiency depends on the energy of the impinging photon.

2.3.3 Detector resolution

In a semiconductor detector, an incident photon generates a number of charge carriers, which is proportional to the resulting pulse amplitude. The theoretical limit for the precision of a measure depends on the mean energy needed to create an electron-hole pair in the active material for detection.

The value obtained, however, is far from a real estimate of the resolution: the number of charge carriers created is subject to statistical oscillations due to the energy-to-charge conversion process, which is described by the Fano relations [112]:

$$\text{Eq. 2.23} \quad N = E_{ph} / \eta$$

$$\text{Eq. 2.24} \quad \sigma_F = \sqrt{\frac{F E_{ph}}{\eta}} = \sqrt{F N}$$

where E_{ph} is the photon energy, η is the average energy needed for electron-hole pair creation (which is equal to 3.66 eV for silicon in SDD at room temperature) and F is the *Fano factor*, which is equal to 0.114 for silicon. The Fano factor F accounts for the deviations from Poisson behaviour due to the not strict independence of the individual events in the energy loss processes in the detector.

An additional contribution to this fluctuation of signal charge comes from the unavoidable electronic noise. The consequent imprecision in measurement of the energy of the initial photons leads to a widening of the electrical pulse height distribution, and the overall noise becomes the following [151]:

$$\text{Eq. 2.25} \quad \Delta E_{Tot} = \sqrt{(\Delta E_{det})^2 + (\Delta E_{el})^2} = \sqrt{8(\ln 2)\eta F E_{ph} + (\Delta E_{el})^2}$$

where ΔE_{el} is the electronic noise and ΔE_{det} is the detector noise.

The electronic noise ΔE_{el} in Eq. 2.25 is a parameter which usually is indicated in the data of the detector: some spectrometers provide an electronically generated zero-energy peak which can directly be used to determine the electronic noise contribution.

Because the response function of most semiconductor detectors is mainly Gaussian, all mathematical expressions for describing the fluorescence lines involve this function. Therefore, a Gaussian peak is characterized by three parameters:

1. the position
2. width
3. and height or area.

It is desirable to describe the signal peak in terms of its area rather than its height because the area is directly related to the number of X-ray photons detected, whereas the height depends on the spectrometer resolution. The evaluation of the resolution is described usually by the *full width at half maximum* (with acronym FWHM) of the peak representing a certain transition [49]:

$$\text{Eq. 2.26} \quad FWHM = 2.35\sqrt{E_{ph}\eta F}$$

while, in first approximation, the profile P of a single peak is given by the following:

$$\text{Eq. 2.27} \quad P(x) = \frac{A}{\sigma\sqrt{2\pi}} e^{-\frac{(x_i - \mu)^2}{2\sigma^2}}$$

where A is the peak area (counts), σ is the width of the Gaussian expressed in channels of detector, and μ is the location of the peak maximum.

We can observe that in Eq. 2.27 the peak area is a linear parameter; the width and position are nonlinear parameters. This means that a nonlinear least-squares procedure is required to find optimum values for the latter two parameters. The use of a linear least-squares method assumes that the width and position of the peak are known with high accuracy from detector calibration.

Optimizing the position and width of each peak independently is not possible. Instead, the energies of the fluorescence lines are known with an accuracy of 1 eV or better.

Because the pattern of peaks in a spectrum is directly related to elements present in the sample, we can predict all x-ray lines that constitute the spectrum and their energies. We then rewrite the Eq. 2.27 in terms of energy rather than channel number. Defining ZERO as the energy of channel 0 and expressing the spectrum GAIN in eV/channel, the energy of i^{th} channel is given by the following:

$$\text{Eq. 2.28} \quad E(i) = ZERO + GAIN \cdot i$$

Thus, the Eq. 2.27 can be written as:

$$\text{Eq. 2.29} \quad G(i, E_j) = \frac{GAIN}{s\sqrt{2\pi}} e^{-\frac{(E_j - E(i))^2}{2s^2}}$$

with E_j the energy, in eV, of the X-ray line and s the peak width given by the following relation:

$$\text{Eq. 2.30} \quad s^2 = \left(\frac{\Delta E_{Tot}}{2.3548}\right)^2 + \eta \cdot F \cdot E_j$$

As final remark, we can observe that the term $GAIN/(s\sqrt{2\pi})$ is needed in Eq. 2.29 to normalize the Gaussian: in this way the sum over all channels gives the unity.

2.4 Minimum detection limit

The limit of detection was the most controversial concept in analytical measurement procedures for a long time. In the last two decades, however, international organizations such as International Organization for Standardization (ISO) and International Union of Pure and Applied Chemistry (IUPAC) and have reached to a consensus in the definition of this important concept, issuing guidelines for the estimation of different performing parameters of measurement procedures [36,77,78].

Typical detection limits for medium- and high-Z elements are in the p.p.m. range, which is satisfactory for many situations. The *minimum detection limit* (MDL), also called *lower limit of detection* (LLD), in XRF is defined as the concentration needed for the number of counts I in the characteristic peak of an atomic element to be [73,187]:

$$\text{Eq. 2.31} \quad I \geq 3\sqrt{B}$$

where B is the number of counts which compose the background below the peak element and the radix of B corresponds approximatively to a standard deviation. Therefore, we have [84,187]:

$$\text{Eq. 2.32} \quad M.D.L. = \frac{3}{k}\sqrt{B}$$

where the constant k is the sensitivity constant measured as the net number of counts in the characteristic peak per unit concentration and time.

In order to get best values of detection, i.e. lowering MDL, we need to improve the intensity of the characteristic peak, decreasing the intensity of the background radiation.

A substantial portion of the background signal is due to incoherent and coherent scattering of the primary radiation in the sample itself, which give place to secondary processes inside the

sample. Therefore, sample properties influencing scattering processes like, for example, thickness and average atomic number, have a great influence on detection limits.

The intensities of peak and background are, moreover, time dependent, but in different ways: the intensity of the characteristic line increases linearly with time, whereas the background signal increases with the square root of time. This means that the detection limit can be reduced increasing analysis time.

3 X-RAY DIFFRACTION

When an X-ray interact with an atom, we have a scattering amplitude of an atom, which is determined by summing the contributions from all Z electrons, Z being the atomic number of the atom. The summation considers the path or phase differences between all the Z scattered waves, getting f , the *atomic scattering factor*, which is the ratio of the scattering amplitude of the atom divided by that of a single (classical) electron:

Eq. 3.1

$$f = \frac{\text{amplitude scattered by atom}}{\text{amplitude scattered by a single electron}}$$

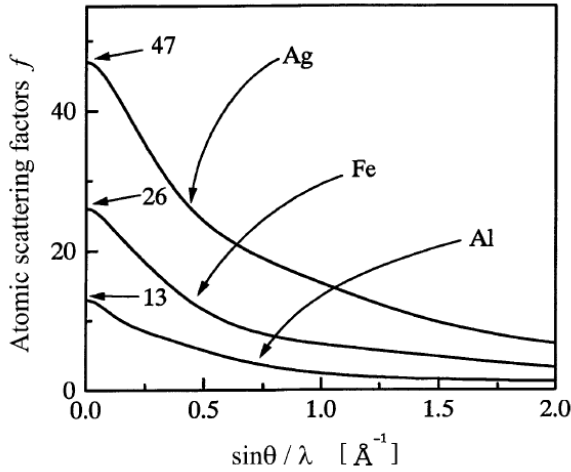


Figure 3.1 Atomic scattering factors of Al, Fe, and Ag

We refer to it also as *form factor* because it depends on the distribution of electrons around the atomic nucleus [35,68].

We can appreciate the fact that at zero scattering angle, all the scattered waves are in phase and the scattered amplitude is the simple sum of the contribution from all Z electrons, i.e. $f = Z$. As the scattering angle increases, f decreases below Z because of the destructive interference effects between the Z scattered waves (see Figure 3.1).

Since a crystal is made of atoms, the scattering amplitude of a unit cell is determined by summing the scattering amplitudes, f , from all the atoms in the unit cell to all the atoms in the motif. Again, the summation must consider the path or phase differences between all the scattered waves and is again expressed by a dimensionless number, F_{hkl} , the so-called *structure factor*, defined as in the following:

Eq. 3.2

$$F_{hkl} = \frac{\text{amplitude scattered by the atoms in the unit cell}}{\text{amplitude scattered by a single electron}}$$

In this case, however, F_{hkl} must not only express the amplitude of scattering from a reflecting plane with Laue indices hkl but must also express the phase angle of the scattered wave. This means that F_{hkl} is therefore not a simple number, like f , but is a vector or, mathematically, a complex number [35,68].

The various techniques for diffracting X-rays from single crystal or powders may simply be considered as methods for visualizing the reciprocal lattice, correcting various distortions

introduced by a specific experimental geometry [68]. Crystal structure determination is therefore a two-part process:

- a) the determination of the size and shape of the unit cell (i.e. the lattice parameters) from the geometry of the diffraction pattern;
- b) the determination of the lattice type and distribution of the atoms in the structure from the (relative) intensities of the recorded diffraction spots.

The first process is in principle an easier process, but it is not the same for the second, because films and counters record intensities, and the intensities of the reciprocal lattice points are related to the types and locations of the atoms in the unit cell and are proportional to the squares of the amplitudes. But the square of a complex number, like F_{hkl} , is always a real number, therefore the information about the phase angles of the diffracted beams is lost [68,83,166].

Another source of difficulty is the fact that we must consider that the incident X-ray beam is attenuated as it is successively scattered by the atoms in the crystal: this means that atoms ‘deeper down’ in the crystal encounter smaller amounts of incident radiation.

Furthermore, the reflected beams also propagate through the crystal at the Bragg angle θ (see Figure 3.5): therefore, they are ‘re-reflected’ in a direction parallel to that of the incident beam. These re-reflected beams then interfere destructively with the incident or direct beam, with further attenuation.

A number of physical and geometrical factors also need to be taken into account, like temperature factor, polarization factor, absorption factor, etc. [14,59,83].

The complete treatment of the diffraction theory is out of the scope of the present research, so we recall here briefly only some of the fundamental aspects.

3.1 Polycrystals X-ray diffraction

The requirement to prepare a suitable single crystal specimen of appropriate size and quality for single-crystal XRD experiments can often represent a limitation of the technique, and many important crystalline materials have eluded structure determination simply because they can be prepared only as microcrystalline powders [35,124].

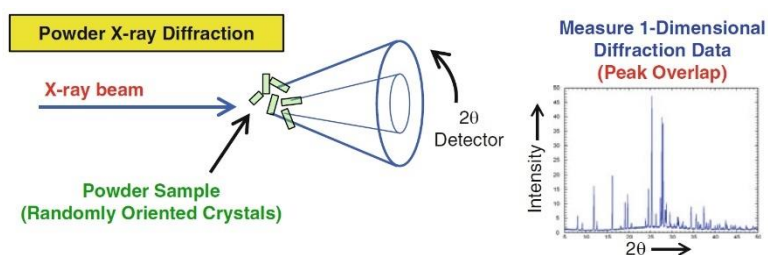


Figure 3.2 Powder XRD measurements [72]

In powder XRD, the diffraction phenomenon for each individual crystallite is the same as the diffraction in a single crystal, but the powder comprises many crystallites with a random distribution of crystallite orientations. Therefore, we get 3-D diffraction data which are compressed into one dimension, as intensity vs diffraction angle 2θ [33,72].

Consequently, there is usually considerable overlap of peaks in the powder XRD pattern. Such peak overlap hides information on the positions and intensities of the diffraction maxima, and this can be challenging in the process of carrying out crystal structure determination [72,164]. This is the case, for example, of molecular solids, with large unit cells and low symmetry, and therefore a high density of peaks in the powder XRD pattern.

A complete powder XRD profile (experimental or calculated) is described in terms of the following components:

- the peak positions,
- the background intensity distribution,
- the peak widths,
- the peak shapes,
- the peak intensities.

The peak shape depends on characteristics of both the instrument and the sample, and different peak shape functions are appropriate under different circumstances. The most common peak shape for powder XRD is the pseudo-Voigt function, which is a linear combination of Gaussian and Lorentzian functions [30,72,164].

There are two general approaches for comparing experimental powder XRD data with powder XRD data calculated for a structural model during the process of structure determination:

- comparison of integrated peak intensities;
- comparison of the complete powder XRD profile.

In the first approach, experimental powder XRD pattern are analysed to extract a set of integrated peak intensities I_{hkl} , and hence $|F_{hkl}|$ values, analogous to those obtained directly in single-crystal XRD [40,41,68]. This method is however affected by the peak overlapping problem, which complicates the analysis.

After extracting a set of integrated peak intensities, the calculated I_{hkl} data can be compared with experimental data with the same approach used in the analysis of single-crystal XRD data. However, a disadvantage is that any errors or uncertainties associated with the process of extracting the integrated peak intensities from the experimental pattern are inevitably propagated into the structure determination process and may limit the reliability of the derived structural information [68,164].

In the second approach, a digitized powder XRD profile is calculated from the hypothetical structural model and then compared to the experimental pattern. A reliable whole-profile comparison between calculated and experimental XRD data requires that the variables describing these aspects of the calculated pattern must accurately reflect those in the experimental pattern. The comparison occurs through an appropriate whole-profile figure-of-merit, the most common of which is the weighted profile R_{wp} , defined in the following:

$$\text{Eq. 3.3} \quad R_{wp} = 100 \times \sqrt{\frac{\sum_i w_i (y_i - y_{ci})^2}{\sum_i w_i y_i^2}}$$

where y_i is the intensity of the i^{th} point in the experimental powder XRD data, y_{ci} is the intensity of the i^{th} point in the calculated powder XRD pattern and w_i is a weighting factor for the i^{th} point [72].

This type of figure-of-merit, which uses experimental data, is used in *Rietveld refinement*, as well as in other implementations of direct-space techniques for structure solution [60,61,72,137].

3.2 Structure determination and quantitative analysis

The preparation or synthesis of single crystals which are sufficiently large to be analysed using the X-ray diffraction methods is a matter of great experimental difficulty. Since the case of polycrystals is the more common one, this will be considered in the following to introduce briefly the general method for structure determination and the Rietveld refinement approach. Moreover, it is not possible to describe here all the currently available geometries, well described in the already cited references [33,68,83] and, if not differently stated, only the case of identification of known structures will be explored.

Powder XRD has reached a good level of accuracy for quantitative analysis of the phases in a homogenous material, as soon as we know all the components, because for every phase j we need to know the mass absorption coefficient μ_j , because the peak intensities are related to volume fraction of every component [33].

Every phase has a specific “fingerprint” which is related to its crystal structure, i.e. the collection of the more relevant reflections, with a proper intensity, identified by the Miller indices and the interplanar distances d . Simplifying the approach, the three stages of structure determination from experimental diffraction data are [33,41,72]:

- unit cell determination and space group assignment;
- structure solution;
- structure refinement.

For powder XRD data, unit cell determination is executed using standard indexing procedures. Structure solution aims to derive an approximately correct description of the structure, using the unit cell and space group determined in the first stage, but starting from no knowledge of the actual arrangement of atoms or molecules in the unit cell [69,123,136].

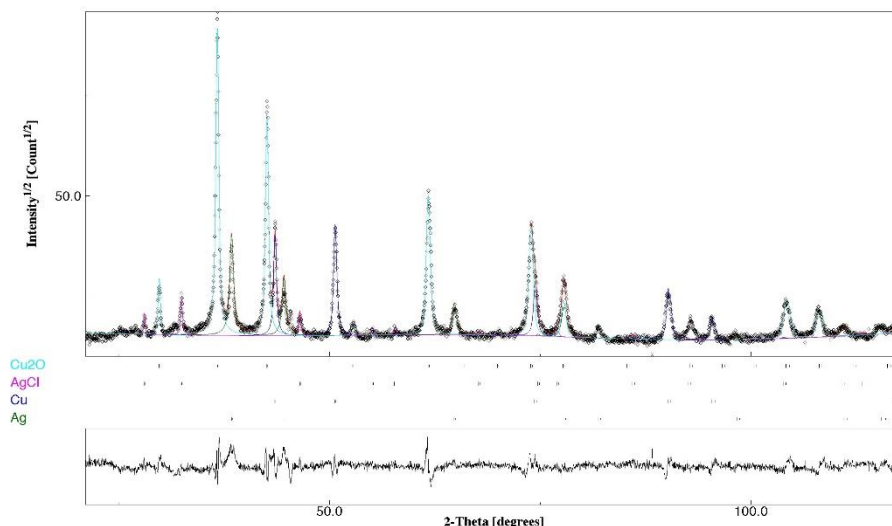


Figure 3.3 Diffraction spectrum of a four-phase structure analysed with Rietveld method in *MAUD* software.

If the structure solution represents a sufficiently good approximation to the true structure, a good quality description of the structure can then be obtained by structure refinement, using the Rietveld profile refinement technique (see Figure 3.3).

All the steps illustrated above are easily executed through modern computer programs, like the largely used MAUD software [105,106,109,110], freely available and downloadable on the MAUD web site <http://maud.radiographema.com/>.

For powder specimens in which the crystals are randomly orientated, the set of d -spacings data and their relative intensities serves as a ‘fingerprint’: with this data, the phase can be identified by comparison with the ‘fingerprints’ of known phases in some public databases. Nowadays, a Crystallography Open Database (COD) has been created, a project whose aim is to gather, with open access model, all available inorganic, metal–organic and small organic molecule structural data in one database [79]. Offered to the scientific community on the Web at address <http://www.crystallography.net/>, the project was founded in February 2003 as a response to Michael Berndt’s letter published in the Structure Determination by Powder Diffractometry (SDPD) mailing list (<http://tech.groups.yahoo.com/group/sdpd/message/1016>). Other databases exist, like the Cambridge Structural Database (CSD) and the Cambridge Crystallographic Data Center (CCDC) [66].

3.3 Rietveld classical method

As we have already stated previously, a powder diffraction pattern does contain the same information as a single crystal data set. The problem is how to deconvolute it in case of overlapped peaks. A method in handling this problem has been developed by Hugo Rietveld in the late 1960s. He introduced a whole-pattern-fitting structure refinement method, now known as the Rietveld method [144,164].

The Rietveld method was at the beginning developed for constant wavelength neutron diffraction [30,144], but over the years several modifications have been made in order to use it also for X-rays.

To date several thousands of structures have been refined and published following this method. The method allows to refine a crystal structure, but a reasonably good model is needed (unit cell dimensions, atom positions, occupancy of atomic sites, etc.) to get the refinements going well. The experimental conditions are no less demanding and may be summarized as follows [30,68,101]:

- accurate alignment of diffractometer (to ensure accurate 2θ values);
- correct positioning of specimen in the diffractometer;
- correct X-ray machine configuration (wavelength, slit sizes, calibration, etc.);
- elimination (as far as possible) of preferred orientation effects;
- constant volume condition: this condition is related to diffractometer geometry and is needed because the area of specimen irradiated varies as $1/\sin\theta$ and the depth of operation varies as $\sin\theta$, hence the volume is independent of θ . For example, the sample thickness is relevant in reflection geometries, to avoid problem of sample transparency.
- a powder particle size of about 1–5 μm ; for sizes smaller than this, line broadening needs to be considered, while for sizes much larger than this, all crystallite orientations may not contribute equally to the intensity (giving problems as in preferred orientation) [83];
- the number of diffracting grains at each position of the sample should be significant (> 1000 grains) and homogenously distributed (only a fraction is in condition for the diffraction);
- well known information about temperature, humidity and pressure, which can affect some sample analysis (especially organic ones).

As soon as all the condition are satisfied, and the data has been collected, the Rietveld method is a least-squares procedure, which minimizes the residual function [29,164,173]:

$$\text{Eq. 3.4} \quad WSS = \sum_i w_i (I_{e,i} - I_{c,i})^2$$

where $I_{e,i}$ is the observed intensity at i^{th} point of the observed powder pattern and $I_{c,i}$ is the calculated intensity. The error associated with counting the profile intensity follows the Poisson distribution: therefore, the weight, w_i , is solely based on the counting statistics, $w_i = (I_{e,i})^{-1}$.

The minimization is performed refining simultaneously crystal parameters which defines the whole structure of the compound, but the Rietveld algorithm uses also all information experimentally available [29]:

- instrumental characteristics (geometry, detector, etc.);
- structural parameters (cell parameters, atomic position, etc.);
- microstructural parameters (crystallite size, microstrains, etc.);
- sample parameters (preferred orientations, thicknesses, absorptions, phase fractions, etc.).

There are also some implementations for allowing the refinement of ‘non-crystallographic’ quantities such as temperature or pressure [165].

The calculated intensity, $I_{c,i}$, for the i^{th} phase in a powder diffractometer can be expressed by the following equation [56,104]:

$$\text{Eq. 3.5} \quad I_{c,i} = S_F \sum_{j=1}^N \frac{f_j}{V_j^2} \sum_{k=1}^M L_k |F_{k,j}|^2 S_j (2\theta_i - 2\theta_{k,j}) P_{k,j} A_j + bkg_i$$

where N is the number of phases in the material and M the number of peaks in the spectrum. The number of peaks, M , is determined by the symmetry and space group of every phase. One peak is composed by all equivalent reflections, whose position is computed from the d -spacing of the (hkl) reflection planes, using the reciprocal lattice matrix. In the next paragraph, we’ll discuss briefly about the components of the Eq. 3.5.

3.4 Anatomy of the calculated intensity

For every material which is analysed with XRD techniques, the diffraction spectrum depends on the following aspects:

- *phases*: crystal structure, microstructure, quantity, cell volume, texture, stress, chemistry etc.
- *instrument geometry characteristics*: beam intensity, Lorentz-Polarization, background, resolution, aberrations, radiation etc.
- *sample*: position, shape and dimensions, orientation.

Each of these quantities can be written in term of parameters that can be refined (and therefore optimized), as we’ll see now, analysing the single components of Eq. 3.5.

3.4.1 Scale factor

Firstly, the first factor considered here for the i^{th} peak in Eq. 3.5 is the so-called *scale factor*, defined by the following:

$$\text{Eq. 3.6} \quad S_i = S_F \sum_{j=1}^N \frac{f_j}{V_j^2}$$

where S_F is the beam intensity, f_j is the phase volume fraction and V_j is the phase cell volume. The scale factor for each j -phase is usually written, in classical Rietveld software, as in the following:

$$\text{Eq. 3.7} \quad S_j = S_F \frac{f_j}{V_j^2}$$

but in the MAUD software, the three terms on the right of Eq. 3.7 are kept separated.

3.4.2 Lorentz-polarization factor

Another important component of Eq. 3.5 for the calculation of i^{th} peak is the so-called *Lorentz-Polarization factor*, given by the factor L_k . It depends on instrument configurations and, in particular, on the following parameters [33,104]:

- geometry
- monochromator (angle α) on the beam
- detector
- beam size
- sample volume
- sample positioning

For example, for a Bragg-Brentano geometry, we have the following [29]:

$$\text{Eq. 3.8} \quad L_p = \frac{1 + P_h \cos^2(2\theta)}{2(1 + P_h) \sin^2 \theta \cos \theta}$$

with $P_h = \cos^2(2\alpha)$. For an unpolarized incident beam $P_h = 1$, while with a monochromator set-up, P_h must be specified.

3.4.3 Structure factor

On the immediate right of the Lorentz-Polarization factor, there is the so-called *structure factor*, $|F_{k,j}|^2$ (see Eq. 3.2). Under a generalized structure, we have the following:

$$\text{Eq. 3.9} \quad |F_{k,j}|^2 = m_k \left| \sum_{n=1}^N f_n e^{-B_n \frac{\sin^2 \theta}{\lambda^2}} (e^{2\pi i(hx_n + ky_n + lz_n)}) \right|^2$$

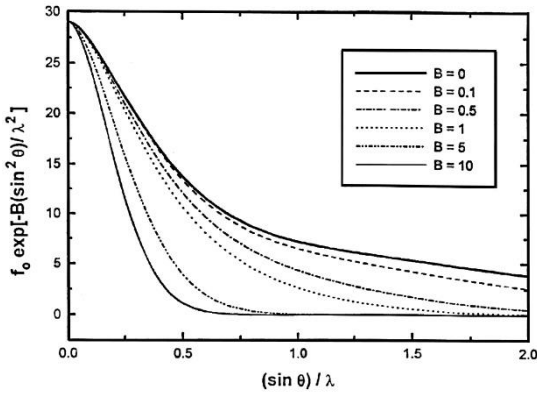


Figure 3.4 The effect of atomic thermal motion on the copper scattering factor [83].

where N is the number of atoms, x_n, y_n, z_n the coordinates of the n^{th} atom, B_n is a temperature factor, f_n is the atomic scattering factor (see Eq. 3.1), m_k is the multiplicity of the reflections, and h, k, l in the exponential are the Miller indices. The formula, therefore, rely on atom coordinates, but this is not always possible when a list of well-known atom types and positions is not available or for complicated structures, and alternatives approaches are needed [104].

As final remark on this factor, as we have already seen, the atomic scattering factor for X-ray, f , decreases with the diffraction angle and is proportional to the number of electrons (see Figure 3.1).

3.4.4 Temperature factor

The temperature factor, B_n , is called *Debye-Waller temperature factor* [29,83] and accelerates the decrease, which is caused by thermal motion of atoms (see Figure 3.4). It is related to the vibrational amplitude of the atom by the following:

$$\text{Eq. 3.10} \quad B = 8\pi^2 U^2$$

where U^2 is the mean-square amplitude of vibration of an atom. So, we can write the following *atomic scattering factor*:

$$\text{Eq. 3.11} \quad f = f_0 e^{-B \frac{\sin^2 \theta}{\lambda^2}}$$

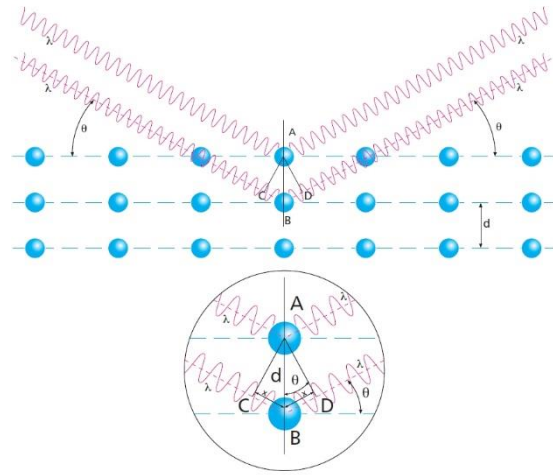


Figure 3.5 Demonstration of Bragg's law [18]

If the surroundings of the atom have cubic symmetry, the temperature factor is the same for all directions of vibration of an atom. Therefore, we can define it as *isotropic temperature factor*.

Generally, most atoms in solids have special directions in which they can vibrate with higher amplitudes. This means that the proper anisotropic motion of an atom may be described by three

vibrational amplitudes, and B becomes a diagonal matrix with six terms. We remember shortly that [68]:

$$\text{Eq. 3.12} \quad \mathbf{d}_{hkl}^* = h\mathbf{a}^* + k\mathbf{b}^* + l\mathbf{c}^*$$

So, direction symbols $[uvw]$ are the components of a vector \mathbf{r}_{uvw} in direct space and plane indices are the components of a vector \mathbf{d}_{hkl}^* in reciprocal space. Therefore, combining Bragg's law (see Figure 3.5) [64,168]:

$$\text{Eq. 3.13} \quad n\lambda = 2d \sin \theta$$

and Eq. 3.12, the Eq. 3.11 can be rewritten as in the following [83,164]:

$$\text{Eq. 3.14} \quad f = f_0 e^{-\frac{B \cdot (\mathbf{d}^*)^2}{4}}$$

and exploding every matrix component, we get:

$$\text{Eq. 3.15} \quad f = f_0 \exp \left[-\frac{1}{4} \left(B_{11}h^2\mathbf{a}^{*2} + B_{22}k^2\mathbf{b}^{*2} + B_{33}l^2\mathbf{c}^{*2} + 2B_{12}hka^*\mathbf{b}^* + 2B_{13}hla^*\mathbf{c}^* + 2B_{23}klb^*\mathbf{c}^* \right) \right]$$

3.4.5 Profile shape function

The next factor in the Eq. 3.5 for the calculation of i^{th} peak, is the so-called *profile shape function*, given by $S_f(2\theta_i - 2\theta_{k,i})$. The shape of the peak contains important information about microstructure, because a diffraction peak can be considered as the convolution product of several effect [29]:

- the small size of the crystallite which coherently diffracts X-ray;
- elastic microdistortions due to defects, heterogeneities, etc.

Different profile shape functions are available [108]:

- Gaussian (the original Rietveld function for neutrons)
- Cauchy
- Voigt and Pseudo-Voigt (PV)
- Pearson VII, etc.

For example, in the case of Pseudo-Voigt shape function, PV , which is of common use, we have:

$$\text{Eq. 3.16} \quad PV(2\theta_i - 2\theta_k) = I_n \left[\eta_k \left(\frac{1}{1 + S_{i,k}^2} \right) + (1 - \eta_k) e^{-S_{i,k}^2 \ln 2} \right]$$

with $S_{i,k} = (2\theta_i - 2\theta_k) / \omega_k$, where the shape parameters are:

$$\text{Eq. 3.17} \quad \omega^2 = W + V \tan \theta + \tan^2 \theta$$

which is the so-called *Caglioti formula*, and the *instrumental broadening* η described by the polynomial function:

$$\text{Eq. 3.18} \quad \eta = \sum_{n=0}^{N_g} c_n (2\theta)^n$$

which must be evaluated and refined first against a known sample in order to fix its contribution. As a rule of thumb, a peak is considered to be down to background level when the intensity is less than $0.1 \pm 1.0\%$ of the peak maximum, but appropriate percentage depends on the peak shape selected.

3.4.6 Absorption factor

The next factor in the Eq. 3.5 for the calculation of i^{th} peak, is the so-called *absorption factor* [104], given by A_j .

Sample absorption affect powder diffraction analysis differently, depending on diffractometer geometry. The Guinier flat-plate geometry is unaffected by absorption, while the Debye-Scherrer and Guinier capillary geometries are strongly affected: with strong absorption, the outer part of capillary will diffract, and peaks will be shifted to higher 2θ [35,164].

The diffracted intensity can also be reduced by sample absorption, and both the positional and the intensity effects will vary with 2θ .

In the Bragg-Brentano geometry, with thick samples, the factor is $A_j = 1/(2\mu)$ where μ is the linear absorption coefficient of the sample. With low sample absorption in reflection geometry we get a shift of peak position to lower 2θ and peak asymmetry [83,164].

Sample geometry alter absorption and, for instance, in the case of thin films or thin layered structures, a specific correction is required [29] which depends on diffractometer geometry.

3.4.7 Texture weight factor

Another important factor in the Eq. 3.5, $P_{k,j}$, is the so-called *preferred orientation function* (or *texture weight factor*) [104].

Preferred orientation in a material means that the crystallites tend to arrange themselves in a preferred orientation, by itself or for the effect of a mechanical modify, which can also retain

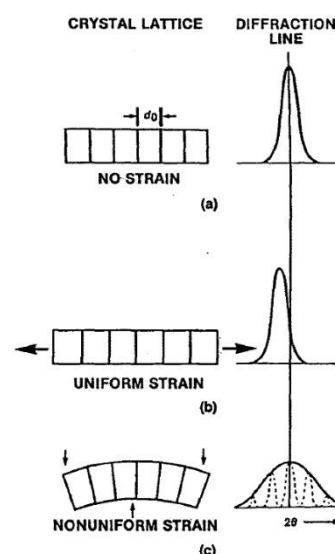


Figure 3.6 Strain expanding and contracting d-values [83].

residual stress and strain inside the crystalline structure [46,83] (see also Paragraph 4.4.3).

A proper powder XRD analysis requires a random crystallite orientation, while with a preferred orientation we get an incorrect intensity distribution and usually a peak shift (e.g. in case of uniform strain, see Figure 3.6(b)) or a peak broadening, even if the peak positions remain virtually the same (e.g. in case of nonuniform strain, see Figure 3.6(c)) [83,142,164].

Clay minerals and other layer structures are notorious in this respect; in serious cases, the XRD analysis will show only a few peaks corresponding to the strongest 00l reflections, and phase identification, in such cases, will be impossible.

For the definition of P_{kj} , there are many empirical formulas, which depends on geometry and on crystal group type [29].

3.4.8 Background contribution

At the end of Eq. 3.5, for the i^{th} peak we have the *background* component, bkg_i , which takes care of background phenomenon in X-ray data acquisition [29,30]. The background contribution can be broken down in separate terms, according to the following:

$$\text{Eq. 3.19} \quad bkg_i = bkg_{ph} + bkg_{si} + bkg_{sc} + bkg_n$$

where bkg_{ph} is the physical contribution not deriving from sample but due to scattering on air, detector electronics, cosmic rays; bkg_{si} is the contribution due to incoherent scattering from crystalline defects, fluorescence, etc.; bkg_{sc} is the contribution of the sample due to coherent scattering, caused by thermal atomic vibrations and lattice imperfections; bkg_n is the noise contribution, with $\langle bkg_n \rangle = 0$.

We have basically two possible approaches in dealing with the background in a powder XRD analysis: it is possible either estimate it by linear interpolation between selected points between peaks and then subtracted, or model it by a function containing several reasonable parameters.

In both cases we have advantages and disadvantages. For a simple pattern where most peaks are resolved to the baseline, both methods work well; but when the overlapping become important, it is not so easy to estimate the background. The more used background in Rietveld refinement is a polynomial function in 2θ .

$$\text{Eq. 3.20} \quad bkg_i = \sum_{n=0}^D a_n (2\theta_i)^n$$

where D is the polynomial degree and a_n are the polynomial coefficients. For more complex backgrounds, there are specific formulas available.

However, if the polynomial describes the background well, then this procedure also works well. Otherwise, neither refining the coefficients of the polynomial, nor increasing the order of the polynomial, can correct the problem and the refinement will not proceed satisfactorily.

In such a case, background subtraction is the better approach. Of course, it is also possible to use the two techniques in combination: we may use an empirical function to fit the background and then describe the deviations by a sequence of fixed points. The advantage is that we minimize the magnitude of the fixed part and, therefore, we reduce the impact of arbitrariness on the refinement.

In any case, in every experiment, the user must ensure that the noise is lower than the intensity of small peaks and, if the total collection time is limited, it is better to have a lower noise than a smaller step size.

Moreover, it is better to collect a little bit more data for some more time than to have to repeat an experiment. The quality of the detector (with his electronic background) can be an issue if is not known from calibration.

3.5 Quality of refinement

As already stated, The Rietveld method is a least-squares procedure, which minimizes the quantity defined by Eq. 3.4. Its absolute value depends on the intensities and number of points. In order to evaluate the quality of the refinement, two major indices are defined [44]. The first one is the weighted profile R_{wp} , defined in the following:

$$\text{Eq. 3.21} \quad R_{wp} = \sqrt{\frac{\sum_i w_i (I_{e,i} - I_{c,i})^2}{\sum_i w_i I_{e,i}^2}}$$

where $I_{e,i}$ is the observed intensity at i^{th} point of the observed powder pattern and $I_{c,i}$ is the calculated intensity, while the weight, w_i , is based on the counting statistics, $w_i = (I_{e,i})^{-1}$. The second index is the profile R_{exp} , defined in the following:

$$\text{Eq. 3.22} \quad R_{exp} = \sqrt{\frac{(N-P)}{\sum_i w_i I_{e,i}^2}}$$

where N is the number of points, and P is the number of parameters.

The weighted profile R_{wp} is the more valuable: its absolute value does not depend on the absolute value of the intensities, but it depends on the background [29]. With a high background is easier to reach very low values. With increasing of the number of peaks (sharp peaks) it becomes more difficult to get a good value. Generally, with $R_{wp} < 0.1$ we get an acceptable refinement with a

medium complex phase. For a complex phase (e.g. monoclinic to triclinic) a value $R_{wp} < 0.15$ is good, while for a highly symmetric compound (cubic) with few peaks a value $R_{wp} < 0.08$ start to be acceptable. With high background it is better to evaluate the R_{wp} with subtracted background.

The index R_{exp} is the minimum R_{wp} value reachable using a certain number of refineable parameters: however, it needs a valid weighting scheme to be reliable. R values are useful indicators for the evaluation of the quality of a refinement, during improvements to the model, but they should not be overinterpreted.

The *goodness of fit*, $GofF$, χ^2 , is defined as the ratio between the R_{wp} and R_{exp} , according to the following relation:

$$\chi^2 = \frac{R_{wp}}{R_{exp}}$$

This quantity cannot be lower than 1, unless the weighting scheme is not correctly defined: for example, in the case of detectors not recording exactly the number of photons. A good refinement gives χ^2 values lower than 2.

The goodness of fit, however, is not a very good index to look at, because with a noisy XRD pattern, it is quite easy to reach a value near 1. With very high intensities and low noise patterns is difficult to reach a value of 2. For having a practical reference, a $\chi^2 = 10$, which means a relatively bad fitting, indicates that the input model is off by 10σ for every I_i .

In any case, user must be conscious that the χ^2 value is sensible to model inaccuracies. The most important criteria for judging the quality of a Rietveld refinement are

- the fit of the calculated pattern to the observed data
- the chemical sense of the structural model.

The first one can be evaluated based on the final profile plot, using the complete range of data collected. The second one depends on a careful examination of the final atomic parameters.

4 COMBINED XRF & XRD

Every investigation technique has its specific advantages, but rarely can cover all the aspect needed for a comprehensive result about a specimen. This is the reason why, in modern research, it is common to proceed with many investigation techniques – especially the non-destructive ones - to achieve a deeper structural information about a sample. The advantages are intrinsically related to the analytical techniques the researcher choose for analysis: the idea is to combine techniques which allow an integrated approach, depending on the investigation goals. There are obviously some caveats on how the analysis is performed and, above all, on the coherence of the elaborated data regarding the sample and the reproducibility of the analysis.

4.1 Complementarity

X-ray diffraction (XRD) and fluorescence (XRF) techniques are useful non-destructive analytical techniques, with useful application not only in industrial field and mining [37,100,154], but also in environmental control and cultural heritage monitoring and conservation [42,107].

As presented in the previous chapters, XRD allows structural and crystallographic characterization of polycrystalline mixture, including phase identification and quantification, microstructure and texture analysis. On the other side, XRF allows accurate quantitative chemical characterization of materials.

One of the most important aspect of the combined use of XRD and XRF techniques is that the information they provide can be considered complementary [16,100].

From a certain point of view, XRD analysis implicitly allows also the full chemical characterization of a sample, but there are practical limitations.

Firstly, sensitivity to the presence of different elements in the same crystal structure mostly depends on the difference in atomic scattering factors and mean atomic radii. These aspects are reflected in relative peak intensities and positions, where differences can be quite small for similar atomic species, generating a significant error in elemental quantification. Moreover, amorphous fractions, which are not accurately quantifiable by XRD, can produce inaccurate quantification of total chemical composition.

To avoid this, XRF can be used to guide at first stage the quantitative characterization of the sample performed by means of XRD, allowing an independent chemical characterization of the sample which can be used in the initial stage of phase identification, limiting the search for

possible phases on the international database [65]. Otherwise, the direct XRD-only search, e.g. through a first match tool like the online FPSM [111], can often be slow and ambiguous when based only on the peak positions and intensities obtained from the diffraction spectrum.

On the other hand, XRD allows to integrate missing or incomplete information coming from an XRF analysis, e.g., the presence of light-elements or, in general, elements outside the sensitivity range of XRF technique. In fact, XRD recognize the presence of the corresponding elements-bearing phases.

Moreover, considering a full crystallographic model instead of a simple list of elements, it allows a more reliable modelling of the matrix effect, because the true absorption factors can be evaluated through a direct measurement of the density from the detected phases.

4.2 Current approach

The combination of collected data from XRF and XRD can occur using data from different machines or from the same instrument.

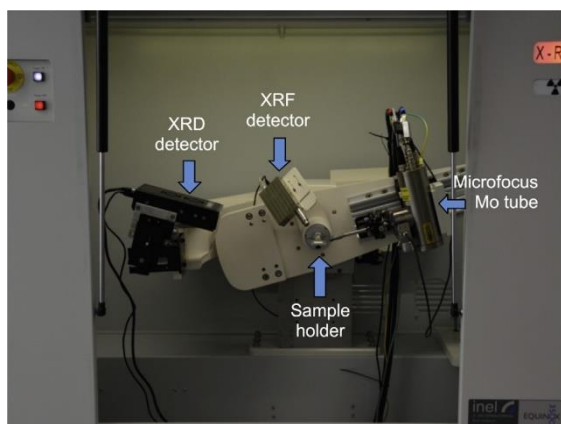


Figure 4.2 INEL Equinox 3500 θ - θ diffractometer with two detectors (XRF and XRD), a fixed sample holder and a Mo X-ray tube [107].

In the first case, diffraction and fluorescence signals are acquired on different instruments [52,134,152]: this has the advantage in adoption of the best experimental set-ups in term of radiation, sample conditioning and detectors adapting them to the desired investigation goal. On the other side, by using different radiation sources, the analysis involves different sample volumes, with the possibly of getting incongruent results when dealing with not completely homogenous samples.

In the second case, an integrated instrumentation is used, where XRF and XRD data are collected simultaneously (Figure 4.2) and recorded, usually in air, and in which the radiation source is the same for both techniques [16,107,180]. In this experimental case, the interested volume from the incident beam is the same, but for the fluorescence the lower energy lines signal is coming mainly from the upper layers of the analysed sample because of the absorption.

After having acquired the data from XRF, the same are

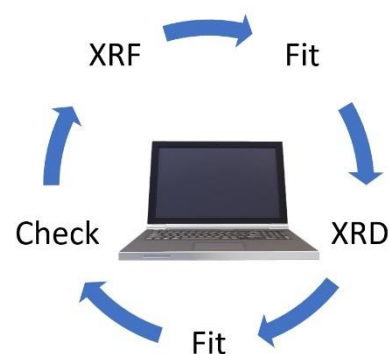


Figure 4.1 Common combined XRF-XRD approach.

used to get the elements and to perform the possible phase selection, in order to search the phases which better fit with the peaks of the XRD spectrum.

In this approach, the fitting and refining of the elemental concentrations and phase distribution are done independently, with a recursive iterative approach where every adjustment on one technique requires the elaboration of the data and the porting of the results on the other technique (Figure 4.1).

4.3 An innovative approach

A new method of combining XRF and XRD data consist not only in acquiring the data, with different machines or the same source, as previously seen, but also in executing the simultaneous computation of the refinement both for XRF and XRD.

In this case, instead of an iterative refinement, passing from XRF to XRD and vice versa, both XRF and XRD data are processed simultaneously with a combined Rietveld refinement (see Figure 4.3) starting from a common model.

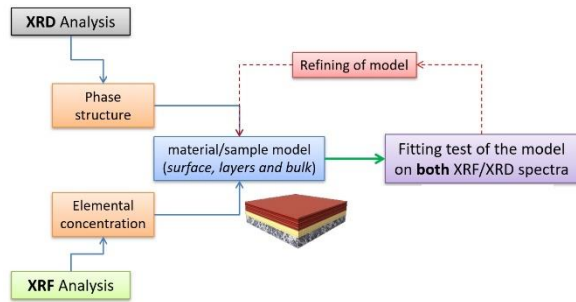


Figure 4.3 Combined approach with XRF-XRD simultaneous refinement.

The general approach is to model the sample through a multilayer description, defining for each layer the specific composition of the crystallographic phases.

The model is built in order to reproduce both the XRD and XRF patterns, defining the phase quantities in each layer, the elemental composition of each phase, and the distribution

of the phases within each layer.

After having defined the characteristics of the X-ray source (usually but not necessarily monochromatic), XRD and XRF spectra are simulated and then fitted against the experimental data; this is performed, in a similar way to the classical Rietveld method [144], through the optimization of the relevant parameters describing the structural model by means of a least-squares optimization. In this case, remembering Eq. 3.4, the corresponding combined fitness function can be written as the following [16]:

$$\text{Eq. 4.1} \quad WSS = \sum_n k_n WSS_n = \sum_n k_n \sum_i w_i (I_{e,i} - I_{c,i})^2$$

where the summation over n is related to the different techniques used (XRD and XRF in this case), k_n are the weights applied between techniques to balance their effective contribution in the

fitting and the summation over i is the usual summation of Eq. 3.4 where the weights, w_i , are solely based on the counting statistics, therefore $w_i = (I_{e,i})^{-1}$.

4.4 Model build-up

As previously stated, the innovation key of the approach is the common sample model: the sample is defined a multilayer description, defining for each layer the specific composition of the crystallographic phases (see Figure 4.4).

Usually, in an XRF multilayer approach, the model is based on chemical element composition of the layers (defining chemical elements and their weight fractions).

Also for this project, an XRF layer manager and layer sample simulator (LaSaX) has been developed (see Paragraphs 5.9 and 5.11), but, as it will be described in a while, they are needed only for a first rapid approach to an unknown material.

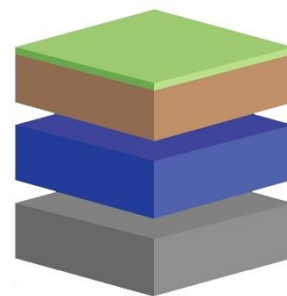


Figure 4.4 Multilayer model.

4.4.1 Phase definition

In the combined approach, the layers are defined in terms of phases and percentage of phase compositions.

Obviously, this implies that we assume that in the single layer, the phase distribution is homogeneous along the thickness assigned to the layer. The modelling must therefore take care of this assumption in defining phase composition.

For every phase, the starting point is the crystalline structure of a single phase. This is a key point, because the structure defines not only spatial distribution of atoms, and indirectly their presence in the volume (in term of weight

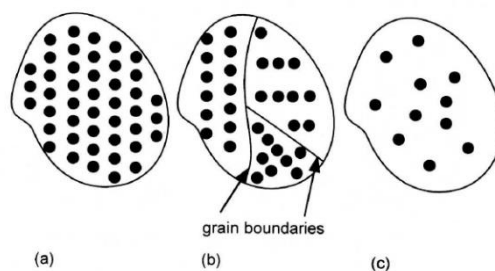


Figure 4.5 Differences between a) single crystal, b) polycrystalline, and c) amorphous [168].

fraction) but also their interaction with X-rays according to Bragg's law (see Figure 3.5 and Eq. 3.13).

Indeed, solids can be classified in three general categories, as shown in Figure 4.5: single crystal, polycrystalline, and amorphous. A crystal is defined as a solid with long-range order because is arranged in a pattern with a regular order in three dimensions: this order is the so-called crystal structure and it extends itself on distances much greater than the interatomic space [166].

This means that in a single crystal the order is all over the volume of the material, while a polycrystalline material, which is the case of interest in this research project, presents single-crystal regions, called *grains*, whose interfaces are the so-called *grain boundaries*. On the contrary, in an amorphous material (e.g. glass), the atoms are not ordered in a regular schema, but there is only a short-range order, limited to the nearest neighbours, less than a nanometer [135,168].

The repeating ‘unit of pattern’, the lattice, inside a material is an array of points in space in which each point has an identical environment; thus, the unit cells of the Bravais lattices [68,131] may be considered as the “*building blocks*” of crystals, precisely as Haüy envisaged in 1784 [68]: they are a purely imaginary construct, but a useful one for the study of materials.

A unit cell is described usually according to the right-hand rule (see Figure 4.6), by the interrelationship between the length (a, b, c) of its sides along the x, y, z cartesian system and the interaxial angles (α, β, γ) between them [68,166]: the lengths are measured from one corner of the cell, which is considered as the origin, and are the so-called *lattice parameters* of the unit (see Figure 4.7).

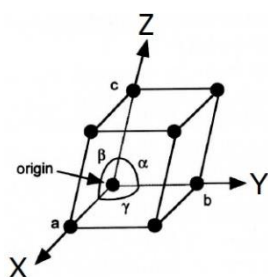


Figure 4.7 Example of unit cell

cell, which is considered as the origin, and are the so-called *lattice parameters* of the unit (see Figure 4.7).

In a real crystal, a lattice point may be occupied by a single atom, or a group of them, in a fixed relationship with respect to each lattice point but in any case, the arrangement of atoms and their number is the same for each lattice point [68,155]. Therefore, the edges of the unit cell are vectors named $\mathbf{a}, \mathbf{b}, \mathbf{c}$, respectively, and the cell contains a number of N atoms at well-defined position \mathbf{u}_k (see example in Figure 4.8).

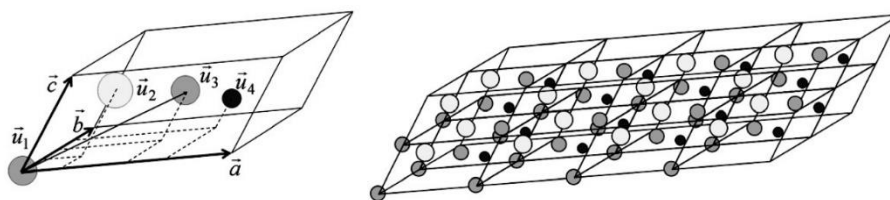


Figure 4.8 A trigonal unit cell with the unit vectors $\mathbf{a}, \mathbf{b}, \mathbf{c}$, and four atoms at different positions \mathbf{u}_k (left) and an assembly of some unit cells forming a small crystal (right) [155].

An important remark is that the lattice point doesn't give neither information about the chemistry of the crystal, nor about the bonding among atoms.

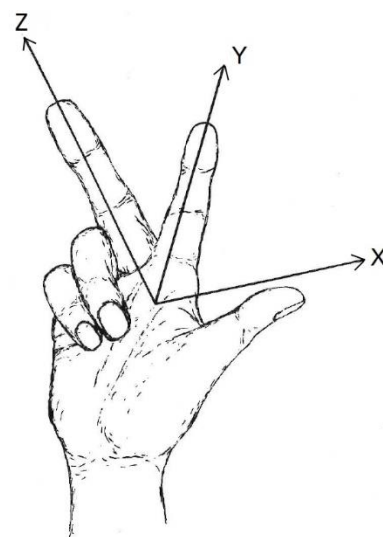


Figure 4.6 Right-hand rule [166]

Therefore, in defining a single phase of a layer, it is necessary to define not only which lattice structure constitutes the phase, but also which atoms fills the positions inside this spatial structure.

A first XRF screening of the material can give useful information on main atomic elements, in order to restrict the search among some known common phases, as available on public databases, e.g. the already cited COD (see Paragraph 3.2).

4.4.2 Substitutional element and impurities

After having defined the main structure, because pure crystals are rare, another step is needed: usually, the crystal structure is defined taking care of substitutional element and/or impurities (Figure 4.9).

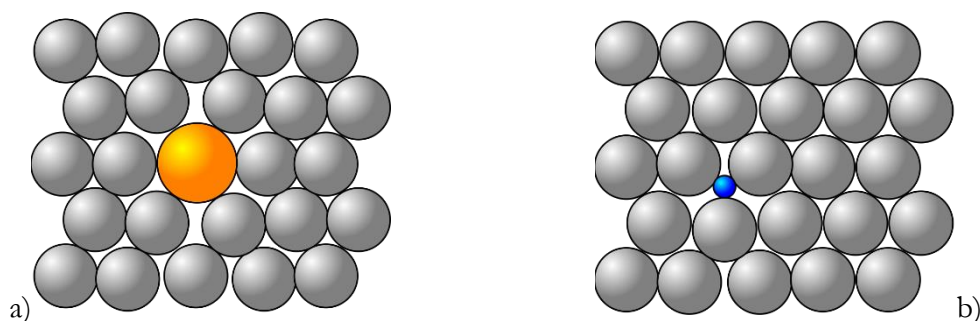


Figure 4.9 Element in a) substitutional position, b) interstitial position [source: Wikipedia].

These elements are conveniently inserted in the model defining the partial site occupation and, in case of interstitial atoms, their position in the lattice (Figure 4.10).

One or more element as substitutional can exist in a crystal, so in the model their percentage of substitution is incorporated.

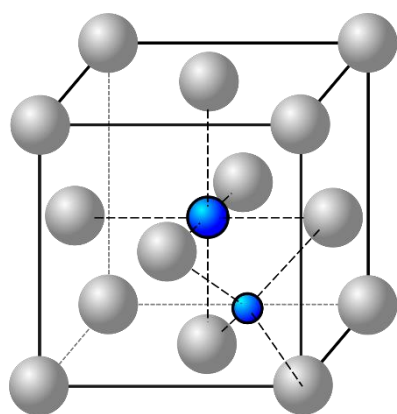


Figure 4.10 Example of interstitial element in FCC lattice [source: Wikipedia].

Moreover, impurities can be more than one, inside the same crystal, and this has impact non only on the chemical structure but also on structure volume distortion of the lattice compared to the pure crystal.

This means that the chemical composition impacts on XRF part of analysis, while in XRD part of analysis, the cell parameters of the single phase must be fitted according to these contributions from substitutional or interstitial elements.

This approach must be implemented for every phase which is part of the single layer definition, and for every layer defined for the material model.

In some samples, however, impurities may be present in more than one place in the crystal: this means that it can be present on one or more layers, and/or substitute different atomic elements in different phases.

In such cases, it is necessary to make some arbitrary assumptions based on the chemistry of the sample (as derived from the first XRF screening) or taking in consideration the production process, if this is known.

When it is not possible to presume a specific distribution, the impurities are conveniently distributed over all the possible phases, and only in a second step, during model refinement, some more precise consideration can be derived from results.

4.4.3 Texture and strain

As stated before, a polycrystalline material presents single-crystal regions, called *grains*, whose interfaces are the so-called *grain boundaries*.

The crystallographic texture can be defined as the relative “organization” of the grains in an polycrystalline material [183].

In a sample where the orientations are fully random is said to have no distinct texture: this means that a solid with perfectly random grain orientation have isotropic properties, considering scales sufficiently larger than the size of the grains.

If, on the contrary, the crystallographic orientations are not random, but have some preferred orientation, then the sample has a weak, moderate or strong texture. The degree is function of the percentage of grains having the preferred orientation.

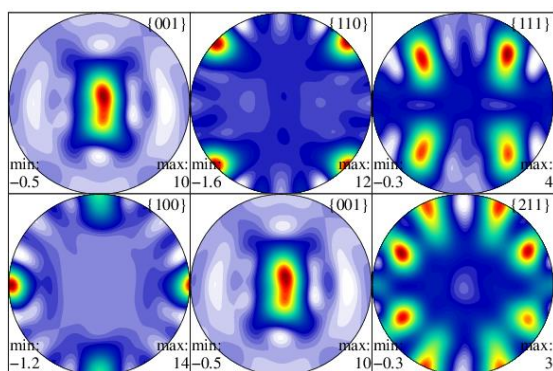


Figure 4.11 Pole figures displaying crystallographic texture of gamma-TiAl in an alpha2-gamma alloy, calculated using MAUD software.

Among the quantitative techniques for analysing texture, the most widely used is XRD using texture goniometers.

Texture is often represented using a pole figure (Figure 4.11): in this figure, a specified crystallographic axis (or pole) is plotted in a stereographic projection, along with directions relevant to the material's processing history [29].

This organization influences frequently its mechanical and physics properties and is seen in almost all engineered materials. Texture can affect many polycrystalline materials: rocks, ceramics, metals, polymers, etc.

In bulk multi-crystalline materials, preferred orientations are in general regularly due to production processes, e.g. solidification, nucleation, grain growth, recrystallization, phase transformation, sintering, plastic deformation.

The effect of texture is a modification of XRD spectra peak intensity, which must be considered in order to fit correctly data.

Moreover, there can also be residual stress inside the grains of the material, e.g. due to production process, lattice distortion or interstitial impurities, with a consequent strain in the lattice.

This means that in considering an XRD spectrum, we can have also a shift in the position of the peaks (e.g. in case of uniform strain, see Figure 4.12(b)) or a peak broadening, even if the peak positions remain virtually the same (e.g. in case of nonuniform strain, see Figure 4.12(c)) [83,142,164].

As already seen previously (see Paragraph 3.4.7), there is the factor $P_{k,j}$, in Eq. 3.5, the so-called *preferred orientation function* (or *texture weight factor*) [104], which helps in considering this structure preferred orientation inside the model definition. For the definition of $P_{k,j}$, there are many formulas, derived from texture models, which depends on geometry and on crystal group type. In the case of random texture the parameters $P_{k,j} = 1$.

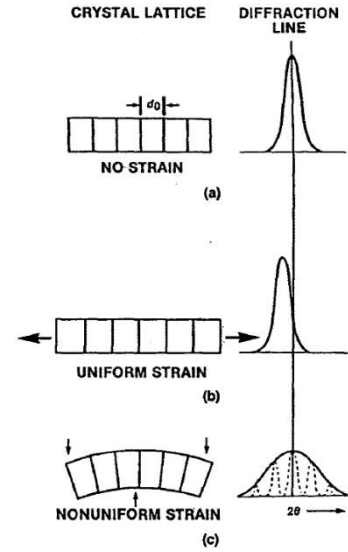


Figure 4.12 Strain expanding and contracting d-values [83].

4.4.4 Problem analysis

After the definition of the model, the data of the model and the parameters regarding layers, thickness, phases, phases distribution, possible texture and strain, contribute to define the problem to analyse through combined approach.

From the point of view of XRF-part of combined analysis, from elemental composition of the phases defined for each layer are derived the weight fraction data and densities, in order to evaluate the XRF contributions. Moreover, also the associated matrix effects are used to evaluate the XRF spectra.

In computation process, the varying angle θ of the incident X-ray beam during the measurement and all filters or media encountered (see Figure 4.13) are also considered.

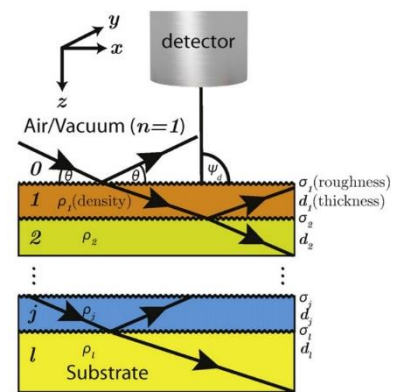


Figure 4.13 Example of multilayer sample model [74].

This allows to correctly model the different absorption path of the excited fluorescence photons traveling to the detector.

All the other structural parameters of the model are contemporary used for XRD-part of combined analysis. The XRD spectrum is fitted starting from the physical model structure (phases, layers, thickness, phase distribution, etc...) and possible effects of texture and/or strain inside the material. Moreover, cell parameters may be fitted in order to taking in count of element inclusion as interstitial or substitutional atoms, and possible strain effect due to production processes.

4.4.5 Software for analysis

This innovative approach has been implemented in the program MAUD [104,106], combining original XRD algorithm with part of the XRF module implementation from the GimPy and JGIXA programs [17,74], creating a comprehensive radiation–matter interaction model, which takes care of both elastic scattering and photoelectric absorption/fluorescence.

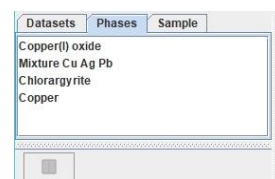
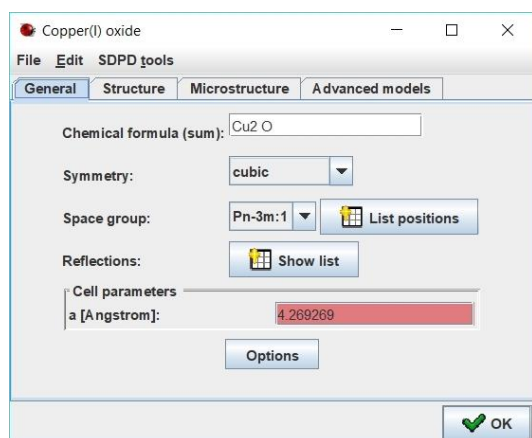
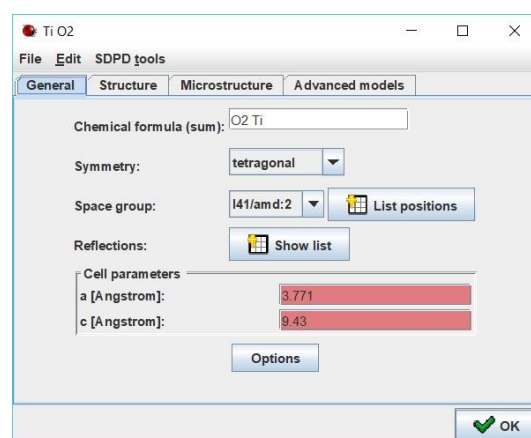


Figure 4.14 MAUD phase list.

Inside MAUD, the phase definition is easily obtained through specific wizards devoted to this important task.



a)



b)

Figure 4.15 Examples of a) Cu₂O and b) TiO₂ phase definition in MAUD.

After having defined the instrument parameters (beam, detector, etc...) and loaded the spectrum data for XRF and XRD, it is required to define the phases inside the “Phases” list in the MAUD parameters definition window (Figure 4.14).

For every phase we can define the lattice and the atoms inside the lattice. An example is given in Figure 4.15, where we can see the phase definition wizard for two different lattices: Cu₂O (a) and TiO₂ (b).

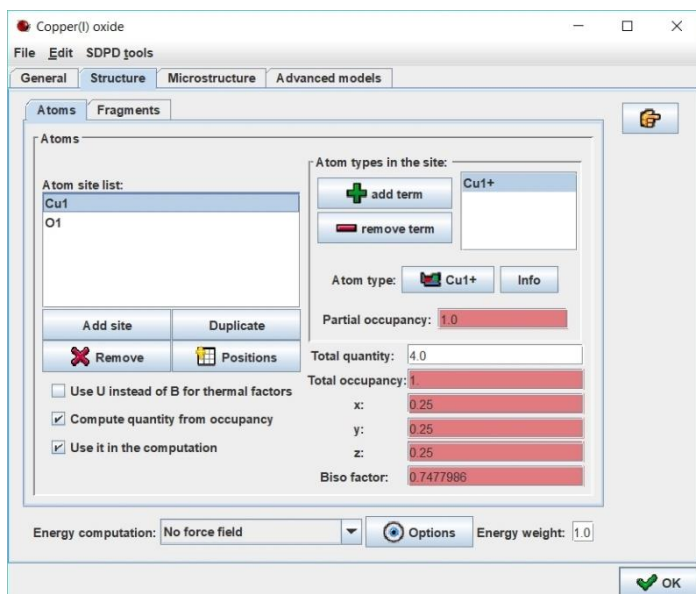


Figure 4.16 Atom content and parameters for Cu_2O phase in MAUD.

4.17).

The task requires to select the position involved and to assign the substitutional element to the position of the original phase element, which is substituted, setting the proper percentage of occupancy.

In case of more substitutional elements inside the same phase, it is simply needed to add them to the list of substitutional atoms, defining for every element the proper percentage of occupancy (which can in a second step refined by the combined analysis), in order that the total sum will be 1.

Through other two panels of the phase wizard, “Microstructure” and “Advanced models”, it is also possible to set-up other analysis parameters, e.g. line broadening

model, the size-strain model, the texture model and the strain model to be used.

In the “General” panel it is defined the lattice parameters, in term of lattice type, space group and cell parameters.

In the “Structure” panel of the same wizard, it is defined every single atom position of the lattice, with partial occupancy (in this case 1 for every atom).

In the case that we have, for example, a substitutional element, it is possible to define it inside “Structure” panel of the same wizard (Figure

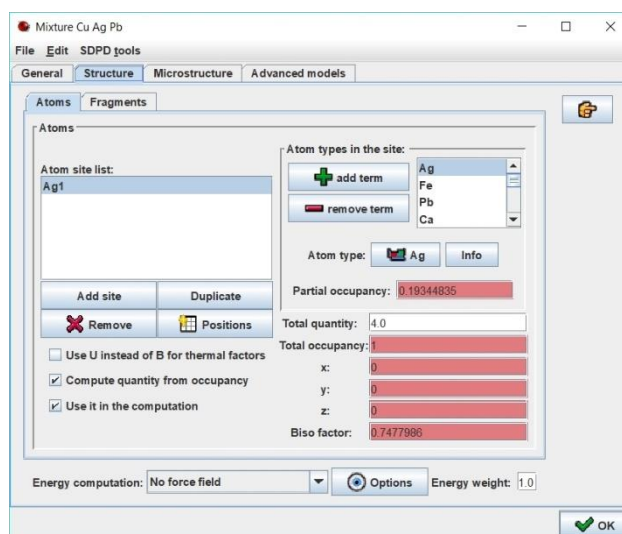


Figure 4.17 Definition of mixture phase $\text{Ag}_{0.88}\text{Cu}_{0.12}$ with multiple impurities in MAUD.

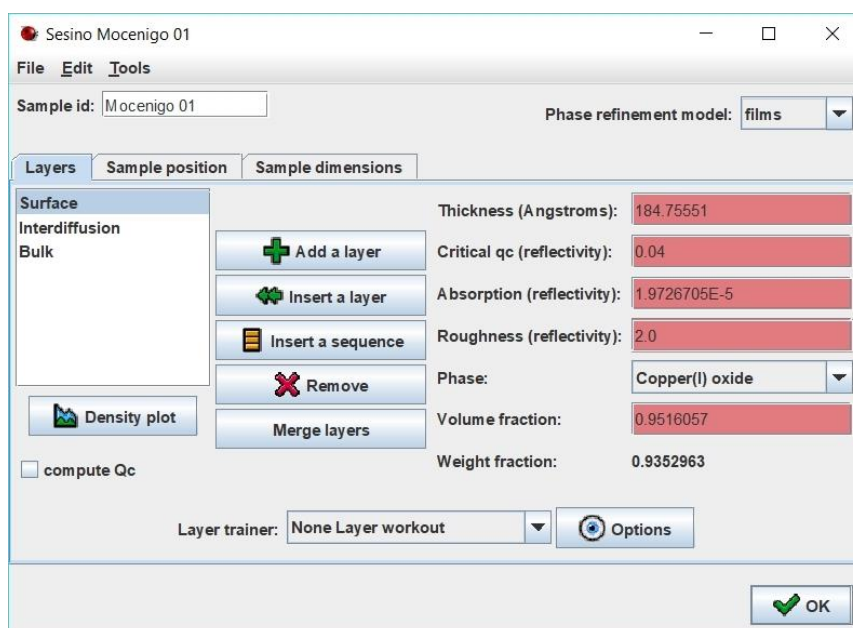


Figure 4.18 MAUD layer structure wizard.



Figure 4.19 MAUD sample list.

A similar wizard approach is provided for the definition of the layer structure modulization of the sample (Figure 4.19). In this case, through the wizard we can define the sequence of layers, and for every layer the main aspect useful for analysis, e.g. thickness, phases and phase volume fraction (

Figure 4.18).

4.4.6 Elaboration tips

Because of Eq. 4.1, an important aspect of this approach consists in the possibility of setting weight factor between the diffraction and fluorescence data in the least-squares fitting. The weighting balance between XRD and XRF data should be evaluated depending on the quality of the analysis data in one with respect to the other, and the information needed.

XRF spectra generally have higher intensities and, therefore, a better signal to noise ratio and, since usually several spectra are acquired for each XRD pattern, this ensures a significant statistical reliability.

It is usually a good practice, in the least-squares refinement strategy, to increase the weight of the XRD contribution in order to establish a first qualitative estimation of the phase content (in MAUD exists a specific parameter associated to dataset loader, see Figure 4.20).

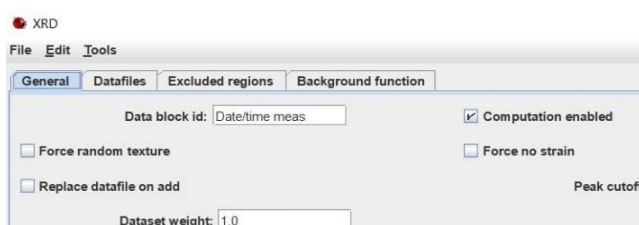


Figure 4.20 MAUD wizard page for spectrum weight definition.

As a rule of thumb, once the main phases have been identified and the model has been set-up, it is possible then shift to a more balanced situation, in which XRD and XRF data have comparable statistical weights.

Another refinement strategy is to resolve the more influencing parameters first, and only in successive steps refining the remaining ones [29]. The aim is to avoid that too many parameters not only increase the time of computation, but also can increase the risk that if the starting point is not good, the convergence can be very hard to get in acceptable time.

5 SOFTWARE DEVELOPMENT

For the analysis of the XRF and XRD data, a software is an unavoidable companion, in order to get reliable information in quick time. For the goal of the present research, the development has been started from two existing tools, GimPy [17] and MAUD [16,107].

The first one is a complex procedure programmed in Python, which can manage ED-XRF, TXRF and GIXRF analysis. It has no GUI interface and must be used creating adapted script from the scratch, using some common examples from the scratch.

MAUD (Material Analysis Using Diffraction) is a general diffraction/reflectivity analysis program mainly based on the Rietveld method, but not limited to. Written in Java, it can run on Windows, MacOS-X, Linux, Unix (it needs Java VM 1.7 or later). More details are available on the dedicated web site: <http://maud.radiographema.com/>.

Because the aim was to combine the techniques XRF and XRD, the natural approach was to combine the two tools, porting the Python code into the MAUD code. This required a Java translation of all the procedures developed under Python, and a complex adapting of data structures, not only because of the differences between the data structure in both languages, but also because of the existing schemas in MAUD, optimized for Rietveld analysis.

On the other side, the original target of MAUD was XRD data, and the interface reflects the complexity of the matter, requiring a deeper knowledge of the parameters involved.

For this reason, in order to simplify the approach to the MAUD software and to the data input, especially for the integrating XRF part, it has been decided to accompany the porting of Python code to Java with the contemporary development of some simplified interfaces for managing basic XRF parameters, like detector configuration and X-Ray tube parameters, and aspects like calibration and peak picking on a XRF spectrum, performed manually in Python and not easily available or missing on MAUD.

In the next paragraphs, therefore, it will be illustrated the interfaces developed, the software complement developed, and their potential, as soon as they will be incorporated in MAUD for non-expert users.

5.1 Common development libraries

For the development of the complements to MAUD and GimPy, and the porting of Python code to the Java side, some existing libraries freely available on internet has been used. This in order to avoid problems with royalties or licenses.

In this paragraph the list of all open source libraries used in the implementations are summarized, accompanied with the public website for download and documentation, if available, as reported in our annexed documentation. The version indicated is the last one adopted.

- Apache Commons IO 2.5: <http://commons.apache.org/proper/commons-io/index.html>
- Apache Common Math3: <http://commons.apache.org/proper/commons-math/>
- Apache Collections 4.x: <https://commons.apache.org/proper/commons-collections/>
- Apache Log4j v. 2: <http://logging.apache.org/log4j/2.x/>
- xraylib 3.3.0, which requires Apache Common Math3: <https://github.com/tschoonj/xraylib>
- JFreechart: www.jfree.org
- ini4j: ini4j.sourceforge.net
- opencsv 4.1: <http://opencsv.sourceforge.net/>
- Apache Batik SVG Toolkit, required by freechart: <https://xmlgraphics.apache.org/batik/>
- Apache commons-beanutils v. 1.9.3, required by opencsv: <https://commons.apache.org/proper/commons-beanutils/>
- Apache commons-lang3 v. 3.3.7, required by opencsv: <http://commons.apache.org/proper/commons-lang/>
- Apache commons-text v. 1.2, required by opencsv: <http://commons.apache.org/proper/commons-text/>
- SQLite JDBC Driver, developed by Taro L. Saito: <https://bitbucket.org/xerial/sqlite-jdbc/downloads>
- DM-Library: www.studio-martorelli.net
- JUnique: <http://www.sauronsoftware.it/projects/junique/>

5.2 Software development tools

The implementation of the software tools and libraries, and the debugging of GimPy and MAUD, has been performed on two computer systems:

- a DELL notebook, from FBK-Fondazione Bruno Kessler, with Intel Core i7-4800MQ CPU, Intel HD Graphics 4600, 16 MB of RAM, two SSD of 256 MB, with Windows 10 OS;
- an ASUS desktop, personally owned, with Intel Core i7-3770 CPU, Nvidia Graphics Geforce GTX550TI, 16 MB of RAM, two HDD of 1 TB, with Windows 10 OS;

For the development, as editor has been chosen the Eclipse IDE for Java Developers, Version: Neon.3 Release (4.6.3), Build id: 20170314-1500, freely available on the website of the Eclipse Foundation (<https://www.eclipse.org/>).

This IDE is available on different platforms (Windows, Linux, MacOS) so allowing future development also on no-Windows-systems.

This IDE is adapted for any Java developer, including a Java IDE, an easy GUI interface developer, called WindowBuilder Editor, a Git client, and a XML Editor. This is useful, because for the synchronization between the two development machines, the Git protocol has been used, which is based on the

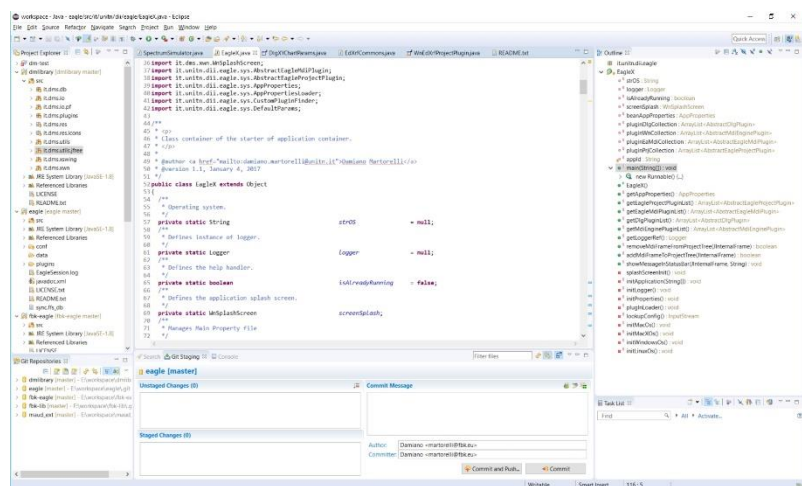


Figure 5.1 The GUI of Eclipse IDE for Java Developers.

GitLab is a single application server for the entire DevOps lifecycle that allows teams to work together and faster, with version control over all the implemented code.

GitLab shortens application cycle time, with a united workflow that reduces engineering risk. Shorter cycles mean more and smaller frequent deploys, which have many advantages:

- higher predictability: smaller iterations are easier to estimate than larger ones;
- better code quality: every small change gets attention;
- easier troubleshooting: a smaller deploy introduces less changes that can potentially introduce issues.

5.3 The FBK X-Ray Java Library

As previously stated, the aim was to integrate the GimPy features into the MAUD software, in order to build a full integrated combined XRF/XRD approach.

All the Java code derived from the original Python code of GimPy has been structured into a library called fbk-lib, where the root structure is built up on the `it.tn.fbk.*` path. In Table 5.1 are resumed all the components of the library pack.

Table 5.1 Resume of the *fbk-lib* library content.

PACKAGE	DESCRIPTION
<code>it.tn.fbk.io</code>	I/O class container.
<code>it.tn.fbk.io.xray</code>	I/O XRF interexchange class container.
<code>it.tn.fbk.math</code>	Mathematics classes data container.
<code>it.tn.fbk.physics</code>	Physics classes data container.
<code>It.tn.fbk.res</code>	Resources container.
<code>It.tn.fbk.res/icons</code>	Standard FBK icons for X-Ray GUIs.
<code>It.tn.fbk.res/images</code>	Standard FBK images for X-Ray GUIs.
<code>it.tn.fbk.tools.db</code>	Database viewer classes.
<code>it.tn.fbk.xray</code>	X-Ray general classes data container
<code>it.tn.fbk.xrf</code>	Basic classe for Xrf analysis management.
<code>it.tn.fbk.xrf.wizard</code>	System wizard classes for applications.
<code>it.tn.fbk.xrf.wizard.event</code>	System events for wizard classes of applications.
<code>it.tn.fbk.xswing</code>	System add-on components for wizard classes of applications.
<code>org.scijava.swing.checkboxtree</code>	Scijava derived classes for FBK xswing extended plugins.

The package for the GUI dedicated to X-ray parameters is the *it.tn.fbk.wizard*, which contains the wizards for easing the work with X-ray data input. The main of them are resumed in Table 5.2.

Now every wizard briefly will be shortly described in the next paragraphs which are dedicated to the software tools developed.

Table 5.2 The list of main wizard in *fbk-lib* library, path *it.tn.fbk.xrf.wizard*, for X-ray data manipulation.

CLASS	DESCRIPTION
<i>DlgBeamEnergyParams</i>	Form for managing of beam energy parameters.
<i>DlgBeamSourceEditor</i>	Form for managing of beam source parameters.
<i>DlgEdDetector</i>	Form for ED detector parameters managing.
<i>DlgEdDetectorList</i>	Form for material list managing.
<i>DlgEdSpectrumEditor</i>	Form for managing of the Energy Dispersive spectrum data.
<i>DlgEdSpectrumPeakSetter</i>	Form for managing of spectrum peak setting.
<i>DlgEdXrfCalibrator</i>	Form for ED-Xrf spectrum calibration.
<i>DlgEdXrfConfigEditor</i>	Form for ED-Xrf experimental condition parameter input.
<i>DlgEdXrfElemPicker</i>	Form for ED-Xrf spectrum picking of atomic elements.
<i>DlgEdXrfImport</i>	Form for ED-Xrf spectrum import from a text file.
<i>DlgEdXrfParams</i>	Form for managing of the single parameter for ED-Xrf spectrum.
<i>DlgEdXrfRoIsSetter</i>	Form for ROIs managing.
<i>DlgEdXrfSpectraSeries</i>	Manages the creation of a series of spectra with different angle of beam incidence for contemporary analysis.
<i>DlgElementDetail</i>	Form for showing the details of every atom in the periodic table.
<i>DlgLayerEditor</i>	Form for managing of single layer parameters.
<i>DlgLayeredSampleEditor</i>	Form for layered sample managing.
<i>DlgLineSetter</i>	Form for single line assignment in calibration.
<i>DlgMatComponentEditor</i>	Form for managing of single component parameters in a material.
<i>DlgMaterialEditor</i>	Form for single material managing.
<i>DlgMaterialList</i>	Form for material list managing.
<i>DlgPeriodicTable</i>	Form for interacting with the periodic table.
<i>DlgSpectrumMatch</i>	Form for confrontation of two different spectra.

5.4 Eagle-X

Because of the complexity of MAUD inner structure, and the need of translating the GimPy code from Python to Java language, in order to integrate it with MAUD and, on the other side, considering the need to simplify the approach to XRF analysis with an easy GUI (Graphic User

Interface) approach, it has been decided to implement in first instance an external tool developed in Java, called for simplicity Eagle-X (**E**asy **G**UI **L**ite for **E**nd-user on **X**-ray; Figure 5.2).

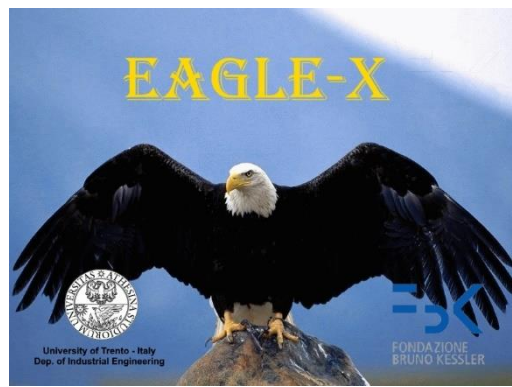


Figure 5.2 The splash screen of Eagle-X

This application has allowed not only to test the single developed components inside the FBK X-Ray Java Library, but also to put them together for some basic approaches to the XRF spectra, with GUI tools not available neither in MAUD nor in GimPy.

The developed interfaces has been derived from an original GUI version in Python, started at the beginning of the current research and presented with a poster [122] at EXRS 2016 Conference in Gothenburg

(Sweden).

The need of Java integration and some problems with the QT GUI libraries encountered on different OS (Operating System) platforms (Linux and Windows), suggested to prefer Java as unique development tool.

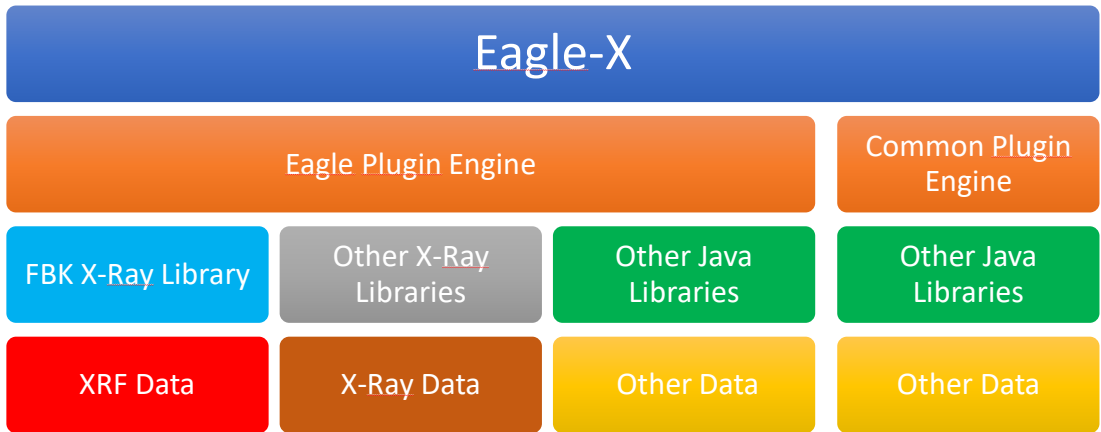


Figure 5.3 Eagle-X: application schema of layered inner structure.

Technically, Eagle-X is only an empty GUI frame where the operative parts are all loaded as external plugins: Eagle-X defines, with two different plugin schemas, only the requirements for linking the plugin to the inner structure of menus and project containers, and the rules associated to them. This allows the developers flexibility in defining the plugin engine for viewing and manipulating data, through a common MDI (Multi Document Interface) approach (see example in Figure 5.4).

This has the advantage to separate the core engine of X-ray analysis from the interface level of the GUI, which is managed through a plugin engine separated from the Eagle-X GUI frame.

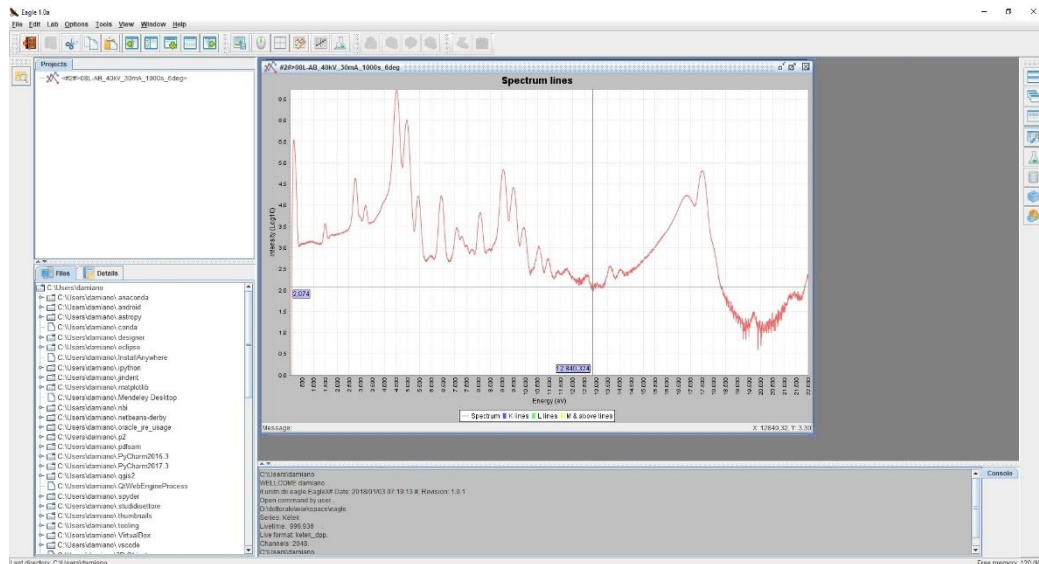


Figure 5.4 Example of Eagle-X application with XRF spectrum viewer in an MDI form.

Eagle-X only gives strict rules through abstract classes which define the minimum requirements for the plugin engine to be loaded inside the plugin loader of Eagle-X, in a four layer approach to data manipulation, as summarized in Figure 5.3.

This allow to extend the capabilities of the application also to fields and data other than X-rays, simply adopting the preferred plugin schema.

For the sake of simplicity, in the following paragraphs it will be used the acronym Eagle-X in any case, in order to refer to the whole X-ray tools.

5.4.1 Common aspects

When Eagle-X is started, after loading all libraries and all plugins loaded in the dedicated folder, the main desktop appears. It is characterized by different areas, which reflect also the different plugin role.

Firstly, it is possible to note the dark grey area, which is the area where the single form with data (e.g., graphics form) will be showed (see example in Figure 5.4). It is the MDI area. Under this, in light grey, it is shown the console area, where the application shows data, information, useful parameters during the application use. It partially intercepts errors and messages from Java console.

On the bottom of the window, the status bar reports on left some useful information related to last process executed, on right the current memory availability.

On the top of Eagle-X application, there is the menu bar, with the following standard menu options:

- File

- Lab
- Options
- Tools
- View
- Window
- Help

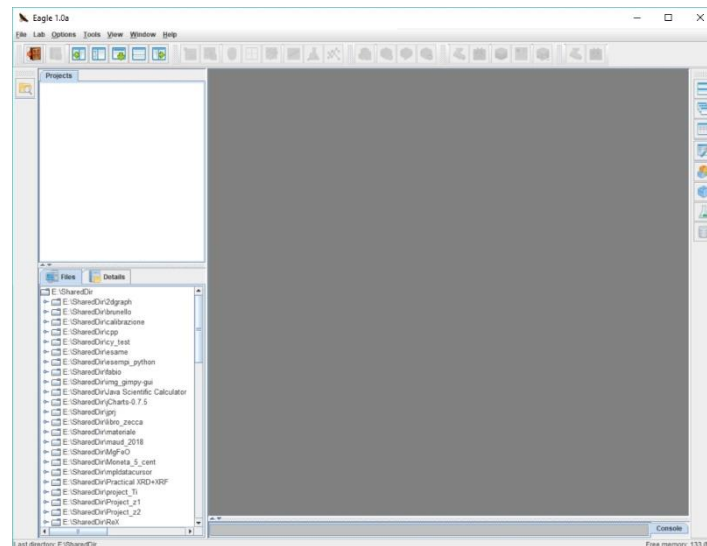


Figure 5.5 Eagle-X main desktop.

These menus have fixed options (e.g. View, Window and Help), while other, like the Lab or Tools, have options which derives from the installed plugins and the interface engine set in every plugin.

On the left of application window, there is another toolbar, which currently supports only the internal directory manager. The other two white areas contain in the top one the current active projects, with related MDI forms (see example in Figure 5.4), on the bottom one the current directory listing of present file



Figure 5.6 Periodic table of elements.

or project. The two areas are resizable by hand with mouse, or by icons in the top toolbar.

On the right of application window, another toolbar shows the icon buttons which controls the MDI form commands (classic Tile, Cascade, Minimize All commands); moreover, here are anchored, if the right parameters are set, the application contained in plugins which respect the

“Common Plugin Engine Interface” contained in Eagle-X. Currently, in the Eagle-X, there are two default plugins:

- Periodic table of elements (see Figure 5.6)
- FBK SQLite Viewer (see Figure 5.7).

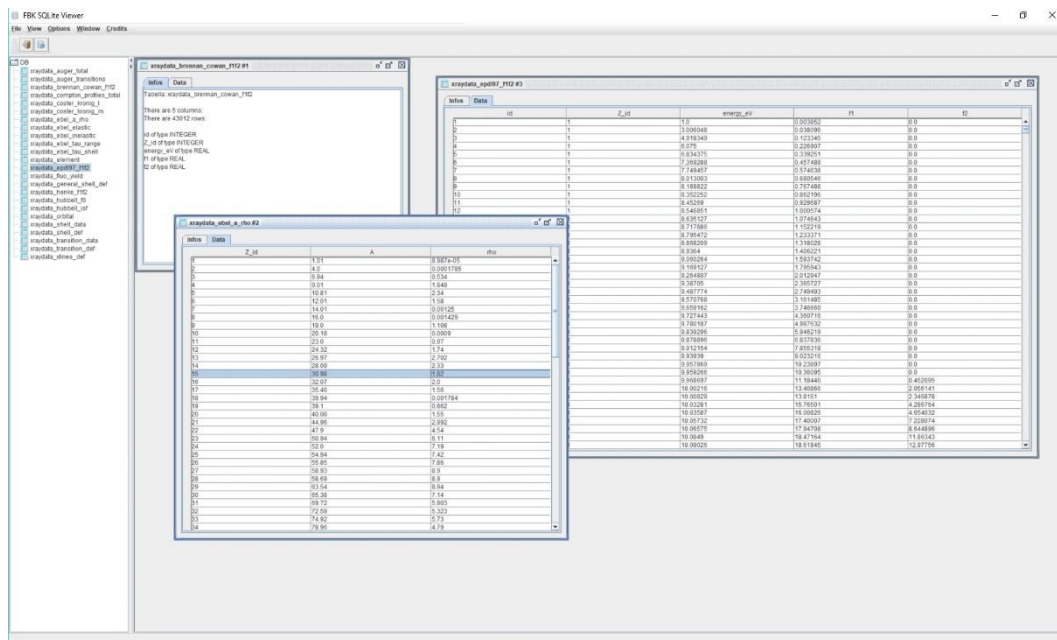


Figure 5.7 FBK SQLite Viewer with some forms about tables in Fbk xraydata database from GimPy.

The main aspects of these two plugins we’ll be described shortly, both of them contained in the Java library fbk-lib, for the forms of applications, and linked in Eagle-X through the engine interface defined in the fbk-eagle plugin interface.

5.4.2 Periodic table of elements

This plugin manages the form (see Figure 5.6) which shows the periodic table of elements for consultation of elements and all the X-ray data contained into the *xraydata* database created for the GimPy application [17] and in common with our fbk-lib.

Clicking with the right button of the mouse on the element cell, a new form is opened, with four sheets regarding different data for the selected elements:

- Basic data, with all the basic aspects of the element (see Figure 5.8a);
- Shells, with the physical data about the shells inside the atomic element (see Figure 5.8b);
- Transitions, with the physical data about the possible transitions inside the atomic element (see Figure 5.8c);

- Lines chart, with the graphical representation of the characteristic lines of the element (see Figure 5.8d).

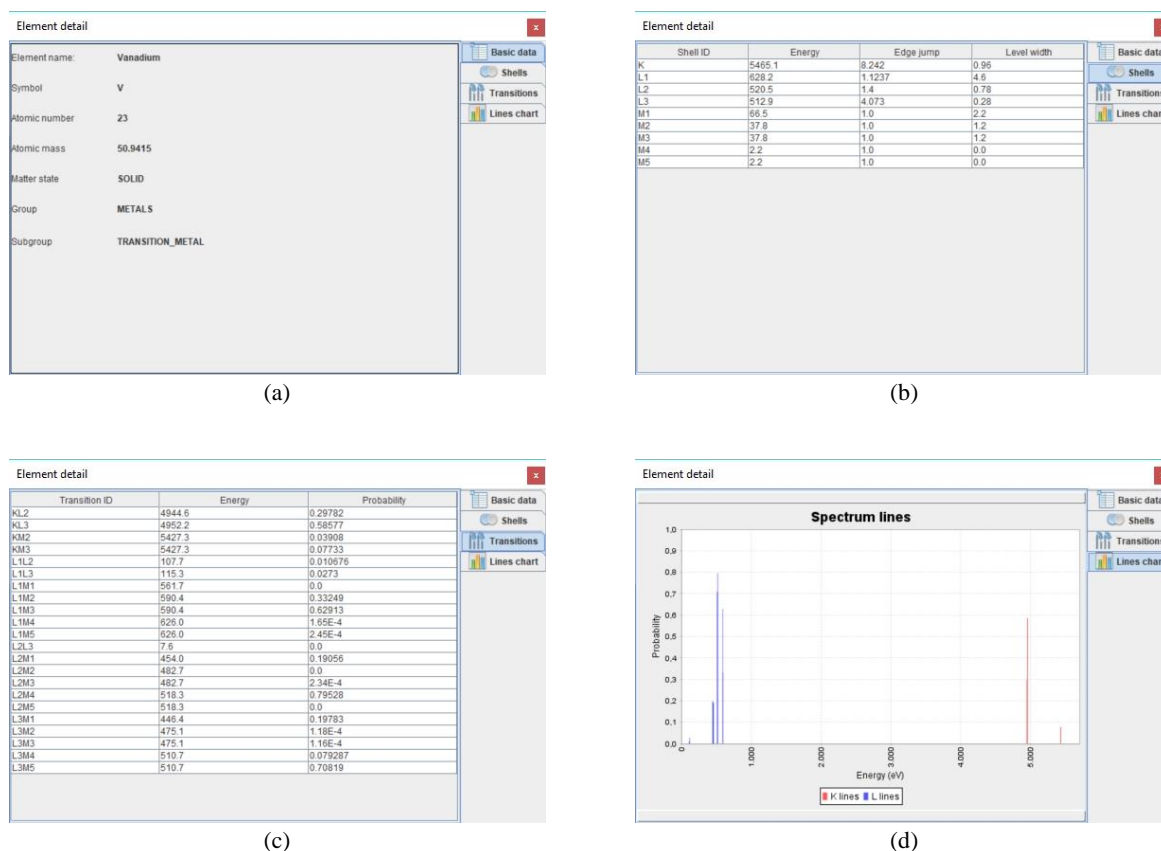


Figure 5.8 Element form with detailed data about (a) element (b) shells, (c) transitions, (d) characteristic lines.

For the chart of Figure 5.8d, it is possible to save the image as PNG file format (as bitmap image) or SVG file format (vectorial image) using the right button of the mouse on the chart itself (it is showed a contextual menu with also other options for personalizing the chart)

5.4.3 FBK SQLite Viewer

This plugin allows through an MDI interface (see Figure 5.7) to show the data inside every SQLite database. SQLite is a self-contained, public-domain, SQL database engine. SQLite is one of the most used database engines, and it is freely available on his website at <https://www.sqlite.org/>.

This easy tool has been programmed in order to have a tool for viewing only the data (it does not allow any modify) inside a SQLite database, and his main target is the *xraydata* database created for the GimPy application [17] and in common with our fbk-lib.

5.5 ED-Xrf Spectrum Viewer

This application is defined as a plugin of Eagle-X, which manages not only the viewing of an ED-Xrf spectrum acquired, but also the calibration of the spectrum and the peak picking of the atomic elements which generate the spectrum itself.

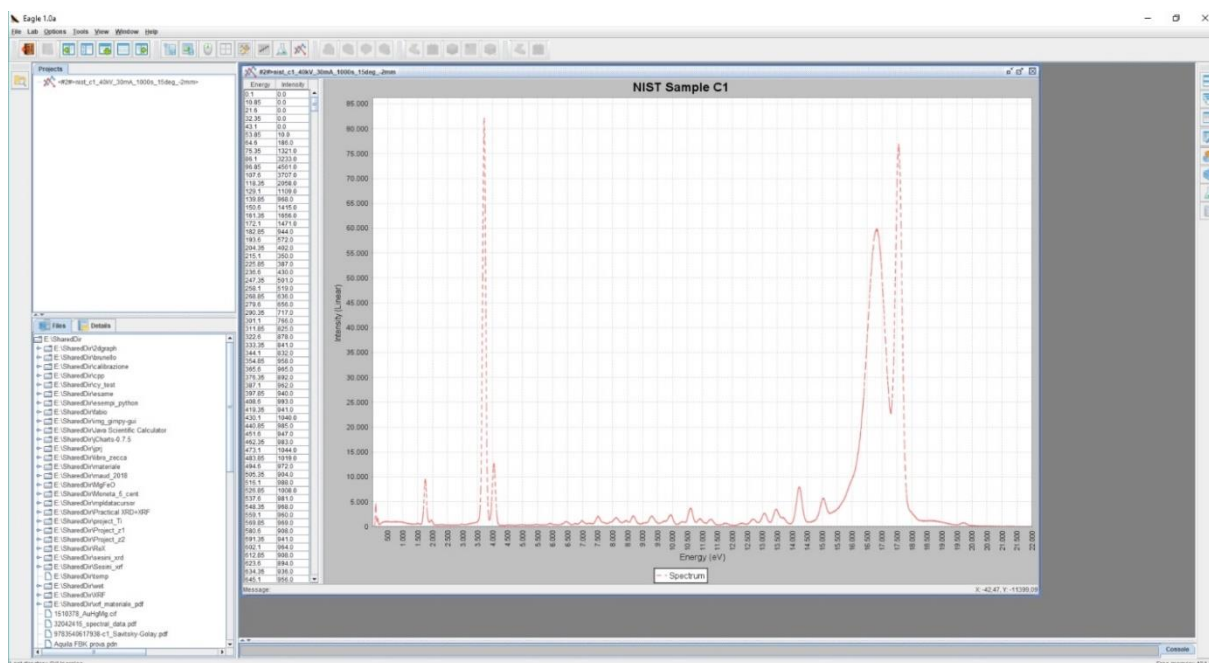


Figure 5.9 ED-Xrf Spectrum viewer example with the spectrum of NIST reference sample.

For opening a spectrum, it is necessary to open the File->Open->View ED-Xrf Spectrum option in Eagle-X. With a wizard, it is possible to select the directory where the spectrum is stored and then, after confirmation, to get what is shown in Figure 5.9, with a form with the drawn spectrum, according to current calibration data stored in Eagle-X, and with an anchored pointer which moves according to mouse motions and shows in real time the coordinates of the point in terms of energy and corresponding intensity of the point on the spectrum..

The plugin interface defines and enables also a new toolbar component, the ED-Xrf Common Toolbar (Figure 5.10), which can be unanchored from the top toolbar and which allows the following options (in order of icons from left to right):

- Save spectrum data;
- Save chart;
- Enable/disable mouse wheel (for zooming the chart);
- Reset chart zoom;
- Chart parameters;
- Calibration of spectrum;
- Get elements from spectrum;

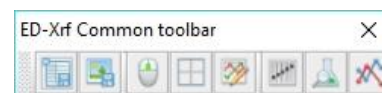


Figure 5.10 ED-Xrf Common Toolbar.

- Confront current spectrum with another one.

The first option simply saves the spectrum loaded to a *.csv file format, allowing the import of data to a spreadsheet, e.g. Microsoft Excel. The last option simply allows to confront two spectra, and will be discussed later, inside the LaSaX simulator (see Paragraph 5.11).

5.5.1 Save Chart

With the “Save Chart” option, the user can store the image of the spectrum in three different formats (Figure 5.11):

- PNG, a bitmap image type;
- JPG, a bitmap compressed image type;
- SVG, a vectorial image type.

The last option is the default one, because, being a vectorial type, it can be used with proficiency in thesis or papers, because it is fully resizable inside every document without loss

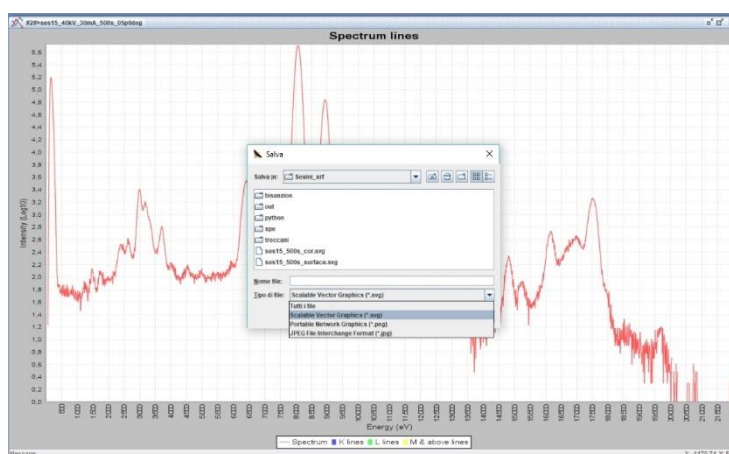


Figure 5.11 Save chart option wizard

of information and quality (for more details on this format, born on web, it is possible to refer to the web address <https://www.w3.org/TR/SVG11/>).

This is not the case of any bitmap type, which is fixed respect to dimensions, and stores the chart according to the current dimension on screen.

5.5.2 Enable/disable mouse wheel and reset zoom

The mouse wheel is useful on the chart because it allows to zoom in or out the chart, respect to the current position of the cross pointer (see Figure 5.12b).

However, this can be not desired in some situations, so the command allows the user to choose *if* and *when* to use this useful option.

An alternative method to zoom the chart is clicking on a chart itself with the left button and, maintaining the pointer clicked, draw a rectangle over the interested area (see blue selected area in Figure 5.12a). After releasing the button, the chart will be zoomed according to mouse selection (see Figure 5.12b).

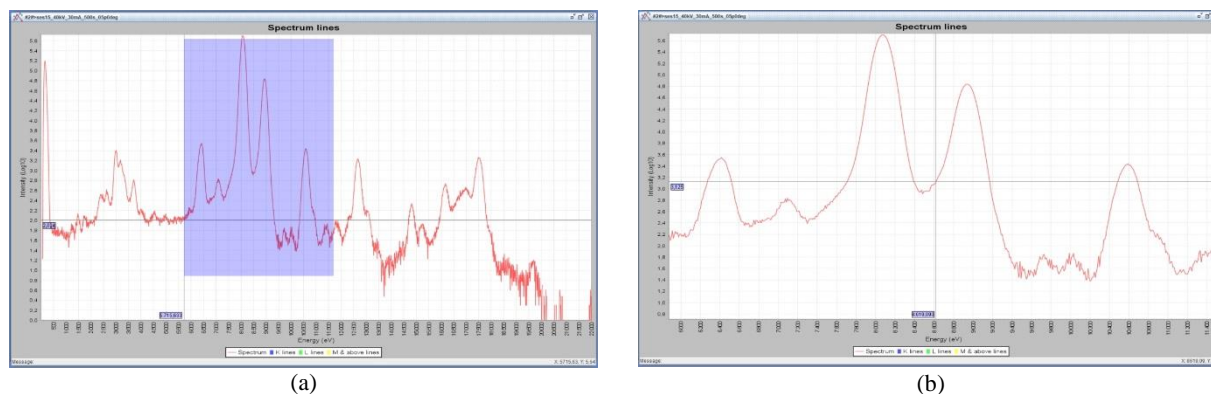


Figure 5.12 The spectrum of S15 (Doge Venier) sample in (a) full view, (b) zoomed view.

For going back to full vision, the command “Reset chart zoom” will redraw the spectrum to full energy vs intensity data array.

5.5.3 Chart parameters

This option allow user to personalize the default parameter of chart drawing: from font to color, from tick presence to tick number, and so on (Figure 5.13).

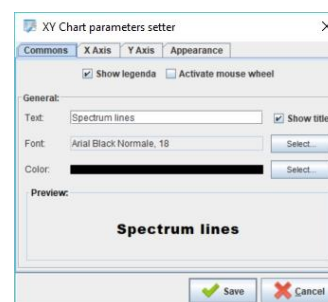


Figure 5.13 Chart parameter manager.

5.5.4 Calibration of spectrum

This is one of the important features of the ED-Xrf Spectrum Viewer: it allows, through a guided wizard, to calibrate an ED-Xrf spectrum according to the peaks of known element inside the spectrum itself. At the end of the process, the user gets the information regarding the zero of the energy detection system, and the gain value of every detector channel.

When a spectrum is loaded into the Viewer, the application uses the last definition of calibration stored inside. This has the advantage to allow an immediate graphical representation of the spectrum on the graphic form and can be useful if the user refers to a series of spectra collected with the same set-up.

Generally, however, a user can load spectra from different source, so it is necessary, for the Viewer, to recalibrate the spectrum referring or to the spectrum itself, or to a spectrum collected on the same machine and with the same set-up from a certified reference sample.

When the calibration command is selected on the toolbar, Eagle-X opens a new modal form which shows again the current spectrum with the current calibration parameters (Figure 5.14).

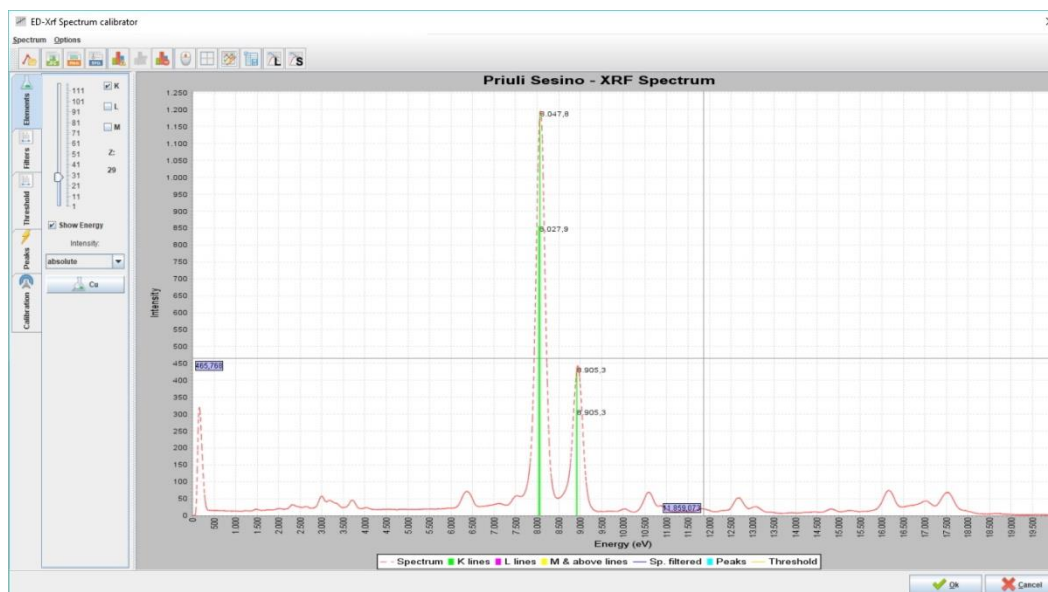


Figure 5.14 Element sheet of calibration wizard

The form has a toolbar on the top, which can be unanchored (in order to allow a greater chart surface, option useful on monitor with lower resolution) and four sheets on the left:

- Elements
- Filters
- Threshold
- Peaks
- Calibration

On the first sheet, a cursor allows to select dynamically the atomic element desired, moving the cursor up or down with the click of the mouse or, if available, with the mouse wheel. The wizard will show immediately the corresponding transition lines on the chart. This option allows the user to identify possible atomic elements directly on the spectrum, in order to match, after, the peaks which will be used for calibration reference.

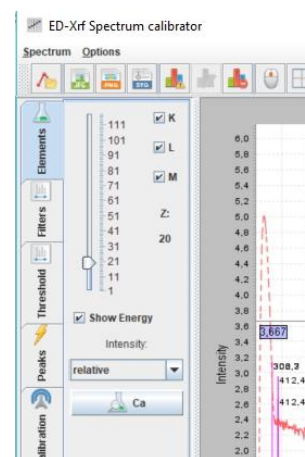


Figure 5.15 Lines sheet of calibration wizard

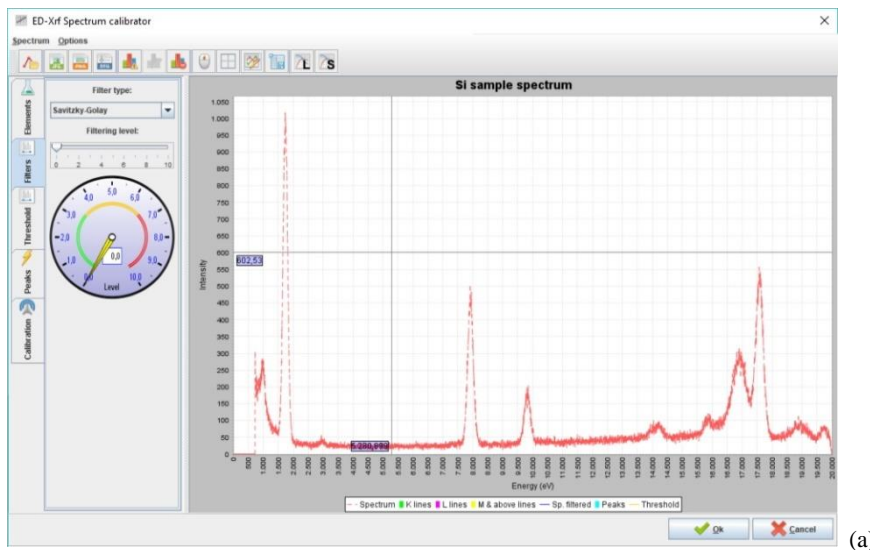
Different colors are used to distinguish among K, L, M or above lines. The intensity of the lines is proportioned to the probability of the transition (see Figure 5.14).

Alternatively, clicking on the button under the cursor, which shows the current atomic element, the wizard opens the form with the periodic element table, already seen in Figure 5.6. Thus, the user can directly access the detailed data of the element for consultation, as already seen previously, or select, with the left button of the mouse, the atomic element desired, to put automatically the cursor at the same level.

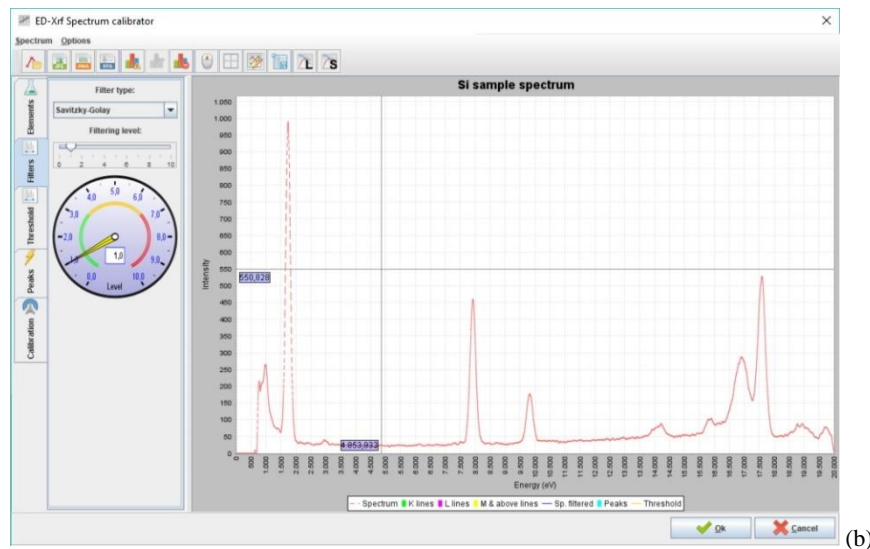
The periodic table wizard is, therefore, closed and, on the chart, the lines of the selected element appear.



Figure 5.16 Lines sheet of calibration wizard with “relative” line option.



(a)



(b)

Figure 5.17 Example of unfiltered (a) and filtered spectrum data for best viewing of peaks.

The Elements sheet allows user also to control which lines are shown on the chart (Figure 5.15) and if, for every line, is showed the corresponding value of energy. Moreover, through the line intensity option, it possible to choose from option “absolute”, which means that intensities of the

line are proportional to maximum value of the spectrum, or “relative” option, which means that lines are proportioned to the local maximum of the spectrum respect to the greater line (see Figure 5.16).

This option is useful because transition lines are scaled respect to the spectrum and this allows to identify that elements which have, for example, K and L lines which overlap lines of other elements: the missing of some lines on the spectrum can help to distinguish among different atomic elements with some lines overlapping.

In case of very noisy spectra, it is possible to simplify lines identification through a real-time filtering of data, using the option on the Filters panel. Currently, only the Savitzky-Golay filter is implemented, but other can be adopted in future. Using the cursor on the sheet, it is possible to apply up to 10 times the filtering on data for best viewing of peaks (Figure 5.17).

The options on the “Threshold” sheet, define the parameters to identify peaks, or excluding smaller ones, in the spectrum, during the process of peak finding through the command of “Peak Finder” available at the menu path Options->Peak Finder or on the toolbar. The threshold is defined as the level under which every peak is ignored.

Here it is possible to define if the picking mode as **absolute** or **relative**: in relative mode, the peak threshold is evaluated taking as reference the 3% of the maximum peak in the spectrum, and the user can only correct the effective level using the cursor.

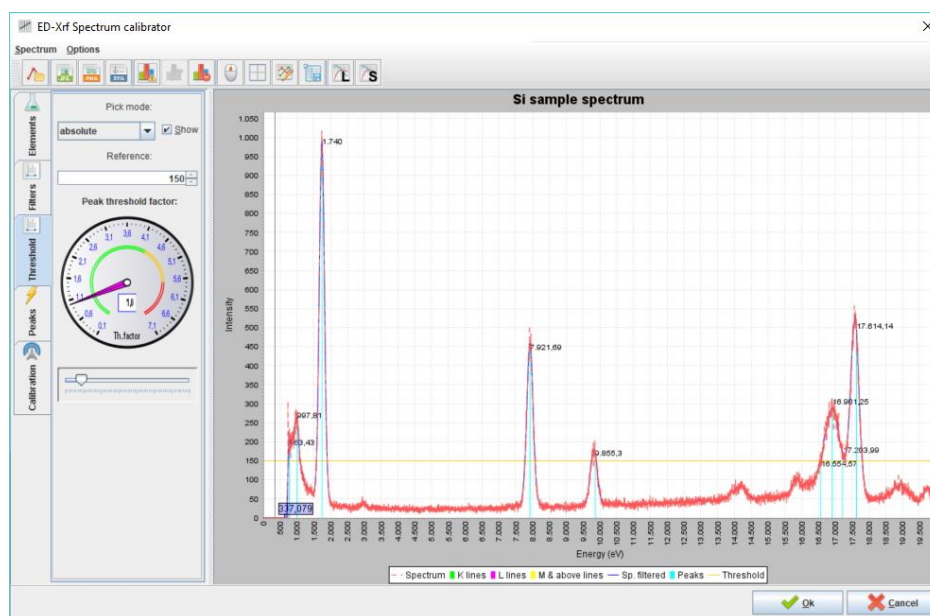


Figure 5.18 Threshold options

In absolute mode, the field of reference is filled by the user with the desired count level, and the he can manipulate the reference using the cursor to best check the filtering using the “Peak Finder” option.

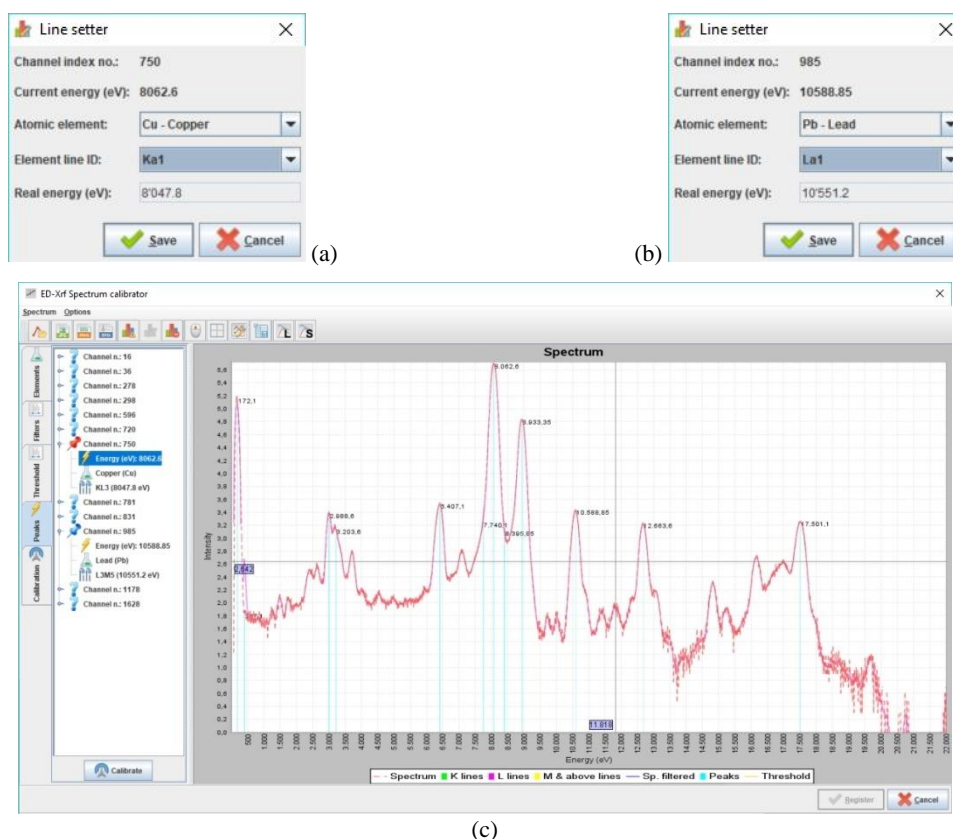


Figure 5.20 (a) peak assignment for Cu; (b) peak assignment for Pb; (c) Peaks sheet with assigned peaks marked by pins.

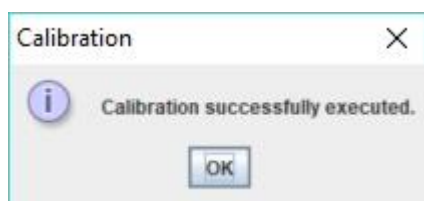


Figure 5.21 Calibration confirmation.

where E_{ell} is the energy of the single element line, E_0 is the zero of the machine's detector, \mathcal{C} is the channel of detector and E_{gain} the energy gain of every channel. If the system is successfully resolved, the application confirms calibration through the dialog window of Figure 5.21, and the spectrum is immediately redrawn with the evaluated data.

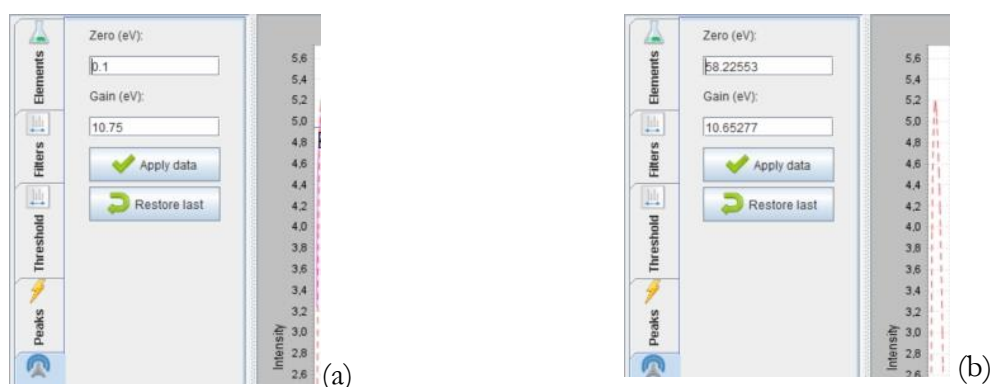


Figure 5.22 Calibration sheet value (a) after calibration; (b) restored from last save.

The data of calibration, in terms of energy zero and gain, can be consulted on the “Calibration” sheet (see Figure 5.22a). It is also possible in any moment to change manually the values, and they

- Elements
- Threshold
- Search
- Element list

On the first sheet, a cursor allows to select dynamically the atomic element desired, moving the cursor up or down with the click of the mouse or, if available, with the mouse wheel, in an analogous way as already see in the previous Paragraph for the calibration form. The corresponding transition lines appear on the chart and the user can manually identify possible atomic elements

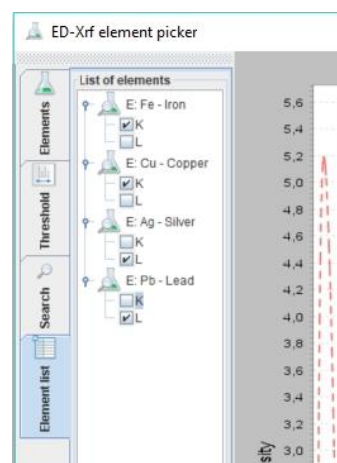


Figure 5.24 Element list sheet

directly on the spectrum, using the button “Select”. This command will add every selected element to the list contained in the list of elements on “Element list” sheet (see Figure 5.24).

Different colors are used to distinguish among K, L, M or above lines. The intensity of the lines is proportioned to the probability of the transition.

Alternatively, clicking on the button under the cursor, which shows the current atomic element, the wizard opens the form with the periodic element table, already seen in Figure 5.6. Thus, the user can directly access the detailed data of the element for consultation, as already seen previously, or select, with the left button of the mouse, the atomic element desired, to put automatically the cursor at the same level. The periodic table wizard is, therefore, closed and, on the chart, the lines of the selected element appear.

The Threshold is analogous at the one already seen for the calibration wizard, so it will not be repeated here (see Figure 5.18) and will filter the peaks on the chart to be considered.

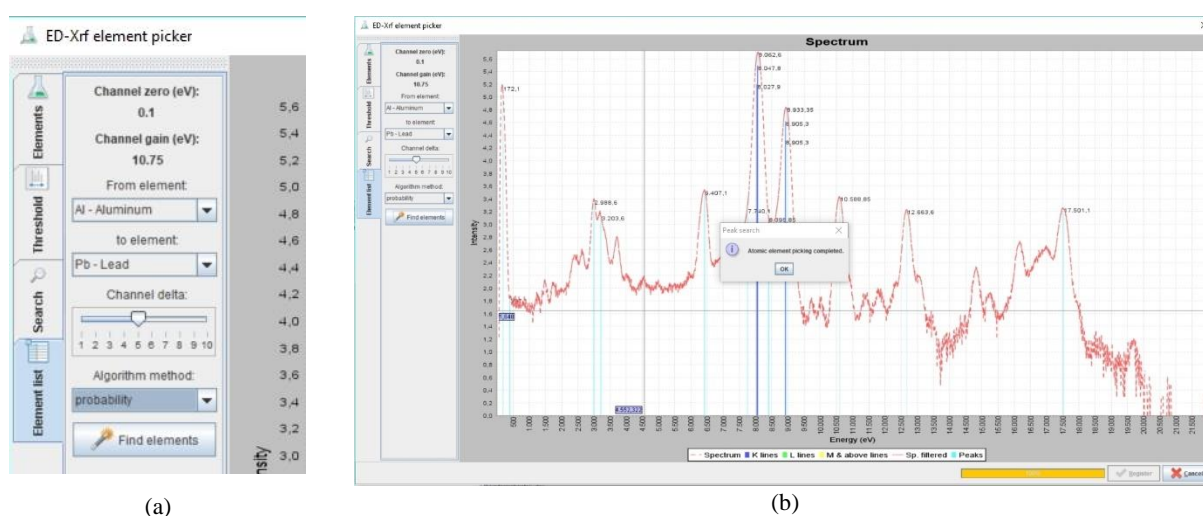


Figure 5.25 (a) Search sheet; (b) search match completed.

The “Search” sheet (see Figure 5.25a) contains all the options for the search match of the element starting from the spectrum. It shows current calibration information, and it is possible to

choose the range of atomic elements which will be used for search match. The “channel delta” options defines the maximum difference in term of energy channels which will be considered for the element-peak search match: greater the delta, greater the possible search match. The “algorithm method” option defines the type of search match executed. There are two possibility:

- Probability;
- Relative.

The first option, which is the default, tells the application that in the search match of the lines must be considered also the probability of the transition as weight: a transition nearer to spectrum peak, if is less probable than another line just a bit farer, is of lower priority in choice. The second option applies the pure search match, considering only the transition nearest to peak.

After having defined all the options, the user can click on the “Fine elements” button, and, after a while which depend on the complexity of the spectrum, the wizard compile the list of elements of the corresponding sheet (see the example in Figure 5.24) and then terminate the evaluation (see Figure 5.25b).

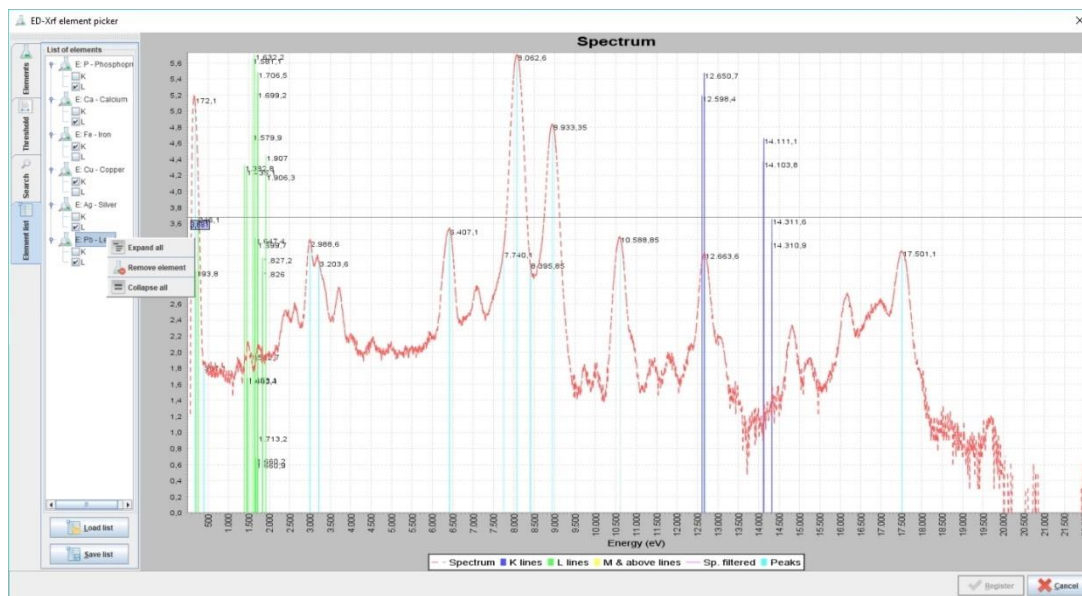


Figure 5.26 Element list sheet of wizard with the found elements, with lines, and the context menu.

On the “Element list” sheet (Figure 5.26) it is possible to consult the found elements with the specific line listed (with selected flag): as soon as the element is selected, on the spectrum appears the corresponding selected line. This allows an immediate control of the quality of the picking. If there are some elements not desired or wrong, it is possible to remove them. At the same time, it is possible to manually integrate other ones if the picking has failed in catching them, using the cursor and the selection button on the “Elements” sheet.

The user can then save the list in a file with XML format, with the dedicated button at the bottom of the list or modify the list with the context menu. The obtained list of elements and lines can then be used as basis for spectrum quantitative analysis in GimPy and MAUD.

5.6 Material list manager

This application is defined as a plugin of Eagle-X, which manages every aspect of a list of materials (Figure 5.27) but, due to the choice of an MDI interface, it is possible to manage more than one list at the same time, allowing the save and reload of them with a specific XML file format, *.xmld (**XML Material List Data**), created for managing them.

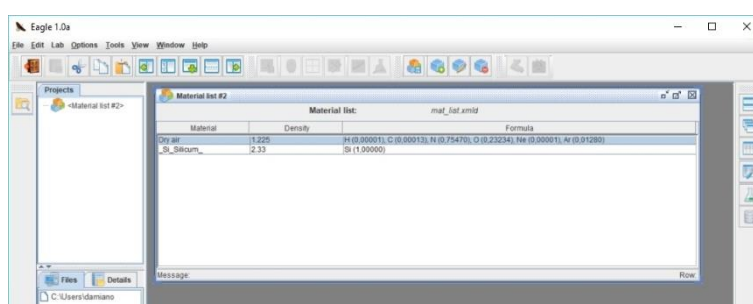


Figure 5.27 Main form of the material list manager

The lists of materials are useful because for every project of analysis, they allow to get all together the materials defined for analysis, for documentation purpose and for future reuse in case of more analysis.

The idea of a visual material manager is born with GimPy and GimPyGUI [17,122], where materials are needed to simulate a layered sample; but it has been fully implemented in first stage on Java language as part of the fbk-lib library and, consequently, as Eagle-X plug-in application.

The developed XML-data format of saving data of the single material and of the list of materials has been subsequently ported also back on Python for GimPy users, developing a specific `gimpy.fbk.xrf.*` Python library for data import, which will not be described here.

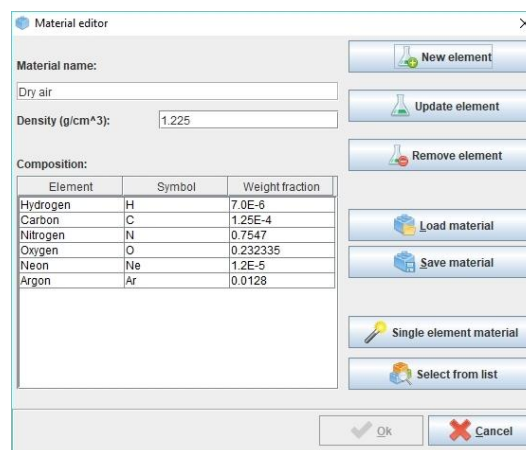


Figure 5.28 Material editor wizard.

From the File menu of Eagle-X, it is possible to generate a new list, or opening an existing one: in both cases, a new form is created where there is the list of current materials in the list. For a new list, no material is default. At the same time, a new dedicated toolbar is enabled in Eagle-X, which allows to insert, update or remove a material from the list, or saving the list itself.

For an existing list, clicking in the form on the row which contains the definition of material, a wizard appears (Figure 5.28) which allows the managing of all the information need for defining a material:

- Name
- Density (in g/cm^3)
- Chemical composition (atomic element and its weight fraction)

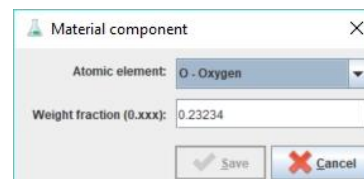


Figure 5.29 Material component editor.

It is then possible to add, update or remove an element from the chemical composition, using the buttons on the right (for updating and removing, the desired element must be selected), which enable the dialog form of Figure 5.29. A popup menu allows also to resync the weight fractions if for some reason they exceed the total sum of 1.

With the button “Save”, it is possible to save the current formulation of the material in a specific file format, *.xmd (**X**ML **M**aterial **D**ata), created specifically and ported also on Python

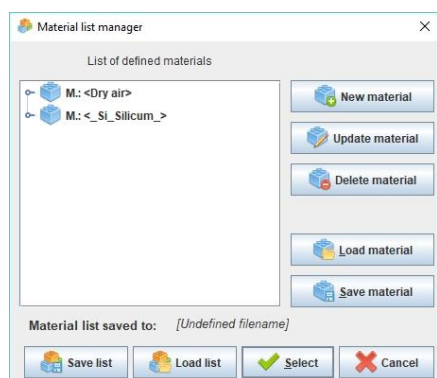


Figure 5.30 Material list wizard.

with the same libraries already cited. With the button “Load” it is possible to load an existing material for adding it to the current list or adding a modified version.

The “Single element material” allows to create a material given by a single atomic element (bulk material), by activating the periodic table wizard already seen in Figure 5.6, for selecting the desired atomic element.

The “Select from list” button allows to select a material from another existing list, through the interface wizard of

Figure 5.30.

In this way, it is possible to replicate in the current list an existing material without entering directly the data or saving it in advance as a single material to load after with the already seen “Load” button.

5.7 ED Detector manager

This application is defined as a plugin of Eagle-X, which through a dialog form (Figure 5.31) manages every aspect of the definition of ED-Xrf detectors, allowing the save and reload of them with a specific XML file format, *.xedd (**X**ML **E**D **D**etector **D**ata), created specifically .

The idea of a visual detector manager is born with GimPy and GimPyGUI [17,122], where detector data are needed to simulate a spectrum and for fitting an existing one; it has afterwards

been fully implemented also on Java language as part of the fbk-lib library and, consequently, as Eagle-X plug-in application.

The developed XML-data format has been ported “*as is*” from Python, where for GimPy users exists a specific `gimpy.fbk.xrf.*` Python library, which will not be described here.

From the File menu of Eagle-X, it is possible to generate a new detector configuration, or opening an existing one: in both cases, a dialog form is opened (Figure 5.31) where the user can insert all the data needed for defining a detector.

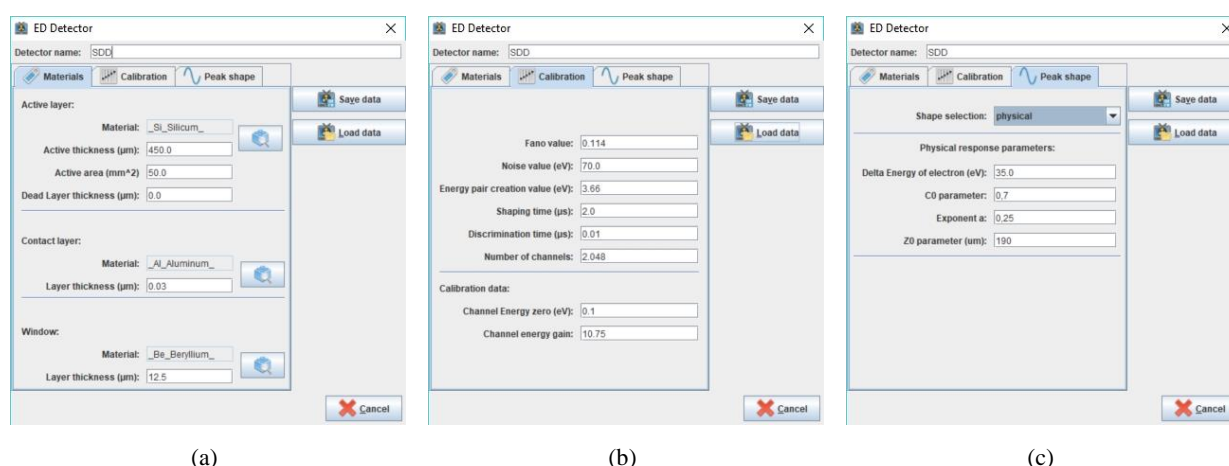


Figure 5.31 ED Detector dialog form for managing detector configuration: a) materials; b) calibration; c) peak shape.

The data can be then saved to a new file, through the “Save data” button, or it is possible to reload an existing one, through the “Load data” button, and saving a modified version in a new file.

5.8 X-Ray Beam manager

This application is defined as a plugin of Eagle-X, which through a dialog form (Figure 5.32) manages every aspect of the definition of X-Ray beam originated by a X-Ray tube, allowing the save and reload of them with a specific XML file format, *.xbd (**X**ML **B**eam **D**ata), created specifically .

The idea of a visual X-Ray beam manager is born with GimPy and GimPyGUI [17,122], where the data are needed to simulate a spectrum and for fitting an existing one; it has afterwards been fully implemented also on Java language as part of the fbk-lib library and, consequently, as Eagle-X plug-in application.

The developed XML-data format has been ported “*as is*” from Python, where for GimPy users exists a specific `gimpy.fbk.xrf.*` Python library, which will not be described here.

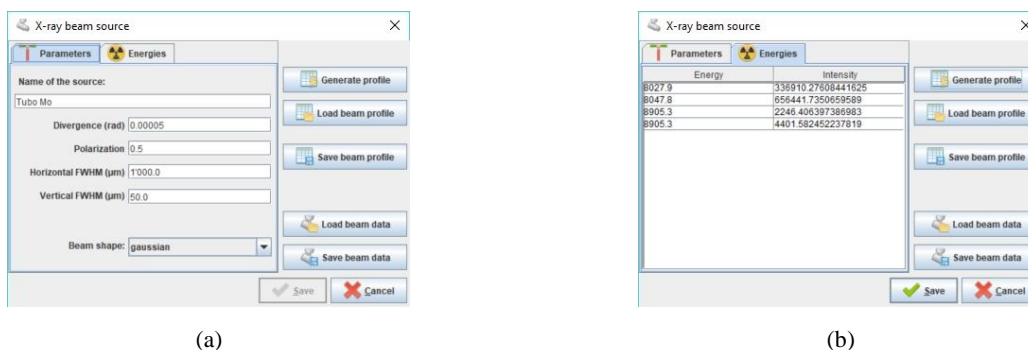


Figure 5.32 X-Ray beam source dialog form for managing beam configuration: a) parameters; b) energy profile.

From the File menu of Eagle-X, it is possible to generate a new X-Ray beam source configuration, or opening an existing one: in both cases, a dialog form is opened (Figure 5.32) where the user can insert all the data needed for defining a beam.

The data can be then saved to a new file, through the “Save beam data” button, or it is possible to reload an existing one, through the “Load beam data” button, and saving a modified version in a new file.

5.9 Layered sample manager

This application is defined as a plugin of Eagle-X, which through a dialog form (Figure 5.33a) manages every aspect of the definition of a layered sample, allowing the save and reload of them with a specific XML file format, *.xsls (**XML Layered Sample Data**), created specifically .

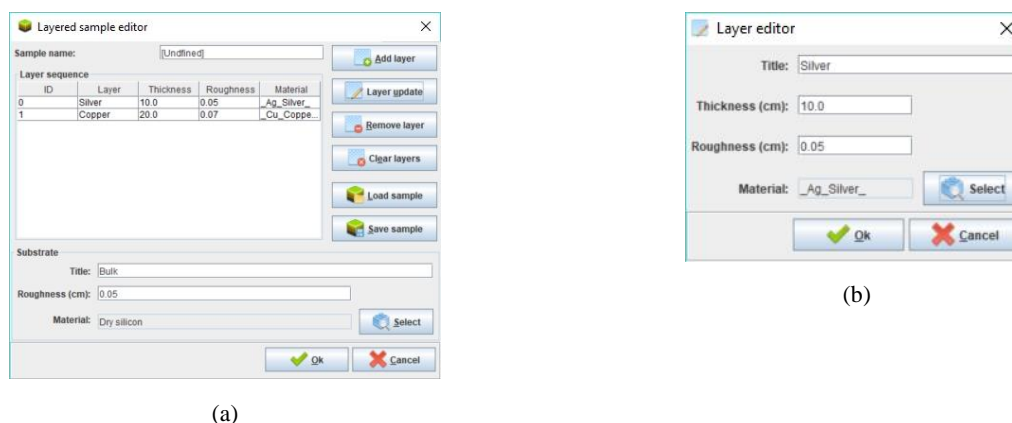


Figure 5.33 X-Ray beam source dialog form for managing beam configuration: a) parameters; b) energy profile.

The idea of a visual layered sample manager is born with GimPy and GimPyGUI [17,122], where the data are needed to simulate a spectrum and for fitting an existing one; it has afterwards been fully implemented also on Java language as part of the fbk-lib library and, consequently, as Eagle-X plug-in application. The developed XML-data format has been ported “as is” form Python, where for GimPy users exists a specific gimpy.fbk.xrf.* Python library, which will not be described here.

From the File menu of Eagle-X, it is possible to generate a new layered sample, or opening an existing one: in both cases, a dialog form is opened (Figure 5.33a) where the user can insert all the data needed for defining a sample. Every layer is managed through a specific dialog wizard (Figure 5.33b), where title of layer, thickness, roughness and material are required. For the selection of the layer material, is recalled the *Material editor wizard* of Figure 5.28.

The data can be then saved to a new file, through the “Save sample” button, or it is possible to reload an existing one, through the “Load sample” button, and saving a modified version in a new file.

5.10 Experimental set-up manager

This application is defined as a plugin of Eagle-X, which through a dialog form manages every aspect of the definition of the experimental condition of a probe (see Figure 5.34), allowing the save and reload of them with a specific XML file format, *.xecd (**XML Experimental Condition Data**), created specifically .

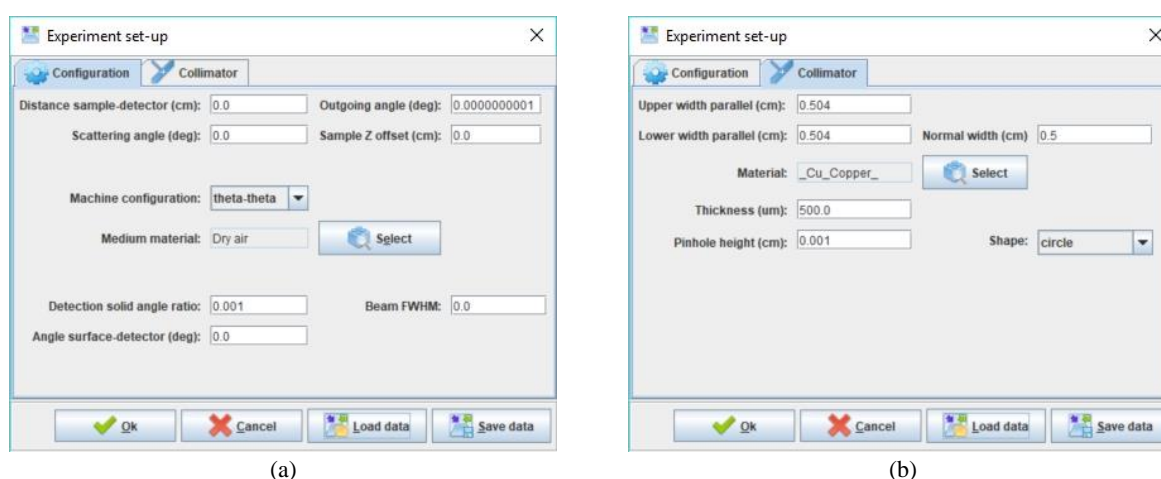


Figure 5.34 E.10 Experimental set-up manager with (a) general parameters, (b) collimator parameters

From the File menu of Eagle-X, it is possible to generate a new set-up, or opening an existing one: in both cases, a dialog form is open where the user can insert all the data needed for defining a set-up. For the selection of the medium material (see Figure 5.34a), is recalled the *Material editor wizard* of Figure 5.28.

The data can be then saved to a new file, through the “Save data” button, or it is possible to reload an existing one, through the “Load data” button, and saving a modified version in a new file.

5.11 LaSaX simulator

This application gets its name as an acronym of “**L**ayered **S**ample **X** simulator” and is defined as a plugin of Eagle-X, which manages the simulation of the ED-XRF spectrum for a defined layered sample. This is the complement of the ED-Xrf Spectrum viewer previously seen (see Paragraph 5.5): with that plugin it is possible to calibrate a real spectrum and, through the peak picking, collect the possible atomic elements inside a sample. As soon as the elements are known, it is possible to start with qualitative hypothesis about the layered structure of the sample and starting a simulation with LaSaX plugin.

The launch menu is under the File menu, on the path File->New->New LaSaX simulation. The application instantiates a project container, with a desired project name and a proper directory where all the file can be saved (Figure 5.35).

As soon as the user confirms the required data of the project, a new folder icon appears on the Eagle-X projects navigator (see Figure 5.36, red arrow). At the same time, the dedicated toolbar is activated on the top of the application (see Figure 5.36, blue arrow).

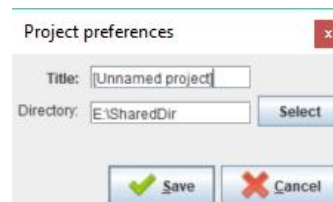


Figure 5.35 Defining the project folder and name.

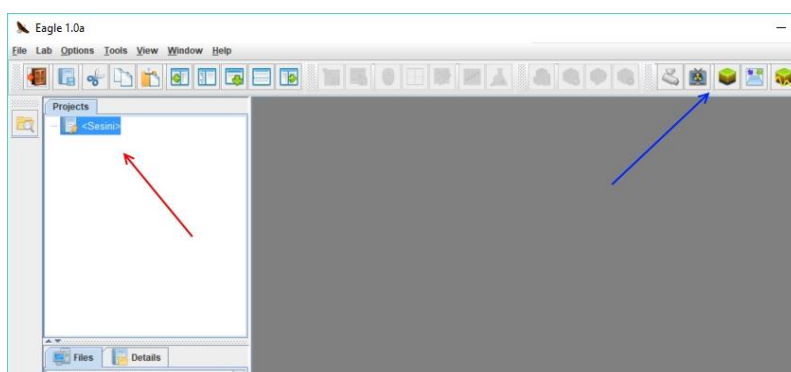


Figure 5.36 The Eagle-X aspect after creation of a new LaSaX simulation project: the project folder in the project navigation panel of Eagle-X (red arrow) and the new toolbar for managing simulation (blue arrow).

The icons of the toolbar allow to control the data needed for the simulation. The first four from the left control the simulation parameters through the interfaces above already seen, respectively:

- Beam source parameters (see Paragraph 5.8);
- ED detector parameters (see Paragraph 5.7);
- Layered sample definition (see Paragraph 5.9);
- Experimental set-up (see Paragraph 5.10).

For the beam source and detector, the default specifications as

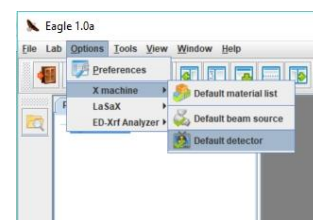
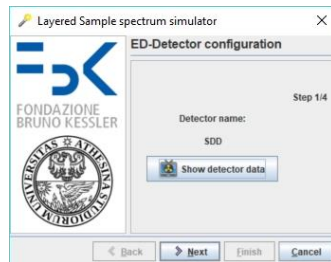


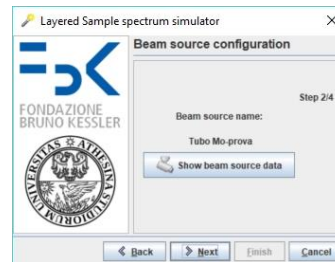
Figure 5.37 Menu for default X machine specifications.

defined in Eagle-X are proposed. This allows to avoid to re-insert data if the same machine is used for simulation.

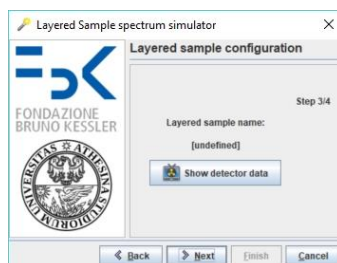
The default specifications can be in any case consulted or modified at the menu path Options menu->X machine, where the user can define and consult the default material list, the default beam source and the default ED detector (Figure 5.37).



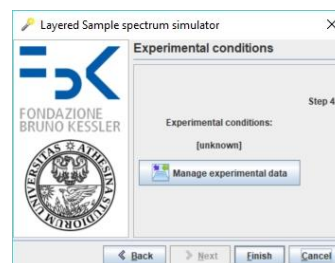
(a)



(b)



(c)



(d)

Figure 5.38 Wizard panels according to sequence: a) detector data; b) beam data; c) layered sample data; d) experimental set-up.

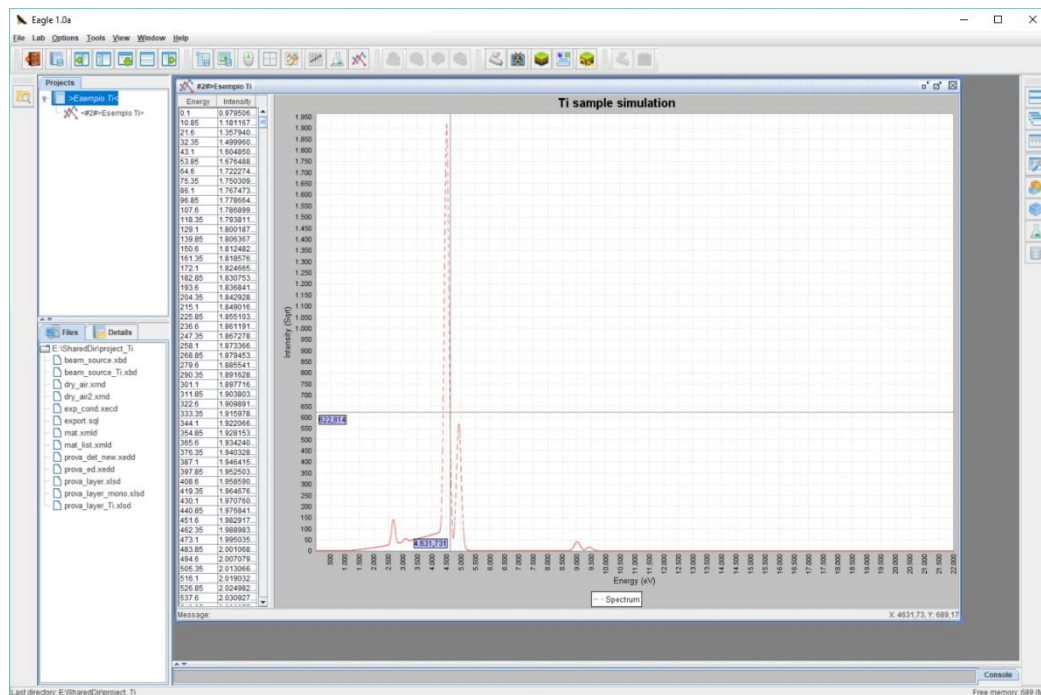


Figure 5.39 The window with the data and the chart of the LaSaX simulation result.

The fifth button launch the wizard (see Figure 5.38) for the complete simulation of theoretical spectrum according to fundamental parameters: if data has been already entered, then the wizard

Through the ED-Xrf common toolbar already described (see Figure 5.10 and Paragraph 5.5) it is possible to personalize the chart and saving data and image itself to a file.



The user interface on the left is dockable, so user with small monitor or complicated spectra can move the control panel on the screen for easier readability (Figure 5.41).

Figure 5.41 Confrontation between spectra with dockable interface.

6 CASE STUDY: VENETIAN *SESINI*

Ancient coins are widely studied in archaeology because they may provide interesting information not only on the material culture, but also on economic and social history of the territories in which they are used [12,114,132,139].

Depending on the Ages and historical contexts, specific coins are made of a somehow certified alloy by a known mint [7,53]. They feature impressed images on both sides, allowing for a complete identification of the emission period, especially when they feature the indication of the year of issue [174]. Alternatively, this information can be obtained from documents. In this regard, coins become very valuable; associated to archaeological sites, they help identifying a *terminus post quem* for relevant dating of buildings, graves, etc. belonging to the relevant context.

Many studies have been devoted to ancient coins [3,75,128,143], although the presence of surface alteration layers has often required many efforts for evaluating their internal composition and structure. An important set of information can be obtained from the results of materials analysis, and the composition of the base alloy, including the concentrations of specific isotopes, and it may provide information on the raw material provenance and extraction methodologies [11,99]. This of course has unavoidable limitations due to the possibility that the examined alloys are obtained not from primary metals, but from recycling-reuse procedures of existing old coins, a practice well documented over the centuries [9,52,85].

In the early times of the modern archaeological research (beginning of the XVIII century), a destructive approach had often to be used [91]. Nowadays, non-destructive methods are definitely preferred [8,143], considering the rarity of samples, their value and, most importantly, the availability of more powerful experimental tools and methodologies.

The present case study investigates for the first time, the characteristics of the so-called *mistura* (mixture) alloy, used for the coinage of the Venetian coin called *sesino*. This coin was minted starting from the second half of XVI century and was withdrawn at the beginning of the XVII century.

The *sesino* was a remarkably successful coin in commercial transactions of XVI century and was widely used and accepted also outside the territories of the Venetian Republic. Indeed, the set of investigated coins is part of a larger collection owned by the public library museum of Ala (Trentino- North Eastern Italy).

Notwithstanding the widespread diffusion of the *sesino* coin, however, only the Venetian coins of greater value, made of gold and silver alloys, have been investigated to date [79,127]. For this

reason, as anticipated no materials investigations had been conducted so far on the actual composition of the *mistura* alloy, used for the *sesino* coinage, and its possible evolution over the years.

A combined approach, based on XRF and XRD analyses was used [16,107]. In this way, a fully non-destructive characterization of the samples was possible. XRF was selected since it is extremely effective for quantitative elemental analysis of archaeological [27,107,116,125] and also numismatics relevant [22,98,99,141,147,190] artefacts.

In the present study, XRD provided complementary information on the phases present in the complex surface alteration layers that formed on the coins as the results of their interaction with the outer environment. The structural and crystallographic characterization of these phases, that, as expected [10,107,190], could be effectively achieved with the XRD methodology, provided an important insight on the surface layer and its contribution to the XRF results.

6.1 Historical context

At the beginning of the XVI century, the political landscape of Italy was dominated by wealthy, powerful, and largely independent city-states, the most important of them being the Republic of Venice, whose power was however threatened by continuous military engagements with the increasing Turkish power in the Eastern Mediterranean possessions, and the relevant political and economical evolution in the European scenery [5,21,114,156].

Over the period interesting for the investigated *sesino* coins, Habsburg Charles V of Spain widened the Spanish territories in Italy, as Holy Roman Emperor starting from 1530 until 1558. In this time, Venice and the Papal State only were outside of Habsburg control.

In this complex political context, under the pressure of the Habsburg dynasty [90,189], the Republic of Venice aimed at consolidating its presence in the strategic territories in Northern Italy, under its possession, like the city of Brescia and the whole area corresponding nowadays to Eastern Lombardy region, including Bergamo [34,130].

During this time of important political changes, with consequences on commerce and trading too, under the ruling of Doge Francesco Donato (1545-1553), it was decided to mint a new type of currency, called "*sesino*" [5]. The Council of the Tens (Consiglio dei Dieci) ordered its first coinage by an official bill dated October 19, 1547. Since then, the *sesino* became a divisional coin of small value, as compared to silver and gold coins [117,177], like the *ducato* and the *zecchino*, outside the city of Venice. This coin, according to documents, consisted in a mixture of silver and copper, in which the amount of precious metal is less than half of the coin weight [53].



Figure 6.1 Europe in 1556, with the Habsburg dominions in evidence [source: Wikipedia].

A consequence of the use of the *sesino* not only over a wide geographical area of the Venetian territories, but also outside them, resulted in forgeries, particularly in the Northern Italy mints, most likely featuring higher copper alloys.

Actually, the clandestine production not only of *sesini* but also of coins of higher value was a serious problem, well known since XIII century [5,130,163], and that caused remarkable damages to the economy and financial stability of the Venetian Republic. In the long run this led to the decision by the Senate of Venice to periodically withdraw of coins minted outside Venice, with a subsequent merger of them at the mint of Venice [162,163] for creating new official coins with controlled weight and content.

The Venetian *sesino* coins were abolished by the decree of December 15, 1600 [5], and emissions were suspended permanently in 1603, and were never resumed.

6.2 Research samples

The analysis was performed on a set of 20 *sesino* coins stored at the Public Library of Ala, a village in the Trentino Province, North-Eastern Italy. They are part of a larger set of 60 *sesino* coins of different emissions from the collection of coins called “Della Laita’s” after the name of the original owner who donated it to the Municipality of Ala.

The coins were codenamed and sorted according to the emission date and Doge's sequence. The 20 *sesino* coins selected for this research (see Table 6.1), have been chosen to have at least one coin for each Doge period identified in the whole collection.

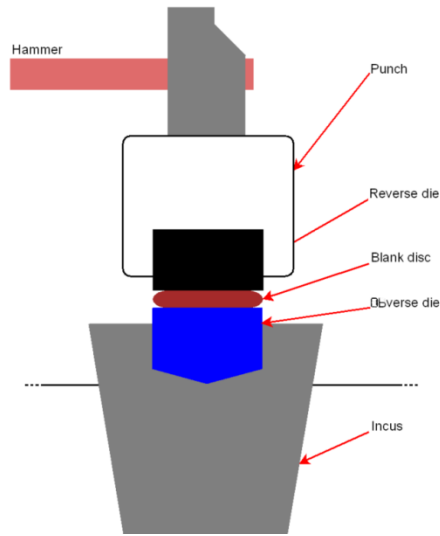


Figure 6.2 Representation of the coinage procedure with hammer and incus [176]

The *sesino* was produced cutting a virgin alloy disc (called “*tondello*”) from plates or bars, with a fixed number of discs for every plate or bar, having a fixed weight so that also the *tondello*'s weight was reasonably fixed [175]. Each *tondello* was then minted with an hammer and two dies (Figure 6.2), with the hammer beating onto the reverse die which impressed the alloy disc sitting on the obverse die [174,176].

The greater or lesser accuracy of the quality of the coins and their impression can be taken as an indication of the socio-economic conditions of the period in which they were minted: a great demand for the circulating coins produces an acceleration of the working times that affect the quality of the coins [53].

For the coins of this study, the obverse is the side with the "cross" and in the label impressed over the turn is the name of the Doge ruling at the minting time of that very coin (see Figure 6.3a). The reverse side exhibits the Venetian lion inside a circle (defined “*leone in soldo*”), an iconography borrowed from the coin called *soldino* of the doge Andrea Contarini (1368-1382) (see Figure 6.3b).

Samples were preliminarily observed for their surface condition using optical microscopy and weighted using a precision balance (see Table 6.1). In the table, the identification sample codes and additional information on the sample coins are also listed.

Each sample has been analysed in its delivery condition, without any preliminary polishing treatment, not to introduce any modification or residuals that might influence the pristine chemical composition [45].

Table 6.1 Classification of analysed samples (according to Montenegro catalogue [127]), ordered by Doge's sequence. The numbers in brackets indicate a variant of the corresponding model in the catalogue.

ID	Weight (g)	Ø (mm)	Doge	Ref. type	Catalogue data
S15	1.28	18.0	Venier Francesco (1554-1556)	516	Ø (mm) 18-19
S25	1.28	17.5	Priuli Gerolamo (1559-1567)	583	Ø (mm) 17-18
S45	1.17	18.0	Priuli Gerolamo (1559-1567)	581	Ø (mm) 17-18
S10	1.58	18.2	Loredan Pietro (1567-1570)	632	Ø (mm) 19
S14	1.33	18.2	Loredan Pietro (1567-1570)	632	Ø (mm) 19
S01	1.31	18.6	Mocenigo Alvise I (1570-1577)	682	Ø (mm) 18-20
S03	0.75	17.7	Mocenigo Alvise I (1570-1577)	677	Ø (mm) 18-20
S09	1.05	18.1	Mocenigo Alvise I (1570-1577)	677	Ø (mm) 18-20
S20	1.21	17.9	Mocenigo Alvise I (1570-1577)	680	Ø (mm) 18-20
S21	0.99	18.5	Mocenigo Alvise I (1570-1577)	677	Ø (mm) 18-20
S29	1.29	17.9	Mocenigo Alvise I (1570-1577)	676	Ø (mm) 18-20
S43	0.79	17.5	Mocenigo Alvise I (1570-1577)	(679)	Ø (mm) 18-20
S44	0.86	17.5	Mocenigo Alvise I (1570-1577)	(679)	Ø (mm) 18-20
S59	1.00	18.1	Mocenigo Alvise I (1570-1577)	678	Ø (mm) 18-20
S54	1.24	18.7	Da Ponte Nicolò (1578-1585)	776	Ø (mm) 17-19
S07	0.84	18.0	Cicogna Pasquale (1585-1595)	877	Ø (mm) 18-19
S28	0.95	18.0	Cicogna Pasquale (1585-1595)	885	Ø (mm) 18-19
S38	0.83	16.5	Cicogna Pasquale (1585-1595)	(875)	Ø (mm) 18-19
S35	1.37	17.8	Grimani Marino (1595-1605)	989	Ø (mm) 17-19
S42	0.73	17.9	Grimani Marino (1595-1605)	(989)	Ø (mm) 17-19
Legenda: ID: sample code; Weight: measured weight; Ø (mm): diameter of each sample; Doge: the Name of the Venetian Doge and his ruling period; Ref. Type: Montenegro reference code; Catalogue data: literature diameter					

6.2.1 First inspection

On eye inspection, the selected coins display quite a wide range of surface appearance conditions, depending on the degree of alteration introduced by wear during the usage time, and corrosion which occurred also during the burial period. Figure 6.3, referring to sample S15 of Doge Venier, shows an example of a very well-preserved coin.

The same is true for the sample S10 of Doge Loredan (Figure 6.4). Figure 6.5, for sample S21 of Doge Mocenigo, shows a situation of a bit more evident wear and patinas and irregular edge, where the legend is partially lacunose. Other coins have a very high degree of consumption, with

irregular edges and a legend not easily readable (see Figure 6.6). This is also reflected in the dimensions and weight of the coins (see Table 6.1).



A)



B)

Figure 6.3 The *sesino* of Doge Francesco Venier (S15), obverse (left) and reverse (right).



A)



B)

Figure 6.4 The *sesino* of Doge Pietro Loredan (S10), obverse (left) and reverse (right).

Moreover, the patinas visible on the coins are not homogeneous, but depending on sample there are areas with different colours, ranging from dark brown (common to all the samples) to yellow or green areas randomly distributed; the green or yellow areas have an extension which covers either localized areas (see again Figure 6.3 and Figure 6.4) or extended portions of the coin

(as in Figure 6.4); the patinas are never present on the areas in relief of the coins, which on the contrary are generally brown.



Figure 6.5 The *sesino* of Doge Alvise Mocenigo (S21), obverse (left) and reverse (right).



Figure 6.6 The *sesino* of Doge Nicolò Da Ponte (S54), obverse (left) and reverse (right).

In sample S35 of Doge Grimani (Figure 6.7), white-green powdery reaction products have been observed (see between the letter M and A in the first quadrant of obverse side), which seem to be due to an aggressive corrosion reaction sadly known as “bronze cancer” for its deleterious and fast kinetics [23,50,51,76,143].



Figure 6.7 The *sesino* of Doge Mariano Grimani (S35), obverse (left) and reverse (right).

6.3 Experimental setup

The weight measurement of every coin (see Table 6.1) has been executed on a Radwag AS 220 analytical balance, maximum weight of 220 g, sensitivity 0.1 mg.

The observation with the optical microscope has been performed on a Zoon Trinoc Stereo Microscope, STMPRO 0.7X - 4.5X with two halogen light sources to enhance the details of the surface topography. Other observations were carried out with a Nikon SMZ25 Stereomicroscope equipped with two interchangeable lenses and a coaxial fiber optic illumination.

The morphology of the surface layers of the coins, including patinas and incrustations, have been investigated with scanning electron microscopy (SEM) observations and energy dispersive X-Ray spectroscopy (EDXS) analyses: it has been used a JEOL IT300 microscope and the microanalysis of QUANTAX Bruker with XFlash 630M detector (Figure 6.8). Moreover, it has been used backscattered electron-imaging mode (BSE) to highlight better the regions of the observed samples, featuring different compositions.

X-Ray investigations of all Venetian coins have been performed on two different instrumental setups.

XRF data were collected on a TNX Phoenix combined spectrometer (Figure 6.9): the machine is equipped with a Mo anode X-Ray source operating at 40 kV, 30 mA, coupled to a parabolic multilayer monochromator (Axo Dresden), and a Silicon Drift XRF Detector produced by Ketek (model Axas-D with Peltier cooling, 50 mm² active area: see Appendix A for details). The XRF detector has been maintained normally to the sample surface, with different incidence angle of the X-Ray beam ranging from 5° to 30°, to analyse the enhance of the penetration depth of the

incoming beam. Every acquisition for measurement has been set to 10 minutes, with an estimated attenuation length equal to 20 μm , assuming a pure copper matrix.

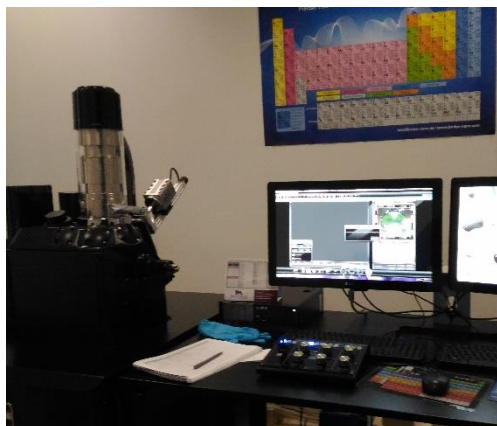


Figure 6.8 SEM/EDXS appliance by Bruker at University of Trento, Dep. of Industrial Engineering.

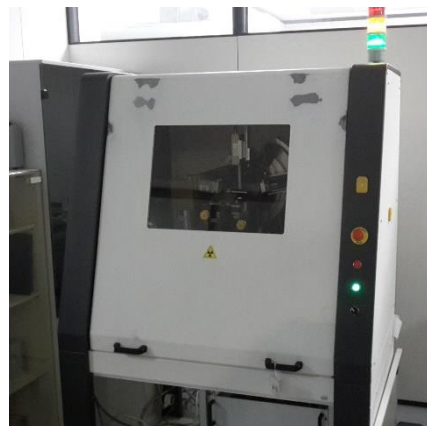


Figure 6.9 TNX Phoenix combined spectrometer at FBK, CMM Laboratories.

Diffraction data have been collected with an Italstructures IPD3000 diffractometer, equipped with a Co anode X-Ray source operating at 40 kV, 30 mA, a flat multilayer monochromator on the incident beam, and an Inel CPS120 curved position sensitive detector on the diffracted beam. The 2θ angular range was from 5° to 100° ; the acquisition time for each XRD pattern was set to 30 minutes. X-Ray beam incidence angle for the XRD set up was set to 5° with respect to the sample surface.

The XRD and XRF tests were conducted pin pointing the incident beam, with a spot size on the samples of $6.0 \times 3.0 \text{ mm}^2$ and $6.0 \times 0.6 \text{ mm}^2$ at 5° (XRD) and 30° (XRF) incidence angle respectively, in both cases, at the centre of the “cross” on the obverse side of the coin.

6.4 First experimental results

The observations with optical microscopy have revealed the microstructure of the layers of impurities and concretions, which in some cases did not facilitate the iconographic interpretation of the surface.

The impurities, especially due to soil and sediment incrustations, tend to pile up in the lower parts of the coin surface delimited by the protruding features of the impressed coin surfaces (see Figure 6.4 and Figure 6.5).

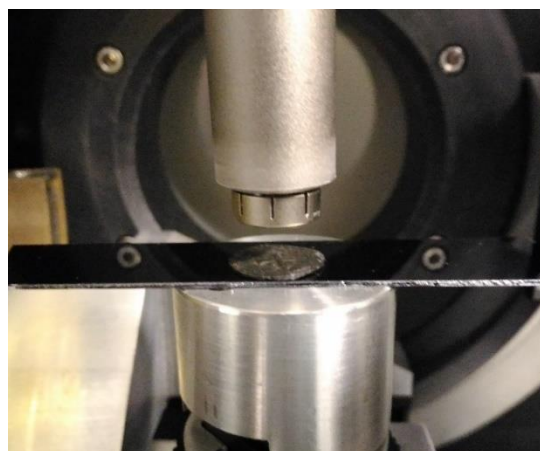


Figure 6.10 Example of XRF set-up for sesino of Doge Priuli

As acquisition spot the intersection of the arms of the cross (see Figure 6.10), on the obverse side of each coin, has been selected for both the XRF and XRD tests in order to minimize the effect of the incrustations [45,141].

To complete the picture provided by the XRF and XRD tests, it has been performed some pin-pointed SEM-EDXS analysis of the coin surface to better characterize minor phases present on outer altered layer. This has been done also in the spots not sampled with the XRF-XRD tools, to gain a better insight into the complex reactions which occurred between the *mistura* alloy and the surrounding environment (Figure 6.5).

6.4.1 First contact with XRF and XRD

A qualitative estimation of the elemental composition of the bulk alloy for each sample has been obtained by means of XRF data analysed at first stage with Eagle-X (see Paragraph 5) and GimPy software [17,122]; at second stage, the results obtained have been introduced into the MAUD software [16,107] with XRD data, by using at the beginning a simplified single-phase bulk model.

This approach showed for all the samples the presence of three main elements, namely Cu, Ag, and Pb.

Moreover, other minor elements (Fe, Hg, V, Mn) have been detected with concentrations below 0.1 % in weight (see for instance the XRF spectrum in Figure 6.10).

Based on the technologies of that time and of the known history of this coins, two main origins can be supposed for these elements:

- they get into the alloy from the production process of alloy from ores [4,15,39,159];
- incrustations may form for the adhesion on the coin surface, possibly already corroded, of elements and components from the outer environment to the coin [19,99,143].

The second source of minor elements as Al, Si, Ca, P, S, K, Cl, is the outer environment providing both agents to form new phases by reacting with alloy components.

Three elements, Cu, Ag and Pb, are fundamental to characterize the evolution in the composition of the *mistura* alloy, over the years.

This information obtained from XRF has been then used in combination with XRD spectra to perform a first phase identification (*search-match*) by means of the FPSM software [111]. The chemical information, i.e. the list of the XRF detected elements and relevant concentrations, was used to short-list candidate phases possibly present in the XRD patterns.

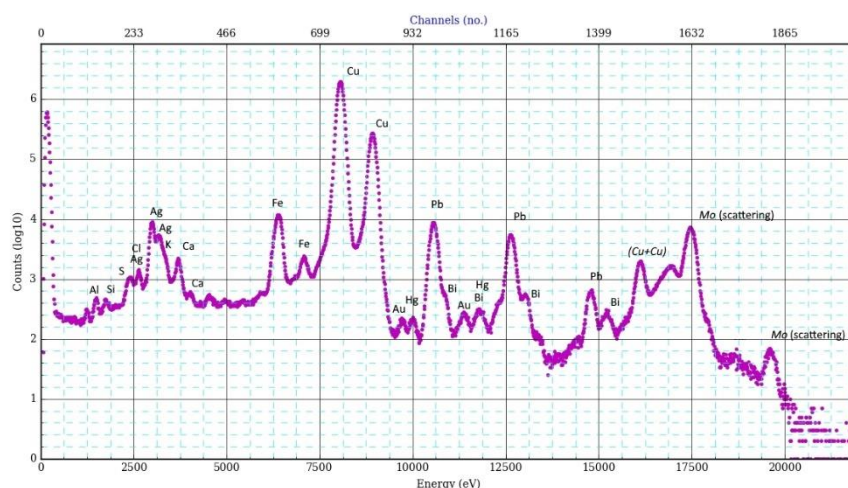


Figure 6.11 XRF spectrum of *sesino* S15 of Doge Venier analysed with the element picker in the ED-Xrf spectrum viewer plugin of Eagle-X (see Paragraph 5.5).

In this process, literature data on similar alloys were also used [3,19,75,99], including the phase composition provided by the equilibrium phase diagrams of the Cu-Ag (Figure 6.12a) and Cu-Pb (Figure 6.12b) systems [28] and that the Ag-Cu alloys, when cooling, undergo phase separation [2,13,28] (the miscibility of the Cu in Ag at room temperature is lower than 1%, and vice versa: see Figure 6.12a).

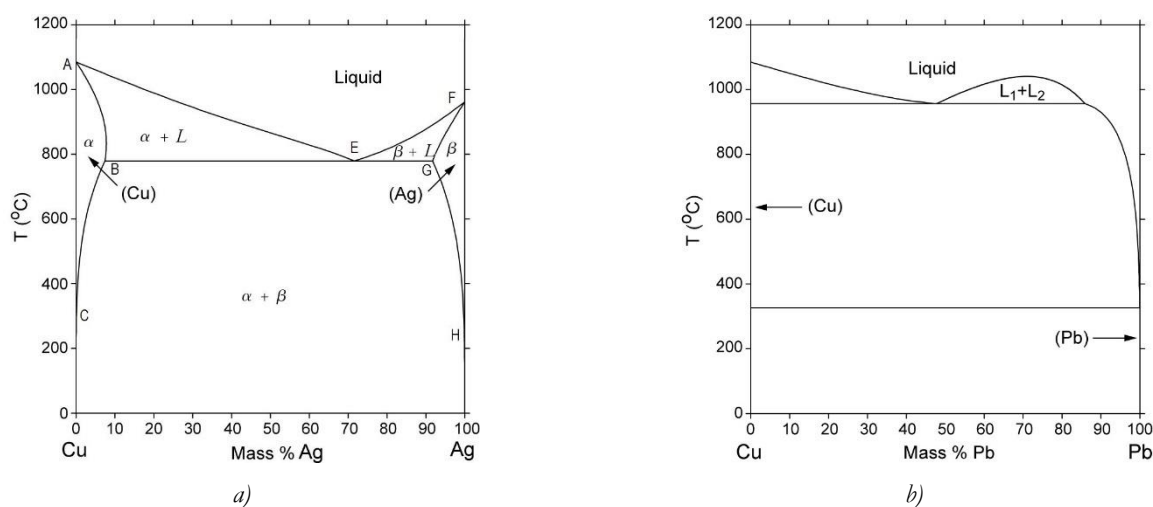


Figure 6.12 Phase diagrams of Cu-Ag (left) and Cu-Pb (right) systems.

The XRD analysis of all the *sesino* coins has evidenced the presence of four main crystallographic phases in all the samples:

- *metallic copper*, which is the main component of the coin;
- *copper oxide* Cu_2O (cuprite) [54,76,119,160], likely located in the surface corrosion patina which appears in his brown colour (the so called “noble patina” [143], see Figure 6.3 for example);
- *metallic silver* which, in a first approximation, could also be considered a solid solution of all other minor contaminants found by the XRF analysis;

- *chlorargyrite* (AgCl), a corrosion product of silver associated to the presence of Cl and induced by oxygen and humidity [91,97,119,146].

The presence of cuprite is associated to a reducing environment typical of a burial [62,119], while the source for Cl are mainly marine atmosphere or coal burning [153].

XRD qualitative results were then used to describe the crystallographic model to analyse through Rietveld quantitative analysis [144] as implemented in MAUD.

This first-approach analysis was performed by considering the four-phase mixture, with all the volume fractions considered as refinable parameters, as well as cell parameters and atomic occupancy factors for the Ag/Pb solid solution. Significant microstructural features, like volume weighted average crystallite size and mean microstrain, were also considered for the majority phases, namely Cu and Cu₂O. An example Rietveld fit for *sesino* sample n. 25 is reported in Figure 6.13 while in Figure 6.14 is reported the corresponding fitted XRF plot.

To simplify the initial analysis, in first approximation a bulk sample has hypothesized, with element and phase compositions constant along the sample volume.

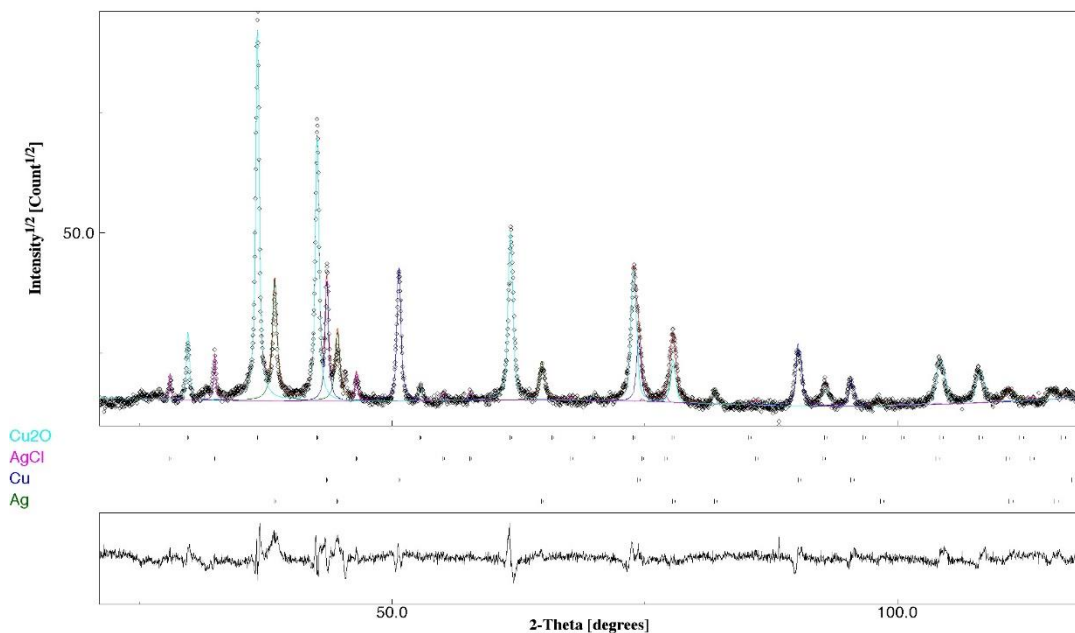


Figure 6.13 Rietveld fit relative to XRD data for sample S15 Venier.

From an analytical point of view, this avoids the complication of considering the absorption paths of different X-Ray radiations in an inhomogeneous medium; this is clearly an oversimplification, because we have the presence of corrosion and oxidation layers several microns thick on the samples surface, considering the low penetration depth of the radiation used in the XRD setups (about 1 micron attenuation length for Co-K α , 5 degrees incidence angle and assuming a pure Cu matrix) in comparison to estimated XRF attenuation length.

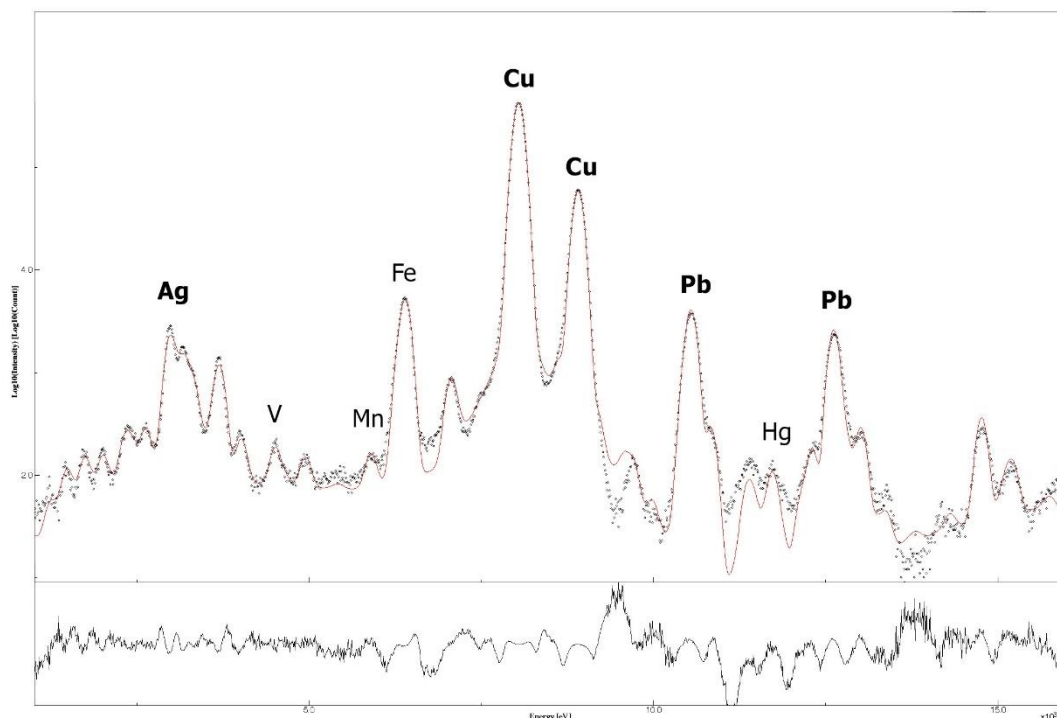


Figure 6.14 Fundamental parameters fit relative to XRF data for sample S15 Venier.

The aim of this simplification was however to collect and fit as many parameters as possible, not influenced by the layer model, like cell parameters of phases, microstrain and phases present on the coins.

Since already at first inspection there are differences among the coins on surface, not only for the different degree of corrosion or wear, it was impellent to identify the phases not common among samples, through this first simplified approach.

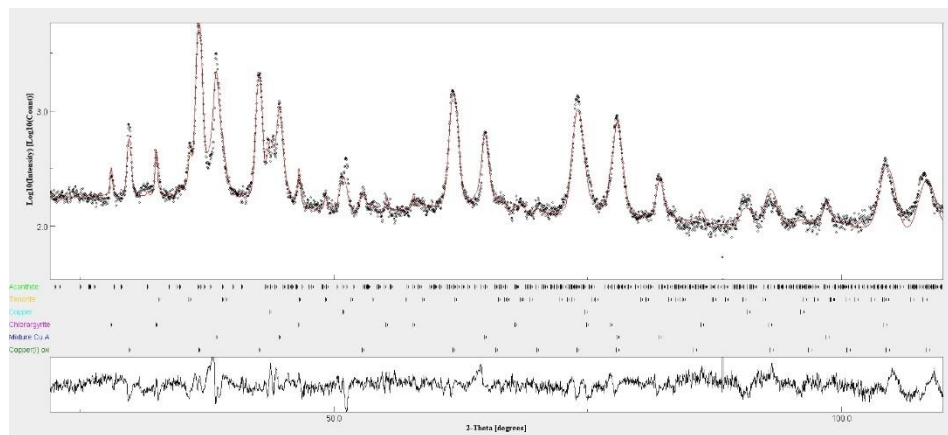
Therefore, the results about the found uncommon phases from this Rietveld first semi-quantitative analysis are shortly resumed in Table 6.2: seven new phases has been identified through this simplified analysis over all the 20 coins; this phases are all corrosion products:

- *copper peroxide*, CuO_2 : it is an oxide of copper, and appears as a dark olive green solid which in wet environment will decompose to oxygen and other copper oxides;
- *tenorite*, CuO : it is a monoclinic copper oxide, appears steel-gray, iron-gray or black and usually occurs in hydrothermal environments with copper sulfide and copper carbonates;
- *villamaninite*, CuS_2 : it is a cubic copper sulphide with small amounts of other elements (usually Ni and Fe);
- *acanthite*, Ag_2S : it is the only stable form of silver sulfide below 173 °C. It crystallizes in the monoclinic system and appears iron-black;

- *oldhamite*, (Ca,Mg,Fe)S: is a calcium magnesium iron sulphide and it has a pale to dark brown colour;
- *copper(I) sulfide* (Cu₂S): at low temperature it has a monoclinic form (called "low-chalcocite") which has a complex structure with 96 copper atoms in the unit cell;
- *spertinite*, Cu(OH)₂: it is a blue to blue green tabular orthorhombic crystal, which usually appears as aggregates in a secondary alkaline environment altering chalcocite copper(I) sulfide (Cu₂S).

Table 6.2 Uncommon phases identified through first simplified analysis

	Doge Priuli		Doge Loredan		Doge Mocenigo							Da Ponte	Doge Cicogna			Doge Grimani	
	S25	S45	S10	S14	S01	S03	S09	S20	S21	S29	S59	S54	S07	S28	S38	S35	S42
CuO ₂					☑												☑
CuO				☑					☑	☑							
CuS ₂						☑			☑				☑		☑		
Ag ₂ S	☑	☑		☑	☑	☑	☑		☑	☑	☑	☑		☑		☑	☑
(Ca, Mg, Fe)S		☑	☑	☑		☑		☑					☑			☑	
Cu ₂ S														☑			
Cu(OH) ₂														☑			

**Figure 6.15** XRD spectrum of S14 of Doge Loredan, with the four common phases plus acanthite and tenorite.

For samples S15 of Doge Venier, S43, S44 and S59 of Doge Mocenigo and S38 of Doge Cicogna, no phases different from main ones have been identified: this can be due to the background noise which hides lower peaks, or because they are under the level of detection. An example of a sample with uncommon phases, tenorite and acanthite, is reported in Figure 6.15.

6.5 Multilayer approach

The selection of the Mo wavelength and the increasing incidence angle for the XRF tests have been deliberately chosen to obtain the dominant fraction of the fluorescence signal from the bulk alloy, of which the composition had to be measured, and to limit the contribution from the alteration surface layer.

This was, on the other hand, the volume probed with the XRD measurements, thanks to the lower penetration of the Co radiation and the glancing incidence angle of 5° . X-Ray wavelength restricted the diffracting volume to the outer surface layer, so that the phases which formed from the interaction of the bulk alloy with the external environment during the burial time were the majority phases in the relevant diffraction pattern, in addition to minor contributions from the bulk alloy.

As we have stated above, the single bulk model of a sample like a mixture Cu/Ag coin allows a rapid approach with some useful consideration already visible in the data obtained, especially for phase presence and atomic element distributions.

The limit consist in the fact that it is clearly an oversimplification, because there are visible corrosion and oxidation layers, as we have seen from first optical inspection (see Paragraph 6.2.1) and confirmed by the found uncommon phases which are distributed among the coins and confirmed by the SEM-EDXS surficial analysis (see Paragraph 6.5.4). These layers may be some microns thick on the samples surface, depending on the unknown history of every single coin.

Moreover, the corrosion products like *chlorargyrite*, *copper oxide*, etc. have different behaviour respect to, for example, water; this means that over the times, the relative production of corrosion product has been differently affected by environment, with unpredictable effects on chemical composition on coin surface.

6.5.1 Three-layer model

Thus, a more consistent approach is a multilayer analysis: in this context, considering the typical corrosion evolution in a copper disk with dimension comparable to the coin ones, it is possible to conjecture a three-layer model (Figure 6.16):

- a *surface corrosion layer* on the top, where it is plausible to find as dominant one, or more, of the common and uncommon corrosion phases already seen above, e.g. *chlorargyrite*, *cuprite*, *acanthite*, etc... and eventually a small quantity of other bulk phases, i.e. copper and mixture Ag-Cu;

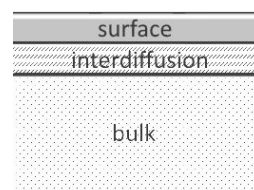


Figure 6.16 Three-layer model proposed.

- an *interdiffusion layer* under the top, where we have a gradient of the corrosion phases in the core of copper and mixture Ag-Cu, considering for example the low diffusion rate of oxygen and chlorine into the coin;
- a *bulk* with the core of copper and mixture Ag-Cu only.



Figure 6.17 The *sesino* of Doge Pietro Mocenigo (S01), obverse

The aim is to refine this model, defining on one side, the phase distribution on the two upper layers, and on the other the thicknesses of the two layers.

It must be recalled here that this assumption is valid because in the analysis the XRF and XRD data has been collected from the center point of the coin, on the obverse side, in correspondence of the intersection of the cross arms: indeed, here the coin is comparable to a disc plate, with same thickness of the coin, with parallel surfaces among layers.

Out of the coin center, because of the minting with the hammer (see Paragraph 6.2), the parallelism is no more true, due to plastic deformation of the disc and the impressing of iconography on both sides.

6.5.2 Software implementation

As a criterion, considering the approximations, also numerical, of the model, to determine the threshold thicknesses of each layer, we have imposed the following limit:

- for the surface, it is assumed as threshold thickness between surface and interdiffusion layer the thickness at which the surface layer contains at least 90% of corrosion products;
- for the bulk, a zero-presence of all corrosion phases; only for cuprite, which is the dominant oxidation product among all coins, it is imposed a quantity lower than 5%.

With these criterion limits, the combined analysis has been configured in MAUD and conducted for every coin, starting from a value of 0.01 μm for the thickness of surface, 10 μm for the thickness of the interdiffusion layer, and 1 mm for the bulk thickness.

Only the thickness and phase composition of surface and interdiffusion layers are refinable. On surficial layer, the refinable starting point for copper and mixture phases is set to zero.

For the bulk, the phases of copper and mixture are refinable, while the chlorargyrite and all other corrosion phases (common and uncommon) is set to zero; only copper oxide is allowed refinable, however starting from zero (we must find a level lower than 5%, according to above criterion).

The reason of this choice is that MAUD is computationally faster with copper oxide refinable also on the bulk, compared to a model where the oxide is blocked to zero or to 5%.

The same limitation is on the side of the surface layer, where there is no option for setting an 90% limit on the sum of corrosion product.

This obviously has the inconvenient that at the end of every cycle of iterations, the user must control the levels of content evaluated by the software, compared to our model criterion, and adapt the interdiffusion thicknesses consequently, increasing or reducing the starting thickness of new iteration, in order to approach better, in the next iteration cycle, the convergence desired.

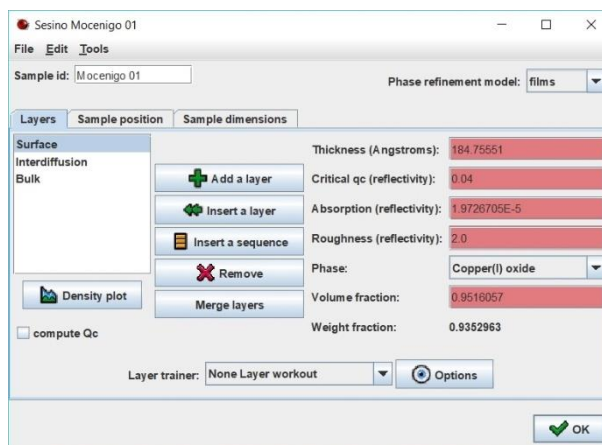


Figure 6.18 MAUD layer structure wizard

6.5.3 Layer model result

Due to the differences among the coins, and the different phases present in every coin, the computation has been very time consuming.

The main problem has been guessing the initial thicknesses of the layers, especially the surface layer, in order to get a consistent “first step” for the model computation: in some situations, an erroneous first step can compromise the analysis, with no convergence of the result.

In Table 6.3 a summary of estimations for the surface layer is reported: there are the MAUD estimation of the volume fractions of phases in surface layer and the estimated thicknesses.

In Table 6.4 are summarized the data for interdiffusion layer and the bulk according to the three-layer model proposed.

The data from Table 6.3 confirms that for every coin there is a different history from the moment of minting to nowadays: this difference is expressed not only in terms of different corrosion products on the surface layer, which depend on the various environments where the coins have been stored in the centuries, but also in terms of different thicknesses of the surface layers, which reflects also the use of the coins, considering that the data are estimated from relief parts of the coin which are mainly subject to use consumption.

Indeed, constructing the diagram of Figure 6.19 with the surface layer data, it is possible to see the dispersion of thicknesses.

Table 6.3 Volume fractions (%) of phases in surface layer, with estimated thicknesses

Sample	thickness (μm)	Surface layer										
		Cu_2O	AgCl	Mixture Ag-Cu	Cu (pure)	CuO_2	CuO	CuS_2	Ag_2S	(Ca, Mg, Fe)S	Cu_2S	$\text{Cu}(\text{OH})_2$
S15 Venier	1.4	88.3	5.8	1.6	4.3	-	-	-	-	-	-	-
S25 Priuli	8.0	88.4	3.0	6.3	1.6	-	-	-	0.7	-	-	-
S45 Priuli	24.5	85.3	3.0	3.2	1.9	-	-	-	2.2	3.6	-	-
S10 Loredan	18.5	89.2	1.2	6.0	0.7	-	-	-	-	2.9	-	-
S14 Loredan	0.9	44.3	8.0	8.1	0.1	-	21.5	-	3.4	14.6	-	-
S01 Mocenigo	1.7	85.2	4.7	6.6	0.3	1.1	-	-	2.1	-	-	-
S03 Mocenigo	0.5	38.1	22.8	4.9	0.7	-	-	33.5	-	-	-	-
S09 Mocenigo	11.0	88.0	2.6	7.2	0.2	-	-	-	2.0	-	-	-
S20 Mocenigo	1.1	88.2	2.5	4.9	4.1	-	-	-	0.3	-	-	-
S21 Mocenigo	3.5	89.1	0.8	11.2	1.3	-	0.5	1.7	2.4	-	-	-
S29 Mocenigo	0.9	81.0	0.8	11.2	1.3	-	0.7	-	5.0	-	-	-
S43 Mocenigo	18.0	88.7	3.3	6.2	1.8	-	-	-	-	-	-	-
S44 Mocenigo	18.0	89.5	0.6	9.0	0.9	-	-	-	-	-	-	-
S59 Mocenigo	5.4	82.0	4.0	5.0	4.9	-	-	-	4.1	-	-	-
S54 Da Ponte	18.0	83.2	5.9	6.1	3.3	-	-	-	1.5	-	-	-
S07 Cicogna	12.5	82.7	0.5	0.5	9.0	-	-	1.1	-	6.2	-	-
S28 Cicogna	3.5	84.4	-	3.6	7.4	-	3.5	-	-	-	0.6	0.5
S38 Cicogna	2.0	89.6	2.5	0.7	7.2	-	-	-	-	-	-	-
S35 Grimali	0.12	44.4	43.8	5.9	0.5	-	-	-	2.3	3.1	-	-
S42 Grimali	15.0	92.9	0.0	4.5	0.5	-	-	-	0.3	-	-	-

Table 6.4 Volume fractions (%) of phases in interdiffusion layer, with estimated thicknesses, and phases in the bulk

Sample	thickness (μm)	Interdiffusion layer					Bulk		
		Cu_2O	AgCl	Mixture Ag-Cu	Cu (pure)	Other phases	Mixture Ag- Cu	Cu (pure)	CuO_2
S15 Venier	15.5	86.6	1.6	0.4	11.4	-	12.7	82.8	4.5
S25 Priuli	50.0	24.7	3.1	21.8	50.4	-	10.2	87.3	2.5
S45 Priuli	43.0	2.0	2.0	6.7	89.3	-	2.1	97.2	0.7
S10 Loredan	19.0	82.6	0.1	5.0	12.3	-	1.0	94.3	4.7
S14 Loredan	37.0	79.0	-	17.8	3.0	$\text{CuO} = 0.2$	2.9	94.3	2.8
S01 Mocenigo	45.0	4.8	1.3	95.8	1.4	$\text{CuO}_2 = 0.2$	11.9	87.8	0.3
S03 Mocenigo	37.0	67.1	0.1	32.0	0.8	-	0.4	96.1	3.5
S09 Mocenigo	37.5	36.3	0.3	41.4	21.9	-	5.2	91.1	3.7
S20 Mocenigo	37.0	1.6	-	97.9	0.5	-	2.5	95.3	2.1
S21 Mocenigo	37.0	17.7	0.7	80.9	0.2	$\text{CuO} = 0.5$	17.2	80.2	2.6
S29 Mocenigo	28.0	67.1	0.7	15.0	16.4	$\text{CuO} = 0.7$	14.1	80.5	5.4
S43 Mocenigo	16.0	60.1	0.8	28.1	11.0	-	11.7	86.8	1.5
S44 Mocenigo	38.0	7.2	4.0	11.9	76.9	-	4.3	91.6	4.2
S59 Mocenigo	39.0	3.2	1.7	27.3	67.8	-	0.2	96.7	3.1
S54 Da Ponte	41.0	84.9	1.9	1.1	6.6	$\text{Ag}_2\text{S} = 5.5$	2.7	93.0	4.3
S07 Cicogna	41.0	4.9	0.3	8.1	86.7	-	0.1	95.0	4.9
S28 Cicogna	41.5	32.6	0.4	1.9	61.6	$\text{Cu}_2\text{S} = 3.5$	19.3	78.4	2.3
S38 Cicogna	16.0	69.5	-	3.0	27.5	-	7.3	88.7	4.0
S35 Grimali	10.2	45.8	7.9	13.1	33.2	-	0.9	97.7	1.4
S42 Grimali	13.0	15.2	-	9.3	72.2	-	9.9	89.8	0.3

The same figure show that also inside the coins of the same period there are surface differences: for example, considering the ruling period of Doge Mocenigo, 1570-1577, there are big differences on the surfaces, only comparing the 0.5 μm of sample S03 with the 18 μm of sample S43 and the composition of the corrosion products (see Figure 6.19).

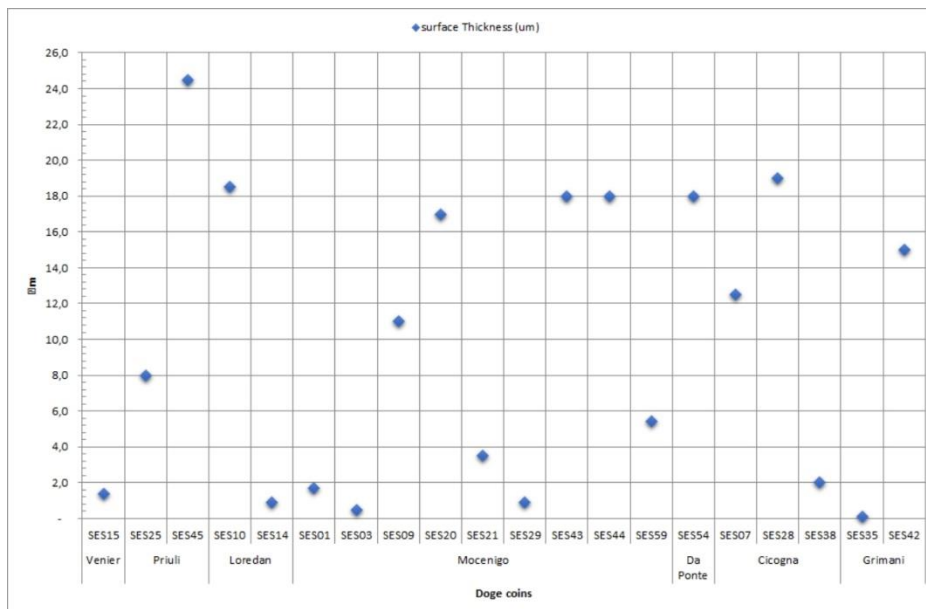


Figure 6.19 Estimated surface layer thicknesses for every “Della Laita’s” coin.

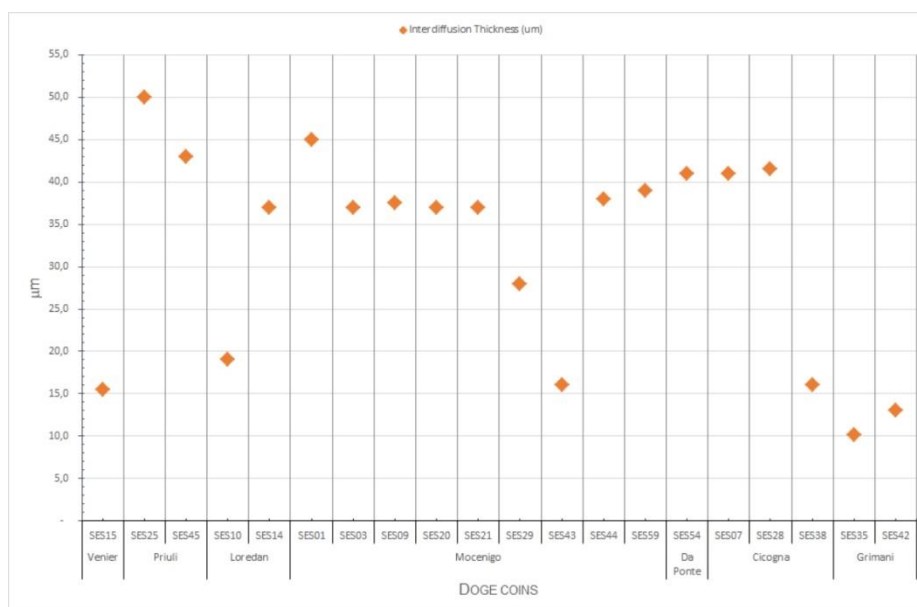


Figure 6.20 Estimated interdiffusion layer thicknesses for every “Della Laita’s” coin.

A less marked difference exists among coins considering the estimated thicknesses of the interdiffusion layers (Table 6.4), as shown in Figure 6.20. Compared to the surface layers, whose values depends on environment, wear, use and consumption of the coin, the inner layer thickness is mostly due to the rate of penetration of oxygen into the coin in order to generate cuprite, and

only indirectly to the aggressiveness of the external environment. So, more than half of the coins have an interdiffusion layer thickness between 37 and 41.5 μm .

XRF datasets, simulated starting from the knowledge of the phase crystallographic model by means of a fundamental parameters approach, were fitted against their experimental counterpart by optimizing the relevant parameters describing the structural model through a least-squares optimization, in a similar way to the classical Rietveld method. Table 6.5 reports the normalized atomic percentages of Cu, Ag and Pb, while the same information is showed graphically in the plots of Figure 6.21 and Figure 6.22.

Table 6.5 Normalized Cu, Ag and Pb weight compositions.

Sample	Cu % norm	Ag % norm	Pb % norm
S15 Venier	80.72	18.95	0.33
S25 Priuli	82.59	16.94	0.47
S45 Priuli	80.23	19.52	0.25
S10 Loredan	88.73	10.89	0.38
S14 Loredan	78.27	21.42	0.31
S01 Mocenigo	72.84	26.69	0.47
S03 Mocenigo	76.24	23.39	0.37
S09 Mocenigo	79.07	20.52	0.41
S20 Mocenigo	86.54	13.24	0.22
S21 Mocenigo	81.48	18.05	0.47
S29 Mocenigo	92.90	5.87	1.23
S43 Mocenigo	85.17	14.52	0.31
S44 Mocenigo	84.32	15.36	0.32
S59 Mocenigo	81.26	18.31	0.43
S54 Da Ponte	83.71	16.11	0.18
S07 Cicogna	99.84	0.01	0.15
S28 Cicogna	83.14	16.54	0.32
S38 Cicogna	99.72	0.03	0.25
S35 Grimani	92.15	7.50	0.35
S42 Grimani	99.32	0.18	0.50

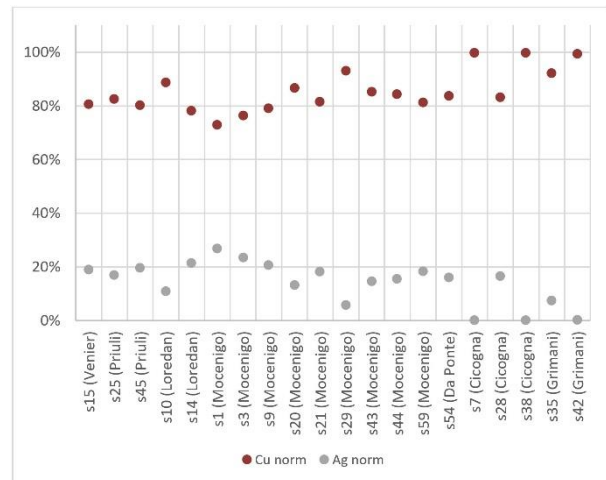


Figure 6.21 Normalized Cu and Ag concentrations (wt.%) in the *sesino* coins

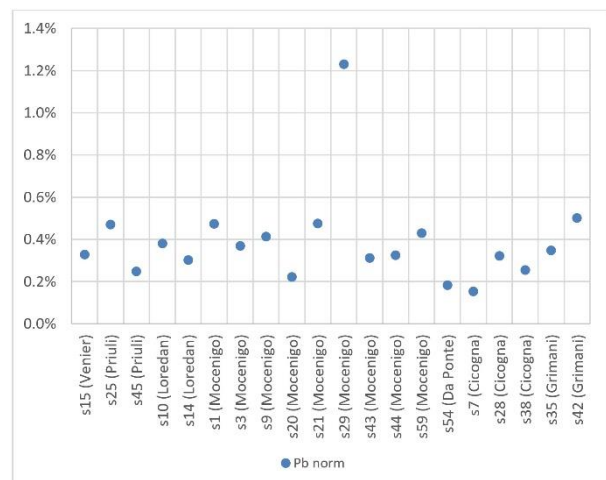


Figure 6.22 Normalized Pb concentration (wt.%) in the *sesino* coins

6.5.4 Qualitative SEM-EDXS surface scan

In order to have a qualitative characterization of the surface of the coins, some SEM-EDXS analysis were performed on the coins.

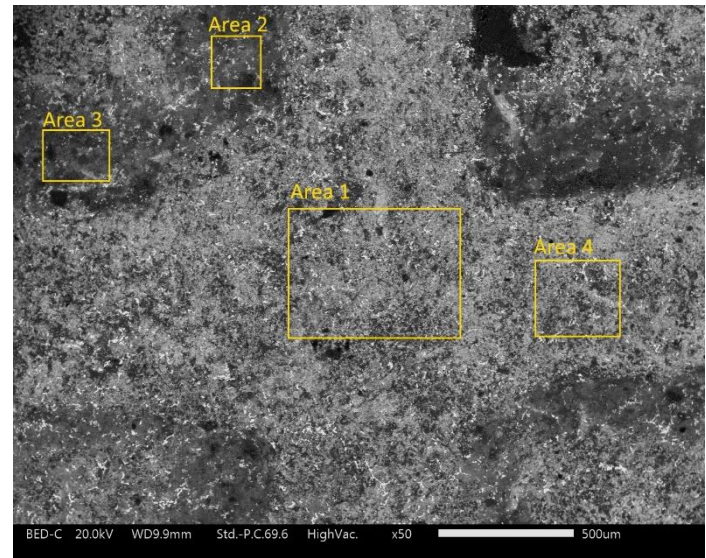


Figure 6.23 Sample SES15 (Doge Venier) with the investigated areas.

The focus was on the incrustations that are typically observed in the lower level part of the coin surface and appear clearly different from the more adherent and comparatively more homogeneous brownish regions, in which the main identified phase is cuprite [54,143]. Because we see in the XRF some atomic elements like Al, Si, Ca, P, S, K, Cl, these ones can be impurities in the original ores from which the coins were produced, or contamination from the environment due to the long unknown history which has taken coins to us.

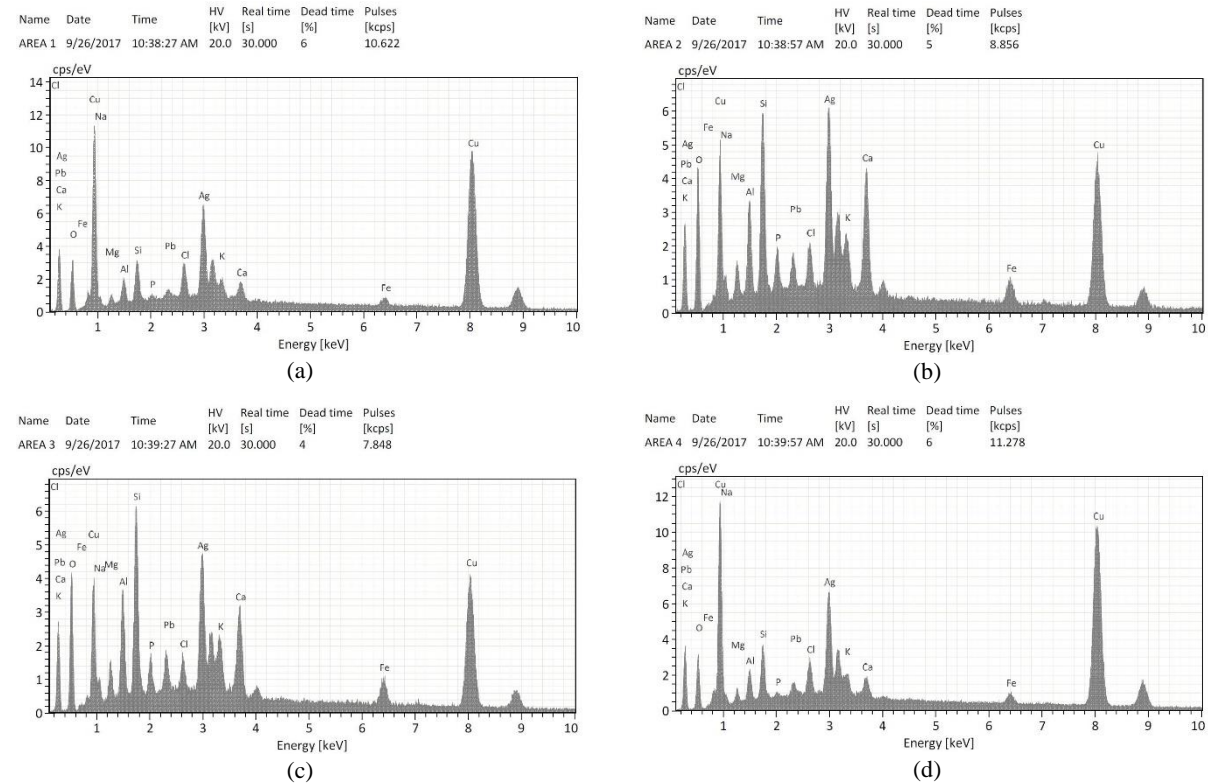


Figure 6.24 EDX spectra of SES15 (Doge Venier) surface in (a) Area 1; (b) Area 2; (c) Area 3; (d) Area 4

The two cases presented herewith refer to S15 (Doge Venier) and S42 (Doge Grimani): the more ancient and more recent coins considered in this study.

Figure 6.23 shows the SEM micrograph of the center of the cross for sample S15, with the indication of the EDXS analysed areas.

The EDX spectrum acquired in region “1” shows the main elements of the alloy, Cu and Ag, in association with oxygen and chlorine. The presence of these chemical elements is coherent with the XRD results (see Figure 6.24a and Table 6.5).

For this coin the presence of the following phases is indeed confirmed: copper, silver, as concerns the metallic phases; cuprite and chlorargyrite for the reaction products. Other elements are visible in the spectra in Figure 6.24b and c: Na, Mg, Si, P, Ca, and Fe that can be interpreted as contribution from soil contamination.

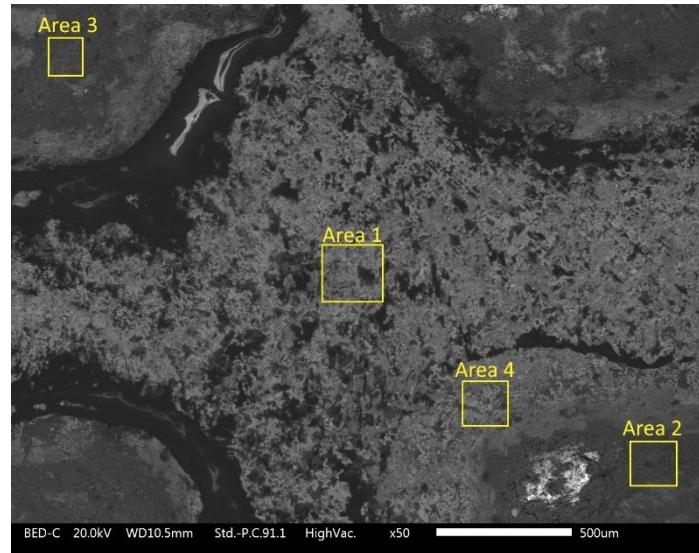


Figure 6.25 Sample SES42 (Doge Grimani) with the investigated areas.

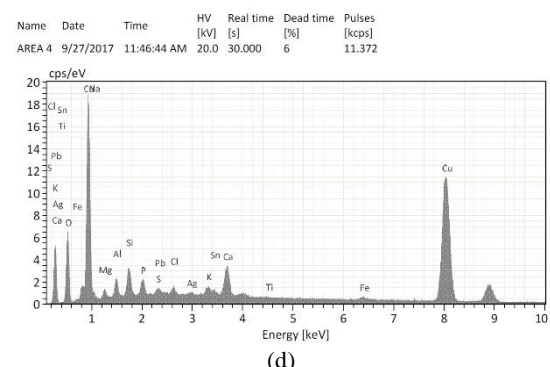
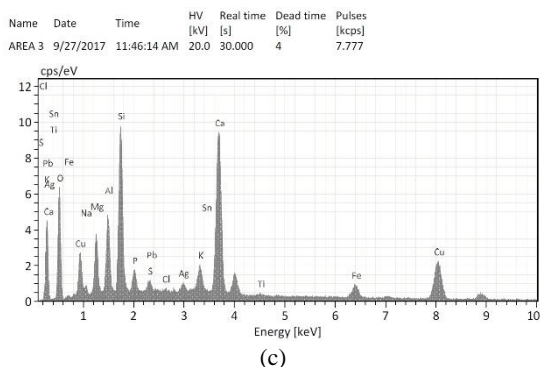
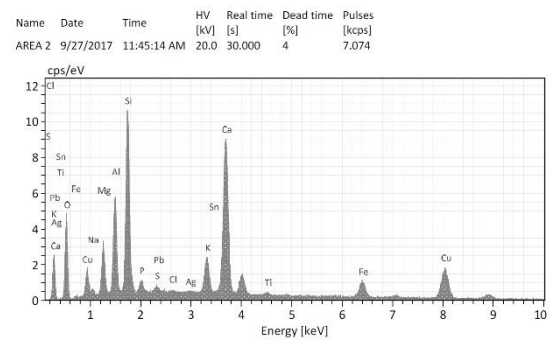
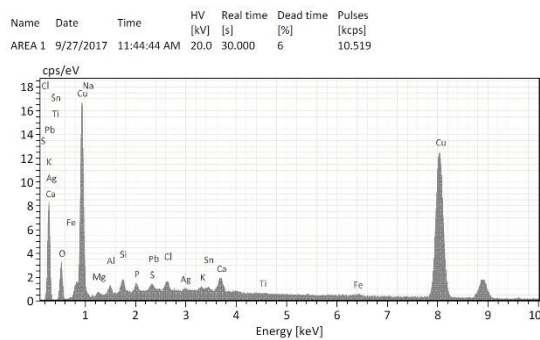


Figure 6.26 EDX spectra of SES42 (Doge Grimani) surface in (a) Area 1; (b) Area 2; (c) Area 3; (d) Area 4

In fact, the relative intensity of the relevant X-ray lines are stronger in the spectrum acquired in region “2” and “3” as compared with region “1” and “4” (see Figure 6.24a and d respect to Figure 6.24b and c). This is coherent with the fact that region “2” and “3” are lower level part of the coin, and therefore are less subject to wear, when compared to region “1” and “4” which are relief areas (on the arms of the cross). A similar situation can be observed in sample S42. The EDX spectrum acquired in region “1” shows the main element of the alloy is Copper, in association with oxygen and chlorine. Silver is very low, compared to the equivalent region “1” of the sample S15. This is coherent with what already observed with XRF and XRD results (see Figure 6.26a, Table 6.3 and Table 6.5). Moreover, surface analysis confirms the presence of high level of sulfur, which it is related also to the presence of the acanthite (see Table 6.2).

The same consideration about silver presence and element content can be done for the other areas (see Figure 6.26b, c and d), also with respect to the presence of other elements (Na, Mg, etc.) as impurities from soil contamination.

The same EDX analysis through the different coins confirms that on the surface there are lower level part of the coin, less subject to wear, which are inhomogeneous areas where the presence of a thin layer of earth attached to the surface of the coin is likely. Here there are in first approximation silico-aluminates, probably of calcium and magnesium, and perhaps also sodium and potassium, whose presence is not homogeneous among the coins, but linked to areas that appear yellow to the naked eye. The presence of silico-aluminates is confirmed by the relative trends of oxygen and silicon and aluminum in these areas: not only silicon and aluminum are substantially in constant relative proportion between the coins, but oxygen has a trend that follows the different content of the two elements.

6.6 Cross test of the approach

To confirm the reliability of the approach and the coherence with the results discussed until now, since it was not possible to apply destructive methods to the samples from the collection of “Della Laita’s” coins, it was decided to perform a parallel study on a couple of certified *sesino* coins, acquired on the numismatic international market.

Several coins of this kind are available on the numismatic market, and two coins has been bought, named respectively “Priuli” (Figure 6.27), after the name of the Doge Lorenzo Priuli, ruling from 1556 until 1559; and “Grimani”, after Doge Marino Grimani, 1595-1605.



Figure 6.27 The obverse (left) and reverse (right) of the Priuli *sesino*.



Figure 6.28 The obverse (left) and reverse (right) of the Grimani *sesino*.

These two specimens have been chosen since they were minted the first one at the beginning (Priuli) and the other one close to the end (Grimani) of the circulation period of the *sesino* in the Venetian Republic, respectively.

On eye inspection, the two specimens exhibited a brownish surface layer of reaction products that formed over the years for the interaction with the surrounding environment, but they appear more homogeneous compared to the coins of collection “Della Laita’s”. This is probably due to a cleaning executed by the numismatic reseller.

The two coins were therefore analysed both with planar and cross-sectional tests [120]: the investigation was executed as the analysis already done for “Della Laita’s” coins, with the same setups both for XRF and XRD before cross-sectional test, in order to get comparable results.



Figure 6.29 Cut direction

After the XRF and XRD sessions, analogous SEM and EDXS analysis on the surface of the two coins were performed.

As final stage, the two coins were sectioned along a diameter passing for the centre of the obverse cross, at about 45° respect to the arms of the cross (Figure 6.29).

6.6.1 XRF-XRD experimental results

The results of XRF analysis confirm what already seen on the coins “Della Laita’s”. The presence of alteration reaction and interdiffusion layers on the outer surface of each coin were confirmed by direct observations.

With XRD the results of analysis indicate for Priuli coin again a complex structure featuring the following main phases: copper, silver, cuprite (Cu_2O) and chlorargyrite (AgCl) (see Figure 6.30).

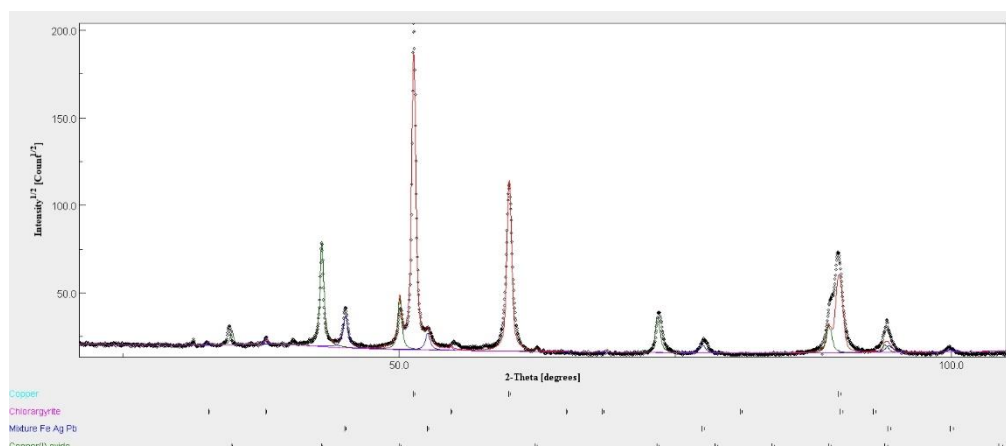


Figure 6.30 Experimental XRD pattern (black dots) acquired on the surface of the Priuli *sesino* coins. The coloured continuous lines are the result of the MAUD software modelling.

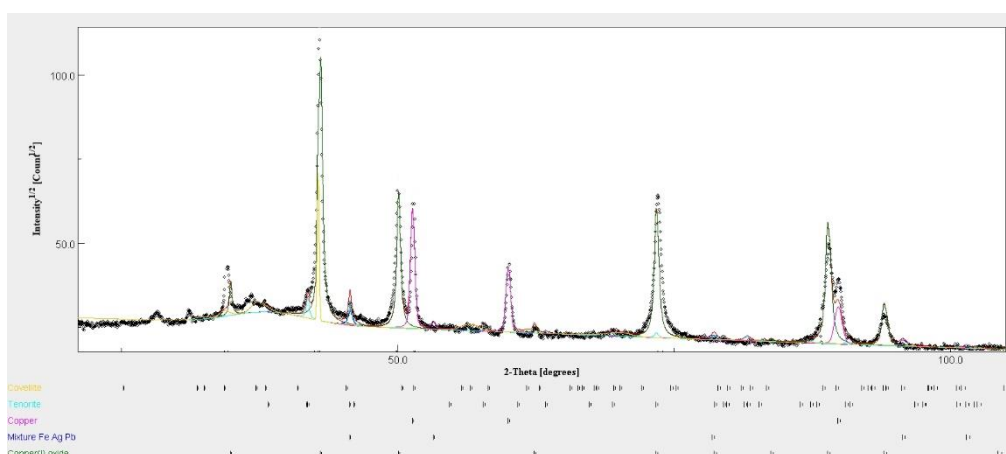


Figure 6.31 Experimental XRD pattern (black dots) acquired on the surface of the Grimani *sesino* coins. The coloured continuous lines are the result of the MAUD software modelling.

Copper oxide is substantially ubiquitous, as demonstrated by acquiring more diffraction patterns in other spots of this same specimen [120]. This is not the case for the chlorargyrite, since

it is not homogeneously spread over the surface of Priuli *sesino*. The situation on the surface of the Grimani *sesino* is simpler to interpret, because cuprite is by far the more common phase, accompanied by tenorite and a new corrosion phase, *covellite*, CuS (see Figure 6.31), not evidenced in “Della Laita’s” coins.

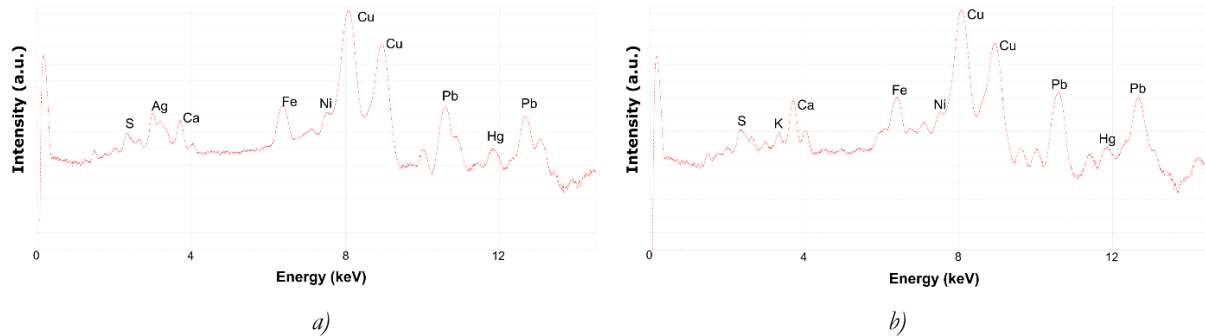


Figure 6.32 Comparison between surficial XRF spectra of a) Priuli coin, obverse, and b) Grimani coin, obverse.

Another aspect important in Grimani coin is that the silver content is very low compared to Priuli coin, so that the mixture phase is very rich in copper. This is also evident comparing the two XRF spectra (Figure 6.32), where the silver signal is well marked on the Priuli coin, but very low and hidden in the noise in Grimani coin.

Again the same multilayer approach has been applied, with a three-layer model and the same criterion of analysis previously defined (see Paragraph 6.5); the results are resumed in Table 6.6 and Table 6.7.

Table 6.6 Volume fractions of phases in surface layer and estimated thicknesses

Sample	Surface layer						
	Thickness (μm)	Cu_2O	AgCl	Mixture Ag-Cu	Cu (pure)	CuO	CuS
Priuli	0.6	85.7	2.2	0	12.1	-	-
Grimani	11	73.6	-	1.6	7.6	5.2	12.0

Table 6.7 Volume fractions of phases in interdiffusion layer and estimated thicknesses

Sample	Interdiffusion layer						Bulk		
	Thickness (μm)	Cu_2O	AgCl	Mixture Ag-Cu	Cu (pure)	CuO	Mixture Ag-Cu	Cu (pure)	CuO_2
Priuli	26.4	85.7	2.2	0	12.1	-	1.2	98.1	0.7
Grimani	35.0	73.6	-	1.6	7.6	5.2	11.6	83.0	5.4

A consideration must be done about the apparent greater level of phase called “mixture” in the bulk of Grimani coin (Table 6.7). This phase has been imposed containing a mixture of Ag with Cu content, whose level was refinable for both, together with some other contaminants. The combined analysis has produced the interesting result that, while in the Priuli coin the content of silver is predominant, as attended by XRF (with a 74% of Ag compared to 0.34% of Cu element inside the phase), this is not the case in Grimani coin, where Ag presence of silver in the phase is

0.5% and copper is the leading element. This is the reason why apparently the phase in Grimani coin is greater than in Priuli coin. In the Paragraph 6.6.3 the SEM-EDXS analysis on the section will confirm the situation estimated by MAUD, with silver depletion of the bulk matrix.

6.6.2 SEM-EDXS surface analysis

The SEM-EDXS analyses on the surface revealed the localized presence of other impurity phases, clearly due to a heterogeneous contamination of the alloy surface probably due to soil residuals (also for the two bought coins it is not known the place of recovery and therefore the history of the coin in term of conservation conditions).

Pure copper and silver in the Priuli *sesino* and copper only, in the Grimani *sesino* are all from the base alloy, that is present beneath multi-layered structure of the outer surface region of each sample.

The SEM observations, conducted on the cross sections of the two coins, provided a further insight in the actual microstructure of the coin and confirmed the data estimated with the multilayer approach.

As supposed, there is a thickness of a few micrometres of the outer multi-layered structure of the alloy surface reaction region (see the example of Figure 6.33 referred to the obverse side of the coin), values coherent with the assumption made in the present case study and with the estimated data in Table 6.6.

This also gives an explanation to the substantial insensitivity of the XRF analytical results on the incident angle of the Mo X-Ray beam (from 5° to 30°), observed both on Priuli and Grimani samples, and on the “Della Laita’s” coins: this means that the contribution to the XRF signal derives mainly from inner bulk alloy. Analysing in detail the three regions clearly visible (according to different grey coloration) on Figure 6.33, we get the results showed in Figure 6.34.

The outer layer is mainly made of cuprite (Area 1 in Figure 6.34*a* and *b*), tenorite and covellite; an intermediate layer (Area 2 in Figure 6.34*a* and *c*) is immediately underneath, from which the metallic cations of copper have migrated towards the coin surface to form the external oxidized layer.

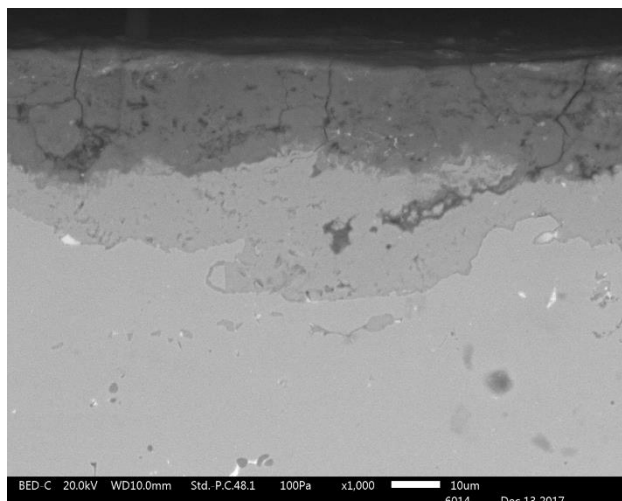


Figure 6.33 Backscattered electron (BSE) SEM micrographs of the cross sections of the Grimani *sesino*, obverse side, showing the microstructure of the outer surface layer.

The internal bulk for Grimani *sesino* is substantially made only of metallic copper (Area 3 in Figure 6.34a and d). In the case of Priuli *sesino*, the differences are:

- the presence also of chlorargyrite in the external layer;
- the presence of silver in the inner layer and bulk;
- a more thinner surface layer of oxide.

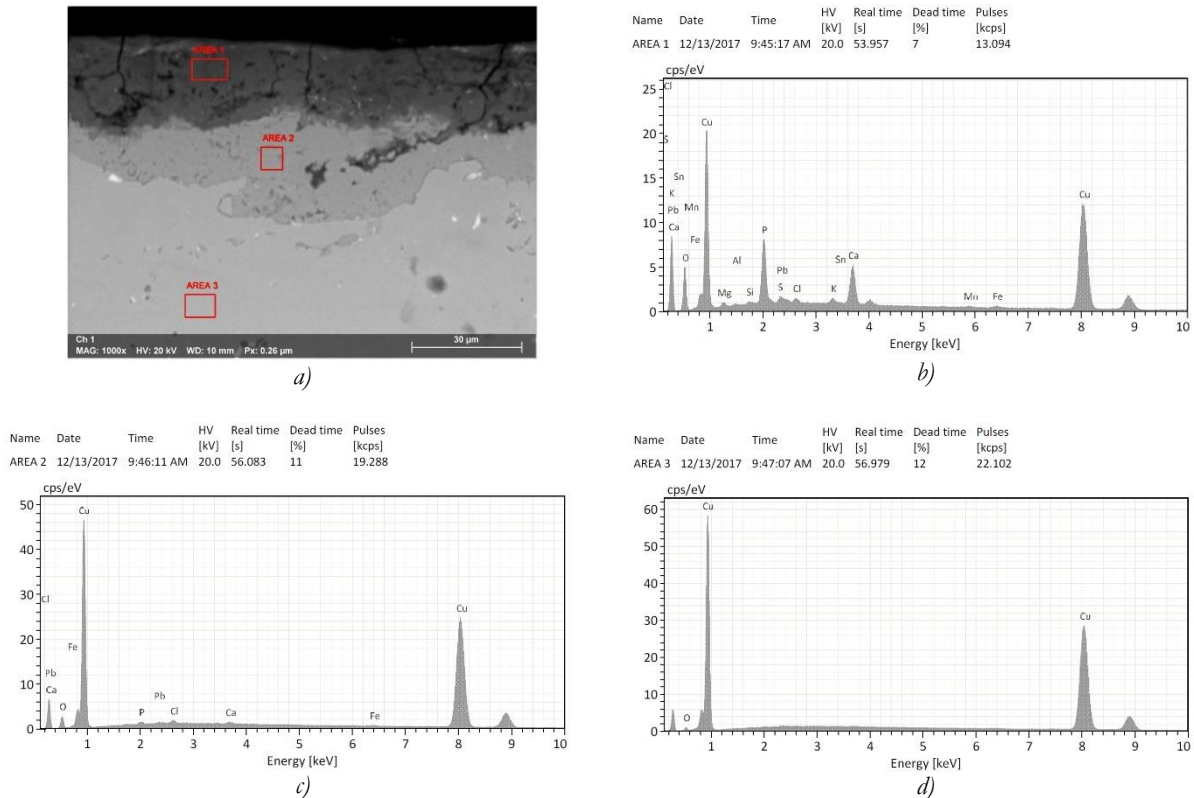


Figure 6.34 SEM micrographs of the cross sections of the Grimani *sesino*, showing a) the area investigated and b), c) and d) the EDXS peaks of the elements.

The pictures of Figure 6.35 confirms the data of table Table 6.6, with a more thinner surface layer in the case of Priuli coin, compared to the Grimani one.

This difference in content between the two coins is well appreciable also in the aspect of the bulk: observing again the pictures from SEM analysis on Figure 6.35, we can see that the Priuli *sesino* shows clearly a two-phase alloy, the copper matrix (grey) and silver rich elongated inclusions (light gray elongated areas, see Figure 6.35a), as foreseen by the relevant Ag-Cu binary phase diagram (see Figure 6.12a) and confirmed by spot acquisition of EDX spectra.

The elongated grains of silver provide clear indications on what might have been the processing and manufacturing route, involving most likely intense plastic deformation.

In case of the Grimani *sesino* (Figure 6.35b), the alloy in the bulk shows a rather homogeneous microstructure, in which the presence of a lead-rich minor phase is occasionally observed, in the form of small grains with a brighter contrast (see Figure 6.35b), and where silver phase is very rare,

with level of detection lower than 0.5% as weight fraction (see Figure 6.36), which confirms what already evidenced by XRF spectra on surface (see Figure 6.32).

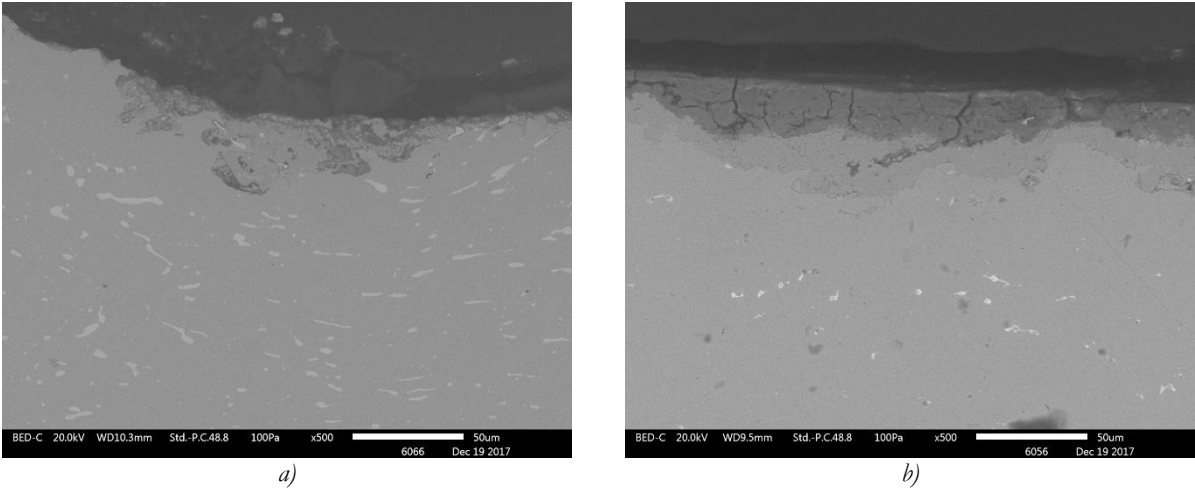


Figure 6.35 Comparison of bulk microstructure between Priuli coin (left) and Grimani coin (right).

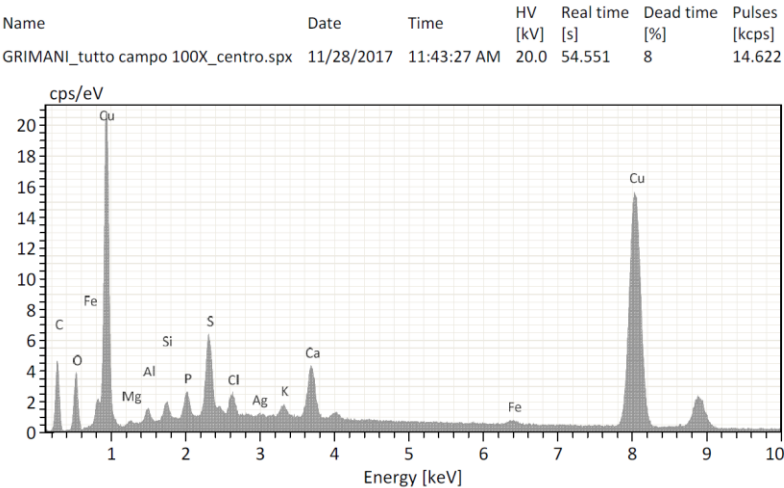


Figure 6.36 EDXS peaks of a rare silver spotted area in Grimani *sesino*

6.6.3 Coin section analysis

To obtain an average alloy composition, several spectra were acquired along the section of the center of both coins: this has been done selecting sufficiently wide regions, so that the effects of possible alloy heterogeneities are averaged out. In Figure 6.37 the cross-sectional views of the two coins are shown.

The composition of each *sesino* coin was evaluated as the average of the EDXS data acquired from a set of eight rectangular areas for each sample (see areas enclosed by the red dotted envelope in Figure 6.37a and Figure 6.37b).

The purpose of this selection is to avoid the two regions of the surface and interdiffusion layers of the sample, where the local composition is altered by oxidation compared to bulk.

For a comparison with the compositional data obtained from the coin surface (Figure 6.32), XRF analyses were conducted also on the cross section of the two coins, sampling their whole thickness. The obtained data are resumed in Table 6.8.

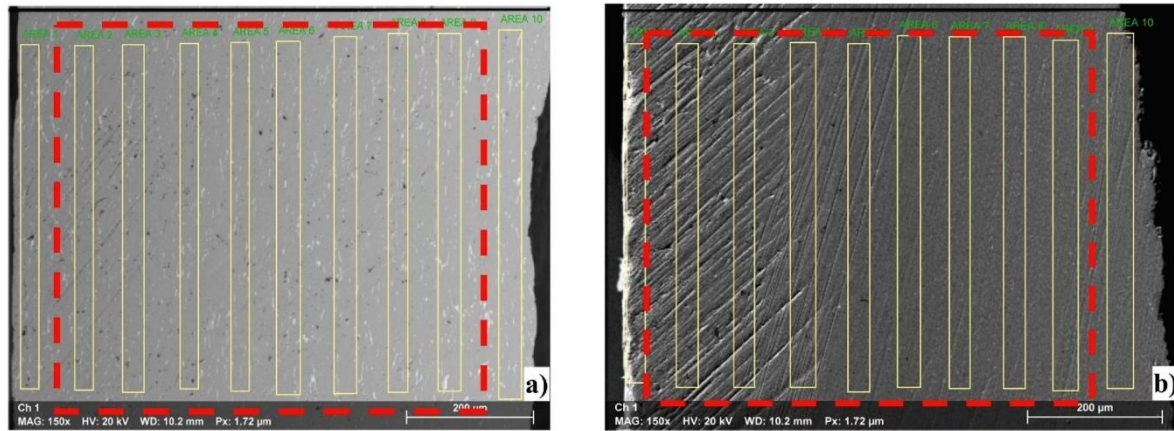


Figure 6.37 SEM micrographs of the cross sections of the: a) Priuli and b) Grimani coins. The yellow rectangular areas sampled for EDXS data acquisition are shown. The red-dot area encloses the regions considered for the evaluation of the average composition of the base alloy of each coin

Table 6.8 Summary of the main chemical elements inside coins from numismatic market

		Cu	Ag	Pb
<i>Priuli coin</i>	XRF (wt%) obverse	90.3 ± 0.3	9.6 ± 0.2	0.10 ± 0.05
	EDXS (wt%) section	94.3 ± 0.2	5.4 ± 0.1	0.3 ± 0.1
	XRF (wt%) section	96.0 ± 0.1	3.9 ± 0.1	0.15 ± 0.05
<i>Grimani coin</i>	XRF (wt%) obverse	99.5 ± 0.2	-	0.5 ± 0.1
	EDXS (wt%) section	99.3 ± 0.2	-	0.7 ± 0.1
	XRF (wt%) section	99.3 ± 0.1	-	0.7 ± 0.1

The EDXS and XRF analyses indicate the presence of a minor concentration of lead, not detected in the diffraction patterns since below the XRD detectability limit of the set up used in the present research. The levels of lead are comparable to that observed in “Della Laita’s” series (see Table 6.5).

The cross-sectional XRF results are coherent with the outcome of the same tests carried out on the coin obverse surface, although the concentration values are not coinciding.

Considering the data in Table 6.8, this discrepancy between the alloy composition values obtained from surface XRF data and those obtained from the cross-sectional tests, is mainly due to the silver enrichment in surface, due to the formation of the surface copper oxide layer and relevant copper depletion in the alloy matrix [120,121]. This enrichment is also confirmed by the fact that from literature we know that the nominal value of silver inside a *sesino* was with about 4.6 wt% [5].

The difference observed in the compositional data for the Priuli *sesino*, as obtained from EDXS and XRF data on section, can be ascribed to two main reasons:

- different sampling volumes: the XRF incident beam partially falls outside the coin cross section. Moreover, the sampled volume falling within the coin comprises both the bulk alloy and the surface altered layers, whereas EDXS results strictly refer to unaltered bulk alloy regions.
- fully different data treatment models, that introduce some precision limitation.

These comments are applicable to the result sets of the two coins and the good agreement observed in the compositional results for the Grimani *sesino* must be regarded as purely occasional.

6.7 Result discussion

The lattice parameter variations of Cu, Ag and Pb with respect to the pure element values has been investigated for each one of the detected phases. The lattice expansion observed in all cases indicates the reciprocal solutioning of the majority element couples: Cu-Ag and Cu-Pb, although also contributions from minor elements must be considered [120]. These were observed in the EDXS spectra, and as expected are generally the same of the coins “Della Laita’s”, but not considered herewith, since present in concentrations not exceeding 0.1 wt.%.

The results obtained from the XRF and XRD analyses of the *sesino* coins provide interesting historical information on the evolution of the alloy composition over the years of emission. Let us consider again here Figure 6.21 and Figure 6.22.

The ubiquitous presence of cuprite in the surface layer of all coins suggests that in the underlying alloy layer a silver enrichment as occurred. In Figure 6.21, plotting the compositional values in Table 6.5, silver has significantly higher concentration than the reported literature values for the *mistura* alloy, that is, 4.6 wt% [5]. The same happens with the coins from the numismatic market (see Paragraph 6.6.3)

On the other side, in samples S07, S38, and S42 (ranging from Doge Cicogna to Doge Grimani), silver is present in extremely low concentrations, so that it seems an impurity rather than an intentional addition. Moreover, apart that for S29 (Doge Mocenigo), lead concentration is comparatively constant in all coins, as shown by Figure 6.22.

6.7.1 Historical implications

The evolution of silver content in copper, during the considered historical lifetime of the coin, confirms that the precious metal remains constant in proportion for a period and starts decreasing

after mid-16th century, until a complete disappearance toward the end of this same century, during the ruling times of Doge De Ponte and Doge Grimani (see Table 6.1 and Table 6.5).

This suggests that despite of what reported in historical documents, various coins editions did not involve only a recast with a new *impressum*, in order to fight forgeries, but also a progressive depletion of the noble metal in the alloy. In the case of the *sesino* coins, silver, once eliminated from the *mistura* alloy, is not replaced by any other metal.

This aspect is also more evident if the data of copper and silver content in absolute weight are reported, considering the nominal values of every series according to official documents [5].

From the beginning of emission, during the ruling of Doge Venier (1554-1556), to Doge Priuli (1559-1567), the *sesino* coin was impressed on a disc of 1.764 g. With Doge Loredan (1567-1570), the nominal weight of the coin was reduced to 1.324 g, and this weight remained until the stop of emission under Doge Grimani (1603).

Therefore, if correcting the data showed in Table 6.5, considering the official weight of the coin, we get an interesting ideal graph in Figure 6.38a. As we can see, with the caveat of silver enrichment already stated, the Ag trend is a constant reduction of silver, and expanding the data in Figure 6.38b, we can clearly appreciate that Venice spared silver content both with weight reduction of the coin at the time of Doge Loredan, but also with a slow process of depletion, completed under Doge Cicogna and Doge Grimani.

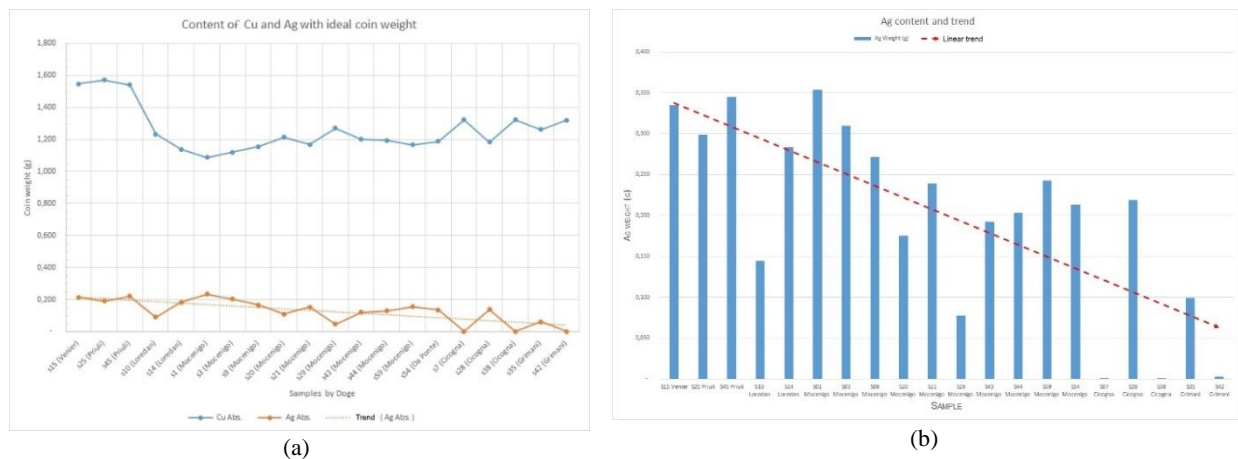


Figure 6.38 (a) Content of Cu and Ag in *sesino* coins for ideal coin weight; (b) Ag content trend (expanded)

This fact reflects a political and economic situation in strong evolution for the Venetian Republic in the second half of 16th century: new competitors appeared in the Mediterranean, primarily the French, Dutch, and English [34,139,189]. Moreover, the harbors of Ancona and Marseilles emerged as new competitors on commercial trades.

Piracy and the lingering threat of the Turks obliged Venice to maintain a very expensive war fleet; at the same time, a continuous series of alliance changes and military threats on the mainland

required the engagement of mercenary armies. At the end of the 16th century, military forces absorbed 60% of the state budget [138,189].

All these situations forced Venice to change the acquisition of capitals from various forcible loans to market. At the same time the Senate introduced also regular direct taxes and parallelly increased trade duties, actions which, however, did not solve the long-term problem of fragile economic bases of the Republic.

Venice was obliged to revise its coin system and values not only for small valued coins like *sesini* but also for the other ones, based on silver, with larger value, in a process called debasement [48,138,139] with large revenues for the monetary authority.

6.7.2 Bulk model vs multilayer model

As we have stated above, the single bulk model of a sample like a mixture Cu/Ag coin allows a rapid first approach for checking the phases and fitting the lattice parameters in first approximation.

The limit consist in the fact that it is clearly an oversimplification, because there are visible corrosion and oxidation layers on the coin samples, as we have seen from first optical inspection (see Paragraph 6.2.1) and confirmed by the found uncommon phases (Table 6.2) which are distributed among the coins and confirmed by the SEM-EDXS surficial analysis (see Paragraph 6.5.4).

We have already seen that these layers may be some microns thick on the samples surface (see Table 6.3 and Table 6.4 and corresponding Figure 6.19 and Figure 6.20), depending on the unknown history of every single coin.

There is another important aspect which emerges from this case study and demonstrates the goodness of the multilayer approach respect to a single bulk model, and it is the best fitting of the data.

Indeed, it possible to compare the quality of the refinement, for every coin, through the weighted profile R_{wp} of the bulk model (see Paragraph 3.5) against the corresponding quantity of the multilayered model.

The data are summarized in Table 6.9. It is immediately clear from the data in the table that there is a general reduction of the R_{wp} of the multilayer model (MLM column) compared to the bulk model one (BM column), with an improvement of the fitting with a reduction of the values of R_{wp} by average 49%.

Table 6.9 Comparison of the quality of the refinement between bulk model (BM) and multilayer model (MLM)

Sample	R _{wp} BM	R _{wp} MLM	% Improvement	Sample	R _{wp} BM	R _{wp} MLM	% Improvement
<i>S15 Venier</i>	0.235	0.143	39.1	<i>S29 Mocenigo</i>	0.267	0.114	57.0
<i>S25 Priuli</i>	0.269	0.157	41.5	<i>S43 Mocenigo</i>	0.229	0.109	52.4
<i>S45 Priuli</i>	0.295	0.186	37.1	<i>S44 Mocenigo</i>	0.275	0.167	39.4
<i>S10 Loredan</i>	0.274	0.139	49.1	<i>S59 Mocenigo</i>	0.276	0.126	63.8
<i>S14 Loredan</i>	0.264	0.157	40.5	<i>S54 Da Ponte</i>	0.276	0.126	54.2
<i>S01 Mocenigo</i>	0.255	0.092	64.2	<i>S07 Cicogna</i>	0.264	0.101	61.8
<i>S03 Mocenigo</i>	0.264	0.082	69.8	<i>S28 Cicogna</i>	0.273	0.161	41.2
<i>S09 Mocenigo</i>	0.269	0.098	63.3	<i>S38 Cicogna</i>	0.273	0.145	46.9
<i>S20 Mocenigo</i>	0.273	0.126	54.0	<i>S35 Grimani</i>	0.271	0.163	39.8
<i>S21 Mocenigo</i>	0.274	0.152	44.4	<i>S42 Grimani</i>	0.273	0.198	27.3
Legenda BM = Bulk model MLM=Multi-Layer Model							

This reflects the obvious fact that the multilayer model applied to sample like the coin with a combined XRF-XRD approach is more adherent to the real structure inside the coins. As a consequence, this allows the combined approach to contemporarily fit data XRF and XRD better compared to bulk layer model, as it is possible to appreciate this result considering the example of S43, as showed in Figure 6.39 and Figure 6.40.

From the comparison of XRD spectra there are only very little differences on the two models, looking at the residual bar below the spectra in Figure 6.40. But on XRF side the situation is completely different, again looking at the residual bar below the spectra in Figure 6.39.

Because the multilayer model is more adherent to reality, the combined approach allows to best fit XRF data using the phases defined in the multilayer model (see Figure 6.39B, where there are only light “waves” on residuals), while the bulk model obliges the software to adapt the XRF-XRD fitting, overestimating, for example, the copper and lead content inside the sample (see Figure 6.39A, where the peaks on residuals curve are clearly marked).

There are in any case some simplifications also in the multilayer model: these are related to the homogeneity of the layer which is a hypothesis not always applicable, due to the type of sample and the corrosion history which can alter the chemistry inside the coin, e.g. the silver enrichment already stated or the distribution of silver inclusions inside the copper matrix, as seen in the SEM-EDXS analysis (see Figure 6.35). But in any case, the assumptions allow generally the combined XRF-XRD approach to better fit spectra, as summarized in Table 6.9.

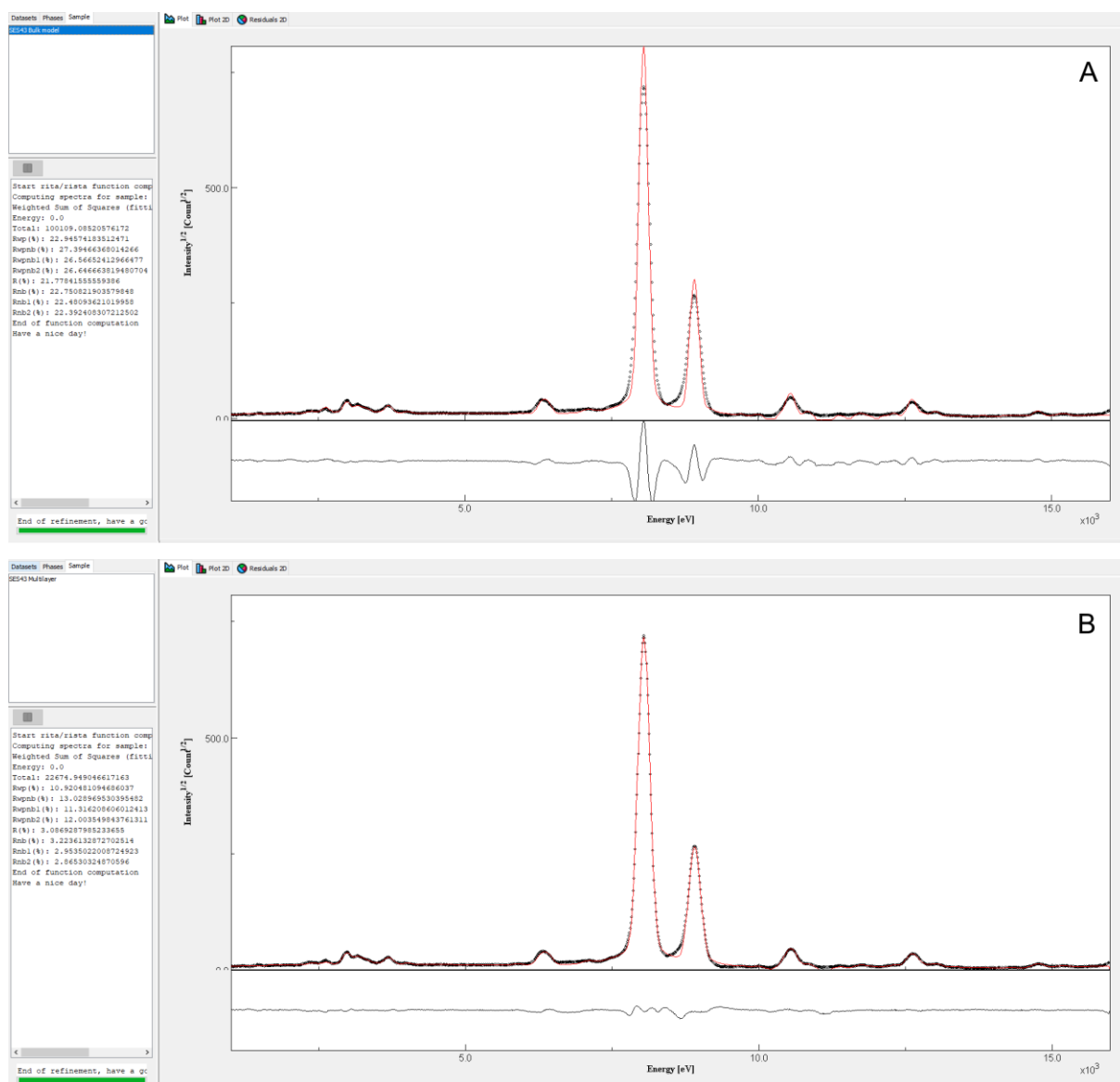


Figure 6.39 XRF fitting spectra (red) of coin S43 of Doge Mocenigo with A) bulk model and B) multilayer model.

For some coins, e.g. S45 of Doge Priuli and S44 of Doge Mocenigo, the improvement is more limited compared to the average one.

The reason is that there are some texture effects which affects the XRD data, with a displacement of the peaks or enhancement of only some peaks of a single phase.

An example is showed in the XRD spectrum of *sesino* S44 of Doge Mocenigo (Figure 6.41), where there are displacement of the lower peak of cuprite (left) and that at high angle (above, 100°, right) and some scattered values on second and fourth peaks, due to preferred orientations, not fitted, as appreciable also from the residual bar under the spectrum. A similar situation with scattered values in correspondence of cuprite peaks, due to preferred orientations, are visible in Figure 6.42 for coin S45.

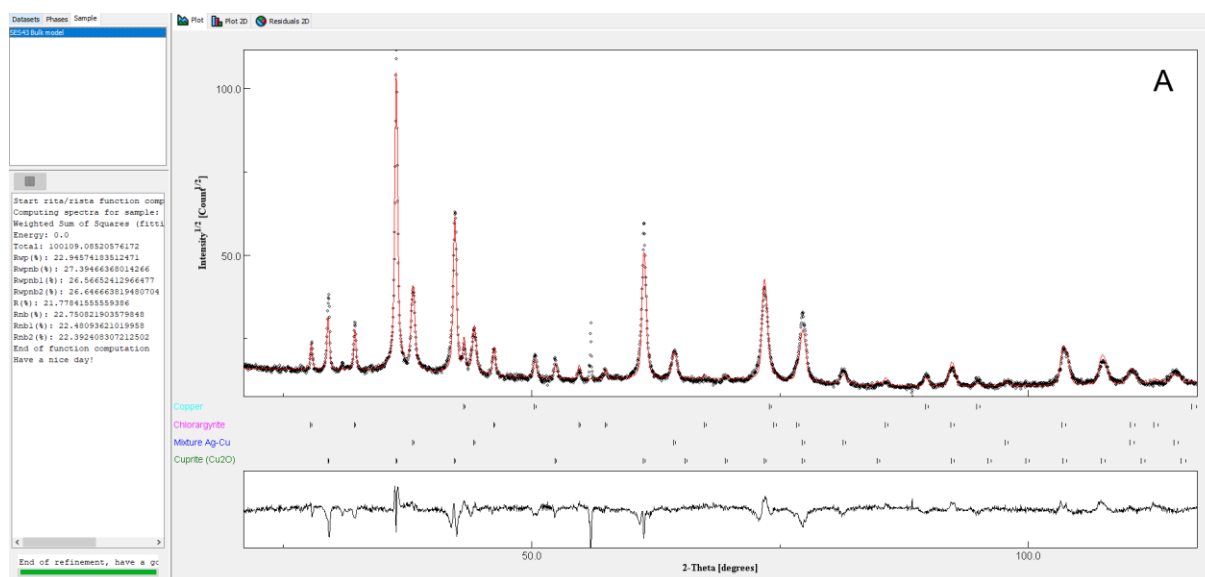


Figure 6.40 XRD fitting spectra (red) of coin S43 of Doge Mocenigo with A) bulk model and B) multilayer model.

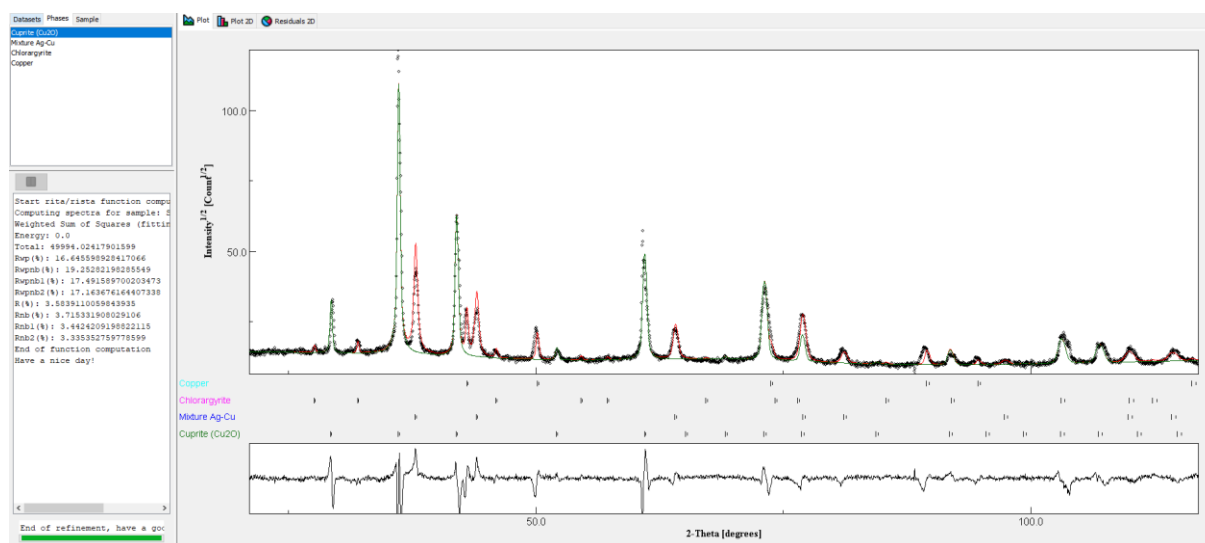


Figure 6.41 XRD fitting spectrum (red) of coin S44 of Doge Mocenigo with multilayer model and some texture effects on peaks of cuprite (green curve) which the model is not able to fit.

This texture effects are usually due to production effect: the oxide growth on copper matrix which retains plastic deformation, because of the hammering of the coin, as described above in Paragraph 6.2.

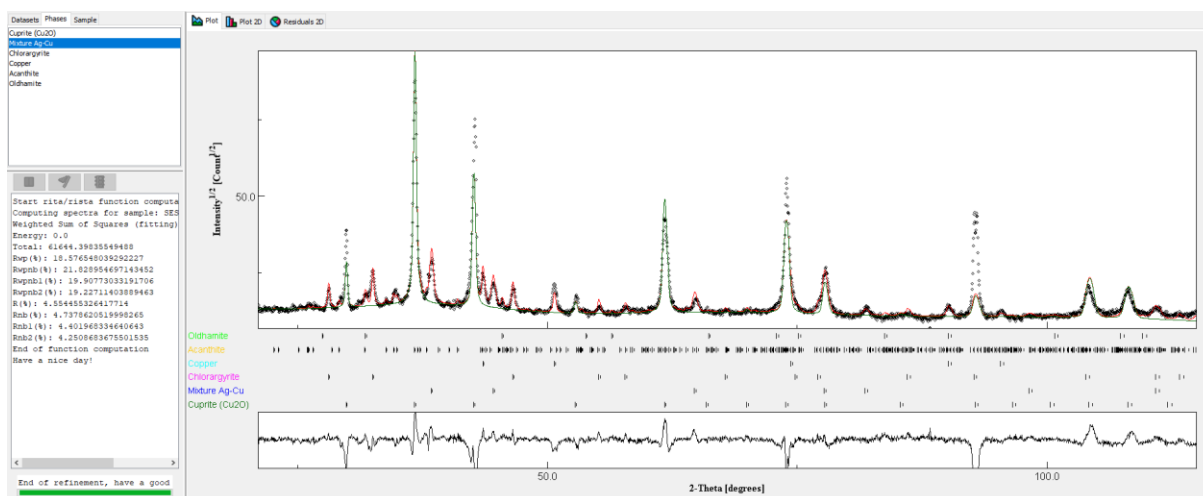


Figure 6.42 XRD fitting spectrum (red) of coin S45 of Doge Priuli with multilayer model and some texture effects on the peaks of cuprite (green curve) which the model is not able to fit.

This complicate the combined fitting, but due to complexity of the samples, considering the evolution of the corrosion patinas so different among the coins, the texture factor has not been introduced in the fitting of the multilayer model for the present research. This obviously reduce the ability of the multilayer model here proposed to describe completely the sample, with a more limited improvement in the quality of fitting compared to bulk model.

The texture analysis of the structure of some of the coins can be an interesting point of interest for future research on the matter, on that samples affected, in order to improve the multilayer model with the combined XRF-XRD approach above presented.

7 CASE STUDY: SINTERED ALLOY

Powder Metallurgy is a technology which uses powders as raw material to produce components for many different applications, through several “consolidation” processes. The powder itself is the product of different technologies that transform the raw material in a high quality product.

Powder Metallurgy may be therefore defined as a two-step technology that transforms the raw material in a final product, through the production of a powder and its consolidation.

7.1 Introduction

Powder Metallurgy is a technology already used occasionally for decorative metallic objects in the early stages of recorded history. Since the beginnings, metal powders such as gold, copper, and bronze, and many oxides in powder form (e.g. iron oxide), were used for decorative purposes. Sintering of metals was however entirely forgotten for many centuries until the end of the 18th century, when in Europe various methods of platinum powder production were recorded [178,186]. The documented metallurgy of platinum, as practiced in the 18th and 19th centuries, is one of the most important stages of development for modern powder technology.

The use of this technology to form complex shaped parts by pressing and sintering was introduced in the 19th century. In 1830 Osann, during his studies on copper, found that the reduced metal could be sintered into a compact solid; then he developed a process for making impressions of coins from copper powder produced by the reduction of precipitated copper carbonate, Cu_2CO_3 [186]. In the following years he improved the process, also producing medals of silver, lead, and copper.

The first commercial applications of powder metallurgy were developed to produce incandescent lamp filaments, starting from carbon filament at the end of 19th century through to the tungsten filament with the Coolidge Process at the beginning of the 20th century.

In the following years of the early 20th century two main application were particularly developed: on one side the creation of composite metals for heavy-duty applications (e.g. refractory metals and their carbides), on the other side the development of porous metal bearings, especially special types of porous bearings defined as self-lubricating.

The 1950s and 1960s witnessed the emergence of powder metallurgy wrought products, with the improvement also of compacting and sintering technologies. The commercialization of

powder-based high-performance materials increased since the 1970s thanks to opening of new markets because of superior performance, cost effectiveness and longer operational life.

Commercial powder metallurgy nowadays spans the density spectrum from highly porous components to Powder Metallurgy parts with controlled density up to fully dense wrought metal components.

The success of the technology is based mainly on being a rapid, economic and high volume production method which allows the making of precision components from powders from easy design to more complex ones.

The research in the field devotes many efforts in the improvement of powder types, new alloys and superior mechanical and anti-corrosion properties due to improvement in sintering and treatment technologies [88,178]. The improvements in this technology make it more competitive than other production methods like casting, machining and stamping, an advantage more evident in the case of large production volumes.

7.2 Titanium

Many efforts in recent years have been devoted to titanium and, above all, titanium alloys, because they combine great lightness and high mechanical resistance, comparable to that of steel [24,148,167].

In practice, metals with a density greater than 5 g/cm^3 are defined as *heavy*, therefore titanium with a density of 4.51 g/cm^3 is the heaviest of light metals. Titanium's low density value is approximately 56% of that of steel (see Table 7.1).

Table 7.1 Comparison of some characteristics among Ti, Al, Fe and Cu [24,25,103].

PROPERTIES (AT ROOM TEMPERATURE)	TITANIUM	ALUMINIUM	IRON	COPPER
<i>Atomic number</i>	22	13	26	29
<i>Density (g/cm^3)</i>	4.51	2.70	7.87	8.96
<i>Molar heat capacity ($\text{J/mol}\cdot\text{K}$)</i>	25.06	24.20	25.10	24.44
<i>Heat of fusion (J/mol)</i>	14.15	10.71	13.81	13.26
<i>Thermal conductivity ($\text{W/m}\cdot\text{K}$)</i>	21.9	237	80.4	401
<i>Expansion coefficient ($\mu\text{m/m}\cdot\text{K}$)</i>	8.6	23.1	11.8	16.5
<i>Resistivity ($\text{n}\Omega\cdot\text{m}$)</i>	420	26.5	96.1	16.78
<i>Corrosion Resistance</i>	Very high	High	Low	High
<i>Reactivity with Oxygen</i>	Very high	High	Low	High
<i>Price of Metal</i>	Very high	Medium	Low	Medium
<i>Melting temperature ($^{\circ}\text{C}$)</i>	1668	660	1538	1084.6

This means that for the same weight (for example 1 kg), titanium occupies a double volume compared to steel, or, in other words, with the first it is possible to make lighter components. Therefore, titanium is as strong as steel, but 56% lighter; moreover, it is 60% heavier than aluminum, but twice as strong.

Titanium has a significantly lower coefficient of thermal expansion than that of ferrous alloys; this property allows it to be much more compatible with ceramic or glass materials than other metals, especially when metal/glass or metal/ceramic joints are involved.

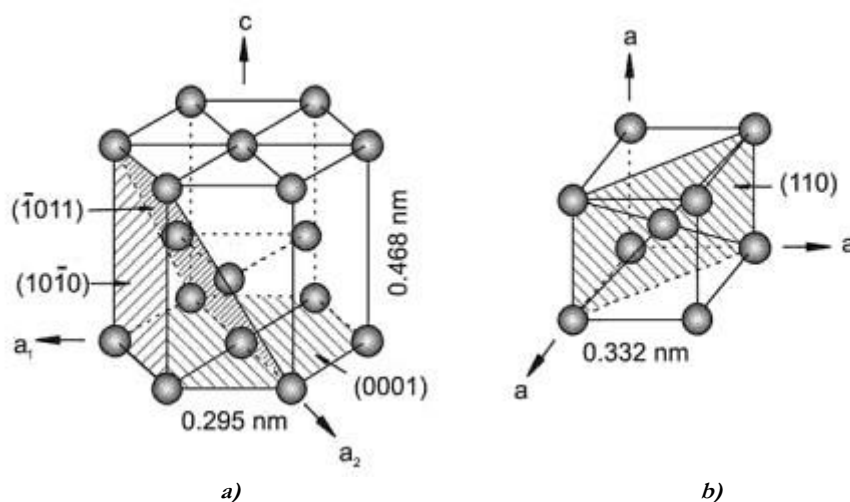


Figure 7.1 Titanium two allotropic forms: a) α phase, hexagonal centered packed; b) β phase, body centered cubic [24].

Pure titanium exists in two allotropic forms [25,148]. At room temperature, titanium has a compact hexagonal cell (HCP, see Figure 7.1a), which is commonly referred to as a α phase, whose values of the lattice parameters at the room temperature are $a = 0.295 \text{ nm}$ and $c = 0.468 \text{ nm}$. The resulting c/a ratio for pure α titanium is 1.587, smaller than the ideal ratio of 1.633 for the hexagonal close-packed crystal structure.

At 882°C , the hexagonal cell α turns into a cubic with a centered body (BCC, see Figure 7.1b), called the β phase, stable up to the melting point (1668°C). This temperature is therefore called “ β transus temperature” (see Figure 7.3). The lattice parameter value of pure β titanium at 900°C is $a = 0.332 \text{ nm}$.

Titanium is resistant to oxidation up to about 600°C and is a reactive metal that can interstitially accept and dissolve elements such as oxygen, hydrogen, nitrogen; generally, however, titanium is used up to temperatures of about 540°C , since the allotropic transformation from HCP structure to BCC structure further limits its maximum application temperature.

There are six types of commercially available pure titanium (labeled with the “CP” acronym) and each contains a different amount of impurities [70,148]; CP titanium “Grade 1” is the purest. In general, these contain from 99.01% to 99.5% titanium, smaller amounts of iron, carbon,

hydrogen, nitrogen and oxygen. These elements are normally present in a residual form and do not have a significant effect on the mechanical properties; hence, strictly speaking, CP titanium is an alloy of titanium and interstitial elements. Furthermore, an alloy type contains from 0.15% to 0.20% palladium to improve resistance to weakly reducing environments, such as sulfuric acid and dilute hydrochloric acid.

Although the different types of CP titanium do not have similar mechanical resistance compared to titanium alloys, they cover a relatively wide range of resistance levels and are used both for structural and non-structural applications.

Low resistance qualities are generally used in applications where corrosion resistance and excellent formability, rather than resistance, are the primary requirements; high strength grades are often used for similar applications, but with higher strength requirements. All types of CP titanium are readily weldable; it can be obtained through all possible milling, casting or powder metallurgy processes.

Generally, titanium CP is used in applications where an excellent resistance to corrosion is desired and in which high resistance is not a determining factor [103,148]. In titanium CP, moreover, oxygen acts as a controlled reinforcer: the resistance increases if the quantity of oxygen increases within a controlled range, since too much oxygen produces an embrittlement of the material. This type of titanium is therefore used for aircraft coatings, reinforcing elements, refractory walls, projectile explosion panels, rings and fasteners in engines. Commercial applications include heat exchangers, valves, processing equipment and marine components.

7.2.1 Titanium alloys

In order to improve properties of pure titanium for many other applications, many alloys have been developed. The main characteristics of the titanium alloys are [133,148]:

- excellent relationship between resistance and density, in particular in the temperature range between $200 \div 500^{\circ}\text{C}$;
- good resilience, even at low temperatures;
- high yield strength: in some alloys, values are comparable to those of high steels;
- resistance;
- excellent corrosion resistance;
- very short time of radioactivity loss;
- nonmagnetic.

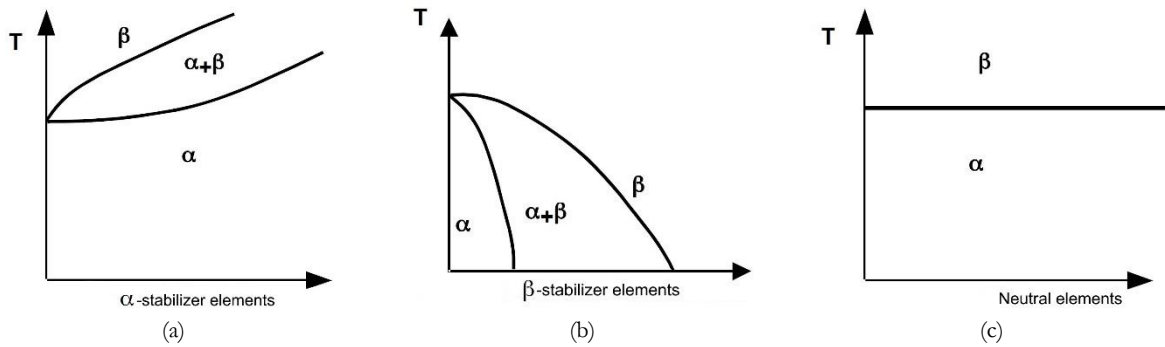


Figure 7.2 Schematic representation of the effect of alloy elements on the state diagram of titanium alloys in case of a) α -stabilizers elements; b) β -stabilizers elements; c) neutral elements [133].

In titanium-based alloys, the temperature of the allotropic transformation is strongly influenced by the alloy elements [24,133], which can favour the α phase, widening the field of existence (Figure 7.2a) or, on the contrary, they can increase the β phase, lowering the transformation temperature (Figure 7.2b). Obviously in these alloys, we can no longer talk about a temperature of transformation $\beta \rightarrow \alpha$ but of an interval of temperature. In the case of α stabilizers the end transformation temperature $\beta \rightarrow \alpha$ it is greater than the β -*transus* of pure titanium [24].

Finally, other elements do not intervene on the transformation temperature, thus being neutral with respect to the transformation allotope (Figure 7.2c).

The elements that favour the α phase are Al, which is a substitutional element, and C, O and N, these ones giving rise to interstitial solutions.

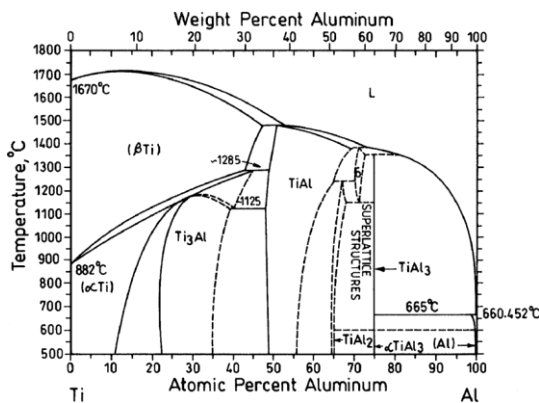


Figure 7.3 Diagram phase of Ti-Al system [38].

The reinforcement effects of these last interstitial elements disappear in the temperature range from 260 ° C to 430 ° C, while the reinforcing effects of aluminium remain up to about 540 ° C. In addition to the reinforcing effect, within these limits the interstitial elements cause embrittlement [148].

The fact that aluminium, as *substitutional* element, stabilizes the α phase is partially explained by the

fact that aluminium has an FCC lattice whose packing factor is the same as HCP lattice; the complete diagram phase of the Ti-Al system [38] is reported in Figure 7.3.

Sn and Zr are substantially neutral when considering the quantities that commonly appear in industrial alloys, neither favouring the formation of the α phase nor the β phase and their presence is justified by the fact that, being soluble in both phases, they improve the mechanical resistance.

It is possible to distinguish the β stabilizers in two subclasses: β -isomorphous and β -eutectoid [24,167].

In β -isomorphous, the temperature of transformation $\alpha \rightarrow \beta$ ends at lower temperature than β -transus (as already seen in Figure 7.2b). In the β -isomorphous type alloying elements are of the substitution type and they have a high solubility in the β phase and do not form intermetallic compounds. This type of β stabilizing elements commonly used are: V, Mo, Nb, while Ta and Re are more rare [103].

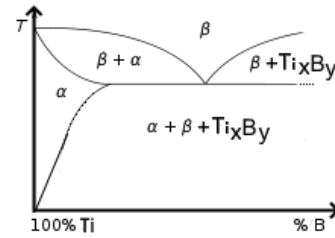


Figure 7.4 Diagram phase of Ti and a β -eutectoid element [103].

Yet in β -eutectoid types, the presence of the alloying elements lowers the temperature of start transformation $\beta \rightarrow \alpha$, but in this case we get also intermetallic compounds (see Figure 7.4).

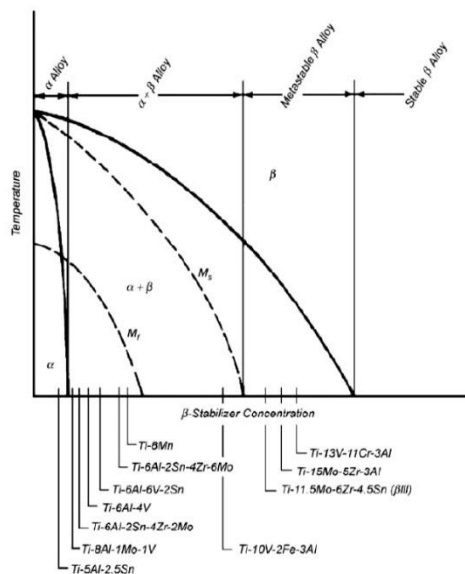


Figure 7.5 Titanium alloys mainly used for structural components [24].

Fe, Cr and Si are typical β -eutectoid elements: other β -eutectoid elements like Ni, Cu, Mn, W, Pd, and Bi have only very limited usage, for special purpose alloys. Moreover, β -eutectoid forming elements, such as Co, Ag, Au, Pt, Be, Pb, and U, are not used at all in titanium alloys [103].

It should be mentioned that hydrogen belongs to these β -eutectoid forming elements, but its use is limited by hydrogen embrittlement above 150 ppm.

Titanium alloys are therefore classified into three broad categories based on the predominant phases present in the microstructure at room temperature (Figure 7.5) [25,103,129]. Thus, we have:

- *alpha alloys*, where β phase percentage $< 5\%$;
- *alpha-beta alloys*, which contain both elements that stabilize the α phase and elements that stabilize the β phase; this last phase is present in a percentage between 10 and 20%. α - β alloys are titanium alloys more widespread (about 70% of the titanium used industrially is used for the manufacture of these alloys), have a high mechanical strength even if they are less workable than alpha alloys.
- *beta alloys*, rich in elements designed to stabilize the beta phase, they can present at room temperature only this phase operating with an appropriate cooling speed (they are unstable at room temperature).

Since the cubic structure of β titanium contains a greater number of sliding planes than those present in the hexagonal alpha form, β titanium is more easily deformed; the alloys in the beta and alpha-beta regions are, therefore, hot-formable.

7.3 Research samples: TiAl6V4 alloy

In this study six samples of TiAl6V4 sintered alloy has been considered: this is one of the α - β alloys (see Figure 7.5) that has the widest use (about 45% of the total production), because of good machinability and excellent mechanical properties. Many studies has been devoted to the ternary phase diagram Al-Ti-V [102].

TiAl6V4 may also be welded by a wide variety of conventional fusion and solid-state processes, although its chemical reactivity typically requires special measures and procedures [1].

The TiAl6V4 alloy offers good performance for a variety of weight reduction applications in aerospace, automotive and marine equipment; moreover, it is an alloy with applications in the medical industry.

Due to the formation of a dense oxide layer TiAl6V4 provides good corrosion resistance in an oxidizing environment. In case of damage the new growth of the oxide layer occurs immediately, if oxygen is present. Biocompatibility of TiAl6V4 is excellent, especially when direct contact with tissue or bone is required [43,71,103], but although this alloy is the most widely used implant material, V and Al can cause allergic reactions, Alzheimer's disease, and neuropathy, which is promoting new research for alternatives [31].

Applications TiAl6V4 is typically used for [20,24,148]:

- direct manufacturing of parts and prototypes for racing and aerospace industry;
- biomechanical applications, such as implants and prosthesis;
- marine applications;
- chemical industry;
- gas turbines.

The chemical specifications for the alloys are reported in the Table 7.2: the specification references here considered are ASTM B367 for cast material [191], C-5 grade, and ASTM F1472 [192], or is equivalent ISO 5832-3 [193], for wrought material. In Figure 7.6 we can appreciate the general phase diagram of this α - β alloy [47].

Here combined XRF/XRD analysis has been applied to six sample of sintered TiAl6V4 alloy: all of them are a parallelepiped of 2 cm wide, 1.0 cm deep with thickness of 0.5 cm (Figure 7.7).

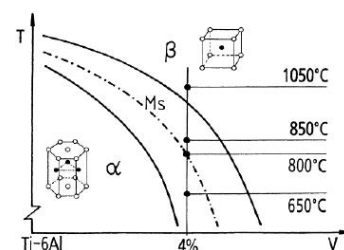
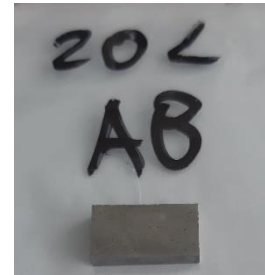


Figure 7.6 Phase diagram of TiAl6V4 alloy [47].

Table 7.2 Chemical specification for TiAl6V4 alloys.

Atomic element	Typical	Cast material (required)	Wrought material (required)
Aluminium, Al 6%	6%	5,5–6,75%	5,5–6,75%
Vanadium, V	4%	3,5–4,5%	3,5–4,5%
Carbon, C	0,03%	< 0,10%	< 0,08%
Iron, Fe	0,1%	< 0,40%	< 0,3%
Oxygen, O	0,15%	< 0,25%	< 0,2%
Nitrogen, N	0,01%	< 0,05%	< 0,05%
Hydrogen, H	0,003%	< 0,015%	< 0,015%
Other elements	-	< 0,4 %	-
Titanium, Ti	Balance	Balance	Balance

**Figure 7.7** One of the samples investigated.

All the investigated sample are produced with the same type of powders and sintering process, i.e. Selective Laser Melting (SLM), and without any other heat treatment (i.e. as built; in the following all samples are marked ‘AB’). According to information provided, for all the sample the cooling rate has been the same. The aim is to correlate the phase composition with alloy content.

7.3.1 Selective Laser Melting

The Metal Additive Manufacturing, or simply 3D printing of metals, is one of the most significant innovations in the world of industrial manufacturing [57,58,140]: the most advanced technology in this field is laser sintering of metal powders, better known as Selective Laser Melting (SLM) [66,181], which is nowadays the most broadly used powder-bed fusion manufacturing process in industry [67].

The improvement in SLM technology allows a density over 99%, and a dimensional error within 0.05 mm. Because it is possible to directly fabricate complex curved surfaces and porous structures, Ti6Al4V alloys find widespread use in the manufacturing of auto and aviation components, in addition to medical applications [184].

The Selective Laser Melting is a laser fusion process that allows to create objects starting from a three-dimensional drawing. Very fine metal powders are deposited and melted, layer by layer, by one or more high-performance lasers.

In Figure 7.8 is shown a general simplified schema of SLM production process: the powder is preventively deposited on the previous layer, or substrate, and the laser beam scans along the directions parallel to the edges of the rectangular area $\{(x, y) | -X \leq x \leq X, -Y \leq y \leq Y\}$ as shown in Figure 7.8b, with the hatching spacing h .

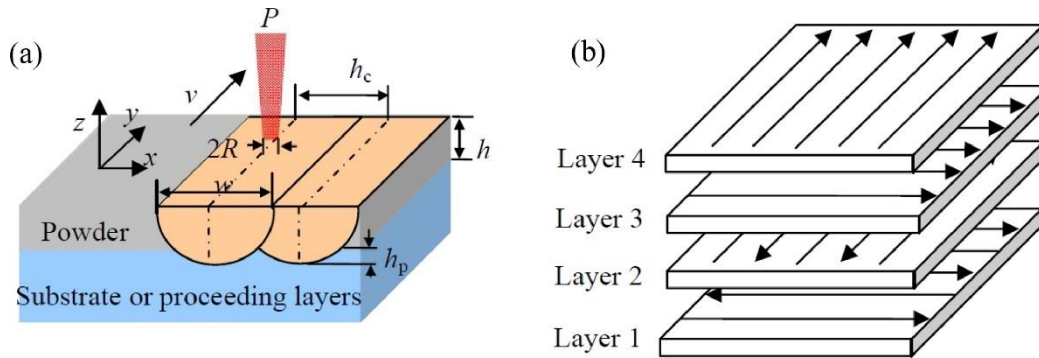


Figure 7.8 Example of SLM technology: a) schematics of process, b) example of scanning strategy [95].

The temperature of the powder particles rises instantly when irradiated by the laser beam of radius R , causing a molten pool when the temperature exceeds the melting point of Ti6Al4V (1660°C). Since it can be supposed that the powder bed is a homogeneous and isotropic medium, therefore the surface profile of the molten pool is a circle [95,96,157].

In this case, the laser beam takes an alternating scanning manner: it scans along the x direction in the odd layers but along the y direction in the even layers. The creation of a discrete volume of consolidated material therefore involves the definition of a deposition strategy that can gradually involve all the sections of the 3D part to be produced. The chosen model (Figure 7.9) is usually defined from the point of view of the profile of the section of each level.

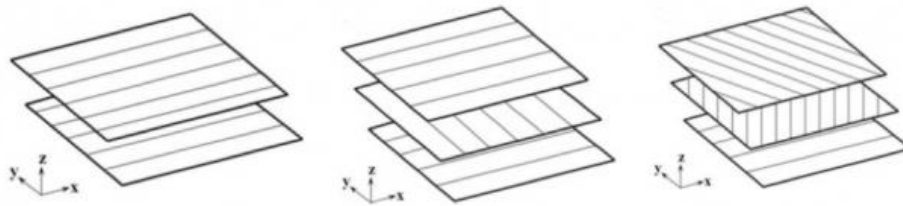


Figure 7.9 Examples of possible SLM scanning strategies [Source: <http://www.addmelab.polimi.it>].

Other factors to be considered in production are relative to powder (composition, size distribution, shape, optical and heat transfer properties, thickness of deposited layer for each cycle of fabrication) and to machine laser specification (laser: power, spot size, beam spatial distribution, scanning velocity and application of protective gas atmosphere) [169,188]. Non-optimal process parameters may cause product local defects, e.g. unmolten powder particles, spherical entrapped gas bubbles, cracks and so on [86,87].

The mechanical and geometrical characteristics of the products obtained with the Selective Laser Melting process are comparable, or better, respect to those made with injection moulding, while the metallurgical characteristics are superior because of the more controlled and uniform cooling.

The components obtained with laser fusion have an excellent density, almost equal to 100%, which allow also a polishing finish with excellent aesthetic results.

Main other advantages of laser fusion of metal powders compared to conventional technologies are [96,157,181]:

- maximum freedom in the design phase: it is possible to produce extremely complex geometries despite typical constraints of the casting, moulding and mechanical processing processes;
- possibility of making very light objects: when studying 3D digital models, thanks to the use of specific software, it is possible to define the material needed without sacrificing structural integrity and robustness of the object, or altering quality, resistance and mechanical properties;
- reduction of production scraps: only the strictly necessary material is used, with very high yields on the use of raw materials and energy consumption, so compared to traditional mechanical processing, SLM generates neither scraps nor chips and, compared to a casting, the typical polluting substances of foundry plants, such as dust, fumes and waste, are avoided;
- independence of costs from the quantity to be produced; without any cost for making moulds and equipment, it is economical to produce few units, as well as samples in unit quantities;
- possibility of performing heat treatments on components with a known, constant and repeatable metallographic structure; materials used are suitable for supporting also mechanical processing (milling, drilling, turning, surface treatments, both aesthetic and protective).

For each samples produced by SLM, the energy density E (i.e. the energy applied per unit volume of the sample) used to represent the energy input can be evaluated according to following formula [31,126,157]:

$$Eq. 7.1 \quad E = \frac{P}{v h h_c}$$

where P is the laser power, h_c is the hatch spacing, v is the laser scanning velocity, and h is the layer thickness of the sample. The SLM production parameters of the samples investigated in this research are resumed in Table 7.3; in the same table the energy density evaluated according to Eq. 7.1 are recorded, assuming for simplicity a cube of 1 mm^3 .

Table 7.3 Production parameters for every investigated sample

<i>Sample ID:</i>	S08L_AB	S10L_AB	S20L_AB	S22L_AB	S23L_AB	S24L_AB
<i>Laser power (Watt)</i>	450	400	450	400	450	500
<i>Scan velocity (mm/s)</i>	1167	2250	2750	2200	2200	2200
<i>Energy density (Joule/mm³)</i>	0.386	0.178	0.164	0.182	0.205	0.227

7.4 Experimental setup

X-Ray investigations of the Ti6Al4V samples has been performed on two different instrumental setups.

XRF data were collected on a TNX Phoenix combined spectrometer (already seen in Figure 6.9): the machine is equipped with a Mo anode X-Ray source operating at 40 kV, 30 mA, coupled with a parabolic multilayer monochromator (Axo Dresden), and a Silicon Drift XRF Detector produced by Ketek (model Axas-D with Peltier cooling, 50 mm² active area: see Appendix A for details).

The XRF detector has been maintained normally to the sample surface, with a fixed incidence angle of 6°. The system has been calibrated with reference samples (see Appendix B) before data acquisition. Every acquisition for measurement, both for calibration and samples, has been set to 1000 seconds.

Diffraction data have been collected with an Italstructures IPD3000 diffractometer (Figure 7.10), equipped with a Co anode



Figure 7.10 Italstructures IPD3000 diffractometer.

X-Ray source operating at 40 kV, 30 mA, a flat multilayer monochromator on the incident beam, and an Inel CPS120 curved position sensitive detector on the diffracted beam. The 2θ angular range was from 5° to 100°; the acquisition time for each XRD pattern was set to 30 minutes. X-Ray beam incidence angle for the XRD set up was set to 5° with respect to the sample surface, with a beam section of 5.0x0.5 mm², the same as for XRF.

7.5 Experimental results

A qualitative estimation of the elemental composition of the alloy has been obtained for each sample by means of XRF data analysed at first stage with Eagle-X (see Chapter 5), calibrating the spectra and using the element picker (see Paragraph 5.5.5).

In Figure 7.11 we have the example relative to sample S08L_AB (peaks not labelled on the picture are due to detector's head contribution).

The elements individuated on samples by Eagle-X, besides Ti, Al, V, are Si, Cr, Fe, Cu. At second stage, the results obtained from Eagle-X plugins have been introduced into the MAUD software [17,117] together with XRD data, in order to execute the combined analysis.

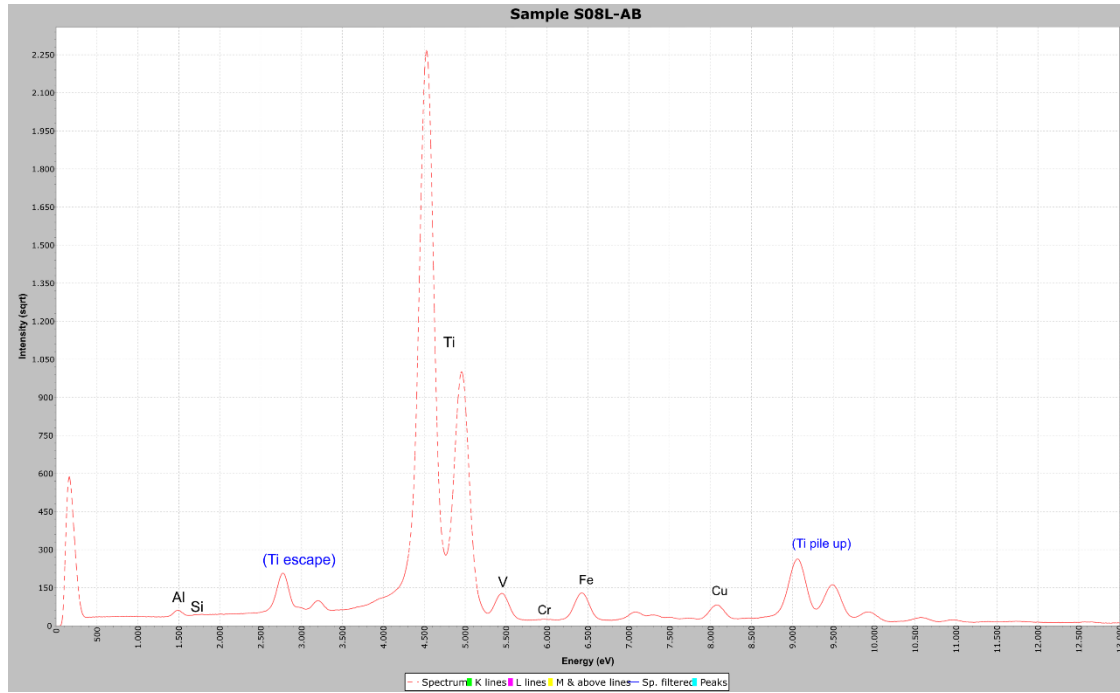


Figure 7.11 Elements of S08L_AB sample individuated through the peak picking plugin of Eagle-X.

7.5.1 Combined XRF-XRD analysis

For the combined XRF-XRD analysis, a sample model with a surface layer and a substrate (bulk) has been conjectured (Figure 7.12): this is based on the fact that we have two main phases (α phase and β phase), but on surface titanium is reactive with oxygen and forms a patina of coherent passive oxide when exposed to air at room temperature [1].

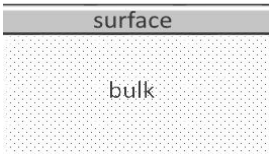


Figure 7.12 2-layer model

Thus, the phase introduced in the analysis are three: the Ti-phases, α phase and β phase, and TiO_2 , an oxide with tetragonal lattice.

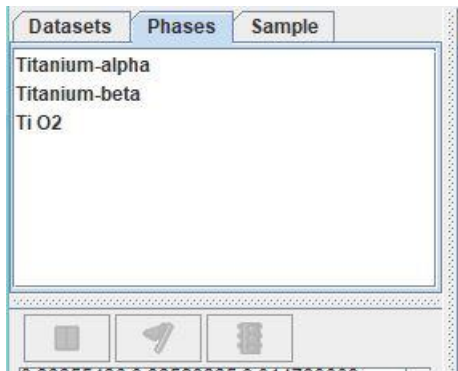


Figure 7.13 Three phases modelling in MAUD structure of the two Ti-phases.

All phases have been downloaded from the Crystallography Open Database website (<http://crystallography.net/cod/>) and loaded into corresponding set-up in MAUD (Figure 7.13).

Since we have two main elements in the alloy, Al and V, we have introduced both into phase structure on MAUD, as substitutional elements of Ti inside the crystal

The other elements, being all β -stabilizers (see Paragraph 7.2.1) and of lower content, has been loaded only in the β -titanium phase. This is an approximation, of course, but it takes care of the

fact that preferentially elements like Cr, Fe and Cu, having a BCC lattice in pure conditions, therefore will be preferentially substitutional inside the BCC lattice of β -titanium phase.

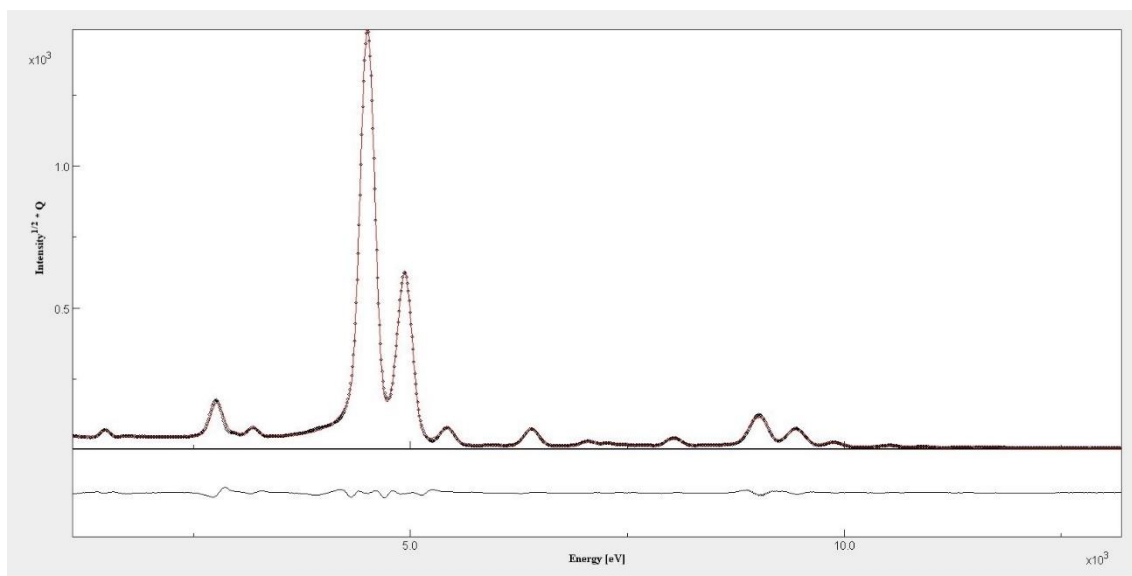


Figure 7.14 Fundamental parameters fit relative to XRF data for sample S08L_AB.

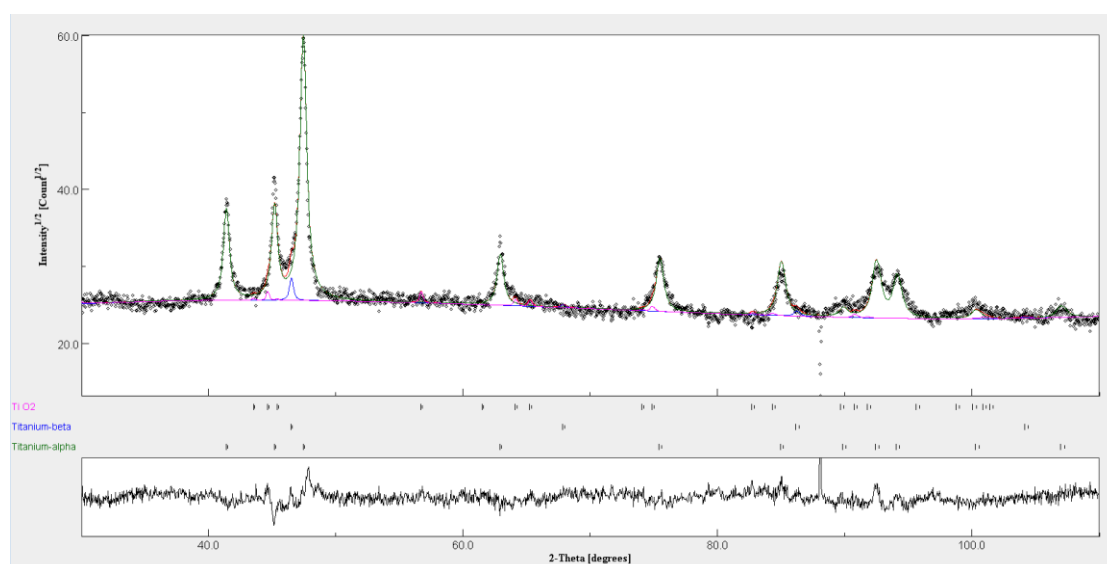


Figure 7.15 Rietveld fit relative to XRD data for sample S08L_AB. The coloured continuous lines are the result of the MAUD software modelling.

As soon as the model has been prepared, we have launched the combined XRF-XRD analysis on MAUD for each sample.

In Figure 7.14 and Figure 7.15 the diagrams of sample S08_AB relative to combined fitting are shown, respectively for XRF and XRD spectra, while Figure 7.16 and Figure 7.17 refer to sample S23_AB.

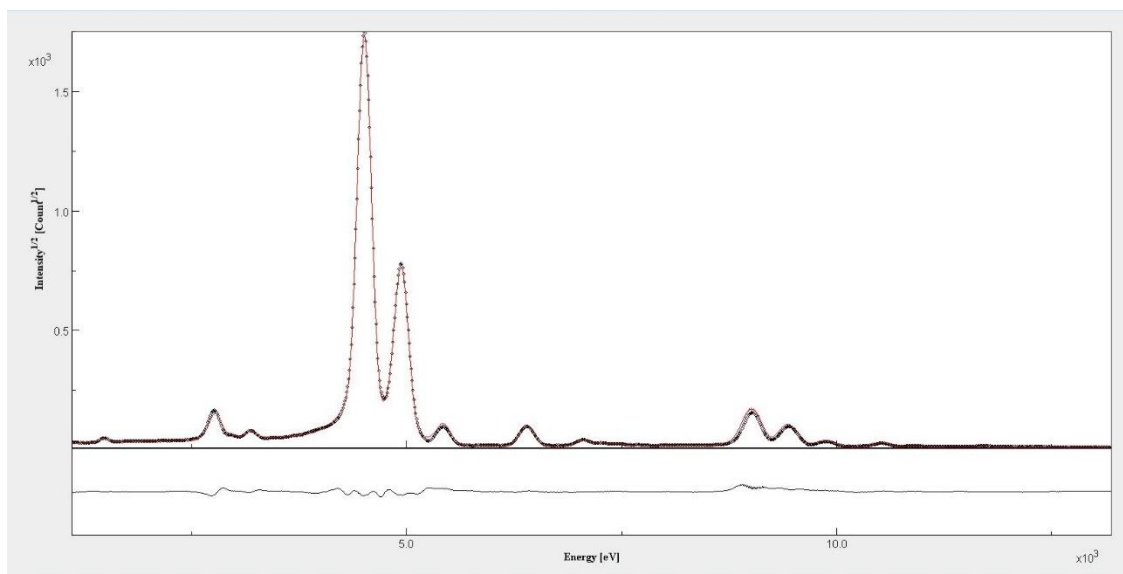


Figure 7.16 Fundamental parameters fit relative to XRF data for sample S23L_AB.

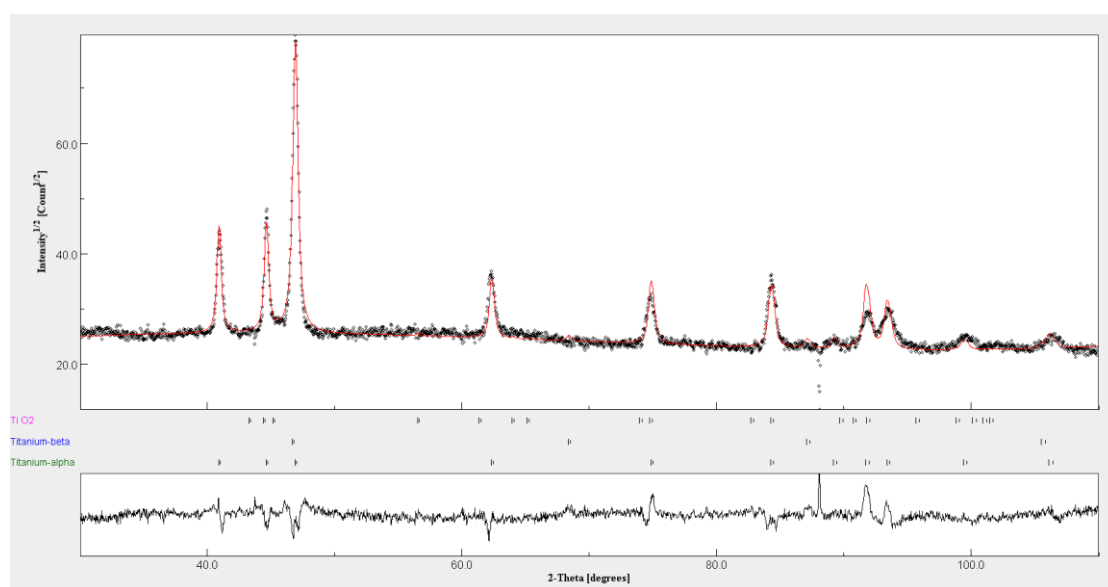


Figure 7.17 Rietveld fit relative to XRD data for sample S23L_AB.

Table 7.4 Elemental composition of sample alloys according to MAUD analysis (in wt%).

<i>Element</i>	S08L_AB	S10L_AB	S20L_AB	S22L_AB	S23L_AB	S24L_AB
<i>Ti</i>	89.40	89.68	89.23	89.22	88.15	89.23
<i>Al</i>	5.99	5.75	5.98	6.00	6.07	5.92
<i>V</i>	3.51	3.50	3.54	4.02	4.11	4.20
<i>Si</i>	0.78	0.68	0.95	0.38	1.42	0.42
<i>Cr</i>	0.03	0.03	0.04	0.05	0.01	0.04
<i>Fe</i>	0.23	0.26	0.22	0.26	0.23	0.19
<i>Cu</i>	0.04	0.05	0.05	0.07	0.00	0.00

Table 7.5 Phase composition of bulk according to MAUD analysis (in wt%).

Phase	S08L_AB	S10L_AB	S20L_AB	S22L_AB	S23L_AB	S24L_AB
<i>Ti-alpha</i>	97.90	98.01	96.53	98.92	96.18	98.54
<i>Ti-beta</i>	2.10	1.99	3.47	1.08	3.82	1.46

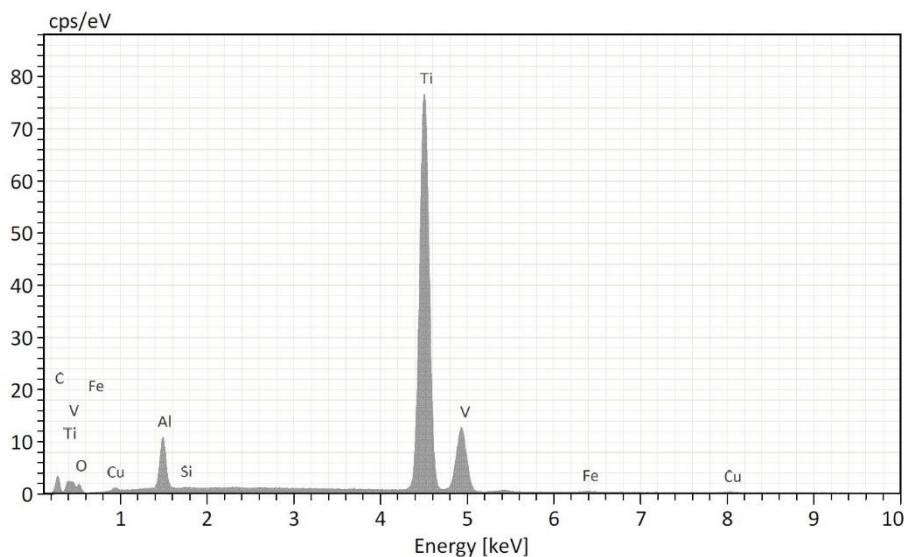
Table 7.6 Phase composition and thickness of surface layer according to MAUD analysis (in wt%).

Phase	S08L_AB	S10L_AB	S20L_AB	S22L_AB	S23L_AB	S24L_AB
<i>Thickness (nm)</i>	40.1	35.0	58.0	27.0	9.5	6.0
<i>Ti-alpha</i>	1,8	-	-	1,2	-	0,7
<i>Ti-beta</i>	0,3	1,6	1,9	-	3,4	1,3
<i>TiO₂</i>	97,9	98,4	98,1	98,8	96,6	98,0

Table 7.4 shows the elemental concentration resulting from combined analysis, while Table 7.5 shows the phase distribution in the bulk of the sample, and Table 7.6 the phase composition and the thicknesses estimated by the combined analysis for the surface layer.

7.5.2 SEM-EDXS

In order to have a qualitative check of the surface situation of the samples, we have executed some SEM-EDXS analysis.

**Figure 7.18** SEM-EDXS spectrum for sample S08L_AB.

All sample screenings confirm the data obtained by XRF, with the same elements, except for the oxygen of the surficial oxides, which is not detectable in air by XRF but is appreciable as Ti-oxide phase by XRD. In Figure 7.18 and Figure 7.19 are shown the spectra for samples S08L_AB and S23L_AB, respectively.

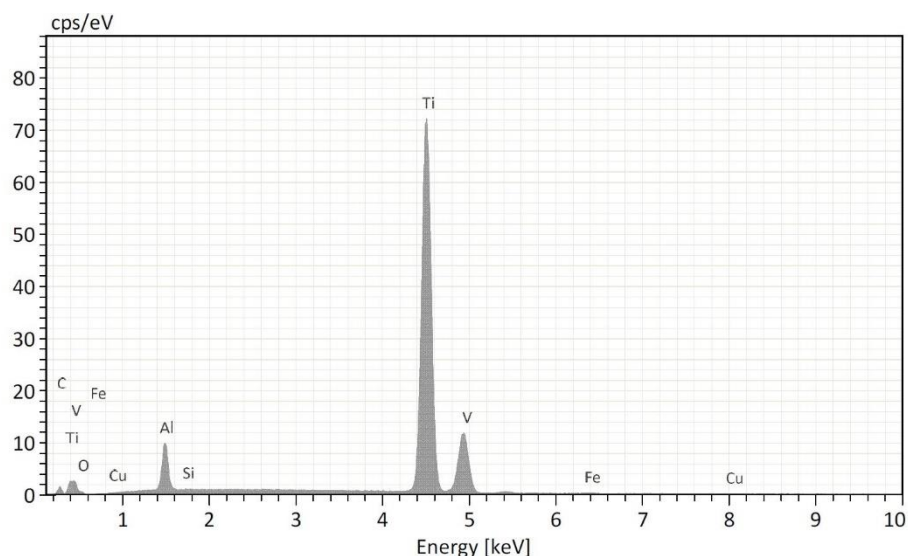


Figure 7.19 SEM-EDXS spectrum for sample S23L_AB.

7.6 Result discussion

The elemental concentration resulting from combined analysis Table 7.4 confirms that for all the samples, the investigated areas report Al e V content inside the specification ranges reported in the Table 7.2. This is also true for the iron content, while the chromium content is negligible, and it will not be considered in the present analysis.

The presence of copper is, on the contrary, unexpected: a more important aspect is that its presence is detected only inside four samples (S08L_AB, S10L_AB, S20L_AB and S22L_AB), while is absent in the other two samples (S23L_AB and S24L_AB). This presence can be considered a surficial contamination due to the cutting process by Electrical Discharge Machining (EDM) [55,161].

The last element we consider here is silicon. It is a β stabilizer and its presence varies among the samples. In order to understand its contribution, we need to consider now the data coming from XRD.

Table 7.5 shows the phase distribution obtained from combined analysis. Taking care of the fact we have a low penetration depth of the radiation used in the XRD setups (about 1 micron attenuation length for Co-K α , 5 degrees incidence angle and assuming a pure Ti matrix), and with all the precision limit of fitted data, we can in any case ascertain a correlation between the presence of silicon and iron (which is also a β stabilizer) inside sample and the β phase content as obtained by the XRD.

To simplify understanding, we diagram the data of all β stabilizers (including vanadium) against β phase content. As we can see (see Table 7.4, Table 7.5 and Figure 7.20), the combined presence of iron and silicon increase as soon as increases the content of β phase inside the samples.

S08L_AB and S10L_AB samples are comparable, both having about 2% of β phase; also, S22L_AB and S24L_AB are comparable respect to silicon and iron content and the content of β phase.

In all samples, vanadium content does not appear to influence particularly the β -phase content, as we can graphically appreciate from Figure 7.20. This is not the case of silicon: we can observe that with the silicon content increase, the β phase increase consequently in content inside samples.

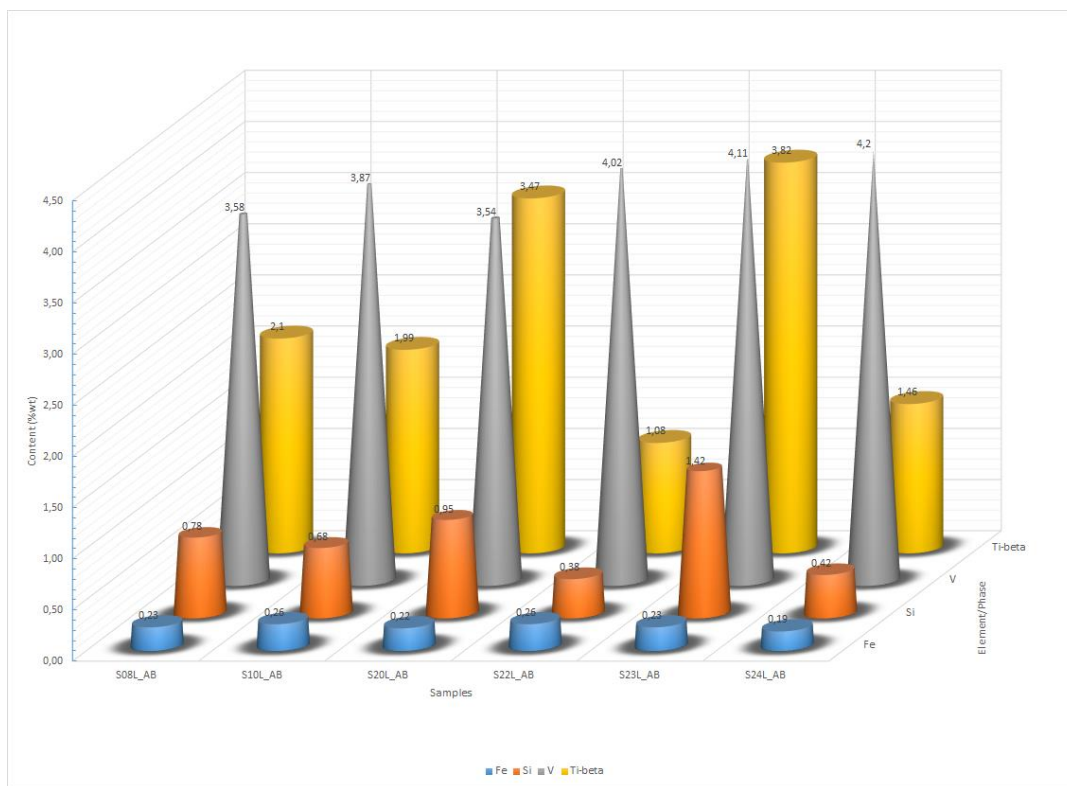


Figure 7.20 Content of β stabilizers against Ti β phase content.

However, the content of silicon is not the only factor to be taken in count. If we consider S22L_AB and S24L_AB samples, we can observe that they have about the same content of silicon and iron, just a bit more of vanadium but the S24L_AB have a Ti- β content about 40% more than S22L_AB. Because S10L_AB has about the same content of vanadium of S22L_AB but double content of Ti- β , this means that another concurrent production factor must be considered.

Remembering the Eq. 7.1 and the production data reported in Table 7.3, we can construct the graph of Figure 7.21.

As we can see now, despite about the same content of β stabilizers, the effect of higher density of energy have some impact on Ti- β content: this is true considering the couple S22L_AB and S24L_AB, and the couple S20L_AB and S22L_AB.

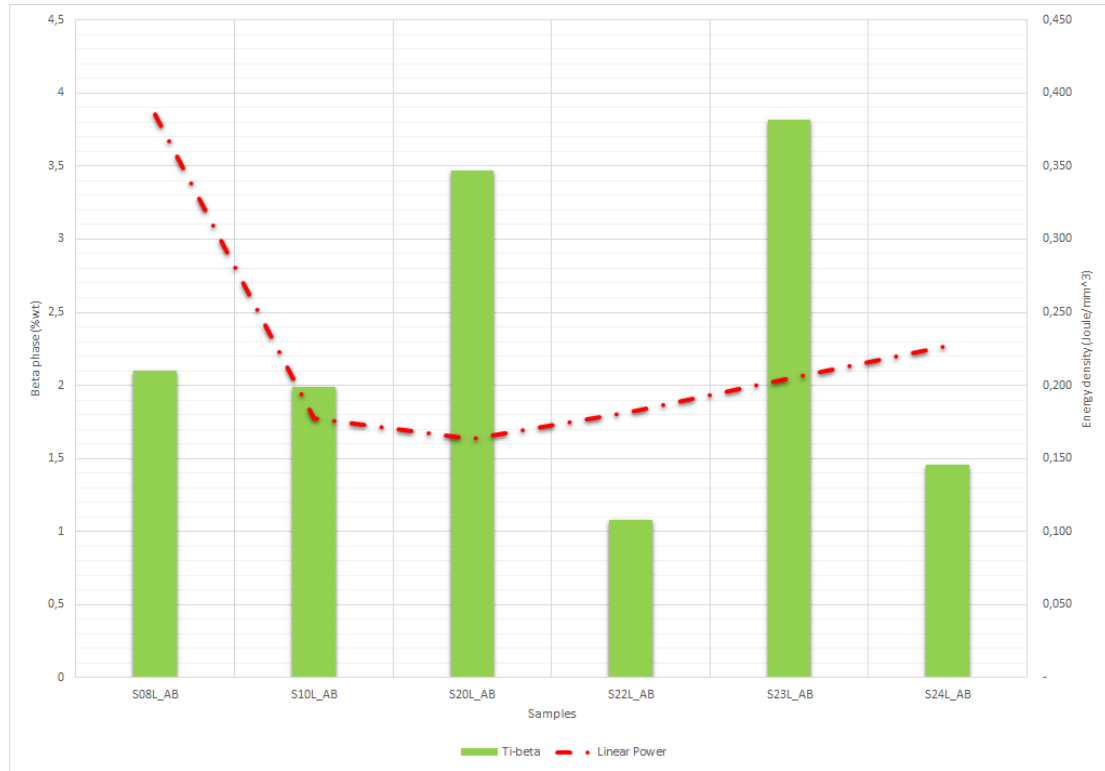


Figure 7.21 Analysis of SLM energy density and β -phase content.

This is consistent with the fact that higher energy allows a higher localized temperature in SLM process and the equilibrium fraction of β phase rises at high temperatures [181], which then leads to a higher fraction of $\alpha + \beta$ phases at room temperature (remember here that the cooling rate was the same for all samples).

The effect, in any case, has not the same impact as the presence of silicon: for the couple S08L_AB and S10L_AB, the higher energy density does not seem to affect so much compensating the lower content of β stabilizers in S08L_AB sample respect to S10L_AB sample. Thus, the S08L_AB has only a slightly higher content of β phase.

We can resume these observations in Figure 7.22. Here, the sum(Fe,Si,V) histogram bar includes all the contribution of β stabilizers. From the confrontation with the bar of silicon, the graph confirms that vanadium does not play a relevant role as silicon itself, whose contribution is on the contrary evident in increasing the β phase.

These aspects are relevant for the production of components: usually TiAl6V4 are not used without treatments (as built), because they are unable to achieve the high material performance of equivalent wrought counterparts [67,185].

In this case, we have investigated only the surface of sample, assuming their homogeneity. A critical factor, from this point of view, is certainly the quality of the powder particle shapes, which influences sample homogeneity and porosity [86,87]; in present study they are unknown from factory and cannot be inferred by XRF or XRD.

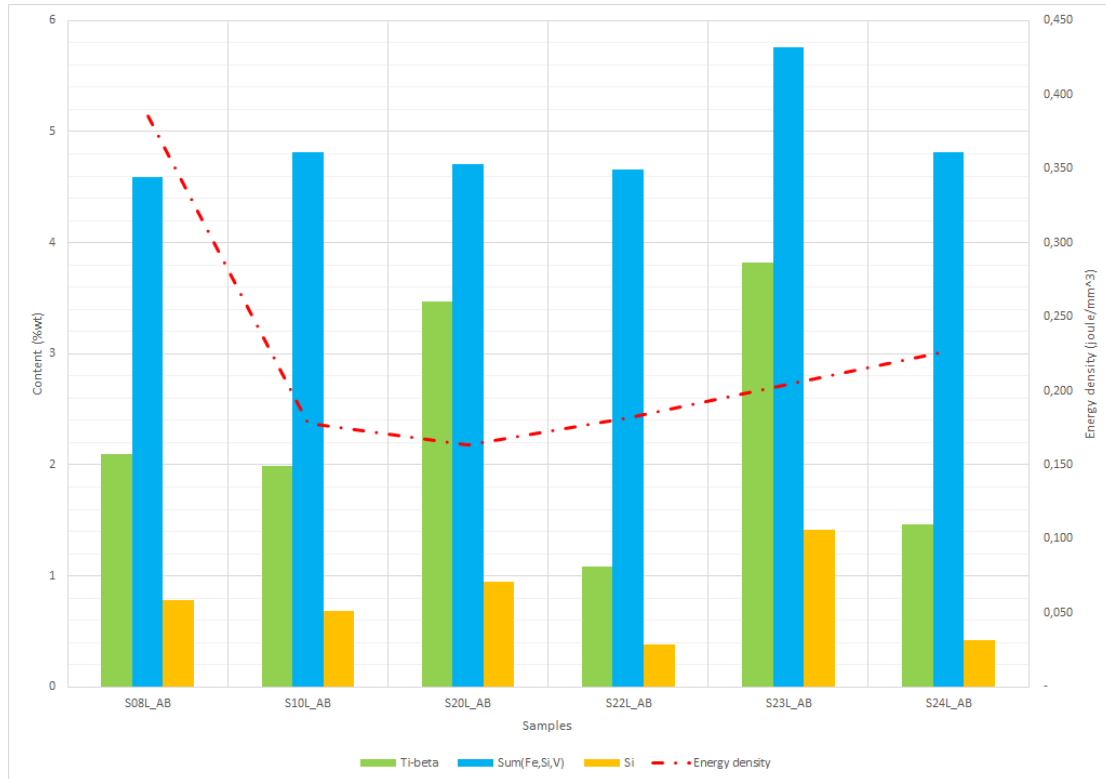


Figure 7.22 Resume diagram of main production parameters.

The combined XRF/XRD approach, however, gives the opportunity to investigate the behaviour of single elements inside the alloy respect to alloy phase compositions. Again, we have limited to surface, but nothing forbids to go deeper inside the sample with an accurate sample cutting (in order to avoid contamination and thermal alteration) and sectioning along sample thickness.

The combined technique, intensively applied, allow to predict phase distribution according to precise production parameters.

In this context, as we have seen, also power and speed of laser are involved, taking care of the fact the short interaction times and highly localized heat input provoke large thermal gradients during SLM process which lead to the formation of inner defects (unmolten particles, entrapped gas bubbles, etc.) [87,126] which can be critical in fatigue conditions [20,66]. This has influence on quality and mechanical properties of titanium alloy fabricated using SLM technology [170,184], because we can have some critical problems (residual stresses, segregation phenomena, etc.) [95,169,181].

8 CONCLUSION AND FUTURE PERSPECTIVES

X-ray diffraction (XRD) and fluorescence (XRF) techniques are useful non-destructive analytical techniques, with application not only in industrial field and mining, but also in environmental control and cultural heritage monitoring and conservation.

In the present research, we have considered the advantages of a combined approach with XRF and XRD techniques, due to their complementarity, and we have presented a new method of combining data, executing the simultaneous computation of the refinement both for XRF and XRD. In this case, instead of the common approach with an iterative refinement, passing from XRF to XRD and vice versa, both XRF and XRD data are processed simultaneously with a combined Rietveld refinement.

This innovative approach has been implemented in the program MAUD, combining original XRD algorithm with the XRF module implementation from the GIMPy application and some other easy external wizards (in Eagle-X container) for preliminary XRF analysis and model set-up.

We have presented the application of this new approach to two case studies, the first one regarding the cultural heritage field with the analysis of ancient Venetian coins, the second one regarding an industrial application concerning a sintered titanium alloy with different production parameters.

As we have seen, the application of technique is very productive from informational point of view, if a good layer-model is adopted, taking care of chemistry and known physical factors. Moreover, the multilayer model, being nearer to real phase distribution inside the sample, allows a better fitting of data, with a consistent improvement of the quality of the refinement, considering that both XRF and XRD refinement are contemporarily executed.

A critical aspect for a successful application of the technique is the sample. No preparation is virtually needed for analysis, but of course this is immediately true for industrial components as soon as they are produced, but it is not so true for archaeological artefacts, where the condition of production, history and store conditions are unknown.

Corrosion patinas can alter the read of the data, and some care must be taken for analysis, not only because the patinas may not be homogenous among samples, as we have seen for the *sesini*, but also because the same layer cannot be homogeneous, although the model can suppose it.

Another important aspect to be considered is that the patinas can reflect or increase the preferential orientation in the sample, with undesired texture effects on surface of the sample.

The cleaning of the artefacts is not always possible or desired by the owners, so this can complicate the approach to combined analysis, regarding the model to be adopted in material simulation for data interpretation.

In any case, the combined analysis remains a valid approach provided that we are aware of the limits in terms of depth of analysis, linked to the analysis tool (X-ray beam, detector, etc...) and to the surface conditions of the sample.

As future perspective, the introduction of a standard approach for taking care of the texture effects on samples can greatly improve the quality of the refinement, allowing a better approach also to complicate situations like that experimented on the coins.

Another aspect is the improvement of usability of the software, a “must” which can greatly improve diffusion and quality of XRF-XRD combined analysis.

In this sense, the integration of the GUI plugins of Eagle-X, which contain the engine of GIMPy translated from Python to Java language, into the MAUD software can give the not-specialized user a valid way to approach a complex and powerful software like MAUD, which was at the beginning born for XRD-only analysis, but in the meantime has evolved to integrate the XRF inside, according to the combined approach.

From the algorithm point of view, MAUD with his power has achieved the initially set purpose, as demonstrated in the present research.

However, the usability of the software remains a necessary and unavoidable requirement for a better diffusion of this software tool with the combined analysis not only in the scientific, but also in the archaeological and / or industrial field, where not-specialized users are commons.

A. APPENDIX – SDD DETECTOR BY KETEK

In FBK there is a machine called Phoenix with combined XRF/XRD technology installed (Figure A.1).

This machine is equipped with a boxed Silicon Drift Detector (SDD) with Peltier cooling, for XRF – EDX – TXRF Applications, and a controlling software on Windows PC developed in C++ internally at FBK.

The detector is an AXAS-D model produced by Ketek (Figure A.2). All information and images, where not explicitly specified, are retrieved from the official Ketek documentation (as available on the website published at www.ketek.net).

The short facts for these models of detector produced by Ketek are:

- Digital system completed with VITUS SDD, reset type preamplifier and Digital Pulse Processor (DPP);
- Detector size 65 mm² collimated to 50 mm², with 1024 channels;
- energy resolution down to 123eV FWHM at Mn-K α ;
- Filtering for SDD operating voltages;
- SDD operating temperature readout;
- Highly integrated design: aluminium housings plated with Nickel. All screws are stainless steel;
- operable at an ambient temperature of up to +80°C;
- high count rate capability up to 1,000kcps;
- efficient integrated Peltier element;
- no liquid nitrogen cooling required;
- radiation hardness during more than 10 years standard count rate exposure;
- peaking times adjustable via Graphic User Interface (GUI) from 1.32 μ s to 13.3 μ s.



Figure A.1 Phoenix machine in FBK



Figure A.2 View of the Ketek detector

a) SDD box geometry

In Figure A.3 is shown the front and the back of AXAS-D model of FBK, with the 100mm finger on top of which is installed the VITUS SDD detector. In Figure A.4 is detailed the geometry of the casing.



AXAS-D front with a 100mm finger



AXAS-D back with preamplifier output and USB port

Figure A.3 Front and back of the detector casing

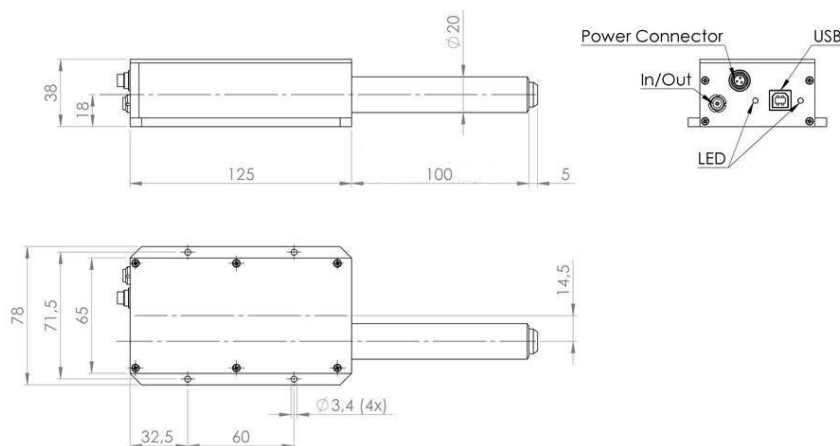


Figure A.4 Geometry of the casing

b) SDD geometry

KETEK's VITUS Silicon Drift Detectors (SDD) are the state-of-the-art X-ray detectors based on a silicon substrate. Their typical X-ray energy range is between 0.2 keV and 30 keV. They are used in applications such as EDX, EDS, XRF, TXRF.

Due to their wide operating temperature range, they are especially employed for industrial and automotive applications. In Figure A.5 we can see the SDD detector with and without the housing (called "TO8 housing").

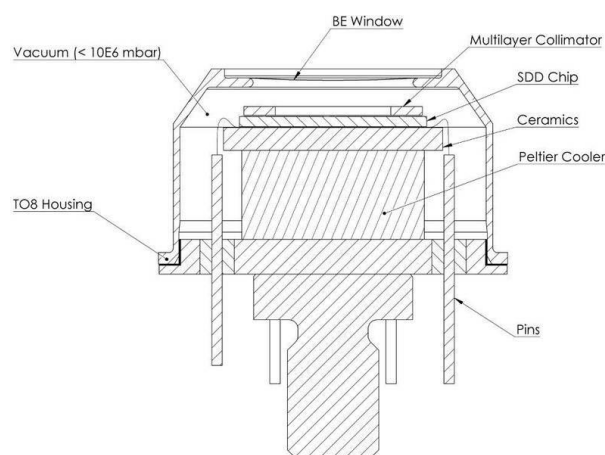
a) VITUS H50 in TO8 housing with 12.5 μm Be window

b) Open VITUS H50 with on-chip multilayer collimator

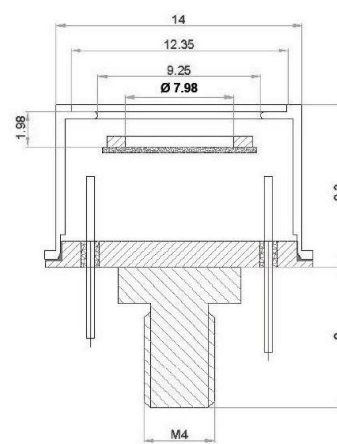
Figure A.5 SDD detector with (a) and without (b) the housing.

In Figure A.6 we can see the schemes of SDD construction with ceramic SDD chip carrier, Peltier cooling element and a multilayer collimator, integrated into a standard TO8 housing.

All VITUS detectors have an on-chip collimator which offers a minimum vertical distance to the radiation entrance plane and therefore a large solid angle. The absorption depth is 450 μm , the maximum input count rate is 1000 kcps (kilocount per seconds).



Cross section



b) VITUS H50 Detector Geometry

Figure A.6 Cross section and geometry of Vitus SDD detector model

c) Operation requirements

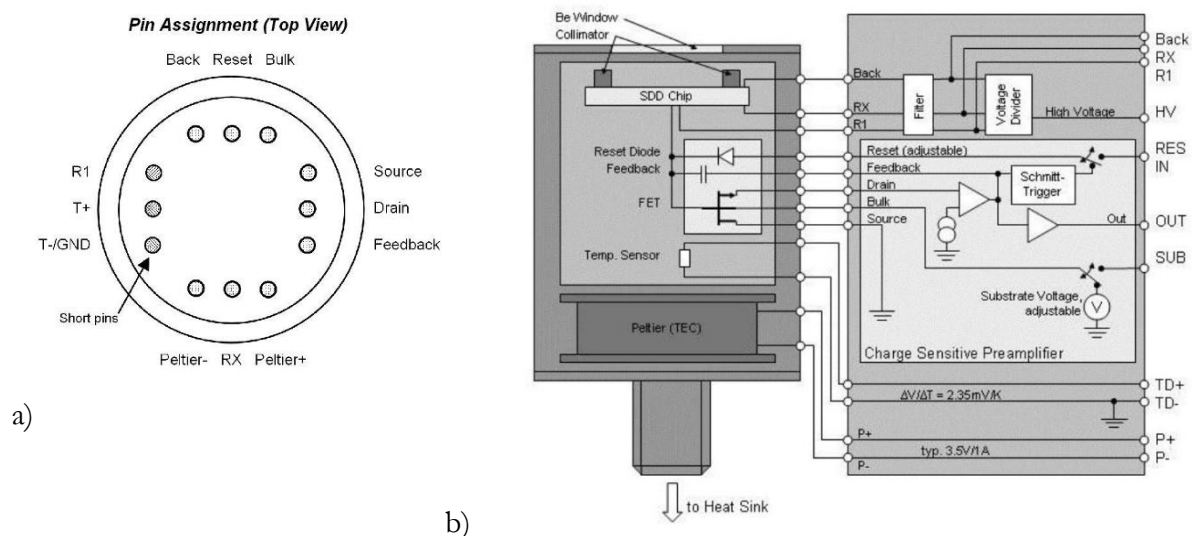


Figure A.7 a) Pin assignment of VITUS SDD, and b) VITUS Operation Block Diagram

Detector operating voltages are RC low-pass filtered and linearly regulated by KETEK electronics. KETEK model has moreover reset type charge sensitive pre-amplifier with internally triggered reset pulses, and short wiring length between detector and pre-amplifier (Figure A.7).

Table A.1 VITUS SDD operation requirements

SDD Voltages and Currents		
Ring1 (R1)	-20 V \pm 5 V	10 μ A typ.
RingX (RX)	-130 V \pm 20 V	10 μ A typ.
Back	-60 V \pm 5 V	<1 nA
Included FET		
Drain	3 V \pm 0.5 V	3 mA
Source	0 V	
Bulk	-5 V \pm 3 V	
Reset	1 V	1 μ s
Feedback	ramped output	
Peltier Element	3.6 V	700 mA max
Temperature Monitor	NTC thermistor	10 k Ω @ 25 $^{\circ}$ C

The operation block diagram of Figure A.7 is shown in more detail in Figure A.8. The diagram shows the principle of operation of the AXAS-D. It consists of a low voltage power supply for 3.3 and 1.2V, a thermoelectric cooler controller for the SDD Peltier, a high voltage (180 V DC) power supply, a sensor parameters control and measurement unit, the preamplifier and the Digital Pulse Processor (DPP) itself. It provides an overvoltage and polarity reversal protection.

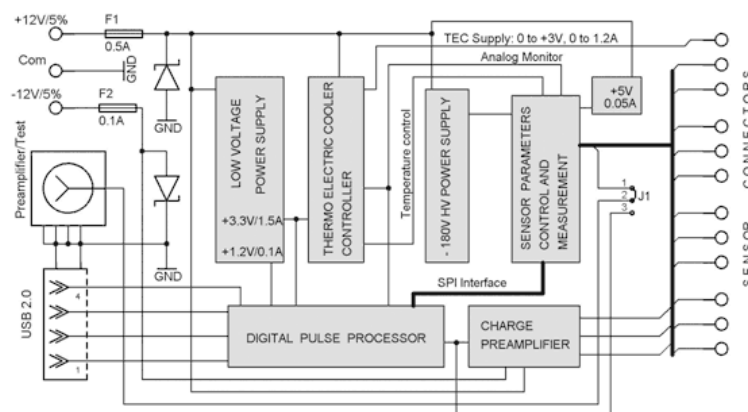


Figure A.8 Operation block diagram of VITUS SDD

The Block Diagram of shows the principle of operation of the Digital Pulse Processor (DPP). The main clock frequency is 25 MHz, using a 12bit ADC at 40 MSPS. It has both an analogue gain before digitizing and a digital gain right after the digital filtering, which consists of digital shaping a digital Baseline Restoration (BLR), a Peak Detection and a digital Pile-Up Rejector (PUR). Also, the SDD operating parameters can be set and read by an additional ADC in combination with an SPI Interface. The DPP is FPGA based and uses USB 2.0 Interface.

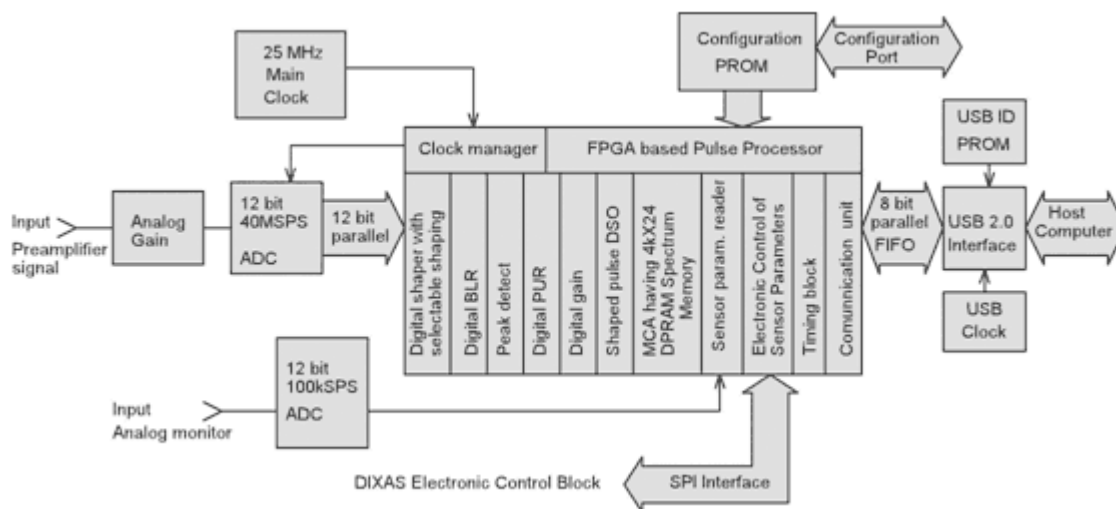


Figure A.9 Block diagram of the Digital Pulse Processor (DPP)

d) AXAS-D Detector behaviour

The diagram in Figure A.11 provides the throughput behaviour of the AXAS-D according to specification. It shows the dependency of the output count rate with the input count rate for different digital peaking times.

The lower is the peaking time, the higher is the maximum throughput for a system.

The energy resolution of the digital system is mostly independent of the input count rate, as we can see in Figure A.10.

The graph shows the dependency of the Full Width at half maximum with the incoming photons (input count rate) for different digital peaking times.

The graph of Figure A.12 shows the independence of the peak position of the Mn-K α line with the input count rate for different digital peaking times.

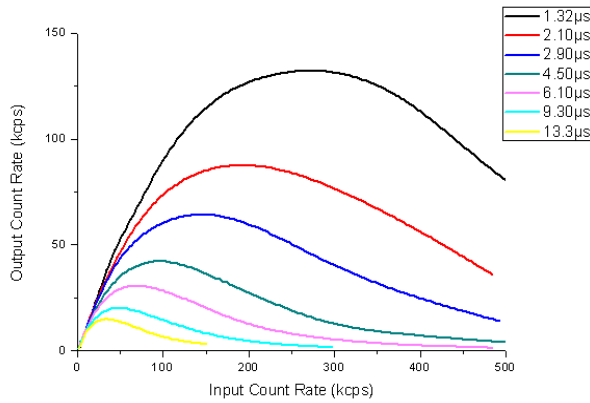


Figure A.11 Throughput behaviour

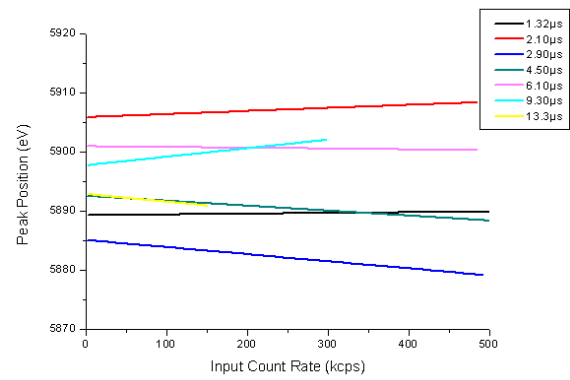


Figure A.12 Peak position of Mn-K α

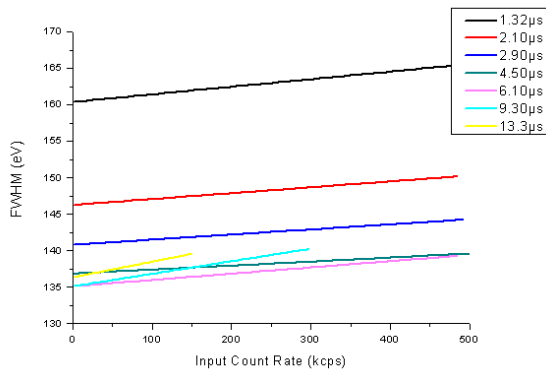


Figure A.10 Energy resolution with input count rate

B.MACHINE CALIBRATION REFERENCES

For the calibration of XRF machine used for the analysis of the sample in this research has been used some certified references. In this Appendix the type of sample used and their certified content has been reported.

BCR 090 titanium with added impurities

This sample (Figure B.1) is prepared by the Institute for Reference Materials and Measurements (IRMM) and certified by BCR (Community Bureau of Reference, the former reference materials program of the European Commission). In **Table B.1** elements are reported as mass fraction.

Table B.1 Titanium sample: list of added impurities.

Element	Mass fraction	
	Certified value (g/kg)	Uncertainty (g/kg)
B	0.0282	0.0014
Co	0.501	0.014
Cr	0.533	0.011
Cu	0.513	0.009
Fe	0.563	0.016
Mn	0.314	0.010
Mo	0.488	0.011
Ni	0.667	0.007



Figure B.1 BCR 090 sample.

NIST 612 Glass with trace elements

This glass sample is prepared by the National Institute of Standards & Technology (NIST) and certified values for 15 elements of SRM 612 are reported in Table 1 as mass fractions.

Table B.2 List of elements inside NIST 612

Constituent	Mass Fraction (mg/kg)
Antimony	34.9 ± 2.2
Arsenic	37.4 ± 2.2
Barium	38.6 ± 2.6
Cadmium	29.9 ± 4.2
Chromium	35.0 ± 3.3
Iron	51 ± 2
Lead	38.57 ± 0.2
Manganese	37.7 ± 3.8
Nickel	38.8 ± 0.2
Rubidium	31.4 ± 0.4
Selenium	16.1 ± 1.6
Silver	22.0 ± 0.3
Strontium	78.4 ± 0.2
Thorium	37.79 ± 0.08
Uranium	37.38 ± 0.08

**Figure B.2** NIST 612 sample

RAuP7 Gold reference material

This reference material is produced by Rand Refinery in South Africa and distributed by Simar Analytical Srl (www.simarsrl.com) under the code RAuP7.

The disk was prepared by melting high purity gold granules and required elements, casted in a graphite mould and machined to yield a surface suitable for optical emission. In Table B.3 are reported the contents in ppm of trace elements.

**Figure B.3** RAuP7 sample**Table B.3** Concentration values of trace elements (ppm)

	Cu	Pt	Pd	Mn	Zn	Pb	Sb	Bi	Se	Fe	Ag	Cr	Ti
RAuP7	185.1	176.4	178.8	143.4	199	202.9	258.2	197.7	173	177.3	212.7	137	128.6
sd*2	5	4	2	4	4	9	9	7	3	9	1	2	1

Mixture Al₂O₃-TiO₂

Three reference mixture of Al₂O₃-TiO₂ from certified powders have been prepared to simulate a composition with different concentration of Al.

<i>Sample no.</i>	Table B.4 Content of powders in mixture				
	<i>Al₂O₃</i>	<i>wt %</i>	<i>TiO₂</i>	<i>wt %</i>	<i>wt tot</i>
1	0,1264	0,12	0,9422	0,88	1,0686
2	0,5619	0,52	0,5268	0,48	1,0887
3	0,9070	0,90	0,0999	0,10	1,0069

Every sample has undergone XRF scanning on the TNX Phoenix combined spectrometer, in order to get spectrum and calibrate response on MAUD software. The spectra and relative fitting of sample 1, 2 and 3 are reported, respectively, in Figure B.4, Figure B.5.

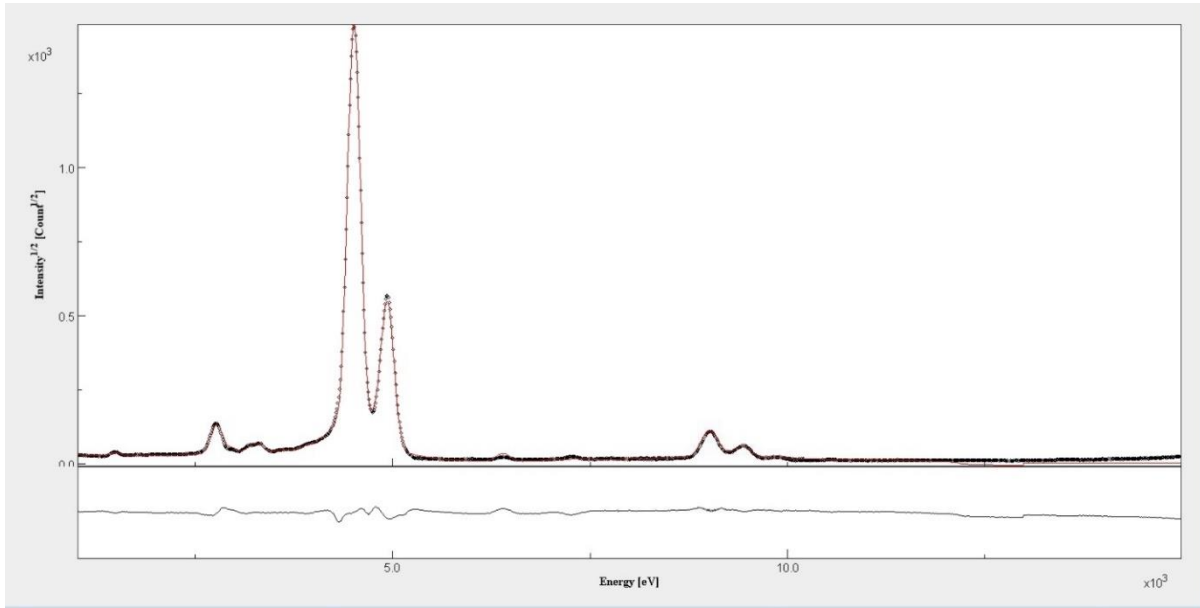


Figure B.4 Spectrum and calibration fitting for Sample 1

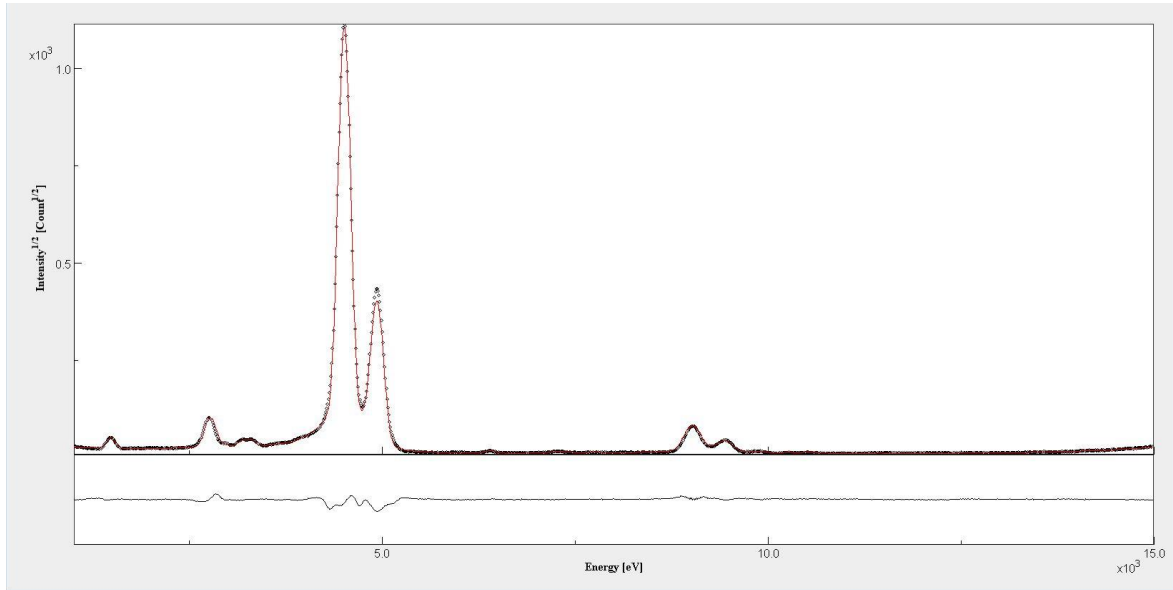


Figure B.5 Spectrum and calibration fitting for Sample 2

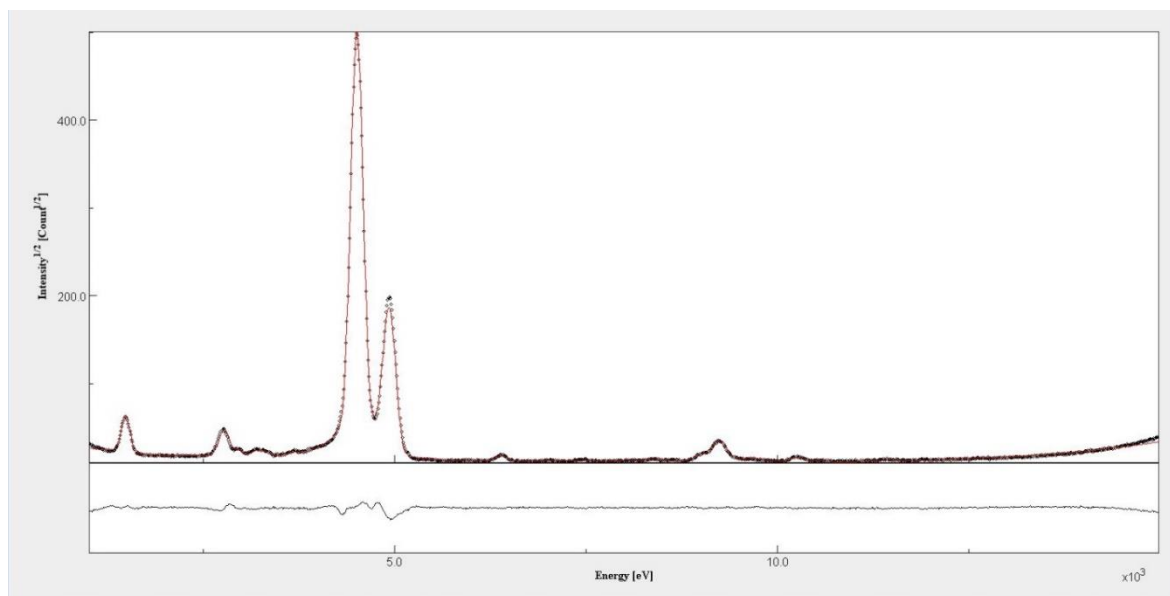


Figure B.6 Spectrum and calibration fitting for Sample 3

INDEXES AND BIBLIOGRAPHY

Index of figures

FIGURE 2.1 THE THREE MAIN INTERACTIONS OF X-RAYS WITH MATTER [18].	17
FIGURE 2.2 MATRIX ABSORPTION EFFECT [18]	19
FIGURE 2.3 CALCULATION OF THE INTENSITY CHARACTERISTIC RADIATION FROM A HOMOGENEOUS SAMPLE.	19
FIGURE 2.4 MATRIX ENHANCEMENTS EFFECT [18]	24
FIGURE 2.5 SCHEMATIC STRUCTURE OF A REVERSELY BIASED SEMICONDUCTOR DIODE USED AS A PHOTON DETECTOR [112]	26
FIGURE 2.6 SEMICONDUCTOR DRIFT CHAMBER STRUCTURE USING THE SIDEWARD DEPLETION METHOD [112].	26
FIGURE 2.7 CYLINDRICAL SILICON DRIFT CHAMBER WITH AN INTEGRATED AMPLIFIER FOR SPECTROSCOPIC APPLICATIONS [112].	27
FIGURE 2.8 SINGLE-SIDED STRUCTURED SDD WITH INTEGRATED TRANSISTOR, COOLED BY A PELTIER ELEMENT [112].	27
FIGURE 2.9 PHYSICAL PROCESSES IN A SEMICONDUCTOR DETECTOR [151]	28
FIGURE 3.1 ATOMIC SCATTERING FACTORS OF AL, FE, AND AG	33
FIGURE 3.2 POWDER XRD MEASUREMENTS [72]	34
FIGURE 3.3 DIFFRACTION SPECTRUM OF A FOUR-PHASE STRUCTURE ANALYSED WITH RIETVELD METHOD IN <i>MAUD</i> SOFTWARE.	37
FIGURE 3.4 THE EFFECT OF ATOMIC THERMAL MOTION ON THE COPPER SCATTERING FACTOR [83].	41
FIGURE 3.5 DEMONSTRATION OF BRAGG'S LAW [18]	41
FIGURE 3.6 STRAIN EXPANDING AND CONTRACTING D-VALUES [83].	43
FIGURE 4.1 COMMON COMBINED XRF-XRD APPROACH.	48
FIGURE 4.2 INEL EQUINOX 3500 θ - θ DIFFRACTOMETER WITH TWO DETECTORS (XRF AND XRD), A FIXED SAMPLE HOLDER AND A MO X-RAY TUBE [107].	48
FIGURE 4.3 COMBINED APPROACH WITH XRF-XRD SIMULTANEOUS REFINEMENT.	49
FIGURE 4.4 MULTILAYER MODEL.	50
FIGURE 4.5 DIFFERENCES BETWEEN A) SINGLE CRYSTAL, B) POLYCRYSTALLINE, AND C) AMORPHOUS [168].	50
FIGURE 4.6 RIGHT-HAND RULE [166]	51
FIGURE 4.7 EXAMPLE OF UNIT CELL	51
FIGURE 4.8 A TRIGONAL UNIT CELL WITH THE UNIT VECTORS A , B , C , AND FOUR ATOMS AT DIFFERENT POSITIONS U_k (LEFT) AND AN ASSEMBLY OF SOME UNIT CELLS FORMING A SMALL CRYSTAL (RIGHT) [155].	51
FIGURE 4.9 ELEMENT IN A) SUBSTITUTIONAL POSITION, B) INTERSTITIAL POSITION [SOURCE: WIKIPEDIA].	52
FIGURE 4.10 EXAMPLE OF INTERSTITIAL ELEMENT IN FCC LATTICE [SOURCE: WIKIPEDIA].	52
FIGURE 4.11 POLE FIGURES DISPLAYING CRYSTALLOGRAPHIC TEXTURE OF GAMMA-TIAL IN AN ALPHA2-GAMMA ALLOY, CALCULATED USING <i>MAUD</i> SOFTWARE.	53
FIGURE 4.12 STRAIN EXPANDING AND CONTRACTING D-VALUES [83].	54
FIGURE 4.13 EXAMPLE OF MULTILAYER SAMPLE MODEL [74].	54
FIGURE 4.14 <i>MAUD</i> PHASE LIST.	55
FIGURE 4.15 EXAMPLES OF A) Cu_2O AND B) TiO_2 PHASE DEFINITION IN <i>MAUD</i> .	55
FIGURE 4.16 ATOM CONTENT AND PARAMETERS FOR Cu_2O PHASE IN <i>MAUD</i> .	56
FIGURE 4.17 DEFINITION OF MIXTURE PHASE $\text{Ag}_{0.88}\text{Cu}_{0.12}$ WITH MULTIPLE IMPURITIES IN <i>MAUD</i> .	56
FIGURE 4.18 <i>MAUD</i> LAYER STRUCTURE WIZARD.	57

FIGURE 4.19 MAUD SAMPLE LIST. _____	57
FIGURE 4.20 MAUD WIZARD PAGE FOR SPECTRUM WEIGHT DEFINITION. _____	57
FIGURE 5.1 THE GUI OF ECLIPSE IDE FOR JAVA DEVELOPERS. _____	61
FIGURE 5.2 THE SPLASH SCREEN OF EAGLE-X _____	64
FIGURE 5.3 EAGLE-X: APPLICATION SCHEMA OF LAYERED INNER STRUCTURE. _____	64
FIGURE 5.4 EXAMPLE OF EAGLE-X APPLICATION WITH XRF SPECTRUM VIEWER IN AN MDI FORM. _____	65
FIGURE 5.5 EAGLE-X MAIN DESKTOP. _____	66
FIGURE 5.6 PERIODIC TABLE OF ELEMENTS. _____	66
FIGURE 5.7 FBK SQLITE VIEWER WITH SOME FORMS ABOUT TABLES IN FBK XRAYDATA DATABASE FROM GIMPY. _____	67
FIGURE 5.8 ELEMENT FORM WITH DETAILED DATA ABOUT (A) ELEMENT (B) SHELLS, (C) TRANSITIONS, (D) CHARACTERISTIC LINES. ____	68
FIGURE 5.9 ED-XRF SPECTRUM VIEWER EXAMPLE WITH THE SPECTRUM OF NIST REFERENCE SAMPLE. _____	69
FIGURE 5.10 ED-XRF COMMON TOOLBAR. _____	69
FIGURE 5.11 SAVE CHART OPTION WIZARD _____	70
FIGURE 5.12 THE SPECTRUM OF S15 (DOGE VENIER) SAMPLE IN (A) FULL VIEW, (B) ZOOMED VIEW. _____	71
FIGURE 5.13 CHART PARAMETER MANAGER. _____	71
FIGURE 5.14 ELEMENT SHEET OF CALIBRATION WIZARD _____	72
FIGURE 5.15 LINES SHEET OF CALIBRATION WIZARD _____	72
FIGURE 5.16 LINES SHEET OF CALIBRATION WIZARD WITH “RELATIVE” LINE OPTION. _____	73
FIGURE 5.17 EXAMPLE OF UNFILTERED (A) AND FILTERED SPECTRUM DATA FOR BEST VIEWING OF PEAKS. _____	73
FIGURE 5.18 THRESHOLD OPTIONS _____	74
FIGURE 5.19 PEAKS SHEET OF CALIBRATION WIZARD WITH LIST OF POSSIBLE PEAKS. _____	75
FIGURE 5.20 (A) PEAK ASSIGNMENT FOR CU; (B) PEAK ASSIGNMENT FOR PB; (C) PEAKS SHEET WITH ASSIGNED PEAKS MARKED BY PINS. _____	76
FIGURE 5.21 CALIBRATION CONFIRMATION. _____	76
FIGURE 5.22 CALIBRATION SHEET VALUE (A) AFTER CALIBRATION; (B) RESTORED FROM LAST SAVE. _____	76
FIGURE 5.23 ELEMENT SHEET OF ELEMENT PICKING WIZARD _____	77
FIGURE 5.24 ELEMENT LIST SHEET _____	78
FIGURE 5.25 (A) SEARCH SHEET; (B) SEARCH MATCH COMPLETED. _____	78
FIGURE 5.26 ELEMENT LIST SHEET OF WIZARD WITH THE FOUND ELEMENTS, WITH LINES, AND THE CONTEXT MENU. _____	79
FIGURE 5.27 MAIN FORM OF THE MATERIAL LIST MANAGER _____	80
FIGURE 5.28 MATERIAL EDITOR WIZARD. _____	80
FIGURE 5.29 MATERIAL COMPONENT EDITOR. _____	81
FIGURE 5.30 MATERIAL LIST WIZARD. _____	81
FIGURE 5.31 ED DETECTOR DIALOG FORM FOR MANAGING DETECTOR CONFIGURATION: A) MATERIALS; B) CALIBRATION; C) PEAK SHAPE. _____	82
FIGURE 5.32 X-RAY BEAM SOURCE DIALOG FORM FOR MANAGING BEAM CONFIGURATION: A) PARAMETERS; B) ENERGY PROFILE. ____	83
FIGURE 5.33 X-RAY BEAM SOURCE DIALOG FORM FOR MANAGING BEAM CONFIGURATION: A) PARAMETERS; B) ENERGY PROFILE. ____	83
FIGURE 5.34 E.10 EXPERIMENTAL SET-UP MANAGER WITH (A) GENERAL PARAMETERS, (B) COLLIMATOR PARAMETERS _____	84

FIGURE 5.35 DEFINING THE PROJECT FOLDER AND NAME. _____	85
FIGURE 5.36 THE EAGLE-X ASPECT AFTER CREATION OF A NEW LASAX SIMULATION PROJECT: THE PROJECT FOLDER IN THE PROJECT NAVIGATION PANEL OF EAGLE-X (RED ARROW) AND THE NEW TOOLBAR FOR MANAGING SIMULATION (BLUE ARROW). _____	85
FIGURE 5.37 MENU FOR DEFAULT X MACHINE SPECIFICATIONS. _____	85
FIGURE 5.38 WIZARD PANELS ACCORDING TO SEQUENCE: A) DETECTOR DATA; B) BEAM DATA; C) LAYERED SAMPLE DATA; D) EXPERIMENTAL SET-UP. _____	86
FIGURE 5.39 THE WINDOW WITH THE DATA AND THE CHART OF THE LASAX SIMULATION RESULT. _____	86
FIGURE 5.40 CONFRONTATION BETWEEN SIMULATED REFERENCE AND EXPERIMENTAL SPECTRUM. _____	87
FIGURE 5.41 CONFRONTATION BETWEEN SPECTRA WITH DOCKABLE INTERFACE. _____	87
FIGURE 6.1 EUROPE IN 1556, WITH THE HABSBURG DOMINIONS IN EVIDENCE [SOURCE: WIKIPEDIA]. _____	90
FIGURE 6.2 REPRESENTATION OF THE COINAGE PROCEDURE WITH HAMMER AND INCUS [176] _____	91
FIGURE 6.3 THE <i>SESINO</i> OF DOGE FRANCESCO VENIER (S15), OBVERSE (LEFT) AND REVERSE (RIGHT). _____	93
FIGURE 6.4 THE <i>SESINO</i> OF DOGE PIETRO LOREDAN (S10), OBVERSE (LEFT) AND REVERSE (RIGHT). _____	93
FIGURE 6.5 THE <i>SESINO</i> OF DOGE ALVISE MOCENIGO (S21), OBVERSE (LEFT) AND REVERSE (RIGHT). _____	94
FIGURE 6.6 THE <i>SESINO</i> OF DOGE NICOLÒ DA PONTE (S54), OBVERSE (LEFT) AND REVERSE (RIGHT). _____	94
FIGURE 6.7 THE <i>SESINO</i> OF DOGE MARIANO GRIMANI (S35), OBVERSE (LEFT) AND REVERSE (RIGHT). _____	95
FIGURE 6.8 SEM/EDXS APPLIANCE BY BRUCKER AT UNIVERSITY OF TRENTO, DEP. OF INDUSTRIAL ENGINEERING. _____	96
FIGURE 6.9 TNX PHOENIX COMBINED SPECTROMETER AT FBK, CMM LABORATORIES. _____	96
FIGURE 6.10 EXAMPLE OF XRF SET-UP FOR <i>SESINO</i> OF DOGE PRIULI _____	96
FIGURE 6.11 XRF SPECTRUM OF <i>SESINO</i> S15 OF DOGE VENIER ANALYSED WITH THE ELEMENT PICKER IN THE ED-XRF SPECTRUM VIEWER PLUGIN OF EAGLE-X (SEE PARAGRAPH 5.5). _____	98
FIGURE 6.12 PHASE DIAGRAMS OF CU-AG (LEFT) AND CU-PB (RIGHT) SYSTEMS. _____	98
FIGURE 6.13 RIETVELD FIT RELATIVE TO XRD DATA FOR SAMPLE S15 VENIER. _____	99
FIGURE 6.14 FUNDAMENTAL PARAMETERS FIT RELATIVE TO XRF DATA FOR SAMPLE S15 VENIER. _____	100
FIGURE 6.15 XRD SPECTRUM OF S14 OF DOGE LOREDAN, WITH THE FOUR COMMON PHASES PLUS ACANTHITE AND TENORITE. _____	101
FIGURE 6.16 THREE-LAYER MODEL PROPOSED. _____	102
FIGURE 6.17 THE <i>SESINO</i> OF DOGE PIETRO MOCENIGO (S01), OBVERSE _____	103
FIGURE 6.18 MAUD LAYER STRUCTURE WIZARD _____	104
FIGURE 6.19 ESTIMATED SURFACE LAYER THICKNESSES FOR EVERY “DELLA LAITA’S” COIN. _____	106
FIGURE 6.20 ESTIMATED INTERDIFFUSION LAYER THICKNESSES FOR EVERY “DELLA LAITA’S” COIN. _____	106
FIGURE 6.21 NORMALIZED CU AND AG CONCENTRATIONS (WT.%) IN THE <i>SESINO</i> COINS _____	107
FIGURE 6.22 NORMALIZED PB CONCENTRATION (WT.%) IN THE <i>SESINO</i> COINS _____	107
FIGURE 6.23 SAMPLE SES15 (DOGE VENIER) WITH THE INVESTIGATED AREAS. _____	108
FIGURE 6.24 EDX SPECTRA OF SES15 (DOGE VENIER) SURFACE IN (A) AREA 1; (B) AREA 2; (C) AREA 3; (D) AREA 4 _____	108
FIGURE 6.25 SAMPLE SES42 (DOGE GRIMANI) WITH THE INVESTIGATED AREAS. _____	109
FIGURE 6.26 EDX SPECTRA OF SES42 (DOGE GRIMANI) SURFACE IN (A) AREA 1; (B) AREA 2; (C) AREA 3; (D) AREA 4 _____	109
FIGURE 6.27 THE OBVERSE (LEFT) AND REVERSE (RIGHT) OF THE PRIULI <i>SESINO</i> . _____	111
FIGURE 6.28 THE OBVERSE (LEFT) AND REVERSE (RIGHT) OF THE GRIMANI <i>SESINO</i> . _____	111

FIGURE 6.29 CUT DIRECTION	111
FIGURE 6.30 EXPERIMENTAL XRD PATTERN (BLACK DOTS) ACQUIRED ON THE SURFACE OF THE PRIULI <i>SESINO</i> COINS. THE COLOURED CONTINUOUS LINES ARE THE RESULT OF THE MAUD SOFTWARE MODELLING.	112
FIGURE 6.31 EXPERIMENTAL XRD PATTERN (BLACK DOTS) ACQUIRED ON THE SURFACE OF THE GRIMANI <i>SESINO</i> COINS. THE COLOURED CONTINUOUS LINES ARE THE RESULT OF THE MAUD SOFTWARE MODELLING.	112
FIGURE 6.32 COMPARISON BETWEEN SURFICIAL XRF SPECTRA OF A) PRIULI COIN, OBVERSE, AND B) GRIMANI COIN, OBVERSE.	113
FIGURE 6.33 BACKSCATTERED ELECTRON (BSE) SEM MICROGRAPHS OF THE CROSS SECTIONS OF THE GRIMANI <i>SESINO</i> , OBVERSE SIDE, SHOWING THE MICROSTRUCTURE OF THE OUTER SURFACE LAYER.	114
FIGURE 6.34 SEM MICROGRAPHS OF THE CROSS SECTIONS OF THE GRIMANI <i>SESINO</i> , SHOWING A) THE AREA INVESTIGATED AND B), C) AND D) THE EDXS PEAKS OF THE ELEMENTS.	115
FIGURE 6.35 COMPARISON OF BULK MICROSTRUCTURE BETWEEN PRIULI COIN (LEFT) AND GRIMANI COIN (RIGHT).	116
FIGURE 6.36 EDXS PEAKS OF A RARE SILVER SPOTTED AREA IN GRIMANI <i>SESINO</i>	116
FIGURE 6.37 SEM MICROGRAPHS OF THE CROSS SECTIONS OF THE: A) PRIULI AND B) GRIMANI COINS. THE YELLOW RECTANGULAR AREAS SAMPLED FOR EDXS DATA ACQUISITION ARE SHOWN. THE RED-DOT AREA ENCLOSES THE REGIONS CONSIDERED FOR THE EVALUATION OF THE AVERAGE COMPOSITION OF THE BASE ALLOY OF EACH COIN	117
FIGURE 6.38 (A) CONTENT OF CU AND AG IN <i>SESINO</i> COINS FOR IDEAL COIN WEIGHT; (B) AG CONTENT TREND (EXPANDED)	119
FIGURE 6.39 XRF FITTING SPECTRA (RED) OF COIN S43 OF DOGE MOCENIGO WITH A) BULK MODEL AND B) MULTILAYER MODEL.	122
FIGURE 6.40 XRD FITTING SPECTRA (RED) OF COIN S43 OF DOGE MOCENIGO WITH A) BULK MODEL AND B) MULTILAYER MODEL.	123
FIGURE 6.41 XRD FITTING SPECTRUM (RED) OF COIN S44 OF DOGE MOCENIGO WITH MULTILAYER MODEL AND SOME TEXTURE EFFECTS ON PEAKS OF CUPRITE (GREEN CURVE) WHICH THE MODEL IS NOT ABLE TO FIT.	123
FIGURE 6.42 XRD FITTING SPECTRUM (RED) OF COIN S45 OF DOGE PRIULI WITH MULTILAYER MODEL AND SOME TEXTURE EFFECTS ON THE PEAKS OF CUPRITE (GREEN CURVE) WHICH THE MODEL IS NOT ABLE TO FIT.	124
FIGURE 7.1 TITANIUM TWO ALLOTROPIC FORMS: A) α PHASE, HEXAGONAL CENTERED PACKED; B) β PHASE, BODY CENTERED CUBIC [24].	127
FIGURE 7.2 SCHEMATIC REPRESENTATION OF THE EFFECT OF ALLOY ELEMENTS ON THE STATE DIAGRAM OF TITANIUM ALLOYS IN CASE OF A) α -STABILIZERS ELEMENTS; B) β -STABILIZERS ELEMENTS; C) NEUTRAL ELEMENTS [133].	129
FIGURE 7.3 DIAGRAM PHASE OF Ti-AL SYSTEM [38].	129
FIGURE 7.4 DIAGRAM PHASE OF Ti AND A B-EUTECTOID ELEMENT [103].	130
FIGURE 7.5 TITANIUM ALLOYS MAINLY USED FOR STRUCTURAL COMPONENTS [24].	130
FIGURE 7.6 PHASE DIAGRAM OF TiAl6V4 ALLOY [47].	131
FIGURE 7.7 ONE OF THE SAMPLES INVESTIGATED.	132
FIGURE 7.8 EXAMPLE OF SLM TECHNOLOGY: A) SCHEMATICS OF PROCESS, B) EXAMPLE OF SCANNING STRATEGY [95].	133
FIGURE 7.9 EXAMPLES OF POSSIBLE SLM SCANNING STRATEGIES [SOURCE: HTTP://WWW.ADDMELAB.POLIMI.IT].	133
FIGURE 7.10 ITALSTRUCTURES IPD3000 DIFFRACTOMETER.	135
FIGURE 7.11 ELEMENTS OF S08L_AB SAMPLE INDIVIDUATED THROUGH THE PEAK PICKING PLUGIN OF EAGLE-X.	136
FIGURE 7.12 2-LAYER MODEL	136
FIGURE 7.13 THREE PHASES MODELLING IN MAUD	136
FIGURE 7.14 FUNDAMENTAL PARAMETERS FIT RELATIVE TO XRF DATA FOR SAMPLE S08L_AB.	137

FIGURE 7.15 RIETVELD FIT RELATIVE TO XRD DATA FOR SAMPLE S08L_AB. THE COLOURED CONTINUOUS LINES ARE THE RESULT OF THE MAUD SOFTWARE MODELLING.	137
FIGURE 7.16 FUNDAMENTAL PARAMETERS FIT RELATIVE TO XRF DATA FOR SAMPLE S23L_AB.	138
FIGURE 7.17 RIETVELD FIT RELATIVE TO XRD DATA FOR SAMPLE S23L_AB.	138
FIGURE 7.18 SEM-EDXS SPECTRUM FOR SAMPLE S08L_AB.	139
FIGURE 7.19 SEM-EDXS SPECTRUM FOR SAMPLE S23L_AB.	140
FIGURE 7.20 CONTENT OF β STABILIZERS AGAINST Ti β PHASE CONTENT.	141
FIGURE 7.21 ANALYSIS OF SLM ENERGY DENSITY AND β -PHASE CONTENT.	142
FIGURE 7.22 RESUME DIAGRAM OF MAIN PRODUCTION PARAMETERS.	143
FIGURE A.1 PHOENIX MACHINE IN FBK	146
FIGURE A.2 VIEW OF THE KETEK DETECTOR	146
FIGURE A.3 FRONT AND BACK OF THE DETECTOR CASING	147
FIGURE A.4 GEOMETRY OF THE CASING	147
FIGURE A.5 SDD DETECTOR WITH (A) AND WITHOUT (B) THE HOUSING.	148
FIGURE A.6 CROSS SECTION AND GEOMETRY OF VITUS SDD DETECTOR MODEL	148
FIGURE A.7 A) PIN ASSIGNMENT OF VITUS SDD, AND B) VITUS OPERATION BLOCK DIAGRAM	149
FIGURE A.8 OPERATION BLOCK DIAGRAM OF VITUS SDD	150
FIGURE A.9 BLOCK DIAGRAM OF THE DIGITAL PULSE PROCESSOR (DPP)	150
FIGURE A.10 ENERGY RESOLUTION WITH INPUT COUNT RATE	151
FIGURE A.11 THROUGHPUT BEHAVIOUR	151
FIGURE A.12 PEAK POSITION OF Mn-K α	151
FIGURE B.1 BCR 090 SAMPLE.	152
FIGURE B.2 NIST 612 SAMPLE	153
FIGURE B.3 RAUP7 SAMPLE	153
FIGURE B.4 SPECTRUM AND CALIBRATION FITTING FOR SAMPLE 1	154
FIGURE B.5 SPECTRUM AND CALIBRATION FITTING FOR SAMPLE 2	154
FIGURE B.6 SPECTRUM AND CALIBRATION FITTING FOR SAMPLE 3	155

References

- [1] AA.VV., *Metallurgia e saldabilità del titanio e delle sue leghe*, Istituto Italiano della Saldatura, 2008.
- [2] R. Abbaschian, L. Abbaschian, R.E. Reed-Hill, *Physical Metallurgy Principles*, 4th ed., Cengage Learning, Boston, USA, 2009.
- [3] F.J. Ager, B. Gómez-Tubío, A. Paúl, A. Gómez-Morón, S. Scrivano, I. Ortega-Feliu, M.A. Respaldiza, *Combining XRF and GRT for the analysis of ancient silver coins*, Microchem. J. 126 (2016) 149–154.
- [4] G. Agricola, *De Re Metallica (1530-1556)*, CLUEB, Bologna, I, 2008.
- [5] N.P. Aldobrandini, *Le monete di Venezia - Vol. II - Da Niccolò Tron a Marino Grimani (1472-1605)*, Tipografia Libreria Emiliana, Venezia, I, 1907.
- [6] T. Arai, *The Discovery of X-Rays and Origin of X-Ray Fluorescence Analysis*, in: B. Beckhoff, B. Kanngießer, H. Wolff, N. Langhoff, R. Wedell (Eds.), *Handb. Pract. X-Ray Fluoresc. Anal.*, Springer-Verlag, Heidelberg, D, 2006: pp. 1–32.
- [7] A. Arles, F. Téreygeol, *Le procédé de blanchiment dans les ateliers monétaires français au XV-XVIème siècle : approche archéométrique et expérimentale*, Anu. Estud. Mediev. (2011) 699–721.
- [8] G. Artioli, *Scientific methods and cultural heritage*, Oxford University Press, New York, 2010.
- [9] G. Artioli, *Archaeometallurgy: the contribution of mineralogy*, Archeometry Cult. Herit. Contrib. Mineral. Semin. SEM 09. (2012) 65–78.
- [10] G. Artioli, *Science for the cultural heritage: The contribution of X-ray diffraction*, Rend. Lincei. 24 (2013).
- [11] G. Artioli, B. Baumgarten, M. Marelli, B. Giussani, S. Recchia, P. Nimis, I. Giunti, I. Angelini, P. Omenetto, *Chemical and Isotopic Tracers in Alpine Copper Deposits: Geochemical Links Between Mines and Metal*, Geo.Alp. 5 (2008) 139–148.
- [12] F. Barello, *Archeologia della moneta*, Roma, I, 2012.
- [13] L. Beck, S. Besonnet, S. Réveillon, D. Eliot, F. Pilon, *Silver surface enrichment of silver-copper alloys: A limitation for the analysis of ancient silver coins by surface techniques*, Nucl. Instruments Methods Phys. Res. Sect. B Beam Interact. with Mater. Atoms. 226 (2004) 153–162.
- [14] G. Bonissoni, R. Ricci Bitti, *La diffrattometria dei raggi X per materiali policristallini : aspetti pratici*, Tecniche nuove, Milano, I, 1988.
- [15] F. Borgese, *Gli elementi della tavola periodica. Rinvenimento, proprietà, usi*, CISU, Roma, I, 1993.
- [16] M. Bortolotti, L. Lutterotti, G. Pepponi, *Combining XRD and XRF analysis in one Rietveld-like fitting*, Powder Diffr. (2017) 1–6.
- [17] F. Brigidi, G. Pepponi, *GIMPy: a software for the simulation of X-ray fluorescence and reflectivity of layered materials*, X-Ray Spectrom. 46 (2017) 116–122.
- [18] P. Brouwer, *Theory of XRF. Getting acquainted with the principles*, PANalytical BV, Almelo, NL, 2003.
- [19] C. Canovaro, I. Calliari, M. Asolati, F. Grazzi, A. Scherillo, *Characterization of bronze Roman coins of the fifth century called nummi through different analytical techniques*, Appl. Phys. A Mater. Sci. Process. 113 (2013) 1019–1028.
- [20] C. Capela, J. de Jesus, L.P. Borrego, J.D.M. Costa, J.A.M. Ferreira, *A study of fatigue notch sensibility on titanium alloy TiAl6V4 parts manufactured by selective laser melting*, Procedia Struct. Integr. 13 (2018) 1000–1005.
- [21] C. Capra, *Età moderna*, Le Monnier, Firenze, 1998.
- [22] F. Caridi, L. Torrisi, M. Cutroneo, F. Barreca, C. Gentile, T. Serafino, D. Castrizio, *XPS and XRF depth patina profiles of ancient silver coins*, Appl. Surf. Sci. 272 (2013) 82–87.

- [23] G. Di Carlo, C. Giuliani, C. Riccucci, M. Pascucci, E. Messina, G. Fierro, M. Lavorgna, G.M. Ingo, *Artificial patina formation onto copper-based alloys: Chloride and sulphate induced corrosion processes*, Appl. Surf. Sci. 421 (2016) 120–127.
- [24] L. Carrino, *Il Titanio e le sue leghe*, Università degli Studi “Federico II,” Naples, I, 2018.
- [25] L. Carrino, *Produzione del Titanio*, Università degli Studi “Federico II,” Naples, I, 2018.
- [26] A. Castoldi, C. Fiorini, C. Guazzoni, A. Longoni, L. Strueder, *Semiconductor Drift Detectors : Applications and new Devices*, X-Ray Spectrom. 316 (1999) 312–316.
- [27] R. Cesareo, A. Castellano, G. Buccolieri, S. Quarta, L.S. Leo, *La tecnica della fluorescenza a raggi X in dispersione di energia (EDXRF) per lo studio e la salvaguardia dei beni culturali*, in: M. Martini, A. Castellano, E. Sibilis (Eds.), Elem. Di Archeometria, Egea, Cesano Boscone (MI), 2007: pp. 155–176.
- [28] Y.A. Chang, K.-C. Hsieh, eds., *Phase Diagrams of Ternary Copper-Oxygen-Metal Systems*, 1st ed., ASM International, Metals Park, Ohio, 44073, 1989.
- [29] D. Chateigner, *Combined Analysis*, ISTE Ltd, London, UK, 2010.
- [30] A.K. Cheetam, *Structure determination from powder diffraction data: an overview*, in: W.I.F. David, K. Shankland, L.B. McCusker, C. Baerlocher (Eds.), Struct. Determ. from Powder Diffr. Data, Oxford University Press, New York, USA, 2002: pp. 13–28.
- [31] W. Chen, C. Chen, X. Zi, X. Cheng, X. Zhang, Y.C. Lin, K. Zhou, *Controlling the microstructure and mechanical properties of a metastable β titanium alloy by selective laser melting*, Mater. Sci. Eng. A. 726 (2018) 240–250.
- [32] H.G. Chotas, J.T. Dobbins, C.E. Ravin, *Principles of digital radiography with large-area, electronically readable detectors: a review of the basics.*, Radiology. 210 (1999) 595–599.
- [33] A. Coda, *Tecniche sperimentali*, in: C. Giacomazzo (Ed.), Introduzione Alla Cristal. Mod., Editori Laterza, Bari, I, 2010.
- [34] G. Cozzi, *Venezia dal Rinascimento all'Età Barocca*, in: G. Cozzi, P. Prodi (Eds.), Stor. Di Venezia. Vol. VI. Dal Rinascim. Al Barocco, Enciclopedia Italiana Treccani, Roma, I, 1994: pp. 3–125.
- [35] B.D. Cullity, *Elements of X-Ray Diffraction*, 2nd ed., Addison-Wesley, Reading, MA, 1978.
- [36] L.A. Currie, *Nomenclature in evaluation of analytical methods , including detect ion and quantification capabilities (IUPAC Recommendations 1995)*, Pure Appl. Chem. 67 (1995) 1699–1723.
- [37] E. Dal Martello, G. Tranell, O. Raanes, L. Arnberg, *Combined XRD and XRF Technique for the Quantification of the Mass Balance in a Si Carbothermic Production Experiment*, ISIJ Int. 51 (2011) 1492–1496.
- [38] K. Das, P. Choudhury, S. Das, *The Al-O-Ti (Aluminum-oxygen-titanium) system*, J. Phase Equilibria. 23 (2003) 525–536.
- [39] W.G. Davenport, M. King, M. Schlesinger, A.K. Biswas, *Extractive Metallurgy of Copper*, 4th ed., Pergamon, Oxford, UK, 2002.
- [40] W.I.F. David, S.S. Devinderjit, *Extracting integrated intensities from powder diffraction patterns*, in: W.I.F. David, K. Shankland, L.B. McCusker, C. Baerlocher (Eds.), Struct. Determ. from Powder Diffr. Data, Oxford University Press, New York, USA, 2002: pp. 136–161.
- [41] W.I.F. David, K. Shankland, L.B. McCusker, C. Baerlocher, *Introduction*, in: W.I.F. David, K. Shankland, L.B. McCusker, C. Baerlocher (Eds.), Struct. Determ. from Powder Diffr. Data, Oxford University Press, New York, USA, 2002: pp. 1–12.
- [42] R. Debastiani, R. Simon, J. Goettlicher, S. Heissler, R. Steininger, D. Batchelor, M. Fiederle, T. Baumbach, *Identification of green pigments from fragments of Roman mural paintings of three Roman sites from north of Germania Superior*,

- Appl. Phys. A. 122 (2016) 871.
- [43] A. Deing, B. Luthringer, D. Laipple, T. Ebel, R. Willumeit, *A Porous TiAl6V4 Implant Material for Medical Application*, Int. J. Biomater. 2014 (2014) 1–8.
- [44] F. Deng, X. Lin, Y. He, S. Li, R. Zi, S. Lai, *Quantitative Phase Analysis by the Rietveld Method for Forensic Science*, J. Forensic Sci. 60 (2015) 1040–5.
- [45] A. Denker, W. Bohne, J. Opitz-Coutureau, J. Rauschenberg, J. Röhrich, E. Strub, *Influence of corrosion layers on quantitative analysis*, Nucl. Instruments Methods Phys. Res. Sect. B Beam Interact. with Mater. Atoms. 239 (2005) 65–70.
- [46] R.B. Von Dreele, *Quantitative texture analysis by Rietveld refinement*, J. Appl. Crystallogr. 30 (1997) 517–525.
- [47] A. Ducato, L. Fratini, M. La Cascia, G. Mazzola, *An Automated Visual Inspection System for the Classification of the Phases of Ti-6Al-4V Titanium Alloy*, Lect. Notes Comput. Sci. (Including Subser. Lect. Notes Artif. Intell. Lect. Notes Bioinformatics). 8048 LNCS (2013).
- [48] C. Elgin, K. Karaman, Ş. Pamuk, *Debasements in Europe and their causes, 1500-1800*, in: Account. Gt. Divergence, University of Warwick, 2015.
- [49] P. Van Espen, K. Janssens, *Spectrum evaluation*, in: R. Van Grieken, A.A. Markowicz (Eds.), Handb. X-Ray Spectrom. Methods Tech., Dekker, New York, USA, 2002: pp. 181–294.
- [50] F. Faraldi, B. Cortese, D. Caschera, G. Di Carlo, C. Riccucci, T. de Caro, G.M. Ingo, *Smart conservation methodology for the preservation of copper-based objects against the hazardous corrosion*, Thin Solid Films. 622 (2017) 130–135.
- [51] T.G. Fawcett, J.R. Blanton, T.N. Blanton, L. Arias, T. Suscavage, *Non-destructive evaluation of Roman coin patinas from the 3rd and 4th century*, Powder Diffr. 33 (2018) 88–97.
- [52] R.C. Fierascu, I. Fierascu, A. Ortan, F. Constantin, D.A. Mirea, M. Statescu, *Complex archaeometallurgical investigation of silver coins from the XVth-XVIIIth century*, Nucl. Instruments Methods Phys. Res. Sect. B Beam Interact. with Mater. Atoms. 401 (2017) 18–24.
- [53] A. Finetti, *Numismatica e tecnologia*, La Nuova Italia Scientifica, Roma, I, 1987.
- [54] K.P. FitzGerald, J. Nairn, G. Skennerton, A. Atrens, *Atmospheric corrosion of copper and the colour, structure and composition of natural patinas on copper*, Corros. Sci. 48 (2006) 2480–2509.
- [55] B. Fleming, *The EDM How-To Book*, 4th ed., Felming Publishing, 2005.
- [56] A. Gagin, I. Levin, *Accounting for unknown systematic errors in Rietveld refinements: a Bayesian statistics approach*, J. Appl. Crystallogr. 48 (2015) 1201–1211.
- [57] A. Gebhardt, *Understanding Additive Manufacturing: Rapid Prototyping - Rapid Tooling - Rapid Manufacturing*, Carl Hanser Verlag GmbH & Co. KG, Munich, 2012.
- [58] A. Gebhardt, J.-S. Höttner, *Additive Manufacturing: 3D Printing for Prototyping and Manufacturing*, Carl Hanser Verlag GmbH & Co. KG, Munich, 2016.
- [59] C. Giacobazzo, *La simmetria nei cristalli*, in: C. Giacobazzo (Ed.), Introduzione Alla Cristal. Mod., Editori Laterza, Bari, I, 2010.
- [60] C. Giacobazzo, *Phasing in crystallography: A modern perspective*, Rend. Lincei. 24 (2013) 71–76.
- [61] C. Giacobazzo, A. Altomare, M.C. Burla, B. Carrozzini, G.L. Cascarano, A. Guagliardi, A.G.G. Moliterni, G. Polidori, R. Rizzi, *Direct methods in powder diffraction—applications*, in: W.I.F. David, K. Shankland, L.B. McCusker, C. Baerlocher (Eds.), Struct. Determ. from Powder Diffr. Data, Oxford University Press, New York, USA, 2002: pp. 190–201.

- [62] P.T. Gilbert, *Copper and Copper Alloys*, in: L.L. Shreir (Ed.), *Corros. Met. React.*, 3rd ed., Butterworth-Heinemann, Oxford, UK, 1994: pp. 4:38-4:75.
- [63] N. Golshani, C.I. Beenakker, R. Ishihara, *Manufacturing uniform field silicon drift detector using double boron layer*, *Nucl. Instruments Methods Phys. Res. Sect. A Accel. Spectrometers, Detect. Assoc. Equip.* 794 (2015) 206–214.
- [64] M. De Graef, M.E. McHenry, *Structure of Materials: An Introduction to Crystallography, Diffraction, and Symmetry*, 1st ed., Cambridge University Press, New York, USA, 2007.
- [65] S. Gražulis, A. Daškevič, A. Merkys, D. Chateigner, L. Lutterotti, M. Quirós, N.R. Serebryanaya, P. Moeck, R.T. Downs, A. Le Bail, *Crystallography Open Database (COD): An open-access collection of crystal structures and platform for world-wide collaboration*, *Nucleic Acids Res.* 40 (2012) 420–427.
- [66] D. Greitemeier, F. Palm, F. Syassen, T. Melz, *Fatigue performance of additive manufactured TiAl6V4 using electron and laser beam melting*, *Int. J. Fatigue.* 94 (2017) 211–217.
- [67] G.M. Ter Haar, T.H. Becker, *Selective laser melting produced Ti-6Al-4V: Post-process heat treatments to achieve superior tensile properties*, *Materials (Basel)*. 11 (2018).
- [68] C. Hammond, *The Basics of Crystallography and Diffraction*, 3rd ed., Oxford University Press, Oxford, UK, 2009.
- [69] C.R. Hammond, *The elements*, in: *Handb. Chem. Phys.*, 90th ed., CRC Press/Taylor and Francis, Boca Raton, FL, 2009: pp. 4–1.
- [70] B. Hanson, *The selection and Use of Titanium. A design guide*, The Institute of Materials, London, UK, 1995.
- [71] A.M. Haque, F. Claeysens, R. Goodall, A. Feteira, Z.J. Wally, G.C. Reilly, *Selective laser melting processed Ti6Al4V lattices with graded porosities for dental applications*, *J. Mech. Behav. Biomed. Mater.* 90 (2018) 20–29.
- [72] K.D.M. Harris, *Powder Diffraction Crystallography of Molecular Solids*, in: K. Rissanen (Ed.), *Adv. X-Ray Crystallogr.*, Springer-Verlag Berlin Heidelberg, Heidelberg, D, 2012: pp. 132–177.
- [73] J.A. Helsen, A. Kuczumow, *Wavelength-Dispersive X-ray Fluorescence*, in: R. Van Grieken, A.A. Markowicz (Eds.), *Handb. X-Ray Spectrom. Methods Tech.*, 2nd ed., Dekker, New York, USA, 2002: pp. 75–150.
- [74] D. Ingerle, G. Pepponi, F. Meirer, P. Wobrauschek, C. Strelj, *JGIXA - A software package for the calculation and fitting of grazing incidence X-ray fluorescence and X-ray reflectivity data for the characterization of nanometer-layers and ultra-shallow-implants*, *Spectrochim. Acta - Part B At. Spectrosc.* 118 (2016) 20–28.
- [75] G.M. Ingo, T. De Caro, G. Padeletti, G. Chiozzini, *Microchemical investigation on Renaissance coins minted at Gubbio (Central Italy)*, *Appl. Phys. A Mater. Sci. Process.* 79 (2004) 319–325.
- [76] G.M. Ingo, C. Riccucci, M. Lavorgna, M. Salzano de Luna, M. Pascucci, G. Di Carlo, *Surface investigation of naturally corroded gilded copper-based objects*, *Appl. Surf. Sci.* 387 (2016) 244–251.
- [77] O. for S. International, *International Standard ISO 11843-1 - Capability of Detection-Part 1: Terms and Definitions*, Geneva, CH, 1997.
- [78] O. for S. International, *International Standard ISO 11843-2, Capability of Detection- Part 2: Methodology in the Linear Calibration Case*, Geneva, CH, 2000.
- [79] H.E. Ives, P. Grierson, *The Venetian Gold Ducat And Its Imitations*, The American Numismatic Society, New York, USA, 1954.
- [80] K. Janssens, *X-ray Fluorescence Analysis*, in: G. Gauglitz, T. Vo-Dinh (Eds.), *Handb. Spectrosc.*, WILEY-VCH Verlag GmbH & Co. KGaA, Weinheim, D, 2003.
- [81] R. Jenkins, *X-Ray Fluorescence Spectrometry*, John Wiley & Sons Ltd, Canada, 1988.
- [82] R. Jenkins, R.W. Gould, D. Gedcke, *Quantitative X-Ray Spectrometry*, Dekker, New York, USA, USA, 1995.

- [83] R. Jenkins, R.L. Snyder, *Introduction to X-Ray Powder Diffractometry*, John Wiley & Sons Ltd, 1996.
- [84] A.N. Kadachi, M.A. Al-Eshaikh, *Limits of detection in XRF spectroscopy*, X-Ray Spectrom. 41 (2012) 350–354.
- [85] V. Kantarelou, F.J. Ager, D. Eugenidou, F. Chaves, A. Andreou, E. Kontou, N. Katsikosta, M.A. Respaliza, P. Serafin, D. Sokaras, C. Zarkadas, K. Polikreti, A.G. Karydas, *X-ray Fluorescence analytical criteria to assess the fineness of ancient silver coins: Application on Ptolemaic coinage*, Spectrochim. Acta - Part B At. Spectrosc. 66 (2011) 681–690.
- [86] G. Kasperovich, J. Haubrich, J. Gussone, G. Requena, *Correlation between porosity and processing parameters in TiAl6V4 produced by selective laser melting*, Mater. Des. 105 (2016) 160–170.
- [87] G. Kasperovich, J. Hausmann, *Improvement of fatigue resistance and ductility of TiAl6V4 processed by selective laser melting*, J. Mater. Process. Technol. 220 (2015) 202–214.
- [88] E. Klar, P.K. Samal, *Powder Metallurgy Stainless Steels: Processing, Microstructures, and Properties*, ASM International, Materials Park, OH, 2007.
- [89] R. Klockenkemper, *Total-Reflection X-Ray Fluorescence analysis*, John Wiley & Sons Ltd, New York, USA, 1997.
- [90] M. Knapton, *The Terraferma State*, in: E.R. Dursteler (Ed.), *A Companion to Venetian Hist. (1400-1797)*, Vol. 42, Koninklijke Brill NV, Leiden, The Netherlands, 2013: pp. 85–124.
- [91] L. Kučera, L. Richtera, M. Zmrzlý, M. Jarošová, P. Kučerová, P. Bednář, *Determination of the Fineness of Medieval Coins-Evaluation of Methods in a Case Study of a Medieval Pfennig*, Archaeometry. (2017).
- [92] P. Lechner, C. Fiorini, R. Hartmann, J. Kemmer, N. Krause, P. Leutenegger, A. Longoni, H. Soltau, D. Stötter, R. Stötter, L. Strüder, U. Weber, *Silicon Drift Detectors for high count rate X-ray spectroscopy at room temperature*, Nucl. Instruments Methods Phys. Res. Sect. A Accel. Spectrometers, Detect. Assoc. Equip. 458 (2001) 281–287.
- [93] P. Lechner, A. Pahlke, H. Soltau, *Novel high-resolution silicon drift detectors*, X-Ray Spectrom. 33 (2004) 256–261.
- [94] M.-C. Lepy, J. Plagnard, P. Stemmler, G. Ban, L. Beck, P.P. Dhez, M.-C. Lépy, P.P. Dhez, *Si (Li) Detector Efficiency and Peak Shape Calibration in the Low-Energy Range Using Synchrotron Radiation*, X-Ray Spectrom. 26 (1997) 195–202.
- [95] Y. Li, K. Zhou, P. Tan, S.B. Tor, C.K. Chua, K.F. Leong, *Modeling temperature and residual stress fields in selective laser melting*, Int. J. Mech. Sci. 136 (2018) 24–35.
- [96] Z. Li, R. Xu, Z. Zhang, I. Kucukkoc, *The influence of scan length on fabricating thin-walled components in selective laser melting*, Int. J. Mach. Tools Manuf. 126 (2018) 1–12.
- [97] H. Lin, G.S. Frankel, W.H. Abbott, *Analysis of Ag Corrosion Products*, J. Electrochem. Soc. 160 (2013) C345–C355.
- [98] R. Linke, M. Schreiner, G. Demortier, *The application of photon, electron and proton induced X-ray analysis for the identification and characterisation of medieval silver coins*, Nucl. Instruments Methods Phys. Res. Sect. B Beam Interact. with Mater. Atoms. 226 (2004) 172–178.
- [99] R. Linke, M. Schreiner, G. Demortier, M. Alram, *Determination of the provenance of medieval silver coins: Potential and limitations of x-ray analysis using photons, electrons or protons*, X-Ray Spectrom. 32 (2003) 373–380.
- [100] M. Loubser, S. Verryin, *Combining XRF and XRD analyses and sample preparation to solve mineralogical problems*, South African J. Geol. 111 (2008) 229–238.
- [101] D. Louër, *Laboratory X-ray powder diffraction*, in: W.I.F. David, K. Shankland, L.B. McCusker, C. Baerlocher (Eds.), *Struct. Determin. from Powder Diffraction*, Oxford University Press, New York, USA, 2002: pp. 29–48.
- [102] X. Lu, N. Gui, A. Qiu, G. Wu, C. Li, *Thermodynamic Modeling of the Al-Ti-V Ternary System*, Metall. Mater. Trans.

- A Phys. Metall. Mater. Sci. 45 (2014) 4155–4164.
- [103] G. Luetjering, J.C. Williams, *Titanium*, 2nd ed., Springer-Verlag Berlin Heidelberg, Heidelberg, D, 2007.
 - [104] L. Lutterotti, *Total pattern fitting for the combined size-strain-stress-texture determination in thin film diffraction*, Nucl. Instruments Methods Phys. Res. Sect. B Beam Interact. with Mater. Atoms. 268 (2010) 334–340.
 - [105] L. Lutterotti, M. Bortolotti, *Object oriented programming and fast computation techniques in Maud, a program for powder diffraction analysis written in java*, IUCr Compcomm Newsl. (2003) 1:43-50.
 - [106] L. Lutterotti, M. Bortolotti, G. Ischia, I. Lonardelli, H.-R. Wenk, *Rietveld texture analysis from diffraction images*, Zeitschrift Fur Krist. Suppl. 1 (2007) 125–130.
 - [107] L. Lutterotti, F. Dell'Amore, D.E. Angelucci, F. Carrer, S. Gialanella, *Combined X-ray diffraction and fluorescence analysis in the cultural heritage field*, Microchem. J. 126 (2016) 423–430.
 - [108] L. Lutterotti, S. Gialanella, *X-ray diffraction characterization of heavily deformed metallic specimens*, Acta Mater. 46 (1998) 101–110.
 - [109] L. Lutterotti, S. Matthies, H.-R. Wenk, *MAUD (Material Analysis Using Diffraction): a user friendly Java program for Rietveld Texture Analysis and more*, in: Proceeding Twelfth Int. Conf. Textures Mater., 1999: p. Vol I, 1599.
 - [110] L. Lutterotti, S. Matthies, H.R. Wenk, *MAUD: a friendly Java program for material analysis using diffraction*, IUCr Newsl. CPD. (1999) 21:14–15.
 - [111] L. Lutterotti, H. Pilliere, C. Fontugne, P. Boullay, D. Chateigner, *FPSM*, [Www://Fpsm.Radiographema.Com](http://Fpsm.Radiographema.Com). (2012).
 - [112] G. Lutz, *Silicon drift and pixel devices for X-ray imaging and spectroscopy*, J. Synchrotron Radiat. 13 (2006) 99–109.
 - [113] G. Lutz, *Semiconductor Radiation Detectors*, 2nd ed., Springer-Verlag, New York, 2007.
 - [114] G. Luzzato, *Storia economica di Venezia dall'XI al XVI secolo*, Marsilio, Venezia, I, 1995.
 - [115] M. Mantler, *Quantitative analysis*, in: H. Beckhoff, B. Kanngiesser, B. Langhoff, N. Wedell, R., Wolff (Eds.), Handb. Pract. X-Ray Fluoresc. Anal., Springer-Verlag Berlin Heidelberg, Heidelberg, D, 2006: pp. 309–410.
 - [116] M. Mantler, M. Schreiner, *X-ray fluorescence spectrometry in art and archaeology*, X-Ray Spectrom. 29 (2000) 3–17.
 - [117] B. Marcinik, *La moneta*, in: Paesaggi Pastor. d'alta Quota. Le Ric. Del Progett. Alpes 2010-2014, University of Trento, Trento, I, 2015: pp. 105–106.
 - [118] A.A. Markowicz, *X-ray Physics*, in: R.E. Van Grieken, A.A. Markowicz (Eds.), Handb. X-Ray Spectrom. Methods Tech., 2nd ed., Dekker, New York, USA, 2002: pp. 1–73.
 - [119] C.M.B. Martins, J.I. Martins, *Identification of corrosion products on a medieval copper-silver coin*, Prot. Met. Phys. Chem. Surfaces. 47 (2011) 128–132.
 - [120] D. Martorelli, M. Bortolotti, M. Capris, L. Lutterotti, L. Maines, G. Peponi, S. Gialanella, *A combined experimental approach to the study of ancient coins and its application: the Venetian “sesino”*, Nucl. Inst. Methods Phys. Res. B. 454 (2019) 1–6.
 - [121] D. Martorelli, M. Bortolotti, L. Lutterotti, G. Peponi, S. Gialanella, *Characterization of the mistura alloy used for Venetian sesino coins: 16th century*, X-Ray Spectrom. 48 (2019) 8–20.
 - [122] D. Martorelli, F. Brigidi, G. Peponi, *GimpyGUI, a graphical user interface for the GIMPY code*, in: Poster Present. EXRS 2016, Guthemburg (S), 2016.
 - [123] L.B. McCusker, C. Baerlocher, *Chemical information and intuition in solving crystal structures*, in: W.I.F. David, K. Shankland, L.B. McCusker, C. Baerlocher (Eds.), Struct. Determ. from Powder Diffr. Data, Oxford University Press, New York, USA, 2002: pp. 307–323.
 - [124] A. Meden, I. Radosavljevic Evans, *Structure determination from powder diffraction data: past, present and future challenges*,

- Cryst. Res. Technol. 50 (2015) 747–758.
- [125] M. Milazzo, C. Cicardi, *Simple methods for quantitative x-ray fluorescence analysis of ancient metal objects of archaeological interest*, X-Ray Spectrom. 26 (1997) 211–216.
- [126] A.K. Mishra, A. Kumar, *Numerical and experimental analysis of the effect of volumetric energy absorption in powder layer on thermal-fluidic transport in selective laser melting of Ti6Al4V*, Opt. Laser Technol. 111 (2019) 227–239.
- [127] E. Montenegro, *I dogi e le loro monete*, Montenegro, Torino, 2012.
- [128] A.I. Moreno-Suárez, F.J. Ager, S. Scrivano, I. Ortega-Feliu, B. Gomez-Tubio, M.A. Respaldiza, *First attempt to obtain the bulk composition of ancient silver-copper coins by using XRF and GRT*, Nucl. Instruments Methods Phys. Res. Sect. B Beam Interact. with Mater. Atoms. 358 (2015) 93–97.
- [129] A. Morri, *Trattamenti Termici Delle Leghe di Ti alpha+beta Fra Microstruttura E Comportamento Meccanico*, Risorgimento. (2008) 1–10.
- [130] R.C. Mueller, *L'imperialismo monetario veneziano nel quattrocento*, Soc. Stor. VIII (1980) 277–297.
- [131] M. Nespolo, B. Souvignier, *The Bravais polar lattice as a didactic tool for diffraction beginners*, J. Appl. Crystallogr. 43 (2010) 1144–1149.
- [132] W. Nicodemi, C. Mapelli, *Archeometallurgia*, Associazione Italiana di Metallurgia, Milano, 2009.
- [133] A. Pandolfo, G. Degli Esposti, *Leghe del titanio*, in: Tecnol. Mecc. Di Process. e Di Prod., RCS Libri SpA, Milano, I, 2012.
- [134] E. Pantos, W. Kockelmann, L.C. Chapon, L. Lutterotti, S.L. Bennet, M.J. Tobin, J.F.W. Mosselmans, T. Pradell, N. Salvado, S. Butí, R. Garner, A.J.N.W. Prag, *Neutron and X-ray characterisation of the metallurgical properties of a 7th century BC Corinthian-type bronze helmet*, Nucl. Instruments Methods Phys. Res. Sect. B Beam Interact. with Mater. Atoms. 239 (2005) 16–26.
- [135] V.K. Pecharsky, P.Y. Zavalij, *Fundamentals of powder diffraction and structural characterization of materials*, Springer-Verlag, New York, USA, 2003.
- [136] W. Per-Erik, *Autoindexing*, in: W.I.F. David, K. Shankland, L.B. McCusker, C. Baerlocher (Eds.), Struct. Determ. from Powder Diffr. Data, Oxford University Press, New York, USA, 2002: pp. 118–135.
- [137] R. Peschar, A. Etz, J. Jonsen, H. Schenk, *Direct methods in powder diffraction—basic concepts*, in: W.I.F. David, K. Shankland, L.B. McCusker, C. Baerlocher (Eds.), Struct. Determ. from Powder Diffr. Data, Oxford University Press, New York, USA, 2002: pp. 179–189.
- [138] L. Pezzolo, *La finanza pubblica*, in: G. Cozzi, P. Prodi (Eds.), Stor. Di Venezia. Vol. VI. Dal Rinascim. Al Barocco, Enciclopedia Italiana Treccani, Roma, I, 1994: pp. 713–773.
- [139] L. Pezzolo, *The Venetian economy*, in: E.R. Dursteler (Ed.), A Companion to Venetian Hist. (1400-1797), Vol. 4, Koninklijke Brill NV, Leiden, The Netherlands, 2013: pp. 255–289.
- [140] W.H. Phillips, *Additive Manufacturing: Opportunities, Challenges, Implications*, Nova Science Publishers, Inc, New York, 2016.
- [141] A. Pitarch, I. Queralt, *Energy dispersive X-ray fluorescence analysis of ancient coins: The case of Greek silver drachmae from the Emporion site in Spain*, Nucl. Instruments Methods Phys. Res. Sect. B Beam Interact. with Mater. Atoms. 268 (2010) 1682–1685.
- [142] N.C. Popa, *The (hkl) Dependence of Diffraction-Line Broadening Caused by Strain and Size for all Laue Groups in Rietveld Refinement*, J. Appl. Crystallogr. 31 (1998) 176–180.
- [143] L. Pronti, A.C. Felici, M. Alesiani, O. Tarquini, M.P. Bracciale, M.L. Santarelli, G. Pardini, M. Piacentini, *Characterisation of corrosion layers formed under burial environment of copper-based Greek and Roman coins from Pompeii*,

- Appl. Phys. A Mater. Sci. Process. 121 (2015) 59–68.
- [144] H.M. Rietveld, *A profile refinement method for nuclear and magnetic structures*, J. Appl. Crystallogr. 2 (1969) 65–71.
- [145] R.M. Rousseau, J. a Boivin, *The fundamental algorithm: A natural extension of the Sherman equation Part 1: Theory*, Rigaku J. 15 (1998) 13–28.
- [146] C.E. Sanders, D. Verreault, G.S. Frankel, H.C. Allen, *The Role of Sulfur in the Atmospheric Corrosion of Silver*, J. Electrochem. Soc. 162 (2015) C630–C637.
- [147] S. Santra, D. Mitra, M. Sarkar, D. Bhattacharya, A. Denker, J. Opitz-Coutureau, J. Rauschenberg, *Analysis of some coins by energy dispersive X-ray fluorescence (EDXRF) and high energy particle induced X-ray emission (PIXE) techniques*, Nucl. Instruments Methods Phys. Res. Sect. B Beam Interact. with Mater. Atoms. 229 (2005) 465–470.
- [148] F. Sartori, D. Colombo, *Titanio, leghe di titanio ed applicazioni nel settore automobilistico*, Università degli Studi di Trento - Facoltà di Ingegneria, Trento, I, 2004.
- [149] M. Schmeling, R. Van Grieken, *Sample Preparation for X-ray Fluorescence*, in: R. Van Grieken, A.A. Markowicz (Eds.), Handb. X-Ray Spectrom. Methods Tech., 2nd ed., Dekker, New York, USA, 2002: pp. 933–976.
- [150] F. Scholze, M. Procop, *Measurement of detection efficiency and response functions for an Si (Li) x-ray spectrometer in the range 0.1 – 5 keV*, X-Ray Spectrom. (2001) 69–76.
- [151] F. Scholze, M. Procop, *Modelling the response function of energy dispersive X-ray spectrometers with silicon detectors*, X-Ray Spectrom. 38 (2009) 312–321.
- [152] J. Schönenberger, T. Momose, B. Wagner, W.H. Leong, V.R. Tarnawski, *Canadian field soils I. Mineral composition by XRD/XRF measurements*, Int. J. Thermophys. 33 (2012) 342–362.
- [153] P.A. Schweitzer, *Fundamentals of metallic corrosion. Atmospheric and Media Corrosion of Metals*, 2nd ed., CRC Press/Taylor and Francis, Boca Raton, FL, 2007.
- [154] M. Secchi, M. Zanatta, E. Borovin, M. Bortolotti, A. Kumar, M. Giarola, A. Sanson, B. Orberger, N. Daldosso, S. Gialanella, G. Mariotto, M. Montagna, L. Lutterotti, *Mineralogical investigations using XRD, XRF, and Raman spectroscopy in a combined approach*, J. Raman Spectrosc. 49 (2018) 1023–1030.
- [155] O.H. Seeck, *Overview of X-Ray Scattering and Diffraction Theory and Techniques*, in: O.H. Seeck, B.M. Murphy (Eds.), X-Ray Diffraction. Mod. Exp. Tech., Pan Stanford Publishing, Boca Raton, FL, U.S.A., 2014: pp. 1–28.
- [156] D. Sella, *L'economia*, in: G. Cozzi, P. Prodi (Eds.), Stor. Di Venezia. Vol. VI. Dal Rinascim. Al Barocco, Enciclopedia Italiana Treccani, Roma, I, 1994: pp. 651–711.
- [157] H. Shipley, D. McDonnell, M. Culleton, R. Coull, G. O'Donnell, D. Trimble, R. Lupoi, *Optimisation of process parameters to address fundamental challenges during selective laser melting of Ti-6Al-4V: A review*, Int. J. Mach. Tools Manuf. 128 (2018) 1–20.
- [158] R. Sitko, B. Zawisza, *Quantification in X-Ray Fluorescence Spectrometry*, in: Shatendra K. Sharma (Ed.), X-Ray Spectrosc., InTech, Rijeka, CR, 2012: pp. 137–162.
- [159] C.S. Smith, M. Teach Gnudi, *The Pirotechnia of Vannoccio Biringuccio: The Classic Sixteenth-Century Treatise on Metals and Metallurgy*, Dover Publications, 1990.
- [160] J.R. Smyth, T.C. McCormick, *Crystallographic Data For Minerals*, in: T.J. Ahrens (Ed.), Miner. Phys. Crystallogr. A Handb. Phys. Constants, American Geophysical Union, Washington, DC, 1995: pp. 1–17.
- [161] C. Sommer, S.M.E. Sommer, *Complete EDM Handbook*, 2nd ed., Advance Pub, 2005.
- [162] C. Stahl, Alan M., Tonini, *Venezia*, in: L. Travaini (Ed.), Le Zecche Ital. Fino All'Unità, Istituto Poligrafico e

- Zecca dello Stato SpA, Roma, I, 2011: pp. 1217–1224.
- [163] A.M. Stahl, *Zecca. The Mint of Venice in the Middle Ages*, The John Hopkins University Press, Baltimore, MA, 2000.
- [164] K. Ståhl, *Powder diffraction and the Rietveld Method*, Lyngby, DK, 2008.
- [165] G.W. Stinton, J.S.O. Evans, *Parametric Rietveld refinement*, J. Appl. Crystallogr. 40 (2007) 87–95.
- [166] G.H. Stout, L.H. Jensen, *X-Ray Structure Determination*, John Wiley & Sons Ltd, 1989.
- [167] M. Suard, *Characterization and Optimization of Lattice Structures made by Electron Beam Melting*, Université de Grenoble, 2015.
- [168] C. Suryanarayana, C. Grant Norton, *X-Ray Diffraction. A Practical Approach*, Plenum Press, New York, USA, 1998.
- [169] P. Tan, F. Shen, B. Li, K. Zhou, *A thermo-metallurgical-mechanical model for selective laser melting of Ti6Al4V*, Mater. Des. 168 (2019) 107642.
- [170] S. Telrandhe, A.K. Saxena, P. Sutar, S. Mishra, *Influence of Laser Heat Treatment on Machinability of Ti6Al4V Alloy*, Procedia Manuf. 5 (2016) 282–294.
- [171] V. Thomsen, *Basic Fundamental Parameters in X-Ray Fluorescence Spectroscopy*. 22 (2007) 46–50.
- [172] T. Tikkanen, S. Kraft, F. Scholze, R. Thornagel, G. Ulm, *Characterising a Si(Li) detector element for the SIXA X-ray spectrometer*, Nucl. Instruments Methods Phys. Res. Sect. A Accel. Spectrometers, Detect. Assoc. Equip. 390 (1997) 329–335.
- [173] H. Toraya, *Weighting Scheme for the Minimization Function in Rietveld Refinement*, J. Appl. Crystallogr. 31 (1998) 333–343.
- [174] L. Travaini, *I conii e le zecche*, in: L. Travaini, A. Bolis (Eds.), *Conii e Scene Di Coniazione*, Edizioni Quasar, Roma, I, 2007: pp. 27–66.
- [175] L. Travaini, *Monete e storia nell'Italia medievale*, Istituto Poligrafico e Zecca dello Stato SpA, Roma, I, 2007.
- [176] L. Travaini, *Zecche e monete*, in: P. Braunstein, L. Molà (Eds.), *Rinascim. Ital. e l'Europa*, Prod. e Tec. Vol. III, Fondazione Cassamarca, Vicenza, I, 2007: pp. 479–509.
- [177] U. Tucci, *Monete e banche nel secolo del ducato d'oro*, in: G. Cozzi, P. Prodi (Eds.), *Stor. Di Venezia*. Vol. VI. Dal Rinascim. Al Barocco, Enciclopedia Italiana Treccani, Roma, I, 1996.
- [178] G.S. Upadhyaya, *Powder Metallurgy Technology*, Cambridge Intl Science Pub, Cambridge, UK, 1998.
- [179] P.O. Verkhovodov, *Effect of crystal structure on the background intensity in XRF*, X-Ray Spectrom. 34 (2005) 169–171.
- [180] L. Van De Voorde, B. Vekemans, E. Verhaeven, P. Tack, R. De Wolf, J. Garrevoet, P. Vandenabeele, L. Vincze, *Analytical characterization of a new mobile X-ray fluorescence and X-ray diffraction instrument combined with a pigment identification case study*, Spectrochim. Acta - Part B At. Spectrosc. 110 (2015) 14–19.
- [181] B. Vrancken, L. Thijs, J.P. Kruth, J. Van Humbeeck, *Heat treatment of Ti6Al4V produced by Selective Laser Melting: Microstructure and mechanical properties*, J. Alloys Compd. 541 (2012) 177–185.
- [182] J.L. de Vries, B.A.R. Vrebos, *Quantification by XRF Analysis of Infinitely Thick Samples*, in: R. Van Grieken, A. Markowicz (Eds.), *Handb. X-Ray Spectrom. Methods Tech.*, 2nd ed., Dekker, New York, USA, 2002: pp. 295–338.
- [183] F. Wagner, *Texture Determination by Using X ray Diffraction*, in: J.M. Rincon, M. Romero (Eds.), *Charact. Tech. Glas. Ceram.*, Springer Berlin Heidelberg, Berlin, D, 1999.
- [184] D. Wang, W. Dou, Y. Yang, *Research on Selective Laser Melting of Ti6Al4V: Surface Morphologies, Optimized Processing*

- Zone, and Ductility Improvement Mechanism*, Metals (Basel). 8 (2018) 471.
- [185] H. Wang, Z.Z. Fang, P. Sun, *Mechanical Properties of a Powder Bed*, Powder Technol. (2010) 335–348.
- [186] D.G. White, *History of Powder Metallurgy*, in: P.W. Lee (Ed.), ASM Handbook, Vol. 7, Powder Met. Technol. Appl., 2nd ed., ASM International, Metals Park, OH, 1998: pp. 10–22.
- [187] P. Wobrauschek, C. Strelt, E.S. Lindgren, *Energy Dispersive, X-ray Fluorescence Analysis*, Encycl. Anal. Chem. (R.A. Meyers Ed.). 2000 (2010) 1–17.
- [188] I. Yadroitsev, P. Bertrand, I. Smurov, *Parametric analysis of the selective laser melting process*, Appl. Surf. Sci. 253 (2007) 8064–8069.
- [189] A. Zorzi, *La Repubblica del Leone. Storia di Venezia*, Bompiani, 2001.
- [190] C.N. Zwicky-Sobczyk, W.B. Stern, *X-ray fluorescence and density measurements on surface-treated Roman silver coins*, Archaeometry. 39 (1997) 393–405.
- [191] *ASTM B367 Specification for titanium and titanium alloy castings*, American Society for Testing and Materials International, 2013.
- [192] *ASTM F1472 Standard Specification for Wrought Titanium-6Aluminum-4Vanadium Alloy for Surgical Implant Applications*, American Society for Testing and Materials International, 2014.
- [193] *ISO 5832 Implants for surgery — Metallic materials — Part 3: Wrought titanium 6-aluminium 4-vanadium alloy*, International Standard Organization, 2016.

SCIENTIFIC PRODUCTION

Posters

GimpyGUI, a graphical user interface for the GIMPy code: by Martorelli D. (1,3), Brigidi F. (2), Pepponi G. (1); presented at **EXRS 2016-European Conference on X-Ray Spectrometry**, June 19 – 24, 2016, Gothenburg (S)

(1) Micro Nano Facility, Centre for Materials and Microsystems, Fondazione Bruno Kessler, Via Sommarive 18, Trento, Italy
(2) Elettra-Sincrotrone Trieste S.C.p.A., Basovizza, Trieste, Italy (3) University of Trento, Department of Industrial Engineering, Via Sommarive 9, 38123 Trento, Italy

Bio-inspired wet confinement sample holders for Total Reflection X-Ray Fluorescence Analysis: by Pepponi G. (1), Ghio S. (1,2), Martorelli D. (1,3), Boscardin M. (1), Bellutti P. (1), Pugno N.M. (1,2,4); presented at **EXRS 2016-European Conference on X-Ray Spectrometry**, June 19 – 24, 2016, Gothenburg (S)

(1) Micro Nano Facility, Centre for Materials and Microsystems, Fondazione Bruno Kessler, Via Sommarive 18, Trento, Italy
(2) Laboratory of Bio-inspired and Graphene Nanomechanics, Department of Civil, Environmental and Mechanical Engineering, University of Trento, Trento, Italy (3) University of Trento, Department of Industrial Engineering, Via Sommarive 9, 38123 Trento, Italy (4) School of Engineering and Materials Science, Queen Mary University of London, Mile End Road, London E1 4NS, UK

Characterization of Venetian coins sesini (XVI century) through a combined XRF/XRD quantitative approach: by Martorelli D. (1,2), Bortolotti M. (1), Lutterotti L. (1), Pepponi G. (2), Marcinik B.; presented at **EXSA Quantitative Methods In X-Ray Spectrometry Autumn School and Workshop**, October 9-13, 2017, Berlin (D)

(1) University of Trento, Department of Industrial Engineering, Via Sommarive 9, Trento, Italy (2) Center for Materials and Microsystems, Fondazione Bruno Kessler, Via Sommarive 18, 38123 Trento, Italy

Modelling Total Reflection X-Ray Fluorescence Analysis spectra: by Pepponi G. (1), Martorelli D. (1,2), Demenev E. (1); presented at the **17th International Conference on Total Reflection X-Ray Fluorescence Analysis and Related Methods (TXRF2017)**, Brescia (I), September 19-22, 2017

(1) Fondazione Bruno Kessler, Micro Nano Facility, Via Sommarive 18, Trento, Italy (2) University of Trento, Department of Industrial Engineering, Via Sommarive 9, 38123 Trento, Italy

Grazing Incidence X-Ray Fluorescence Analysis of nano-rippled semiconductor surfaces produced by ion bombardment: by G. Pepponi (1), E. Iacob (1), M. Barozzi (1), L. Vanzetti (1), D. Martorelli (1,2), D.

Giubertoni (1), R. Dell'Anna (1)); presented at the **17th International Conference on Total Reflection X-Ray Fluorescence Analysis and Related Methods (TXRF2017)**, Brescia (I), September 19-22, 2017

(1) Fondazione Brino Kessler, Micro Nano Facility, Via Sommarive 18, Trento, Italy (2) University of Trento, Department of Industrial Engineering, Via Sommarive 9, 38123 Trento, Italy

Papers

Martorelli, D.; Bortolotti, M.; Lutterotti, L.; Peponi, G.; Gialanella, S.; *Characterization of the mistura alloy used for Venetian sesino coins – 16th century*, X-Ray Spectrometry 2019, v. 48, 1, 8-20. DOI: 10.1002/xrs.2979

Martorelli D.; Bortolotti, M.; Capris, M.; Lutterotti, L.; Maines L.; Peponi, G.; Marcinik, B.T.; Gialanella, S.; *A combined experimental approach to the study of ancient coins and its application the Venetian "sesino"*, Nuclear Inst. and Methods in Physics Research, B. <https://doi.org/10.1016/j.nimb.2019.06.010>

Bortolotti, M.; Lutterotti, L.; Borovin, E.; Martorelli, D.; *Combined XRD-XRF cluster analysis for automatic chemical and crystallographic surface mappings*, Powder Diffraction, Published online: 03 May 2019, DOI: 10.1017/S0885715619000216

Oral presentations

XRF/XRD analysis of ancient Venetian coins of XVI Century (sesini) from Ala (TN), presented at the Conference “Antiche monete veneziane del sec. XVI delle raccolte numismatiche alensi: studi e prospettive”, December, 14th, 2017, Ala (TN-Italy)

PARTICIPATION TO *CONGRESSES, SCHOOLS* AND *WORKSHOPS*

Year 2016

SCHOOLS:

- *Russian language*, level A1a (prof. Urkhanova – CLA, Trento - Italy), 50 hours. Assessment: Yes.
- Summer School *Neutron Detectors and Related Applications-NDRA 2016*, Organizer: University of Trento, TIFPA & INFN; at Riva del Garda (TN-Italy), 29th Juny-2nd July 2016. Assessment: passed, 3 ECTS/credits
- Summer School *Smart Materials & Structures 2016*, Organizer: University of Trento, at Trento (TN-Italy), July 14th-16th 2016. Assessment: passed, 3 ECTS/credits
- Summer School “*Science and Cultural Heritage: from non-invasive analysis to 3D reconstruction*”, Organizer: University of Messina - Dipartimento di Scienze Matematiche e Informatiche, Scienze Fisiche e Scienze della Terra (MIFT), Messina (Italy), September 18th-23rd, 2016, Assessment: passed, 5 ECTS/credits

SEMINAR & WORKSHOPS:

- Seminar: “*Nuclear Physics and Painting: Sub-Topic of The Wide And Fascinating Field Of Science And Art*” by prof. R. Leonardi, Faculty of Physics, Trento (I), February 24th, 2016
- Seminar: “*Industrial Engineering Day 2016 Innovation and Careers*”, Faculty of Industrial Engineering, Trento (I), Round table and presentations, March 1st, 2016
- Seminar: “*CRASH COURSE: Introduction to Patent Law*”, by prof. Craig Nard, University of Trento (I), March 3rd, 2016
- Seminar: “*Automatic Mixed Mode 3-D Crack Propagation Calculations*”, by prof. Guido Dhondt, University of Trento (I), March 23th, 2016
- Seminar: “*STAR – A New Hard X-Ray Source*”, by Prof. Raffaele Giuseppe Agostino, FBK, Trento (I), April 1st, 2016
- Seminar: “*Plasma Non Equilibrium at Work: Key to Success of Energy Technologies?*”, by prof. Richard van de Sanden, University of Trento (Italy), March 30th, 2016
- Seminar: “*Phd Research – Software for The Management of The Bibliography*”, by dr.ssa Perillo University of Trento (Italy), April 5th, 2016
- Seminar: “*CRASH COURSE: Intellectual Property*”, by G. Reniero University of Trento (Italy), April 4th, 2016

- Seminar: “*Spoken Language Processing*”, by. Prof. Renato De Mori, University of Trento (Italy), April 14th, 2016
- Seminar: “*CRASH COURSE: Managing an innovative Biotech corporation and creating new start-ups*” by Peter Georg Haag, University of Trento (Italy), April 21st, 2016
- Seminar: “*Covalent and Noncovalent Functionalization of Graphene*”, by prof. Michal Otyepka, FBK, Trento (I), April 21st, 2016
- Seminar: “*Biotechnology-opportunities and challenges*”, by Prof. Mark Perry and Prof. Priti Krishna, Faculty of Law (Trento-Italy), April 26th, 2016
- Seminar: “*Ontology Lexicalization: a core task for the Semantic Web*”, by prof. Prof. Dr. Philipp Cimiano, FBK, Trento (I), April 26th, 2016
- Seminar: “*Sottogruppi algebrici connessi massimali del gruppo Cremona*”, by. Andrea Fanelli (from Universität Basel), University of Trento (Italy), 2 Hours, April 26th, 2016
- Seminar: “*Dealing with context and perspectives for natural language understanding*”, by prof. Prof. Piek Vossen, FBK, Trento (I), April 27th, 2016
- Seminar: “*Seeing the invisible*”, by Dr. Celine Boehm, 1 Hour, April 27th, 2016
- Seminar: “*CRASH COURSE: The Fundamentals of financial statements and start up creation*”, by Giorgio Degasperi, University of Trento (Italy), 2 Hours, May 4th, 2016
- Seminar: “*Inference in the early phase of an epidemic outbreak*” by prof. Gianpaolo Scalia Tomba, University of Trento (Italy), 1,5 Hours, April 28th, 2016
- Seminar: “*Information-flow security for concurrent programs: pitfalls, solutions, and challenges*”, by prof. Heiko Mantel, University of Trento (Italy), 1 h, April 29th, 2016
- Seminar: “*CRASH COURSE: Case study: Robosense Srl*”, by A. Fornasier, University of Trento (Italy), 2 Hours, May 4th, 2016
- Seminar: “*CRASH COURSE: Horizon 2020: The EU Framework for Research and Innovation – Introduction to research opportunities for young researchers*” by Samanta Voltolini, University of Trento (Italy), 2 Hours, May 11th
- WorkShop: “*What next in radiobiology at INFN*”, FBK Trento (Italy), 2 Days, May 12-13th
- Seminar: “*CRASH COURSE: A practical approach to Horizon 2020 Proposal writing - How to write and present a competitive proposal*” by Martina Calamusa, University of Trento (Italy), 2 Hours, May 18th
- Seminar “*CRASH COURSE: How to manage H2020 European research and innovation projects*” by Samanta Voltolini, University of Trento (Italy), 2 Hours, May 25th
- Seminar: *Chemistry of Polycarbosilane and Derivative Silicon Carbide Fibers for Super High Temperature Applications*, Lecturer: Masaki Narisawa (Osaka Prefecture University), Juny 13th 2016.
- Seminar: *Thermodynamic Analysis on Polymer Pyrolysis Process and Recent Spectroscopic Approach on Amorphous Structures*, Lecturer: Masaki Narisawa (Osaka Prefecture University), Juny 15th 2016.

- WorkShop: *Materials Science in Palaeo-environment and Palaeoclimate Research*, University of Trento (Italy), Department of Industrial Engineering, November 18th and 25th 2016
- WorkShop: *Plasma-Therm Technical Workshop: Fundamentals of Plasma Processing (Etching and Deposition)*, FBK, Trento (I), November 28th, 2016.

CONFERENCES:

- *EXRS 2016 Conference* (www.exrs2016.se) at Gothenburg (Sweden) on Juny 19th -24th 2016:
- *EAGLE 2016 - Eagle-Rare-Earth Doped Glass Materials and Fibre Lasers*, FBK Trento (Italy), October 18-19th

Year 2017

SCHOOLS:

- *Russian language*, level A1b (prof. Urkhanova – CLA, Trento - Italy), 50 hours. Assessment: Yes.
- *Russian language*, level A2a (prof. Urkhanova – CLA, Trento - Italy), 50 hours. Assessment: Yes.
- TOP STARS 2017 EIT Raw Materials Winter School November 6-15, 2017, Department of Industrial Engineering University of Trento (I). WINNER of the “***La Galvanica Trentina Challenge AWARD***”.

SEMINAR & WORKSHOPS:

- Workshop: *Macro X-ray Fluorescence Scanning in Conservation, Art and Archaeology*, Palazzo dei Congressi della Stazione Marittima, Trieste (Italy), 24-25 September 2017.
- Workshop: *EXSA QUANT 2017 - Workshop on Quantitative Methods in X-Ray Spectrometry*, Berlin (D), 9th-11th October 2017.
- Seminar: *UV Resonant Raman scattering beamline at Elettra Sincrotrone Trieste: a platform for material science*, 19/04/2017, by Barbara Rossi, FBK, Trento (I),
- *PhD Short Course Contact and fracture mechanics*, by Sergey Verlinsky, Department of Industrial Engineering University of Trento (I), May 30th and June 1st, 2017

CONFERENCES:

- *TXRF2017 - 17th International Conference on Total Reflection X-Ray Fluorescence Analysis and Related Methods*, Brescia (I), September 19-22, 2017.

- *Antiche monete veneziane del sec. XVI delle raccolte numismatiche alensi: studi e prospettive*, Ala (TN-Italy), December 14th, 2017

Year 2018

SCHOOLS:

- *Maud 2018, Materials Characterization by the Combined Analysis*, Department of Industrial Engineering University of Trento (I), 26 - 30 November 2018.

SEMINAR & WORKSHOPS:

- *Qualisteelcoat Classi Di Corrosività E Protezione Dell'acciaio*, Department of Industrial Engineering University of Trento (I), June 04 2018.

CONFERENCES:

- EXRS 2016 European Conference on X-ray Spectrometry, Ljubljana (SLO), 24 - 29 June 2018

ACKNOWLEDGEMENTS

I will thank here:

- 1) Dr Mauro Bortolotti and dr. Evgeny Borovin for their important support in machine set-up.
- 2) Prof. Stefano Gialanella, Dr. Lorena Maines and dr. Gloria Ischia for SEM-EDXS support.
- 3) Dr. Elena Corradini, of the Biblioteca of Ala (TN-Italy), for his precious support and assistance in the temporary transfer of the Venetian coins of the Ala Museum to the University X-ray laboratory.
- 4) Prof. Diego Ercole Angelucci for intermediation with the Ala Museum.
- 5) Prof. Alberto Molinari for titanium alloys samples.
- 6) Dr. Giancarlo Pepponi and prof. Luca Lutterotti for their precious suggestions with GIMPY and MAUD software.